RICE UNIVERSITY

OBSERVATION OF JET PHOTOPRODUCTION AND COMPARISON TO MONTE CARLO SIMULATION

by

DON LINCOLN

A THESIS SUBMITTED
IN PARTIAL FULFILLMENT OF THE
REQUIREMENTS FOR THE DEGREE
DOCTOR OF PHILOSOPHY

APPROVED, THESIS COMMITTEE

Dr. Marjorie D. Corcoran
Professor of Physics, Director

Dr. Gordon S. Mutchler
Professor of Physics

Dr. Richard A. Wolf
Professor of Space Physics and Astronomy.

Houston, Texas

August 1993

Observation of Jet Photoproduction and Comparison to Monte Carlo Simulation

by

Don Lincoln

Abstract

The photon is the carrier of the electromagnetic force. However in addition to its well known nature, the theories of QCD and quantum mechanics would indicate that the photon can also for brief periods of time split into a $q\overline{q}$ pair (an extended photon.) How these constituents share energy and momentum is an interesting question and such a measurement was investigated by scattering photons off protons. The post collision kinematics should reveal pre-collision information. Unfortunately, when these constituents exit the collision point, they undergo subsequent interactions (gluon radiation, fragmentation, etc.) which scramble their kinematics. An algorithm was explored which was shown via Monte Carlo techniques to partially disentangle these post collision interactions and reveal the collision kinematics. The presence or absence of large transverse momenta internal ($k_\perp$) to the photon has a significant impact on the ability to reconstruct the kinematics of the leading order calculation hard scatter system. Reconstruction of the next to leading order high $E_\perp$ partons is more straightforward.

Since the photon exhibits this unusual behavior only part of the time, many of the collisions recorded will be with a non-extended (or direct) photon. Unless a method for culling only the extended photons out can be invented, this contamination of direct photons must be accounted for. No such culling method is currently known, and so any measurement will necessarily contain both photon types.

Theoretical predictions using Monte Carlo methods are compared with the data

and are found to reproduce many experimentally measured distributions quite well. Overall the LUND Monte Carlo reproduces the data better than the HERWIG Monte Carlo. As expected at low jet $E_\perp$, the data set seems to be dominated by extended photons, with the mix becoming nearly equal at jet $E_\perp > 4$ GeV. The existence of a large photon $k_\perp$ appears to be favored.

Acknowledgements

Zippety doo dah, zippety ay...my oh my, what a wonderful day, plenty of sunshine coming my way...zippety doo dah, zippety ay....[1]

You should pardon the rather nauseating enthusiasm, but like the albatross of the Ancient Mariner, when a thesis is no longer hanging around your neck, you're relieved. It is true, though, that work like this should not go unpunished and, borrowing from Claude Raines, it is time to round up the usual suspects.

Marj Corcoran, as a thesis advisor, should be singled out for special blame. In the seven or so years that I've worked for her, I've learned a lot and grown from an interested amateur to a passable professional. This is in large part due to Marj. She helped me when I didn't have a clue and generally stayed out from underfoot when I did. I owe her a debt which I will not be able to repay, except perhaps by someday doing the same for a student of mine. I hope to be able to do it as well.

Donna Naples, my co-conspirator, has helped a lot over the years. She blazed out a few paths ahead of me so I didn't have to and I have used her work more than I've used anyone else's. Together, we have hammered out a lot of problems, gleaned valuable insights into the experiment, and the combined work has usually been better than either of ours alone. Of course, what with her being one of the finest people ever known and all, this should be expected.

Peter Kasper has been described the E683 scape-kangaroo. Somehow, I think a wombat would be a better description, but since I don't even like Fosters, I'm prepared take other people's word for it. Peter has the very useful talent of being able to critically evaluate an idea. He cuts through the extraneous crud and gets right to the heart of it. He has probably been the best defense we have had against sinking into a warm, fuzzy, introspective fog. I recommend he be retained, with no more than a 10% pay cut.

John Marraffino has proven over the years to be a great drinking buddy. This is somewhat ironic, as I don't recall if we've ever had a drink together, but you get the

[1] With apologies to Walt Disney for stealing lyrics from the film 'Song of the South.'

idea. When the enormity of it all has gotten to be too much, he always has good jelly beans and wildly improbable stories. He's also taught me a lot about computers, and I don't hold it against him that he has become the local PAW/HBOOK guru.

The rest of the E683 collaborators have all helped in their various ways and while I do not list them here, their contributions should not be minimized. I would like to explicitly like to thank Med Webster and George Chang for writing umpteen letters of recommendation.

Special thanks go to all of the serious tennis players at Fermilab, without whom we might have taken only nuclear data.

And of course there is my family. Unfortunately, they weren't much help in working on the experiment and thesis. Lord knows, I've tried. Several times I've said 'You know dear, a really *good* wife would type this for me.' Usually I have to sleep on the couch those nights. Actually, Maureen and Renée have both been great. They have understood when 2-3 years somehow turned into 5-6 years. For a while, they decided I didn't know how to count, but I mumbled convincingly about relativity and Einstein and all that and they seem to have bought it. This is not the proper forum for effusive sentiment, but I'm glad they're mine.

It seems to have become standard on E683 to wrap these things up with a quote in a foreign language or a bit of philosophy. My French is rusty, so I will offer a thought from R.A. Heinlein that physicists once knew but we are collectively beginning to forget.

> A human being should be able to change a diaper, plan an invasion, butcher a hog, con a ship, design a building, write a sonnet, balance accounts, build a wall, set a bone, comfort the dying, take orders, give orders, cooperate, act alone, solve equations, analyze a new problem, pitch manure, program a computer, cook a tasty meal, fight efficiently, die gallantly.
>
> Specialization is for insects.

- Don Lincoln

February 26, 1994

Table of Contents

List of Figures

List of Tables

1 General Theoretical Considerations

1.1 Broad Overview

Historically the field of physics has alternated between reductionism and search for structure.[2] Democritis is reported to have postulated that all matter was created from atoms, which were thought to be indivisible. This theory was debated for millenia but was finally supported in a scientific manner by the birth of the field of chemistry. However in the late nineteenth and early twentieth century, the investigations of Rutherford, Bohr, and others showed that atoms were made of smaller particles that eventually became known as protons, neutrons and electrons. The 'indivisible' atoms were finally shown to have a substructure, a fact which was viewed with roughly equal parts of delight and dismay: delight because new discoveries are always interesting and dismay because a badly or non-understood structure is usually viewed as unaesthetic.

Subsequent investigations observed previously unknown symmetries, most notably isospin which demonstrated the fundamental 'sameness' of protons and neutrons and suggested that they were simply two different phases of a more basic 'nucleon'.

However the anomalous magnetic moment of the proton and neutron suggested a deeper level of structure; a suggestion reinforced by the explosive proliferation of new particles in the early cosmic ray and accelerator experiments. The relationships between these particles led Gell-Mann and Zweig [2] to independently propose that the new 'zoo' of particles could be explained by a substructure of a particular type, the now familiar 'quark theory,' which is a subset of the very successful Standard Model.

[2]Author's Note: It is assumed that the reader has a working knowledge of the nature and history of high energy physics (HEP.) The concepts of quarks, leptons, vector bosons, the three known forces (strong, electro-weak, and gravity,) should be understood at least at the 'Scientific American' level. Most importantly for this dissertation, the general nature of photons, quarks and gluons and the quark and gluon content of baryons and mesons should be familiar ideas. Further, the reader is assumed to generally understand what a jet is. If the reader is unfamiliar with these concepts and the whirlwind tour of the birth of modern physics given in this section, it is suggested that they peruse an introductory text (c.f. [1].)

Current theory holds that the baryons and mesons visible in high energy physics (HEP) experiments are actually composite objects made primarily of quarks and gluons (these are collectively known as partons.) Using quasi-classical terminology, the quarks are 'matter' and the gluons are self-interacting color force mediating particles, although the size and energy scale typical of quarks and gluons make such a description rather fuzzy. Baryons are made of three valence quarks and a cloud of surrounding gluons. Mesons are different in that they consist of a quark/anti-quark ($q\bar{q}$) pair, with the requisite gluon cloud. In both cases, it is possible for the gluons to temporarily pair-produce $q\bar{q}$ pairs, thus increasing the complexity of the structure of baryons and mesons (known collectively as hadrons.)

Given that there appeared to be a rich hadronic sub-structure, scientists wanted to investigate the internal degrees of freedom of the various hadrons. Since the leptons remain pointlike particles,[3] they are ideal probes for investigating this (at that time) unexplored domain. The reason for this is simple: leptons act as point-like fermions and therefore they have no sub-structure to complicate the interaction. As we will see later, the fact that they only interact via the electro-weak force is another, more subtle, reason. Some of the first questions asked about the nature of quarks were: (1) What is their charge? (2) What is their spin? and, (3) What is their momentum distribution within the hadron (i.e. structure functions)?

In 1972 Kendall and Friedman [3] published results of a series of experiments that investigated questions like these. Questions (1) and (2) proved relatively easy to answer and the quarks were shown to be fractionally charged fermions. Question (3) was also investigated but turned out to be a more difficult thing to measure. It is a measurement of this nature that this dissertation attempts to make and so a more detailed outline of the problem is given in the next section.

[3]It is more correct to say that at presently available energies, no leptonic sub-structure has been observed.

1.2 Early Structure Function Experiments

The earliest experiments to probe the structure of hadrons was done at SLAC using an electron beam to probe the proton's structure. While earlier experiments investigated the exclusive reaction $e+p \rightarrow e+p$, these experiments were performed with a sufficient amount of energy to ensure that the proton was destroyed: $e+p \rightarrow e+$(anything) and were therefore called Deep Inelastic Scattering (DIS). The essential idea was that if the incoming electron and proton kinematics were well known and the outgoing particles' kinematics were well measured, any discrepancies in energy conservation had to come from an inelastic channel (i.e. the energy flowed in to or out of an internal degree of freedom.)

Figure (1) shows a schematic of a DIS experiment along with the standard terminology. Conservation of 4-momentum at the virtual photon-proton vertex yields (dropping the covariant indices, all dot products are between 4-vectors):

$$(P+q)^2 = W^2 \tag{1}$$

which, given $P^2 = M^2$ becomes

$$2P \cdot q = -q^2 - M^2 + W^2$$

obviously if the collision were elastic then $M = W$ and

$$\chi \equiv \frac{-q^2}{2P \cdot q} = 1.$$

So the extent to which χ deviates from 1 indicates the level to which the inelasticity (and internal degrees of freedom) of the proton come into play.

In 1969, Feynman [4] suggested the following ansatz. Suppose that the incoming particles were of sufficient energy that the masses and internal (i.e. primordial) $p_\perp$'s were negligible. If this were the case, it would be possible to write the fractional 4-momentum of a particular parton as $p^\mu = xP^\mu$ where lower case indicates partonic and upper case indicates hadronic level. While equation (1) is written as a collision between a virtual photon and the proton, if it were written as a collision between the virtual photon and a *parton*, it could be formulated

$$(xP+q)^2 = W^2$$

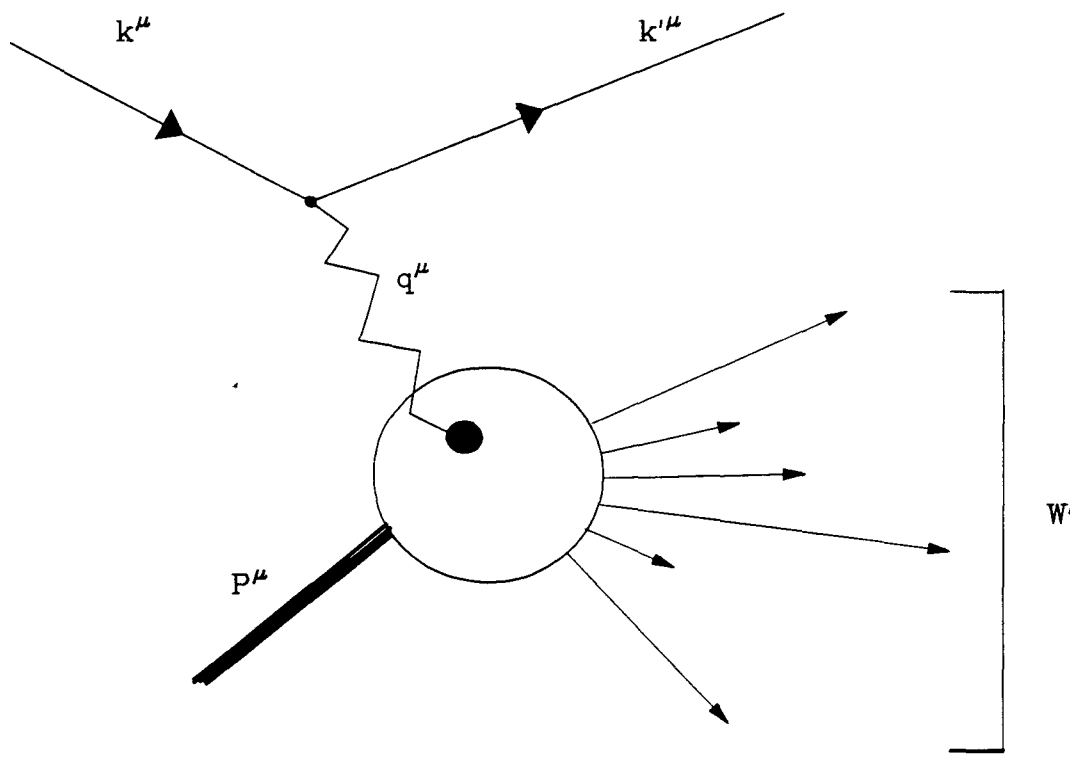

Figure 1: Shown is a schematic of a typical DIS experiment. k^μ and k'^μ indicate the 4-momentum of the incoming and outgoing probe leptons respectively. P^μ is the 4-momentum of the incident target particle, while W^μ is the combined 4-momentum of all of the final state particles, excluding the recoiling probe lepton. q^μ is the 4-momentum of the probing virtual photon, measured from the difference between the momentum of the incoming and outgoing probe lepton.

following a similar solution, and applying the fact that the masses are considered small $W^2, M^2 \ll q^2$, we see that

$$x = \frac{-q^2}{2P \cdot q} \tag{2}$$

which demonstrates that in the limit of the Feynman ansatz, the fractional 4-momentum of the parton within the proton is accessible by simply measuring the 4-momentum of the virtual photon or, as a practical matter, by measuring the change in energy and momentum of the probe electron.

1.3 Photon Structure

At first glance, the concept of photon structure seems somewhat silly. Quite early in a physicist's education, the properties of photons are discussed. They are the quantized carrier of the electromagnetic force, carrying no mass, continuously travelling at the speed of light, and certainly containing no level of substructure. However, along with the acknowledgement that the photons are quantized comes the 'non-intuitive' effects of quantum mechanics. As an example, the Heisenberg Uncertainty Principle allows that energy need not be conserved as long as the non-conservation occurs for a sufficiently short period of time. A consequence of this principle, in conjunction with some ideas culled from the theory of **Q**uantum **E**lectro**D**ynamics (QED,) is that the photon is allowed to spontaneously (and for very short periods of time) disassociate into e^+e^- pairs. These pairs quickly recombine, but for that short moment it makes sense to wonder about the fractional momentum distribution of these temporary constituents.

In a similar vein, another possibility is that the photon will disassociate into a $q\bar{q}$ pair. Like the mesons mentioned in section (1.1,) it is possible that these quarks and anti-quarks will further emit gluons, but the requirement that they annihilate to reform the 'normal' photon necessarily suppresses such a complication. One would therefore expect that each parton typically has on the order of half of the momentum of the photon.

At this time, it is appropriate to make a small digression. In the familiar theory of QED, the coupling constant α is quite small ($\approx 1/137$), which allows perturbative

expansions of the relevant matrix elements in powers of α. However, for Quantum ChromoDynamics (QCD,) the theory of strong interactions, the coupling constant α_s is much larger. This implies that an expansion of the matrix elements in terms of α_s is not viable, as the 'perturbative' terms are of a similar magnitude as the 'lower order' terms.

However, α_s is a 'running coupling constant' which means that the strength of the interaction is dependent on the magnitude of the energy transferred. As the energy transfer increases, α_s decreases. Typical values of α_s at fixed target energies are ($\approx 0.1 - 0.2$). The implications of α_s's variability are that some aspects of the photon's structure are presently calculable and some aren't. For this reason, the photon's structure function is sometimes artificially split into two parts: a calculable, 'perturbative' section and a non-calculable, non-perturbative part. Figure (2) illustrates the two domains.[4] As can be seen from the figure, this distinction reflects our ignorance more than any physical difference.

Equation (2) shows that in the limit of the Feynman ansatz, x can be taken as the four momentum fraction a parton carries of the parent hadron. We define the notation $f_{i/\gamma}(x, Q^2)$ to be the probability that an i flavor parton can be found in the photon with a four momentum x at a probe scale of Q^2. If we define further e_i to be the electromagnetic charge of the i flavor parton in units of the electron charge, we may define the F_2 structure function as:

$$F_2(x, Q^2) = \alpha \sum_i e_i^2 x f_{i/\gamma}(x, Q^2) \tag{3}$$

where i is summed over the kinematically accessible quark flavors (i.e. $m_i^2 < Q^2$.) As is usual for photon structure function physics, the F_l structure function is not discussed, since its contribution to the cross-sections is negligible in the kinematic region of interest.

First we investigate the non-perturbative (VDM) photon structure function. Since the probe scale for VDM is low, the gluon cloud surrounding the valence quarks

[4]Historically this non-calculable part has been called VDM (for Vector Dominance Model). This is because the photon has been assumed to have the same internal structure as a ρ or ω vector meson. Except for the angular momentum quantum numbers, the structure is very similar to that of a pion.

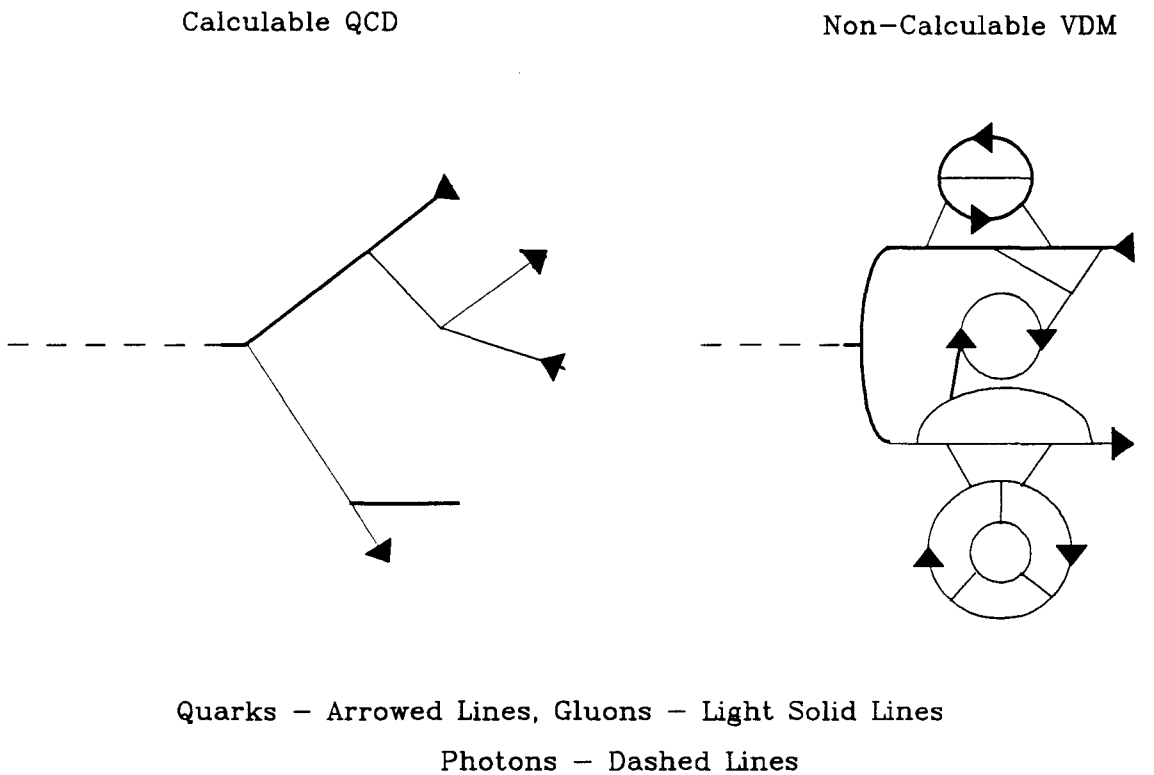

Figure 2: The extended (i.e. hadronic) photon is often split into two different aspects. It is thought to be possible to calculate part of the photon's structure (the calculable QCD part,) but it is also thought that there is a portion of the structure that is poorly understood (the non-calculable VDM part.) The difference is one of complexity and this figure tries to illustrate the difference between the two. As our understanding of how to calculate low energy partonic splittings improves, the artificial distinction between these two aspects of the photon's nature will be reduced. Note that in Reference [18] a method for removing this distinction has been explored.

is taken to be well developed and it is therefore assumed that the VDM structure function may be modelled by that of a pion, suitably renormalized for the different color factors. Using the measured $\overline{u}$ content of the pion [17], one can model the VDM structure of the photon as [15]

$$F_2^{\mathrm{VDM}}(x, Q^2) = (0.20 \pm 0.05)\alpha(1 - x) \tag{4}$$

Because the coupling between the 'true' photon and the $q\overline{q}$ pair is purely electromagnetic for the perturbative photon, the predicted momentum fractions are (relatively) easy to calculate and predictions exist at asymptotically free order [5, 6, 7, 8], leading order [7, 9, 10, 11] and next to leading order [12, 13] levels.[5] The reader should be aware that many of these papers are quite theoretical and are therefore not particularly illuminating for someone wanting a 'quick read.' Berger and Wagner [16] have written a nice review article of $\gamma\gamma$ (explained below) physics which discusses these calculations in a more friendly manner.

Throughout this thesis, I use notation that is standard to the field, but not obvious to the uninitiated. Work on the photon structure function from first principles has been going on for 20 years, and has gone through various levels of sophistication. The earliest calculations used only QED arguments. The photon couples to the $q\overline{q}$ pair merely through its electromagnetic charge. No gluons are emitted and the 'two body' nature of the problem greatly simplifies the calculation. Such models are collectively called the QPM or **Q**uark-**P**arton **M**odel, or occasionally asymptotically free order. Note that QCD plays no role in these structure functions.

In the late 1970's, the calculations were made more sophisticated and leading order QCD corrections were made to the QPM. Now the quarks from the initial splitting were allowed to gain QCD vertices (i.e. gluon radiation and the like) up to leading order. Such structure functions are called either QCD structure functions, QCDLO or alternatively leading order structure functions.

Next to leading order structure corrections to the QPM are also available. There does not appear to be a special name for structure functions of this form. They

[5] Leading order indicates the simplest $q\overline{q}$ splitting. Next to leading order requires an additional gluon vertex.

are simply called QCD next-to-leading order, or QCDHO. Figure (3) illustrates the differences between the different types of structure functions.

The QPM model (or asymptotically free order) has been calculated and this structure function may be written

$$F_2(x,Q^2)^{(\mathrm{QPM})} = \frac{3\alpha}{\pi}\sum_f e_q^4 x(x^2+(1-x)^2)\log(\frac{Q^2}{m_q^2}\frac{1-x}{x}) \tag{5}$$

The most striking feature of this structure function is its increase with x. Note how different this is compared to equation (4.)

Mathematically QCDLO and QCDHO are not very illuminating. I give a generic LO result below.

$$F_2(x,Q^2)^{(\mathrm{QCDLO})} = \frac{3\alpha}{\pi}\sum_f e_q^4 f_{i/\gamma}(x)^{\mathrm{QCDLO}}\log(\frac{Q^2}{\Lambda^2_{\mathrm{LO}}}) \tag{6}$$

where $f_{i/\gamma}(x)^{\mathrm{QCDLO}}$ is calculation dependent and Λ^2_{LO} is the QCD scale parameter in LO.

The Drees-Grassie structure functions [18, 19] remove this (artificial) distinction between perturbative and non-perturbative behavior at the expense of no longer being able to separately calculate the perturbative part. The structure functions of more obviously hadronic particles (pion, protons and the like) can not be calculated perturbatively (see above.) However, via a number of techniques, the evolution of the structure function as Q^2 changes is an easy thing to calculate. Using this technique, a 'base structure function' (i.e. an experimental measurement) is needed. Essentially, the measured structure function supplies a boundary condition for the integro-differential equations that describe the Q^2 evolution. Such a technique has been applied to the photon structure function [18, 19], and has been shown to adequately represent the data. While subsequent authors have improved the early result, I shall refer to this type of photon structure function as Drees-Grassie after the inventors [18]. This structure function has been implemented in the HERWIG [35] Monte Carlo. As we shall see later, the difference between Drees-Grassie and the split VDM/QCD approaches to photon structure functions complicates the comparison between the various Monte Carlos.

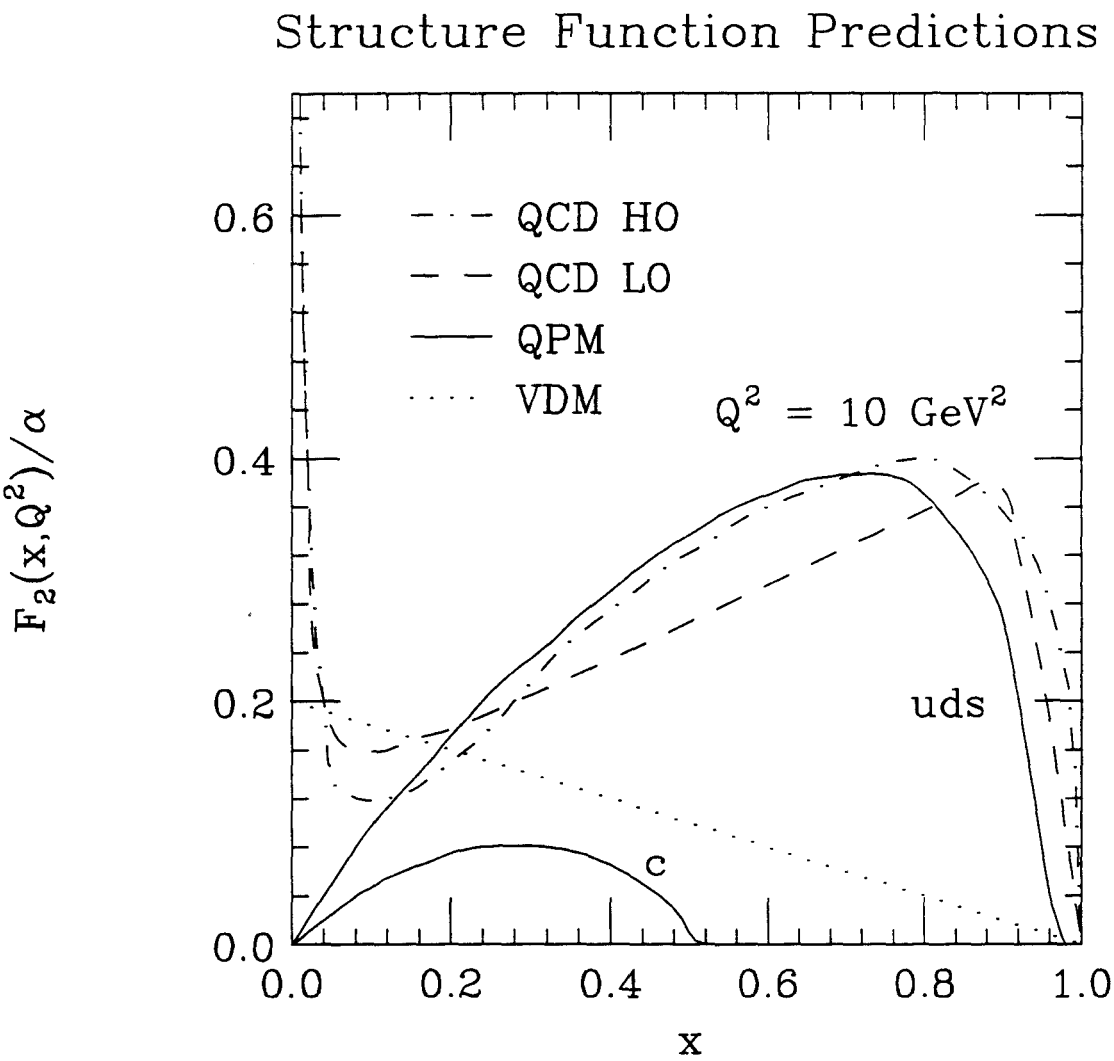

Figure 3: Shown are examples of different photon structure functions. This plot should not be taken to be complete, as dozens have been proposed. However, the different classes shown should be taken as representative. The figure is courtesy reference[16] and the details of how this particular figure was generated can be found there. The difference between the three shown perturbative structure functions shows the scale of the theoretical ambiguity. Except at the highest values of x, this discrepancy is less than the VDM contribution. This figure is especially interesting in that it highlights the level of precision and statistics needed by an experiment in order to distinguish between the proposed structure functions.

1.4 Previous Measurements of the Photon Structure Function

The standard (and very clever) way to measure the photon structure function is by using an e^+e^- collider to induce photon-photon ($\gamma\gamma$) scattering. If one lepton emits a photon that is very nearly on the mass shell (i.e. approximately collinear with the original lepton) and the photon pair-produces into $q\bar{q}$ pair, the other lepton forms the probe and the result is a tricky DIS experiment. Such experiments have been done and the following experiments have published relevant results: from the DESY PETRA ring-JADE [20, 21, 22], PLUTO [23, 24, 25], CELLO [26], TASSO [27]; from the SLAC PEP ring-TPC/Two-Gamma [28, 29], and from KEK's Tristan ring-AMY [30, 31]. Perhaps surprisingly no LEP photon structure function measurements have been published at this time.

With so many measurements, the theory is quite constrained. While figure (3) shows the discrepancy between the various perturbative structure functions is small, it also highlights the large difference between the pion (or VDM) structure function and those accessible by perturbative calculation. Figure (4) shows some experimental data at a $Q^2 = 23$ GeV^2 from the TASSO collaboration overlaid on a theoretical curve. It is apparent that the photon structure function is not well described by a VDM model. It is less clear that a simple QPM model is insufficient to model the data, although a mixture of the QPM and VDM model is favored. While it would be possible to look at many other plots, they would merely reinforce these observations. The interested reader is invited to peruse [16] for an exhaustive review.

1.5 Parton Intrinsic Transverse Momentum

At first, a theoretical section on parton intrinsic transverse momentum (generically called $k_\perp$) seems out of place, but its relevance will presently become apparent. The simplest source of $k_\perp$ stems from a combination of 1.) the compositeness of hadrons, 2.) the approximate 1 femtometer (a.k.a. fermi or fm) radius of hadrons, and 3.) Heisenberg's Uncertainty Principle, which states that if the position of an object is

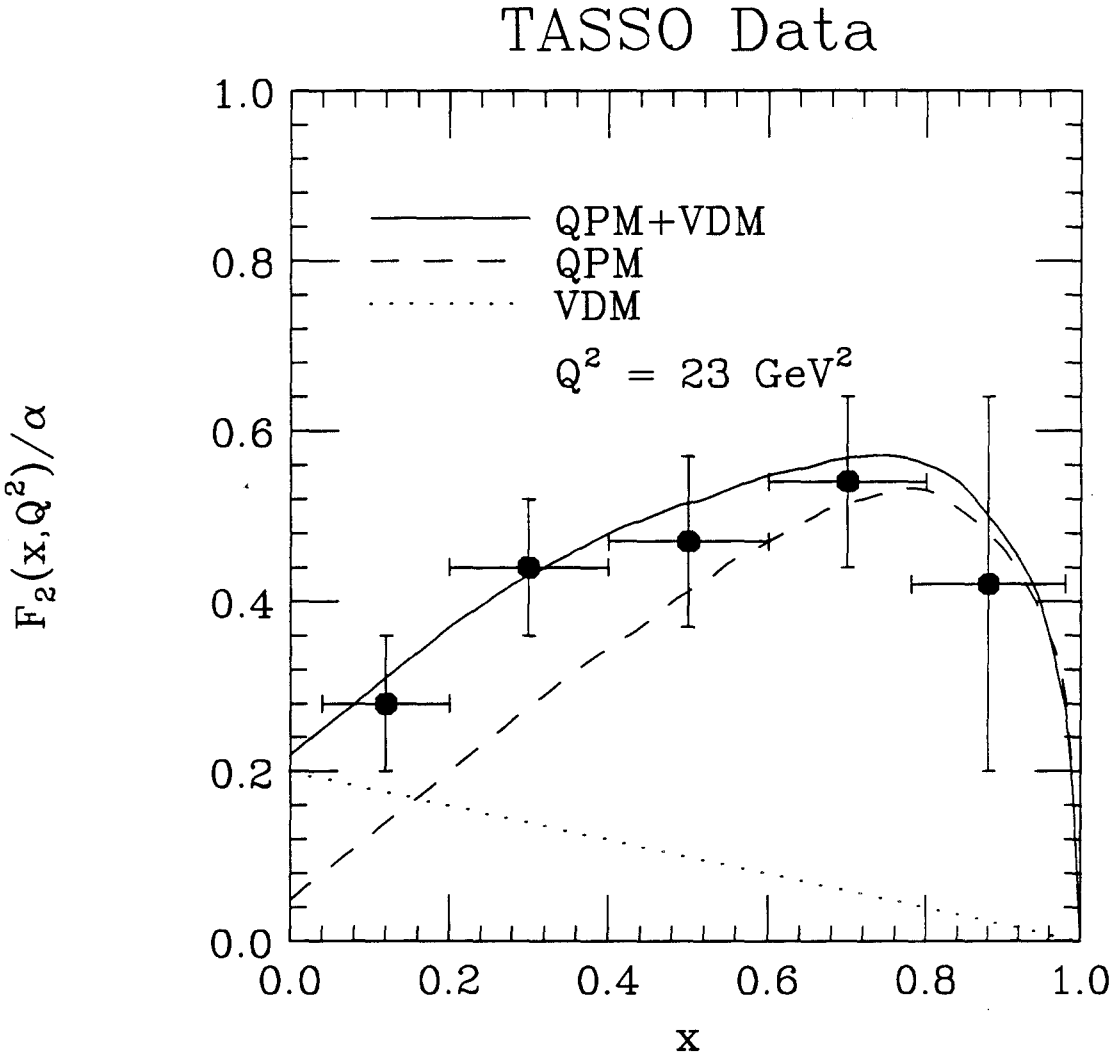

Figure 4: Shown is charm subtracted TASSO data taken at a $Q^2 = 23$ GeV^2. Overlaid are the VDM, QPM and combined QPM/VDM model. It is apparent that the VDM model does not represent the data. The QPM model may represent the data, but the combined model is favored.

known with a certain resolution (e.g. a parton is localized as being within a hadron,) the uncertainty of its momentum follows the relationship $\Delta x \Delta p \sim \hbar$. Using the transverse size of a hadron (typically 0.7 fm), we may estimate this $k_\perp$

$$k_\perp \sim \frac{\hbar c}{r_{\text{hadron}}} \sim 300 \text{ MeV}$$

This contribution to the $k_\perp$ of the parent hadron is often called the primordial $p_\perp$ and is typically modelled by a double Gaussian with $\sigma_x^{k_\perp} = \sigma_y^{k_\perp} = 300$ MeV.

A second source of $k_\perp$ is conceptually easy to understand, although less straight forward to express mathematically. As a parton moves through space, QCD predicts that it will undergo spontaneous self interactions, that is, gluons will split into two gluons ($g \to gg$) or a $q\bar{q}$ pair ($g \to q\bar{q}$) and quarks will emit gluons ($q \to qg$). Unless the emission results in two partons collinear with the initial parton, each will gain an equal and compensating $k_\perp$ with respect to the initial parton's direction. These emitted partons may undergo subsequent splittings resulting in essentially a shower of partons all with different $k_\perp$'s. A comprehensive theory of multiple splittings is not available, but the (well understood) theory of single splittings may be iteratively applied via Monte Carlo techniques.

The theory of individual splittings was pioneered by Altarelli and Parisi [37]. While the original work should be perused, [38] and [39] give unusually accessible treatments. For a generic branching $a \to bc$, the Altarelli-Parisi evolution equations may be written:

$$dP_{a\to bc} = \frac{\alpha_s(Q^2)}{2\pi} \frac{dk_\perp^2}{k_\perp^2} P_{a\to bc}(z)\, dz \tag{7}$$

where $P_{a\to bc}$ is called the splitting kernel and is characteristic of the splitting type.

$$\begin{aligned} P_{q\to qg}(z) &= \frac{4}{3}\frac{1+z^2}{1-z} \\ P_{g\to gg}(z) &= \frac{6(1-z(1-z)^2)}{z(1-z)} \\ P_{g\to q\bar{q}}(z) &= \frac{1}{2}(z^2+(1-z)^2) \end{aligned} \tag{8}$$

where z is the fractional momentum that one of the post-splitting partons carries of the pre-splitting parton (obviously the other must carry $1-z$), Q^2 is a probe scale

(related to $\hat{p}_\perp$, $\hat{t}$ and variables of the like,) and $k_\perp$ is the transverse momentum of the split partons with respect to the parent parton's direction. Equation (7) essentially gives the probability of a splitting ending up with a parton with fractional momentum z and transverse momentum $k_\perp$.

The Altarelli-Parisi evolution equations are sometimes written as

$$dP_{a\to bc} = \frac{\alpha_s(Q^2)}{2\pi}\frac{dm_a^2}{m_a^2}P_{a\to bc}(z)\,dz.$$

This is an equivalent notation because in terms of longitudinal momentum development, m and $k_\perp$ are indistinguishable ($E^2 - p_z^2 = m^2 + p_\perp^2$.) A $k_\perp$ in the final state kinematically reflects a virtual mass in the pre-split initial state.

A final mathematical note deduces the functional form of the $k_\perp$ probability distribution function. Using $dk_\perp^2 = 2k_\perp dk_\perp$, we see

$$P_{a\to bc} \propto \frac{dk_\perp^2}{k_\perp^2} = \frac{2k_\perp dk_\perp}{k_\perp^2} \propto \frac{dk_\perp}{k_\perp}$$

and therefore one expects the $k_\perp$ distributions of partons b and c in $a \to bc$ to go as $1/k_\perp$. In the case of a $\gamma \to q\bar{q}$, the situation is much the same, except for a different color factor normalization and so the $k_\perp$ distribution of partons coming from a perturbatively split photon should likewise go as $1/k_\perp$. This is the ansatz used throughout this thesis, however one should recall that in reality the parton from the photon is likely to undergo a number of soft subsequent gluon emissions which should slightly soften the $k_\perp$ distribution.

For two related reasons, the $1/k_\perp$ distribution is not valid for all $k_\perp$: 1.) Altarelli-Parisi evolution (and all of QCD) is only valid for large enough Q^2 (e.g. $Q^2 \gtrsim$ a few GeV^2,) and 2.) At low $k_\perp$, equation (7) is unphysical because it indicates a pole at $k_\perp = 0$. At low Q^2, the wavelength of the probe particle is large enough that it is unable to resolve the constituents of the hadron (also recall that at large enough length scales, the hadron is color neutral.) In order to regularize the behavior near $k_\perp \to 0$, a minimum $k_\perp$ cutoff is imposed. Clearly a sharp, arbitrary, cutoff in not desired, but it is a method for approximating the nominally smooth transition from perturbative to non-perturbative QCD. In practice, the Altarelli-Parisi equations are

used in the perturbative region and the simple double Gaussian discussed at the beginning of this section is used for the non-perturbative region.

One should realize that if the $k_\perp$ distribution indeed goes as $1/k_\perp$, this is of some significance since such a behavior is harder than the spectrum (typically $1/p_\perp^4$) expected from leading order calculations. This $k_\perp$ would then have a large impact in the large $p_\perp$ behavior of the overall interaction.

1.6 Monte Carlos

There are a number of 'standard' Monte Carlos (MC) available that generate events (e.g. ISAJET, HERWIG, and PYTHIA.) These programs are a great boon to the HEP community because they are used by many independent researchers and are therefore thoroughly debugged. In addition, since these MCs are used to simulate many different disparate types of physics, they must necessarily better reflect reality than programs written for a more limited goal (they are more constrained.) However, even such complicated MCs necessarily reflect the authors' prejudices and for that reason it is wise to use at least two MCs to estimate the effect of modelling. With this point in mind, the LUND and HERWIG models were investigated.

While the Standard Model forms the basis of most of the standardized MCs, they differ substantially at the fringes of understood physics. Extremely high energies, the Higgs and SUSY sectors and at the other end of the spectrum low $E_\perp$ and Q^2 physics all are model dependent. Perhaps the most striking difference between the MCs lies in the realm of fragmentation. There are three main fragmentation models currently extant: independent fragmentation (IF), string fragmentation (SF) and cluster fragmentation (CF) [32].

The string model has been shown to work quite well in e^+e^- physics. Conceptually it can be visualized as a rubber band that connects the two outgoing partons. As the partons separate, the rubber band stretches and stores potential energy. When the local potential energy densities get sufficiently high, $q\bar{q}$ pairs are 'percolated' out of the vacuum and these form the mesons seen in the lab. The failure of this model lies in its consistent underestimate of the spectator system [33]. This model is

championed by the LUND Monte Carlo [34].

The cluster model is more obviously motivated by QCD. After a collision, a parton has a high virtual mass. This mass is 'radiated away' by gluon emission and $q\bar{q}$ pair production. Perturbative QCD can predict this showering evolution down to an energy scale where α_s becomes large (say $Q^2 \approx 1-2$ GeV^2.) At this time, there is no strongly defensible model for the subsequent evolution, so the model then 'clusters' the q and $\bar{q}$'s into color neutral pairs which are then forced to become mesons [35].

Independent fragmentation is in many ways the least satisfying model. In this model, all of the partons exiting the collision fragment entirely independently. This poses severe problems: a massless, colored, fractionally charged parton becomes a color neutral jet with integral charge. Obviously, this can not be. However, our γp data is best described by IF [40] (at least in some variables that we can measure, most notably gross kinematic and event structure features.) Therefore, this 'ugly duckling' model is what this dissertation uses.

The bulk of this dissertation uses the TWISTER/LUCIFER [65, 66] as the Monte Carlo model to be compared to the data. In addition, the Monte Carlo HERWIG [35] was investigated, although my treatment of the two Monte Carlos is not symmetric. There are subtle fundamental differences in the two Monte Carlo's underpinnings. While such a statement should wait until after the discussion of section (2,) it is possible to say that one of the largest differences between the two lies in their treatment of the virtuality (i.e. $m^2 \neq 0$) of both the incoming and outgoing partons from the collision point. Appendix (A) details how one can reconstruct x from kinematic arguments for various ideas about the partons mass (virtual or otherwise.) It can be seen that massive incident partons complicate the situation because it is no longer possible to write x solely in terms of final state observables. Because HERWIG allows initial and final state gluon radiation (with its attendant highly virtual partons) as the core of its implementation of QCD, it is difficult to use this ansatz to get back to the desired x. TWISTER/LUCIFER uses a different model of the mass of the particles undergoing the hard scatter (i.e. massless partons.) In this case x can be determined solely from final state measurements which makes life easier. There is no

fundamental reason to choose TWISTER/LUCIFER over HERWIG, unless it can be shown that the first models the data far better than the second. However, one must walk before one runs and one must see if an idea can work on an easy problem before it tackles a hard one. For this reason, the ansatzes natural to TWISTER/LUCIFER have been investigated more thoroughly. HERWIG results will pop up sporadically to reinforce points that are made by TWISTER/LUCIFER and to show that many properties of the hard scattering model are seen in both. However, the theoretical ambiguity in how one deals with parton virtual masses is still an unresolved one, and results I am presenting are necessarily model dependent.

An additional difference between the HERWIG and LUND Monte Carlo's is their treatment of spectator partons. In LUND independent fragmentation, the spectator partons are treated as one would treat hard scatter partons of lower energy. In HERWIG, the situation is much different. Cluster fragmentation is central to the HERWIG model, and it is fully applicable only to perturbative systems. Since the underlying event does not satisfy this requirement, the model fails to properly represent the data. For this reason, an extra 'enhanced' underlying event was added to the model. This underlying event simply is an overlay of additional particles onto the hard scatter event, with an ansatz provided by UA5 minimum bias data [36]. This additional underlying event has been shown to be necessary to reproduce our pion data [42], but to be excessive for our photon data. For this dissertation, the enhanced underlying event has been turned off.

There is an entirely separate aspect of Monte Carlo's that can not easily be standardized: the simulation of the experimental devices. While some generalized packages do exist (c.f. GEANT, a CERN developed package,) such programs are generally much slower than one which has been specifically written for an experiment. In E683, we have written device simulators which parameterize our calibration data and these simulations are discussed in section (3.3.)

2 E683 Techniques for Probing the Photon Structure

E683 is a very different kind of experiment than the standard $\gamma\gamma$ probes of the photon structure function. A broad band (i.e. large energy range) real photon beam is made to hit a hydrogen target. When the experimental motivation is to investigate the proton, this situation is rather nice as the photon is a very clean probe.

However, when the intent is to investigate the photon, the situation is significantly messier. In this case, the proton is the probing particle. Since the proton is (a) an extended, composite object, and (b) fundamentally hadronic in nature, a lot of the simplicities of the normal $\gamma\gamma$ DIS experiments are lost. This leads to a number of conceptual difficulties, which I will now discuss.

Figure (5) illustrates the situation when two extended bodies (A) and (B) collide. While Appendix (A.1) derives the equations for x in a Lorentz invariant form, if one assumes massless kinematics it is easy to show that in the AB center-of-mass (CM) frame the fractional momentum of the two hard scattering partons (x_1 and x_2) can be written:

$$x_{1,2} = \frac{E_3(1 \pm \cos\theta_3) + E_4(1 \pm \cos\theta_4)}{\sqrt{s}} \tag{9}$$

(c.f. equation (16) and figure (5)), where E denotes energy, θ the polar angle of the outgoing parton with respect to the direction of travel of particle A, and $\sqrt{s}$ is the CM energy of the AB system. As is apparent from the equation, by measuring the energy and scattering angle of the outgoing partons, one is able to completely determine the fractional momenta of both incoming partons.

However in reality the partons do not cleanly exit the collision point. As the partons draw apart, they fragment [32]; so what is seen in the lab, rather than a single parton, is a collimated 'jet' of particles. In order for equation (9) to apply, it is necessary to understand the extent to which parton kinematics are preserved by the jets.

The theory of jet fragmentation is still in its infancy, so any statements about them are necessarily model dependent. There is a feature of all fragmentation models

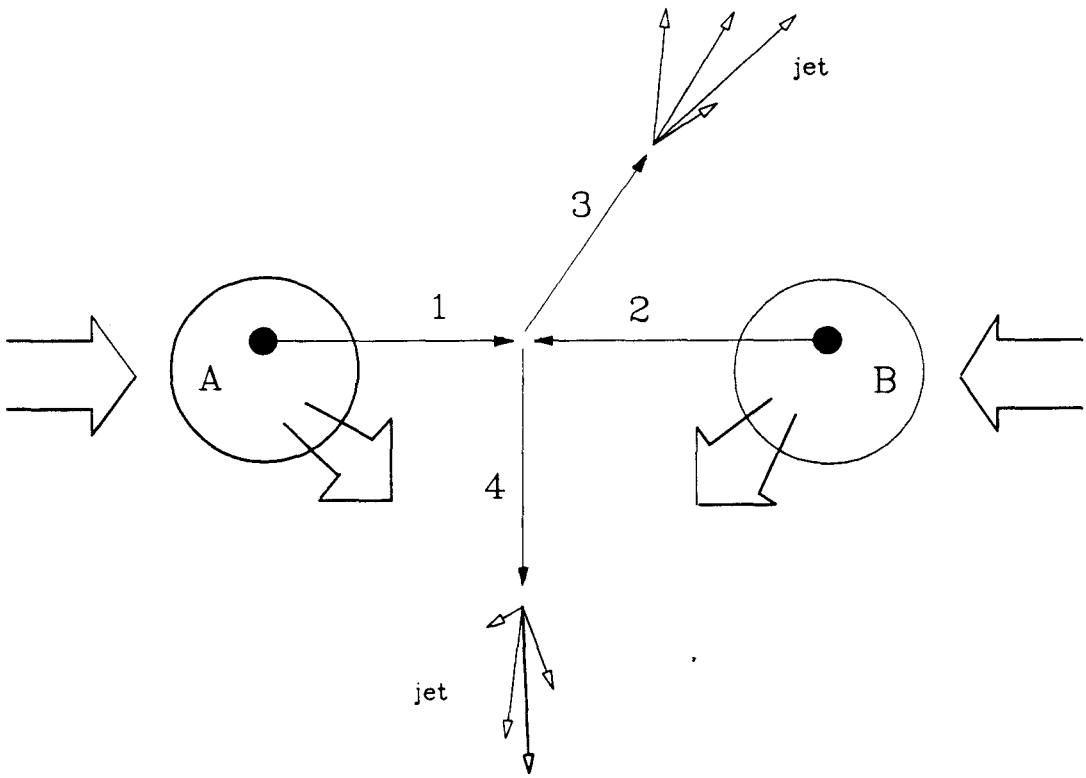

Figure 5: Two extended bodies A and B are allowed to collide. Parton 1 from body A undergoes a hard collision with parton 2 from body B and the result of this hard scatter is a two parton final state (labelled 3 and 4 respectively.) The post collision partons undergo final state interactions which form jets as the observable final state. The non-interacting fraction of bodies A and B which are illustrated schematically as the fat, tipped arrows, also form jets.

which is exceedingly relevant for the purposes of this measurement. The simplest model of parton scattering neglects mass, which implies that the partons exiting the collision are massless (or possibly have $\approx$ 300 MeV mass.) However, after fragmentation, each parton has become a number of particles (typically π's.) Conservation of energy and momentum does not allow for a fission of a massless particle into massive decay products. Even more fatal in terms of energy and momentum conservation is the fact that jet particles have a momentum component of the order half a GeV perpendicular to the original parton direction. This effect gives the jet a large mass– perhaps a fuzzy concept.

Since a jet is an ensemble of particles, the question: 'What does a jet mass mean?' arises. Simply, you can define

$$m^2 = E^2 - \vec{p} \cdot \vec{p},$$

where $E = \sum_i E_i$ and $p_{x,y,z} = \sum_i p_{(x,y,z)i}$ and the sum is taken over all of the particles within a jet. Obviously, if for each particle $E = |\vec{p}|$, the fact that some of the momentum components balance one another ensures that $m_{\rm jet} \geq 0$. It is therefore possible to say that the jet kinematics can not perfectly reflect massless parton kinematics. These ideas are also discussed in [41].

Independent fragmentation is unique in that it unambiguously links each final state particle with a specific parton. This allows the true jets to be known by identifying those particles that came from the two hard-scatter partons. Reference [41] shows that if a particular parton with kinematic variables $(E_{\rm parton}, |\vec{p}_{\rm parton}|, \theta_{\rm parton}, \phi_{\rm parton})$[6] is allowed to fragment many times, the resultant distributions $(E_{\rm jet}, |\vec{p}_{\rm jet}|, \theta_{\rm jet}, \phi_{\rm jet})$ will have the property: $<E_{\rm jet}> = E_{\rm parton}, <\theta_{\rm jet}> = \theta_{\rm parton}$, and $<\phi_{\rm jet}> = \phi_{\rm parton}$, but $<|\vec{p}_{\rm jet}|> \leq |\vec{p}_{\rm parton}|$. To the extent that one believes that massless partons determine the hard scattering kinematics, we see that it is possible to replace the variables in equation (9) with jet variables. Figures (6) and (7) show the correspondence between jet and parton kinematics. The Monte Carlo used was TWISTER using independent fragmentation, but the plots for LUCIFER are comparable. There

[6] E means energy, $|\vec{p}|$ is the magnitude of momentum, θ and ϕ are the polar and azimuthal angles respectively.

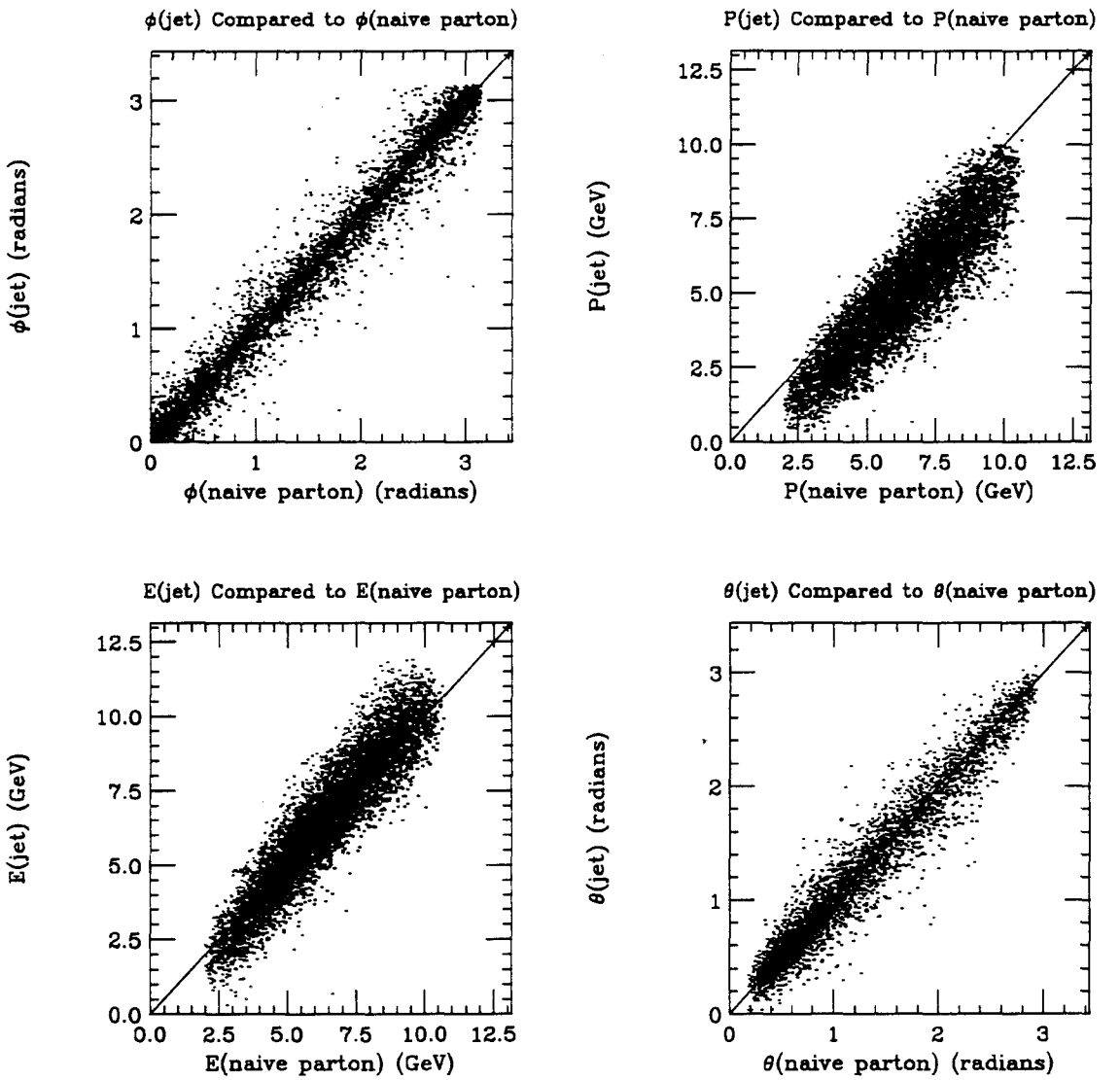

Figure 6: These scatter plots show the correspondence between massless parton kinematics and true jet quantities (using Independent Fragmentation.) $(E, \theta, \phi, |\vec{p}|)$ (CM frame) are shown. The overlaid line shows what perfect parton-jet correspondence would give.

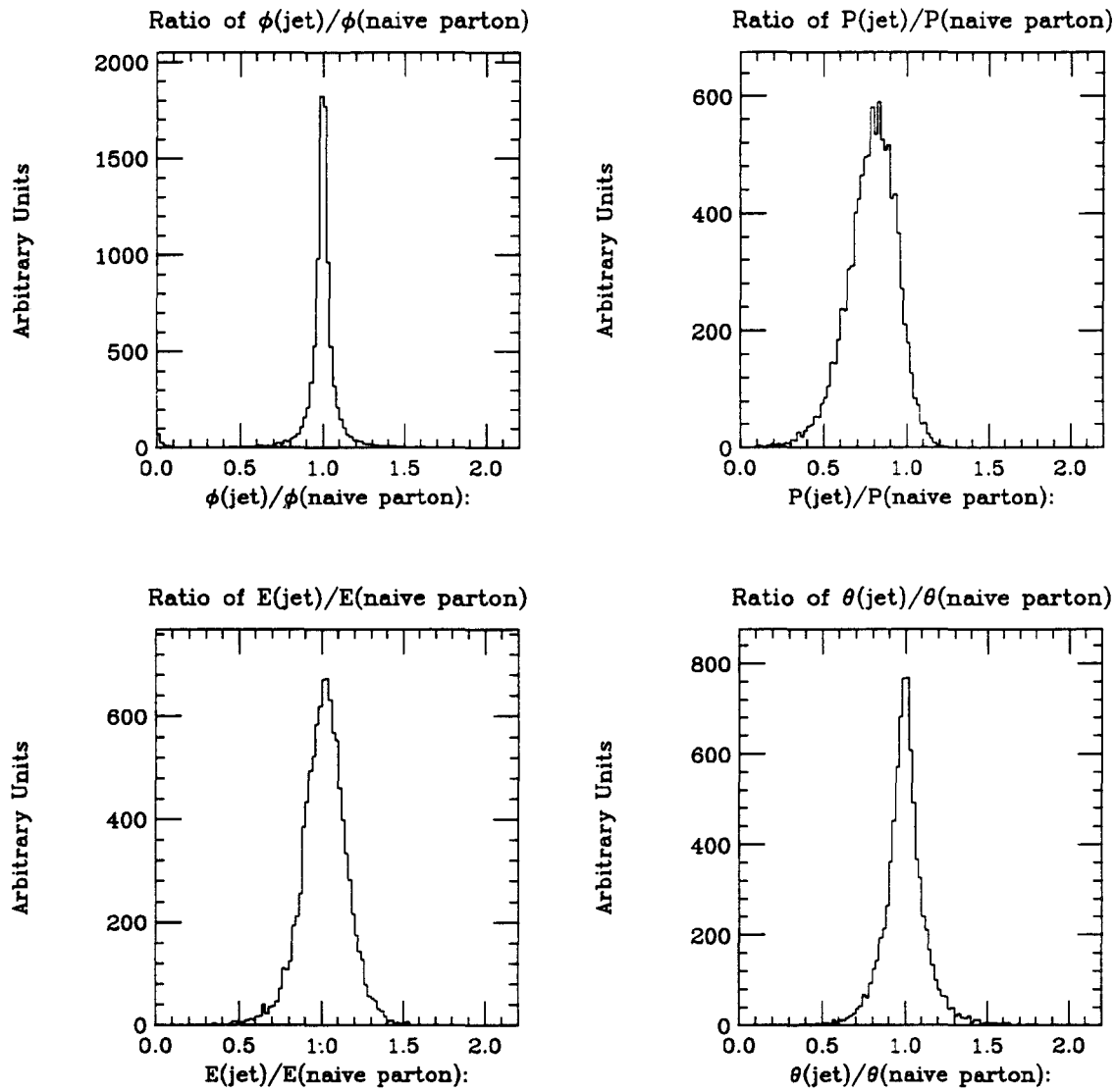

Figure 7: These plots show the ratio of (Jet Kinematics)/(Massless Parton Kinematics) using Independent Fragmentation. Ratios of $(E, \theta, \phi, |\vec{p}|)$ (CM frame) are shown. In the θ and ϕ plots, I have required that the $\theta_{\text{parton}} > 0.5$ radians and $\phi_{\text{parton}} > 0.5$ radians to ensure there will be no divisions by 0. In the case of E, θ, and ϕ the mean ratio is 1.00. In the case of $|\vec{p}|$, the mean ratio is about 0.75.

are no significant energy, structure function, or minimum hard scatter $\hat{p}_\perp$ dependences to the correspondence. Figure (6) shows jet quantities scatter-plotted against parton quantities. The overlaid line shows perfect preservation. Figure (7) plots the ratio quantity(jet)/quantity(parton). There has been a small cut to ensure quantity(parton) $\neq 0$. From the figures, we see that within the context of the Monte Carlo that E, θ and ϕ are preserved (on the average) across fragmentation, but that $|\vec{p}|$ is not, as claimed. These figures were made by generating events that are similar to those that E683 is measuring, and we may estimate an effective jet mass for these processes. Using a jet energy of 5 GeV and the fractional jet momentum of 0.75 (i.e. $|\vec{p}_{\rm jet}|/|\vec{p}_{\rm parton}| \sim 0.75$,) we see that the jet mass is $m \sim \sqrt{5^2 - (0.75 \cdot 5)^2} = 3.3$ GeV!!! This mass is far in excess of any reasonable estimate of the up, down, strange, and charm quarks or gluon masses.

The origin of such a large jet mass is obviously something that needs to be understood. Unfortunately, there is some debate as to the cause. Clearly the answer must lie somewhere between two extremes. Extreme # 1 is that the partons scatter entirely massless and it is only post-collision interactions that cause the mass to appear. In this case, the jet mass is a feature that obscures the 'interesting' hard scatter and must be removed. The above discussion shows how one might do this.

Extreme # 2 is that the jet mass identically reflects the parton kinematics. In this interpretation, the idea of massless parton scattering is a farce, done only for calculational simplicity. In this case, the scattering kinematics must reflect the outgoing parton's heavy mass. Appendix (A.2) calculates x for arbitrary incoming and outgoing kinematics in the beam-target CM frame. It is not possible to express x exclusively in terms of final state quantities unless some assumptions are made. Equation (22) is the analog to (9) when the incoming partons are assumed massless, but the outgoing partons have the large mass that is reflected in the jets. One can see that the difference is the replacement of $E\cos\theta$ by $p_z (E\cos\theta = p_z$, in the limit of massless kinematics.)

What seems to be a consensus among modern QCD theorists [43] is that the truth lies somewhere between these two extremes, with considerable disagreement in

the details. The scattering occurs with the outgoing partons carrying a non-zero, real (i.e. $m^2 > 0$) mass [44]. This mass decays, or is 'radiated away' by gluon emission and $q\bar{q}$ pair production, which occurs until the virtuality has been reduced to a cutoff scale $Q_o^2 \sim 1 - 4$ GeV^2. At this point, non-perturbative forces take over and complete the fragmentation, further creating additional mass. Since the Q_o^2 range of proposed cutoffs is of the same magnitude as E683's hard scatter scale, small theoretical differences can have maximally large consequences for our measurement.

If one estimates the range of discrepancies of found x's possible due to these theoretical ambiguities, one is aided by the fact that for E683 in the CM frame p_z is small ($\theta \sim 60° - 90°$). Taking the maximally bad (i.e. large $\cos\theta$) $\theta = 60° \rightarrow \cos\theta = 1/2$ we can write:

$$\frac{x_1^{\text{virtual}}}{x_1^{\text{massless}}} = \frac{E_3 + p_{z3} + E_4 + p_{z4}}{E_3(1+\cos\theta_3) + E_4(1+\cos\theta_4)}$$

Imposing the (rough but reasonable) conditions that $|\vec{p}| \sim 0.75E, E_3 \simeq E_4$ and the above guess for $\cos\theta$,

$$\frac{x_1^{\text{virtual}}}{x_1^{\text{massless}}} \approx \frac{E_3 + (0.75)\cdot(1/2)\cdot E_3 + E_4 + (0.75)\cdot(1/2)\cdot E_4}{E_3(1+1/2) + E_4(1+1/2)} = 92\%$$

A more sophisticated Monte Carlo estimate (TWISTER), yields $<x_1^{\text{virtual}}/x_1^{\text{massless}}> \approx$ 91%, with an RMS of 5.5%. Obviously the fractional ambiguity has an x dependence, but for typical beam particles, the theoretical ambiguity is of the order 10%.

Using the proper ansatz for scattering for the Monte Carlo that best reproduces our data[7], we can use equation (9), inserting true jet kinematic variables where appropriate. Figure (8) shows the true x_{beam} compared to the x evaluated from equation (9) and post-fragmentation jet kinematics. x is preserved on the average across the fragmentation step with a resolution of 5-10%. If jets can be accurately found, this technique for measuring x will work.

If jets can not be convincingly found, we are not without hope, although such a result will be unfortunate. It is expected that there are distributions (e.g. total energy observed in the detectors, etc.) which will look different as the structure of the photon

[7]TWISTER/LUCIFER with independent fragmentation.

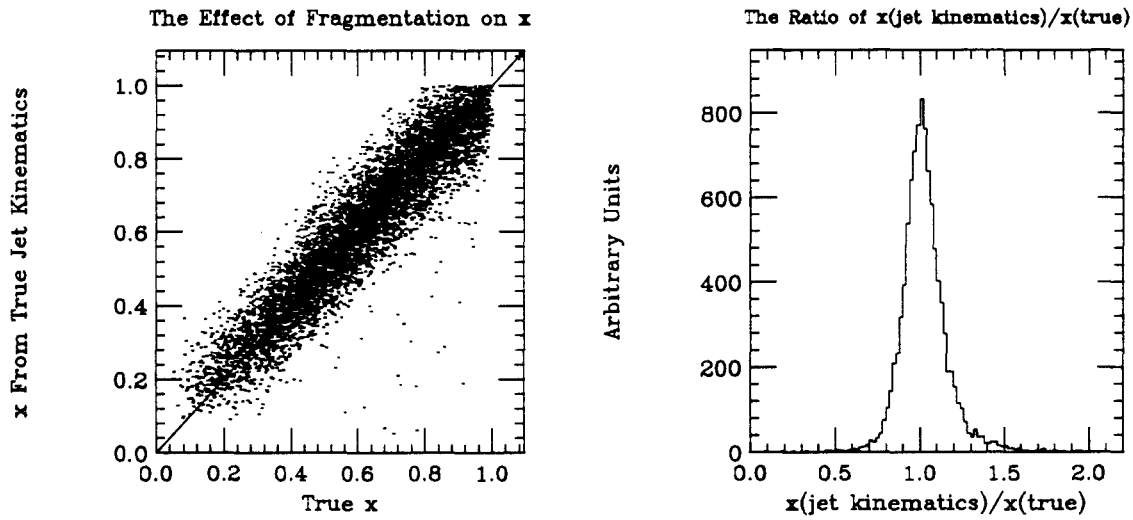

Figure 8: The correspondence of true x_{beam} (as used in the structure function) and x_{beam} as measured from true jet kinematics inserted in equation (9.) On the scatter plot, a line showing perfect preservation is overlaid. The particle type shown is a hypothetical one with all x's equally likely (the so-called 'flat' distribution particles.)

is varied. If this is the case, we will be able to investigate the composition of our data sample (i.e what fraction of our data is VDM, QCD and direct photons?) Since the VDM contribution is expected to be small, if the data distributions are bracketed by the QCD and direct photon distributions, it is conceivable that a fit of the data to a mixture of the two photon types will reveal the sample composition. As we shall see, a significant amount of work has been done to investigate the distributions of final state observables for different photon structure functions.

3 Beamline and Experimental Apparatus

3.1 Beamline

Experiment 683 (E683) is a jet photoproduction experiment located at the end of the Wide Band beamline at FNAL. The Wide Band Beam is at present the highest energy source of real photons in the world and gains its name from its broad momentum

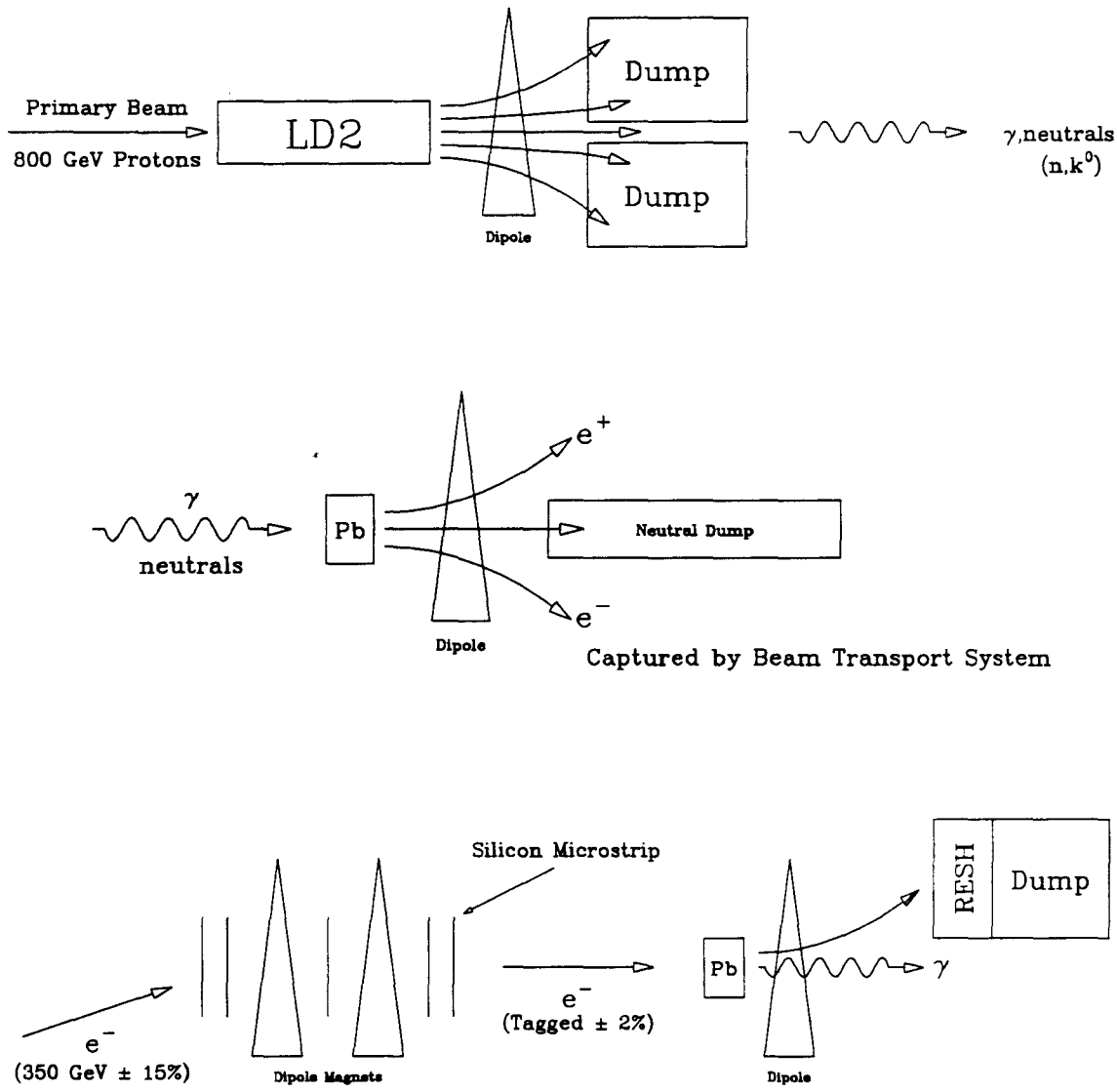

(Figure courtesy of Greg Morrow [49].)

Figure 9: FNAL Wide Band Beam Schematic.

spectrum. While the beam has been discussed in detail elsewhere [45, 46, 47], the method by which the photons are generated is quite interesting and bears mentioning here. (See figure (9).)

During fixed target running, the FNAL Tevatron delivers 800 GeV protons of which a fraction are extracted and steered onto our deuterium primary production target. A tremendous number of particles are produced and are made to pass through strong dipoles which bend the charged particles into total absorbtion dumps and allow the neutral particles (primarily photons from π° decay, but with a largish contamination of n°, K_L^o, etc.) to pass through.

These neutral particles are allowed to pass through a thin lead sheet (50% of a radiation length) the primary effect of which is to cause the photons to pair-produce. The resulting electrons and positrons are again swept out by dipoles into high acceptance beamlines. The remaining neutral particles go forward and are absorbed in a thick beam dump. For technical reasons, only the electrons are used, which decreases the final gamma flux by a factor of 2 but greatly reduces the final beam contamination. The electrons and positrons are created with a large range of momenta and it is the subsequent beam optics that determine the delivered energy range. In order to maximize flux, the beam line was designed with a very large acceptance and the electron's energy has a range of $\pm 15\%$.

These electrons are guided through a momentum measuring spectrometer and finally focussed on the experimental target. Long before the electrons actually hit the target, they are passed through 20% of a radiation length lead radiator and then a strong dipole field. This radiator provides the electrons with a high Z target to induce bremsstrahlung photons. The sweeper dipoles bend the recoil electron and its post-radiation momentum is measured. This will be discussed in more detail below.

3.2 Experimental Apparatus Overview

E683 is essentially an energy flow measuring experiment with a high transverse energy trigger. As one would expect of a high energy physics experiment of this nature, the primary detection mechanism is calorimetry. In addition, the experiment also

includes several proportional wire chambers (PWCs) and drift chambers (DCs), along with a wide aperture magnet. These chambers are not used for this analysis, but it is intended that they will eventually be used for finding the interaction vertex and ensuring that the interaction actually came from the target. This will be especially useful for cross section measurements. In addition, certain measurements will attempt to use the magnet and chambers to measure the charge of the leading particle in a jet or, in the case of a higher twist signal, the charge of the isolated pion.

Before the E683 detectors are discussed in detail, it is necessary to step back and view the Wide Band area as a series of semi-structureless blocks. Conceptually, we can break up the Wide Band area into 4 different modules. These modules are: (1) the Tevatron and the primary beamlines, (2) the electron portion of the beamline, which notably contains the devices that measure each electron's energy before and after the bremsstrahlung photon(s) are produced, (3) E687–an experiment that sits immediately upstream from our detectors and from our perspective can be viewed as a series of apertures, magnets, and an annoying 25% of a radiation length of material in the beam, and (4) the E683 detector apparatus.

For the purposes of this dissertation, module (1) is not important. Module (3) is not very important except to the extent that it affects the beam. E687 contains 25% of a radiation length of material and two strong dipole magnets. The material can cause photons to pair produce and the magnets sweep out all but the most energetic pairs. This has an appreciable effect in measuring beam rates and will be a tricky cross section correction, but this effect does not seriously affect the methodology chosen to measure structure functions so it is mentioned here only for completeness.

3.2.1 Equipment Shared with E687

Module (2) would have been lumped with (1) except for the existence of the beam energy measuring devices, which were designed and built by experiment E687. As stated before, the measuring of the photon's energy occurs in two steps. The first measurement determines the momentum of the photon-generating electron. This measurement is done by using: (1) two planes of silicon strips to determine an initial

trajectory, (2) a third silicon plane, sandwiched between two dipoles, measures the mid-bend displacement, and (3) a final two planes to measure the electron's exiting trajectory. This sampling of the electron's path in the (well known) magnetic field is fitted via a relatively simple χ^2 analysis and the electron's momentum is inferred.

Each of the 5 silicon planes is, in effect, 256 adjacent strips 300 μ apart. This granularity, which sounds small, is a dominant contributor to the electron's momentum measurement resolution. The silicon spectrometer was calibrated by E687 against their rather precise spectrometer. We have been told that the beam electron momentum resolution is $\approx 2\%$ [48]. A sketchy picture of this system can be seen at the bottom of figure (9.)

Measuring the incoming electron's momentum is only part of the job. In order to measure the photon(s) energy, we must in addition measure the electron's energy after the bremsstrahlung photons have been produced. This measurement is done in the **R**ecoil **E**lectron **S**hower **H**odoscope (RESH), which is a series of small calorimeters that function as a hodoscope (i.e. the recoil energy is measured by *which* calorimeter is hit, rather than from pulse-height analysis.) By knowing both the incident and recoil electron energies, it is possible to infer the photon energy.

There is a small subtlety that needs to be noted here. The measurement of the energy difference between the incident and recoil electron does not strictly give the energy of the interacting photon. In fact, as an electron passes through matter, it undergoes a series of interactions of varying degrees of violence. This results in a number of photons being produced, typically all of low energy. Our trigger requires that at least one of the photons be of moderate to high energy[8]. Energy conservation necessarily suppresses, but does not exclude, the existence of an additional photon of appreciable energy. The existence of multiple photons, in conjunction with the measuring technique: $E_e(\text{in}) - E_e(\text{out})$, has two troublesome side effects:

- Since the presence of multiple photons ensures that the interaction photon's energy is different from the energy difference measured, it is impossible to precisely know the energy of the interaction and thus transform between the lab and center

[8] On the order of $\gtrapprox$ 100 GeV.

of mass (CM) frame; and,

- The presence of the multiple non-event-generating photons complicates the measurement of the event forward energy flow.

The implications of these effects will discussed in more detail at a later point.

In addition to the energy measuring devices, there is another detector situated in the electron beam line: the so-called pile up monitor [52]. This detector was used in part to monitor multiple electrons in a single bucket, but more importantly to monitor electrons in adjacent buckets. Since the beam calorimeter's (discussed below) response time (60-ish ns from beginning of signal to within 5% of quiescent) was long compared to the beam cycle time (18 ns,) it was possible for electrons in nearby buckets to generate photons that could contaminate a forward energy flow measurement. This device allowed us to have a software tag which flagged those events where such a contamination might be a problem.

3.2.2 E683 Apparatus

A somewhat detailed schematic of E683 can be seen in figure (10). The first major component of the experiment is a six foot thick steel wall with a 7.5" x 7.5" hole centered on the beamline to allow the beam particles through. This steel wall is needed to shield our primary calorimeter from debris created upstream from our apparatus. While this steel wall is very effective in stopping hadronic and electromagnetic particles, it is essentially transparent to muons and for this reason the steel is followed by a hodoscope to veto these off-axis muons.

The next component along the beamline is the target. E683 took hydrogen, deuterium and nuclear target data. This was done by mounting a hydrogen target and a rotating nuclear target wheel alongside one another. Every few hours, we would switch target types: Hydrogen $\rightarrow$ Nuclear $\rightarrow$ Hydrogen Target Empty $\rightarrow$ Nuclear $\rightarrow$ Hydrogen $\rightarrow$ Repeat. During nuclear running, the target wheel would index to a new element between each spill in an attempt to wash out systematic effects. Since we had only one liquid target vessel, it was not possible to intersperse hydrogen and deuterium

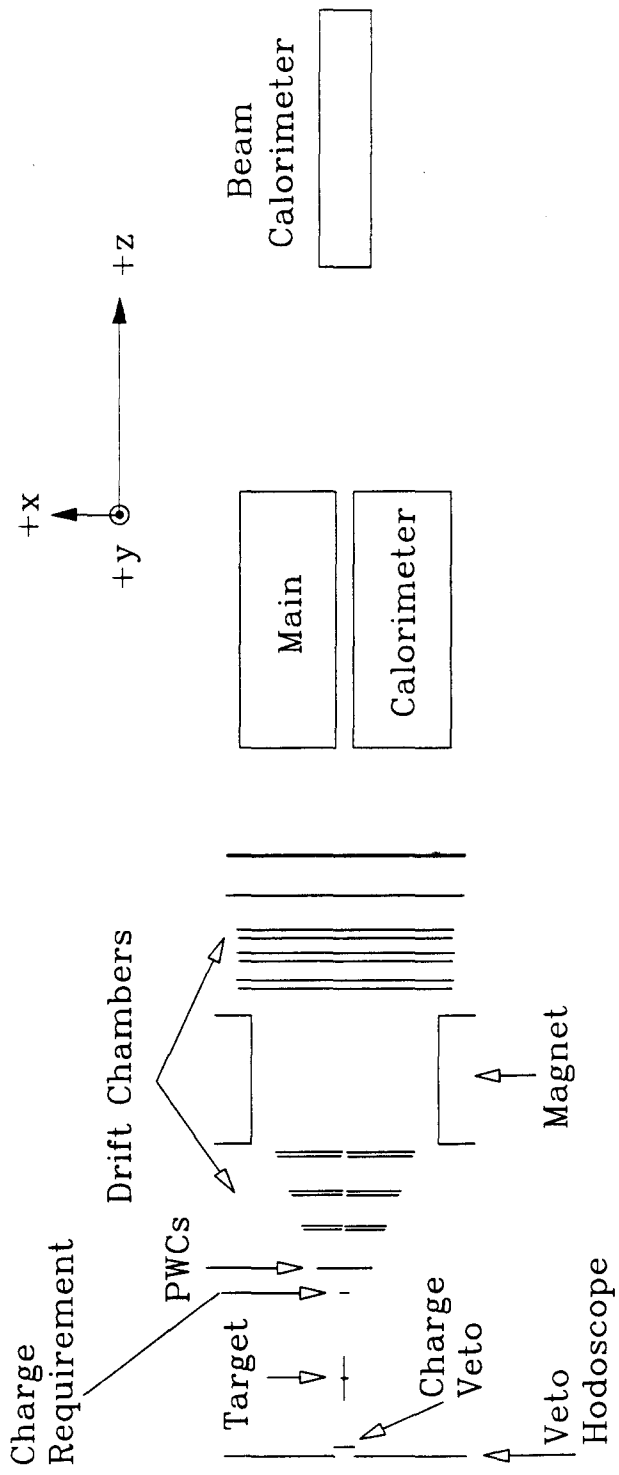

Figure 10: Overview of E683 Experimental Apparatus

Plane	Direction of Measurement
PWC 3, DC 1-13, 16, 17	x
PWC 1, 2	y
PWC 4, 5, DC 14, 15, 18, 19	u or v
DC 2, 6, 12	Delay Line

Table 1: E683 Chamber Types

data. Therefore we would take a few months with the flask filled with hydrogen and then several weeks of deuterium. The liquid hydrogen target, which is the one that is relevant to this dissertation, was a cylindrical mylar flask of approximate dimensions 20" long by 4" diameter. No nuclear data are reported here.

This experiment used scintillator paddles to define the beam. There were two 9" x 9" paddles that completely covered the beam hole, one on each side of the steel wall. These counters were used in the trigger as a veto, thereby ensuring the interaction was not caused by, or accompanied by, charged particles. In addition, there was a 4" x 4" scintillator immediately downstream of the target. This counter was used in the trigger to force the condition that charge left the target. When we were taking photon induced data, these counters formed a beam trigger than can be summarized as 'no charge into target, charge out of target' and is referred to hereafter as **BEAM-γ**. When we were using a pion beam, the beam vetos were made to be a requirement, and the beam trigger became 'charge into target, charge out of target', hereafter referred to as **BEAM-π**.

Following the target and scintillator counters is a weak spectrometer. Since this system is not used in this analysis, I only mention it here briefly. There were 5 PWC (proportional wire chamber) planes, followed by 6 DC (drift chamber) planes, a magnet and finally 13 more DC planes. See table (1) for a description of each plane.

The analysis of the spectrometer is currently being worked on, so no definitive

statements as to the detector's performance can be made. The magnet nominally gives a 65 MeV $P_\perp$ kick to each singly charged particle. It is expected that, when finished, the chamber system should be sufficient to reconstruct the event vertex and to measure the charge of the leading particle.

Since E683 is primarily an energy flow measuring experiment, our best detectors are our calorimeters. Our calorimetry is separated into two devices: (1) a wide angle, highly segmented calorimeter designed to measure energy flow direction as well as magnitude (which we call the MCAL, or Main Calorimeter [49, 50]), and (2) an unsegmented calorimeter placed in the beam to absorb forward energy flow (which we call the BCAL, or Beam Calorimeter [53].) While these two calorimeters are not conceptually distinct, historically they have been treated separately (having been designed and built on the order of a decade apart) and I will preserve this distinction.

The MCAL was designed and built circa 1980 and has been discussed in detail in several theses [49, 50]. For this reason, I will not repeat all of the mechanical details here. However, it is our primary detector and therefore requires some explanation.

The MCAL is made up of 532 modules. Each module is a series of scintillator sheets, separated by metal and coupled to a single photomultiplier. These modules are stacked in 4 layers and form 132 towers, each of which is designed to cover roughly the same CM (center of mass) solid angle (see figures (11) and (12) for a clearer view of the relevant geometry.) The 8" x 8" hole in the center of the MCAL allows the beam to pass unhindered into the BCAL.

The first layer's passive absorber is lead and layers 2-4 are steel, with the intent of using the (high Z) lead to contain EM showers to the front of the MCAL. In practice, the second layer had the largest energy deposition of both electromagnetic and hadronic showers. There is more to be said about the MCAL system, but I will defer discussion until the section on electronics and triggering (section 4.)

Section (8) discusses the effect of the MCAL's center of mass acceptance on jet finding. Figure (11) defines the points A, B, C and D on the face of the MCAL. Figure (13) shows the CM polar angle acceptance of the MCAL for various beam energies. This figure is quite revealing as it shows the limited extent of polar angle coverage in

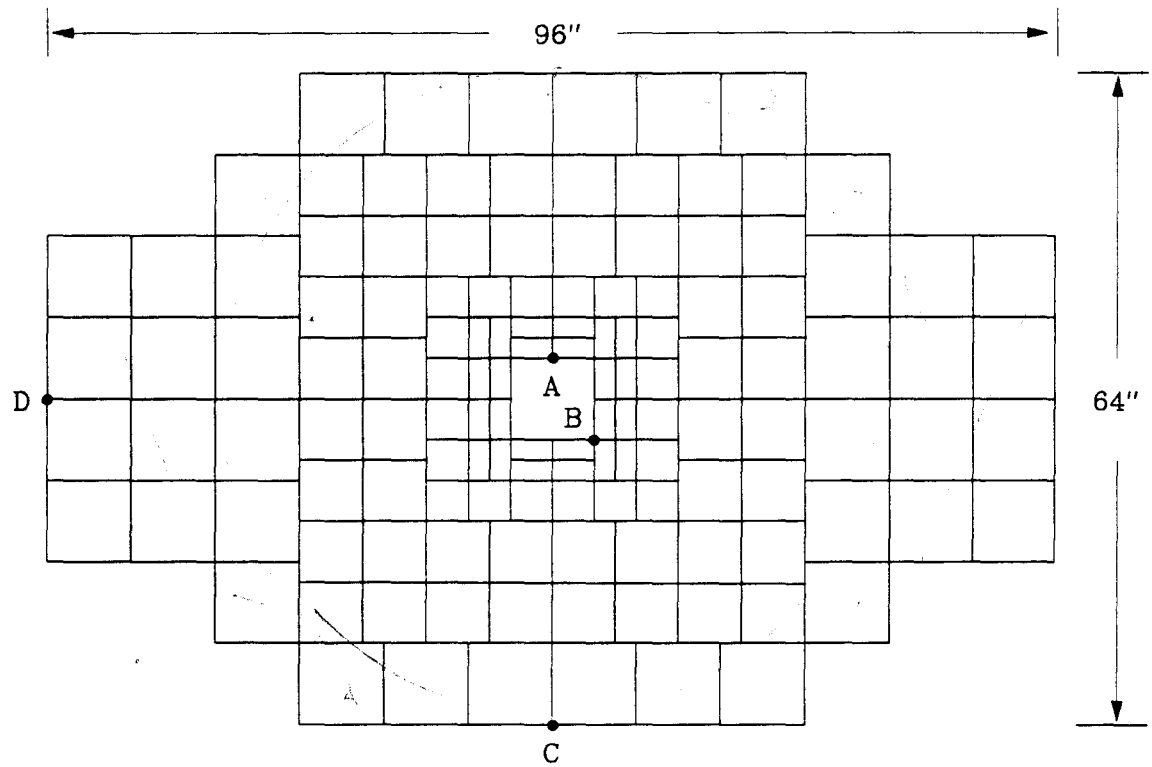

Figure 11: Beam's eye view of the MCAL in the lab frame. Each square or rectangle indicates a separate tower, with the exception of the one in the center of the MCAL which illustrates the beam hole. The CM angles of points (A,B,C,D) are shown in figure (13.)

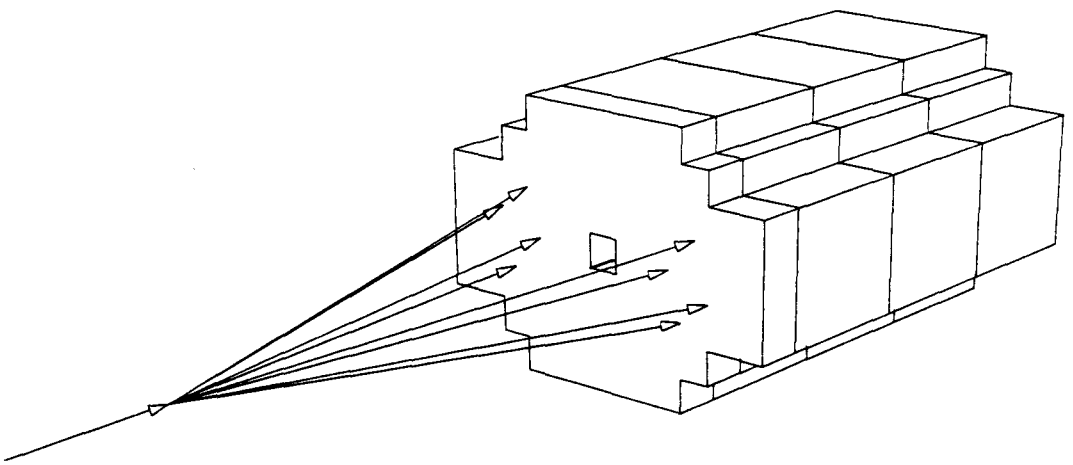

Figure 12: Three dimensional view of the MCAL in the lab frame.

the CM, as well as the the coverage's rather significant dependance on beam energy.

Our other calorimetry subsystem, the BCAL, is of a simpler, iron-scintillator sandwich design [53]. Its dimensions are 2' x 2' transverse to the beam. There are forty six 1.5" thick iron slabs interspersed with scintillator. The light is collected from each piece of scintillator on the top and bottom by a strip of WLS shifter bar. The light from each piece of scintillator is collected by two photomultipliers (PM's), with the WLS along the top of the scintillator going to one PM and the WLS along the bottom going to the other.

A total of eight PM's are needed. The light is collected from several scintillators and sent to a PM, with the collection scheme being (from upstream to downstream) 6, 8, 16, 16 scintillators collected together (recall that there are two PM's for each scintillator–this implies that we must have 4 PMs on the top, and 4 on the bottom.)

3.3 Device Simulation

In any experiment, the detectors form an integral part of the measurement process. The quantity that one wishes to measure is changed by the devices one uses to measure (e.g. a microphone measures sound by converting it into electricity, or a car

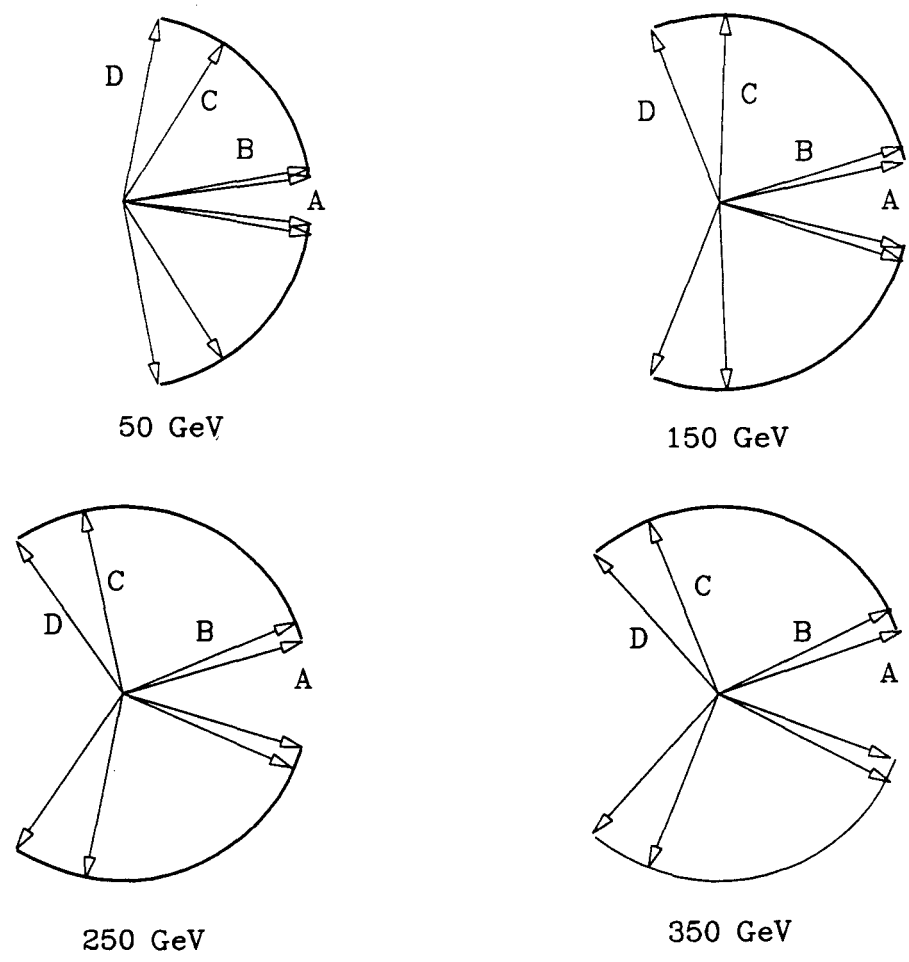

Figure 13: Center of mass polar angle MCAL acceptance as a function of beam energy. The points (A,B,C,D) are defined in figure (11.) The value in degrees of the angles (A,B,C,D) are: 50 GeV (7.8,11.1,57.6,79.0), 150 GeV (13.6,19.1,87.2,109.9), 250 GeV (17.5,24.5,101.7,122.9), and 350 GeV (20.6,28.9,111.0,130.6). The angles are calculated assuming massless kinematics.

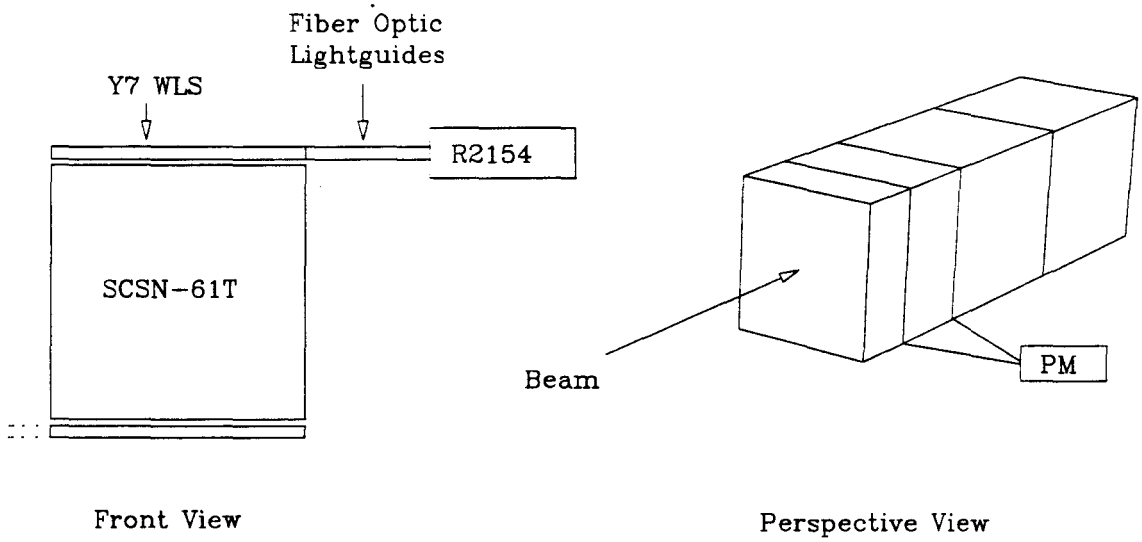

Figure 14: BCAL Schematic Diagrams

speedometer measures speed by converting car motion into the rotation of a cable, etc.) The measuring process needs to be understood so that one can understand how to use one's data to extract the desired quantities. In the complicated situation of a modern HEP experiment, Monte Carlo techniques are generally used and in E683 we have opted to use home-grown device simulators. For this dissertation, only the two calorimeters are relevant (see section (3.2.2) for a description of the relevant detectors.) A beam calorimeter simulator was written such that it was a straight parametrization of the calibration data taken 26-JUN-1991. All relevant correlations were taken into account and the simulator slavishly reproduced the data. Data was taken at four hadronic energies (30, 60, 90, 150 GeV (nominal)) and five electromagnetic energies (30, 60, 90, 150, 350 GeV (nominal)). Given the 15% momentum spread of the beam (see section (3.1),) the 30 GeV point actually contains beam particles with energies in the range of 20-40 GeV. For particles with energies less than 20 GeV, the simulator merely extrapolated the (very linear) high energy behavior. There is no available data to check the few-GeV behavior of the detector, although pulsed laser calibration data shows the phototubes to be linear over the entire range. While I

expect the low energy behavior to reasonably track the high energy behavior, very low energy calorimetry is a region where the otherwise linear response is most likely to break down. The simulator reproduces all measured data and makes reasonable extrapolations, but the low energy simulation could be a weak point.

The main calorimeter simulator was written for FNAL E609, the father experiment of E683. This simulator was tested carefully, but a check against E683 data is needed. Unfortunately, such a test can not be done until the E683 calibration is completed. It is my expectation that this simulator distributes energy along the beam direction approximately correctly, but that close inspection will find that it falls short in its transverse distribution of the incident energy. If the transverse energy distribution is not correct, it will have consequences on jet finding (see section (8)). The fact that the main calorimeter simulator has not been rigorously tested against E683 calibration data is a weak point in this analysis.

4 Electronics and Triggering

As usual in a modern high energy experiment, we have a substantial amount of electronics. While all of the detectors had electronics associated with them, I will discuss primarily those that were used to form the triggers.

The MCAL electronics were built for E609. Figure (15) outlines the system, which is described in detail in [54].

As mentioned before, the MCAL consists of 532 PM's arranged in 4 layers and 132 towers. The signal from each tube is amplified by a (x5) amplifier (called a calamp) and the signal is converted to differential mode for transmission over twinax cable. The cables run approximately 135' to the main counting room where they are received by modules called summing and weighting amplifiers (S/W A.) After converting from differential mode, the (S/W A)'s, as their name implies, take the signals from each of the 4 modules in a tower and linearly adds them together after each signal has been weighted to give similar pulse height per energy deposited. At this point, each tower is represented by a single signal which corresponds to the energy deposited within

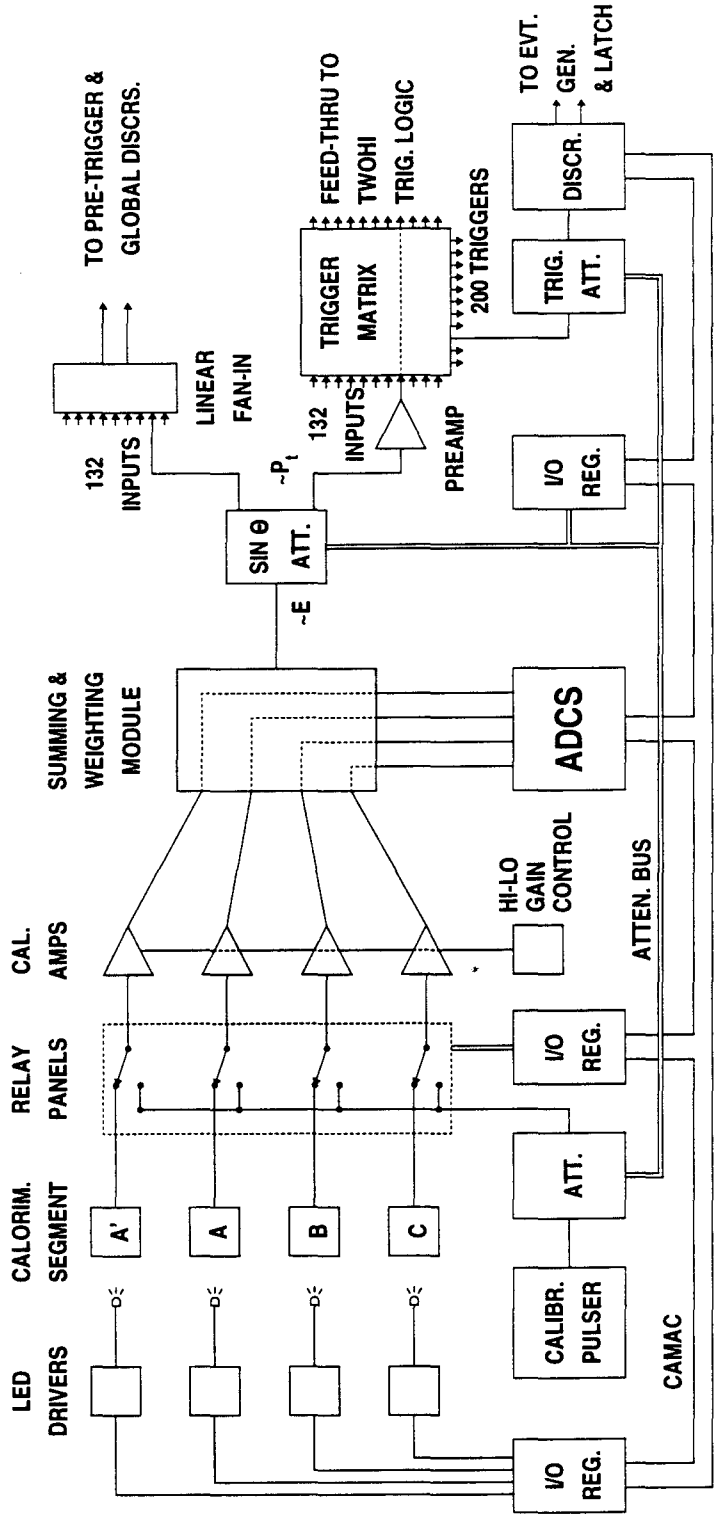

(Figure courtesy of Reference [54] and Randy Herbert.)

Figure 15: MCAL Trigger Electronics Schematic

that solid angle. These signals are then run through attenuators whose effect is to modify the signal by a factor of $\sin\theta_{\rm LAB}$, thereby resulting in signals proportional to $E_\perp = E_{\rm LAB}\sin\theta_{\rm LAB}$, the transverse energy deposited in that tower. It is this $E_\perp$ signal that is used to form our various triggers.

4.1 Gamma Triggers

E683, like its predecessor E609, had 3 different high $E_\perp$ triggers: Global, 2HI, and Trigger Matrix (TM). The global trigger is the easiest to understand. The various towers' $E_\perp$ signals were linearly added, passed through a variable attenuator, and then a fixed threshold discriminator. Rather than the more common technique of leaving the signal untouched and varying the discriminator setting, we opted to leave the discriminator alone and change the attenuation of the signal. This trigger monitors the *total* $E_\perp$ in the MCAL. The hardware $E_\perp$ threshold was set at $\approx$ 6 GeV.

The 2HI trigger has a different philosophy. In this case, the signal from each tower is passed through an individual (nominally identical) discriminator. Each time a discriminator threshold is passed, a short ($\approx$ 50 ns) voltage level is applied to a bus. If the voltage level were 300 mV and a single tower had passed its discriminator, a 300 mV, 50 ns signal would appear on the bus. If two towers were hit, a 600 mV signal would appear, for 3 - 900 mV, and so on. The signal on the bus was fed to a final discriminator which was set for at least 2 towers simultaneously firing. This trigger monitored energy density, due to its insistence that at least two towers were hit hard. The tower thresholds were set to $\approx$ 0.75 GeV/tower.

The final trigger type, the trigger matrix (TM), is somewhat of a mutation of the other two. A large circuit was formed that would add the $E_\perp$ of subsections of the MCAL and impose an $E_\perp$ threshold on these restricted modules. An example of a TM trigger would be to add the $E_\perp$'s of all of the small modules on the left hand side of the MCAL and all of the large modules on the right. These TM triggers encompass a number of very different geometries and were designed to cover the hybrid region between the global and 2HI triggers. The TM triggers have not been explored in detail as of this writing.

With this preliminary information in hand, our interaction triggers are easy to understand.[9] In section (3.2.2) we discuss the trigger requirement **BEAM-γ**. Our gamma trigger is (**BEAM-γ**)$\oplus$ (one of the above $E_\perp$ triggers) $\oplus$ (computer isn't busy.) In English, this can be stated: no charge into target, charge out of target, a lot of $E_\perp$ in the MCAL and the computer isn't busy. For a pion beam, the charge veto is turned into a requirement; the remainder of the trigger is unchanged with the possible exception of fiddling the $E_\perp$ threshold to get an acceptable dead time $\lessapprox 40\%$.

4.2 Flux Monitoring Triggers

In addition to the above described interaction triggers, we took a series of what we called (somewhat incorrectly) flux monitoring triggers. These trigger types are called: RESH, BCAL, PAIR, and LED.

- **RESH** - RESH triggers insisted that one of the RESH elements had a significant signal. It was intended that this represent an energetic recoil electron, although pathological low energy electrons could hit a RESH element and cause a fake trigger.
- **BCAL** - BCAL triggers insisted that there was $\gtrapprox$ 100 GeV in the BCAL.
- **PAIR** - PAIR triggers insisted that no charge entered the target and that at least 2 charged particles left the target.
- **LED** - LED triggers required that the LED's attached to each PM in the MCAL fire simultaneously. This trigger will be used for MCAL stability studies.

5 Data Acquisition System

Our DA system, while entirely suitable for our needs, was somewhat primitive by today's standards. We used a parallel CAMAC highway hanging off a Jorway 411 which was attached to a μ-VaX II. The data was stored on 6250 bpi tapes. The overall

[9]For historical reasons, these are called gamma triggers even when we use a pion beam.

system we used was the FNAL VAXONLINE [58]. The system had a maximum event acceptance rate of $\approx$ 20 Hz. Many different CAMAC modules were used as a part of the DA and triggering systems. Primarily (but not exclusively) we used LeCroy electronics, the most notable being the 2280/2285 ADC system for the MCAL readout, the 4299/4298/4291 TDC/memory system for the drift chamber readout and PCOS II and III readout systems for the PWC's.

6 Calibration

The calibration methods applied to both of the BCAL and MCAL systems were similar. I am more familiar with the BCAL so I shall explain the methodology in this context and briefly relate it to the MCAL.

6.1 BCAL

The BCAL initially had its tube high voltages set by looking at muons. However, this was insufficiently precise for a final calibration and for this reason 'fixed' energy beams of electrons and pions were used (30, 60, 90, 150, and 350 GeV).

As you might recall, each scintillator was viewed by two PM's. Obviously, the first order of business is to balance these two tubes with respect to one another. This was done by taking an appropriate beam and sending it into the center of the BCAL. The two tubes each gave a signal T_1 and T_2. A value of λ was found that minimized the quantity:

$$Q = \sum_{\text{events}} (T_1 - \lambda T_2)^2$$

The values of λ for each layer were found to be similar to, but slightly different from 1.0 and were surprisingly stable over the course of the run.

Once the λ's for the layers were found, a signal for each layer could be assigned (e.g. $L_1 = T_1$(layer 1) + λ_1 T_2(layer 1)). Then each layer needs to have its response made uniform with respect to the others. This was done by finding the quantities

(a, b, c, d) that minimized the quantity:

$$Q = \sum_{\text{events}} [\frac{a\mathrm{L}_1 + b\mathrm{L}_2 + c\mathrm{L}_3 + d\mathrm{L}_4 - \mathrm{E}_{\text{true}}}{\mathrm{E}_{\text{true}}}]^2$$

where $\mathrm{L}_{\#}$ is the ADC signal for the #'th layer and E_{true} is the particle's energy measured by the silicon strips. A lot of effort, outlined in E683 technical documents [56, 57], went into making this technique work. The final result was that the BCAL was found to be admirably linear with somewhat less stellar energy resolution (although still reasonable for the design.) The resolution was found to be (EM means electromagnetic, HC means hadronic):

$$\text{EM}: \qquad \frac{\sigma(E)}{E} = \frac{45\%}{\sqrt{E}}$$

$$\text{HC}: \qquad \frac{\sigma(E)}{E} = \frac{75\%}{\sqrt{E}} \oplus 4.6\%$$

where the symbol $\oplus$ indicates added in quadrature. The constant term EM is often written as 2% and the HC term 5%, but this is something of an error, since the silicon system that measures the beam energy has a 2% resolution that must be removed in quadrature. The numbers listed in the table are the ones appropriate exclusively for the BCAL.

One interesting feature that was discovered was that certain PM's of the BCAL were losing pulse height. The reason for pulse height loss was determined to have at least two components. The first component was easily understood radiation damage to the scintillator. This damage was concentrated at EM shower maximum and corresponded to an approximate 10% signal loss for the BCAL as an ensemble. The cause of the second component is still not understood, but it appears to be beam related. This loss was larger ($\approx$ 40% of initial pulse height.)

The total loss of 50% was gradual and monitored by a series of re-calibrations. In the end, a time dependent correction factor was created and the loss relegated to the status of an interesting, but ultimately fixable curiosity.

6.2 MCAL

The MCAL calibration has been the MA thesis of two people ([49] for E683) and ([50] for E609.) In E683, a calibration methodology similar to that used on the BCAL has been applied. Unfortunately, the granularity of the MCAL greatly complicates the analysis. What has been done is to calibrate each tower separately, assuming constant response in the surrounding towers and then iterating the procedure. This methodology has been shown to improve the MCAL resolution, but still some outstanding inconsistencies remain. For this reason, the calibration of the MCAL is an ongoing project and the constants used here should be taken to be preliminary. It is expected that the MCAL resolution will ultimately improve although the mean energy scale is unlikely to drastically change. Preliminary resolution measurements yield (silicon system contributions already removed):

$$\text{EM}: \qquad \frac{\sigma(E)}{E} = \frac{35\%}{\sqrt{E}}$$

$$\text{HC}: \qquad \frac{\sigma(E)}{E} = \frac{75\%}{\sqrt{E}} \oplus 6.4\%$$

A subtle feature of the calibration that has not yet been taken into account is the effect of the EM/HC ratio (i.e. the response of the detector due to electromagnetic showers versus hadronic showers.) When the two showers are separated, it is possible to apply different calibration factors to the signal and recover the correct energy. However when a particular calorimeter element contains energy from both kinds of showers, the fact that both electromagnetic and hadronic showers generate different amounts of signal for the same amount of energy deposited makes determining the correct energy deposition quite difficult.

In the MCAL, the EM showers are contained in the first two layers. The HC showers are dispersed over all four layers. Therefore the signal in (especially) layer 2 is of some worry. Somehow one must sort out the ratio of electromagnetic to hadronic energy deposited in this layer and compensate. As of this writing, this is not possible. The best that can be done is to make an adjustment to the calibration factors of layer 2 to improve the calibration to an arbitrary amount of energy deposition. Such

a correction can only be done when a careful calibration is available and for this reason, I have opted to use a more primitive approach.

Using the MCAL simulator (discussed elsewhere), along with the EM/HC ratio of 1.33 (which is likely much too large,) it can be determined that due to the decreased signal for hadronic showers, the energy reported as being present in the MCAL is 90% of the actual energy present in the detector. One needs to multiply the response of the entire calorimeter by about 110% (i.e. 1/90%) in order to recover the correct amount of energy incident on it. Obviously such a technique degrades the resolution of the device (as compared to doing the correction 'right' by twiddling the layer 2 balance factors.) Also, the 110% number is dependent on the EM/HC response ratio, something undetermined at this time. So as an attempt to make a primitive correction to the effect, I have occasionally divided the apparent energy of the MCAL by 0.9. I will be sure to point out when this has been applied and when it has not.

7 Gross Data Reduction Features

It is a danger in any HEP experiment that various people will do their analyses sufficiently differently so that their results are difficult to compare. As an example, if two people used different calorimeter calibration factors and their final results disagreed, one would immediately suspect the calibration. In order to keep this from occurring, it is common for a collaboration to pre-analyze the raw data and write this new information to a data summary tape (DST.) The data on DSTs typically have had simple operations applied to them; e.g. pedestal subtraction, ADCs converted to energy, TDCs converted to distance, etc.

On E683, we have opted for an equivalent but different route. Over the course of building and running the experiment, a series of tightly integrated code packages have been written. These packages were [59, 60]:

UNPACKER: This package took raw data from the tapes (or straight from memory as the tapes were written), picked it apart, and presented the very raw data to the user in Fortran COMMON blocks in a coherent, detector-oriented and easy

to use manner.

GET_PEDS: This package allowed the user to easily access the pedestal data base for any of our data runs.

ANALYSIS: This package took the output of the UNPACKER package and did simple analysis on the data; pedestals were subtracted, ADCs converted to energies, electron beam energy as measured by the silicon was calculated. This data is also presented in COMMON blocks.

DISPLAY: This package easily presented an event in graphical form. The 'guts' of this was formed by the Rice version of TOPDRAWER [61].

HOUSEKEEPING·CUTS: This package made it easy to throw out 'obviously' bad events. This will be discussed more later.

These codes were all easy to use and were organized in such a way to discourage casual tinkering. Further, their use was pervasive throughout the experiment and they were therefore thoroughly debugged. Given the simplicity of using these packages and their 'standardized' nature, the need for an early DST pass was greatly reduced. For a data set of this size ($\approx$ 100 exabyte tapes (2.3 Gbyte capacity each),) the flexibility of this system in the early analysis stages has proven invaluable.

7.1 Simple Cut Criteria

At an early stage of analysis, one does not want to toss out events capriciously. However there are certain reasons whereby events are obviously bad and should therefore be rejected.

If the data aquisition system was broken, it would record garbled data which would not be useful. Similarly, if a device gave back results far outside normal operating ranges, this would be grounds for rejection. The UNPACKER and ANALYSIS packages were effective in catching these type problems. However, even structurally clean data can have problems. These are outlined below.

Quite often two electrons would occupy the same radio frequency (rf) bucket and be seen in the silicon chambers. Alternatively, occasionally it would be impossible to track an electron in the silicon. Further, it was not uncommon for multiple electrons to hit the RESH in ways that made the measurement of electron recoil energy ambiguous. These make the photon beam energy indeterminate, which is unacceptable for this analysis.

In addition, sometimes there was much more energy visible in the detector system than was available in the beam. This could happen due to pile up in the detectors or device glitches.

One of the larger operational difficulties has been called (somewhat incorrectly) hot muons and the explanation requires some digression. You might recall that in section (3.2.2) it was mentioned that there was a large chunk of steel in front of our experiment to absorb hadronic and electromagnetic debris from upstream. This steel was followed by a hodoscope used to veto muons. Even though muons typically do not deposit much energy at any specific point while traversing matter, occasionally they can have a direct collision with an atomic electron, thereby creating a δ ray, which would create a large signal in the MCAL. These δ rays were created at the rate of on the order of 1000 Hz.

During the experiment, it was also discovered that there was a problem with the photomultiplier photocathodes undergoing spontaneous discharge to their magnetic shield. This discharge gave large pulses (corresponding to $\approx$ 50 GeV) which occurred at $\approx$ 100 Hz.

One needs to further recall that the photons that hit the target often underwent pair production and created charge exiting the target. The rate for this was $\gtrapprox$ one MHz.

If you recall our trigger (no charge into target, charge out of target, lots of $E_\perp$ in the MCAL,) it was inevitable that these effects would conspire to give (accidental) false triggers. Even though we had the hodoscope to veto muons and trigger electronics to veto the breakdown events (we rejected events with energy in only one tower), inefficiencies in the vetos caused some contamination. Luckily these events

were easily rejected offline.

Another odd effect we saw does not qualify as a cut, but logically should be mentioned here. Our counting room was air conditioned. The A/C blew air under the floor and up through our electronics relay racks. While the fans were blowing, the temperature at our electronics was lower than when the fans were off. Unfortunately, our MCAL ADCs had a non-zero temperature coefficient. As the A/C cycled, the ADC pedestals would vary by $\approx$ 1 ADC count. While this is a small variation (pedestals were typically 300), it was coherent and therefore each of the 528 modules contributed roughly equally and in phase. This pedestal fluctuation corresponded to an approximate 10% fluctuation in the MCAL $E_\perp$ scale and was therefore unacceptable.

An algorithm was invented that fixed the pedestal fluctuation problem. The flux monitoring triggers (which had essentially no energy in the MCAL) from the previous spill formed a 'running pedestal'. Use of this algorithm reduced the effect of pedestal fluctuation to less than the statistical fluctuations.

7.2 Summary of Housekeeping Cuts

The housekeeping cuts [62] were adapted to work with the standard code package. They are listed in technical detail below. The following definitions need to be made: E_{MCAL} is the MCAL energy, E_{BCAL} is the BCAL energy, E_{TAG} is the initial electron's energy, E_{RESH} is the recoil electron's energy, E_γ is the calculated photon energy (E_{TAG} - E_{RESH}), $E_\perp$(up) - $E_\perp$(down) is the up/down MCAL $E_\perp$ misbalance, similarly $E_\perp$(right) - $E_\perp$(left) is the right/left MCAL $E_\perp$ misbalance. For a symmetric event, these misbalance quantities would be 0.

Silicon -

1. 100 GeV $<$ E_{TAG} $<$ 550 GeV
2. χ^2/dof $<$ 12 for the fit of the electron track to the data (Note: dof means degree of freedom.)
3. There was exactly one electron tracked in the silicon.

RESH -

1. The pattern of RESH elements hit made sense within the context of being hit by a single electron.

Energy Conservation -

1. Both Silicon and RESH cuts were satisfied.
2. $E_{MCAL} < E_{\gamma} + 50$ GeV
3. $E_{BCAL} < E_{\gamma} + 50$ GeV
4. $(E_{MCAL} + E_{BCAL}) < E_{\gamma} + 75$ GeV

Muon -

1. Number of towers with (E > 0.250 GeV) ≥ 30
2. Number of towers with (E > 0.500 GeV) ≥ 15
3. MAX($E_{\perp}$(up) - $E_{\perp}$(down), $E_{\perp}$(right) - $E_{\perp}$(left))/$E_{\perp}$(Total MCAL) ≤ 0.80
4. $E_{\perp}$(Hottest MCAL tower)/$E_{\perp}$(Total MCAL) ≤ 0.5

Ped Fixer -

1. The pedestal fluctuations were corrected. This was made an UNPACKER-ANALYSIS package option.

These cuts were preceeded by checks on scrambling by the DA and data being within the equipments' normal operating range. All of my results have these cuts imposed on them.

7.3 Other Optional Cuts

The above cuts are mandatory for most analyses, although some topics may not require knowledge of the photon's energy (c.f. [69].) However there are a number of cuts that can be very useful, but are typically less necessary. The two most notable cuts are called: Pile Up and POSH.

The pile up cut uses the pileup monitor [52] to veto events in which there were other beam particles incident within a specified time window. Such a cut is critical when one is worrying about forward energy flow, as the additional particles can and do contaminate the BCAL distributions. The simplest cut allowed requires that there be no additional beam particles either before or after the trigger bucket for 80 ns. It is this cut which I use when I am worried about pile up. Reference [52] shows how a more sophisticated cut will gain back half of the data I throw away. For the plots I am interested in, the gain in statistics does not outweigh the effort required to be more clever.

The POSH cut is completely misnamed and I use this terminology only to be consistent with the rest of the experiment. The POSH is the equivalent to the RESH, except it would measure the recoil arm of the e^+ beam if and when it is used. Our POSH cut is unrelated to this device.

As mentioned in section (3.2,) there is an experiment (E687) upstream from us that is for practical purposes 20% of a radiation length, combined with powerful magnets. Photons can pair-produce in the inert material and the magnets will sweep the pairs away. For a measurement that is not concerned with beam flux normalization (like mine,) the effect of sweeping out the hard photons is not a concern, as it merely reduces the flux.

However each hard photon is often accompanied by a number of softer photons. If these soft photons are removed by the effect of the experiment upstream from us, there will be a discrepancy between the measured photon energy and the energy seen in our detector (irrespective of the confusion of E683 acceptance concerns.) Since it was hoped that seeing the soft photons in the BCAL would be of some use to monitor the multiple bremsstrahlung problem, the loss of these photons was a worry.

E687 had most of its mass localized in its production target and this is where the bulk of the pair-production would occur. Just downstream from this target was a scintillator counter. Those events where the target caused pair-production could be tagged by looking at the signal in this counter. In addition, in the bend plane of their magnets there were two long scintillator counters which were intended to tag

those pairs produced downstream from the first counter. These three counters had their signal discriminated and latched. Some of the multiple bremsstrahlung problem can be ameliorated by insisting that these counters had no signal in them, as the extra photons are statistically quite likely to cause such a signal. This is what the POSH cut really means. It was called the POSH cut for historical reasons—these counters were read out in some spare inputs to the POSH latch. This cut has proven invaluable in the calibration of the whole photon momentum measuring system, but does not affect this data analysis in a sufficiently large way to warrant its use.

8 Jet Finding

Understanding what a jet is is not the same as being able to find one. Figure (16) illustrates the nature of the problem. Shown is the face of the MCAL with a Monte Carlo event superimposed. Each particle is represented by a circle. The area of each circle is proportional to the $E_\perp$ (i.e. $E \sin\theta$) of the particle it represents. The different types of circles each represent a particular parent parton. Note that the one-to-one correspondence of a particular final state particle to a particular parent parton is unique to the Independent Fragmentation model. The circles filled with random dots and the bold empty circles indicate the two hard scatter partons, with the dot-filled circles indicating the forward scattered parton. The cross-hatched circles come from those partons from the non-interacting system (also known as the underlying event or UE.)

In addition, the figure shows the two found jets using a particular jet finding algorithm, the details of which will be discussed later. The found jets are shown by outlining those MCAL towers that were included in the found jet. Those towers containing no energy even if they are contained within the jet's geometrical acceptance, are not outlined. One jet is outlined by solid bold lines, the other by dashed bold lines.

There are many striking features one must note. The first is the fact that the particles from each hard scatter parton are typically clustered near one another. How-

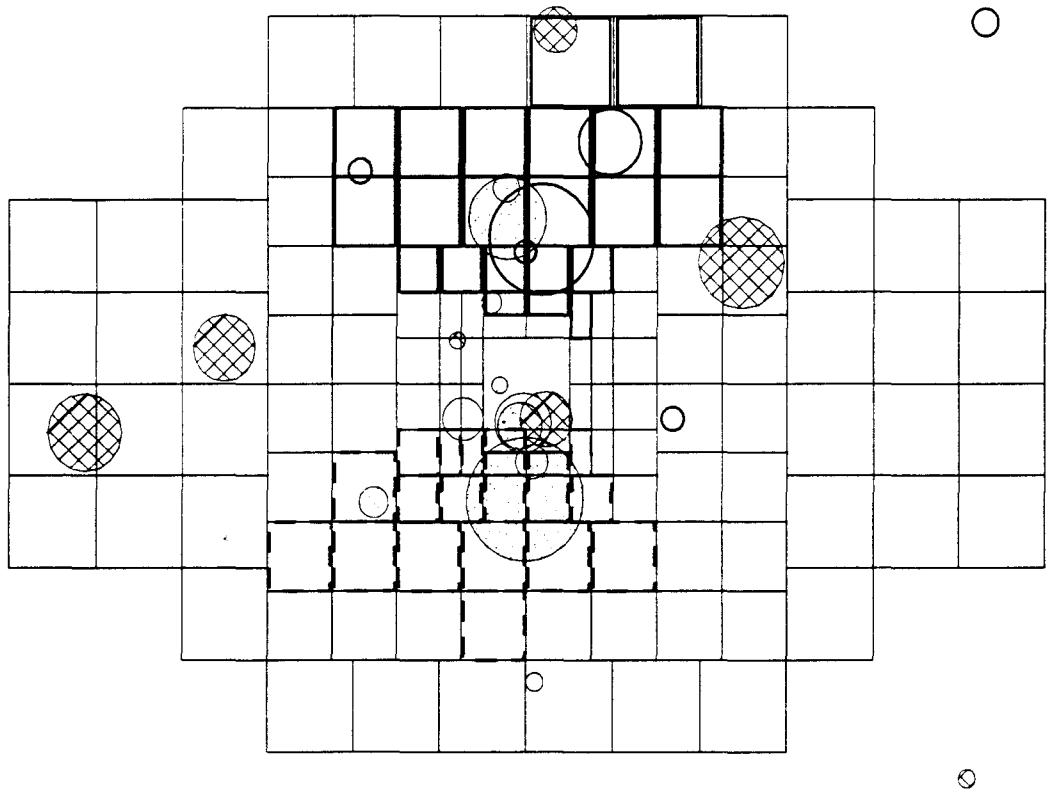

Figure 16: Shown is a beam's eye view of an event with two reconstructed jets. Each circle represents a single particle, with its *area* proportional to its $E_\perp$. The bold empty circles and the dot filled circles indicate particles from the two hard-scatter partons. The cross-hatched circles show particles from the spectator system. The two reconstructed jets are shown by outlining those towers included in them. The event shown is one of relatively low $E_\perp$, with a $\hat{p}_\perp = 3$ GeV. The two reconstructed jets have $E_\perp$'s of 2.5 GeV and 3.0 GeV respectively. Insisting on higher $E_\perp$ reconstructed jets significantly improves the situation (discussed in the text.) There is nothing particularly unique about this event and it should be taken only as a demonstration of the sorts of things that one needs to worry about.

ever there is considerable overlap between the particles of the two jets. In addition, random bits and pieces of the UE are under the jet cones. Further, many particles miss the MCAL and are either found in the BCAL or lost altogether. Somehow an algorithm must be invented that does a good job of identifying those particles associated with the parent parton and excluding the rest.

Many jet finding algorithms have been proposed [63], however I will discuss here only the one that was found to work best.[10] A detailed technical description of the algorithm used is found in Appendix B. The reader should be familar with this algorithm before proceeding with the text below. The jet finder is a CM (η, ϕ) cone based algorithm with radius $R = 1$. The jet kinematic variables to be measured were $(E, |\vec{p}|, \theta, \phi)$. The true jet was determined in the Monte Carlo by identifying those particles that came from each hard scattered parton. These jet kinematics were compared to those of the found jets. (Note: Define true jet 1 to be the most forward jet. Define found jet 1 to be the one with the highest seed.)

We start with the unphysical case of scattering two hypothetical particles with uniform x distributions (i.e. in both particles, all x's are equally likely.) This is done to ensure the jet finding is effective for all possible kinematic regions. The first variable compared was ϕ. Figure (17) shows a scatter plot of the ϕ of found jet 1 against true jet 1. The correlation is striking. The triple band structure stems from the fact that sometimes found jet 1 corresponds to true jet 2. The cut $|\phi_{\rm jet}^{\rm found} - \phi_{\rm jet}^{\rm true}| < 1$ ensures the proper true and found jet are being compared.

The second kinematic variable looked at is θ. Note that all angles are compared in the center of mass frame. Figure (18) shows the scatter plot of found versus true θ for both found jets 1 and 2. One thing that is clearly visible is that the θ correspondence is worse than ϕ for both jets, and that jet 2 is significantly worse than jet 1. The cause of both problems is illustrated in figure (19 a). When the true jet axis lies outside the MCAL's acceptance (see figure (13)), it is obvious that the found jet must lie within the MCAL and therefore is systematically offset. The ϕ acceptance is better than the θ acceptance and even when some of the misses the MCAL due to θ acceptance,

[10]It should be noted that many of the others were of similar and only slightly lesser quality.

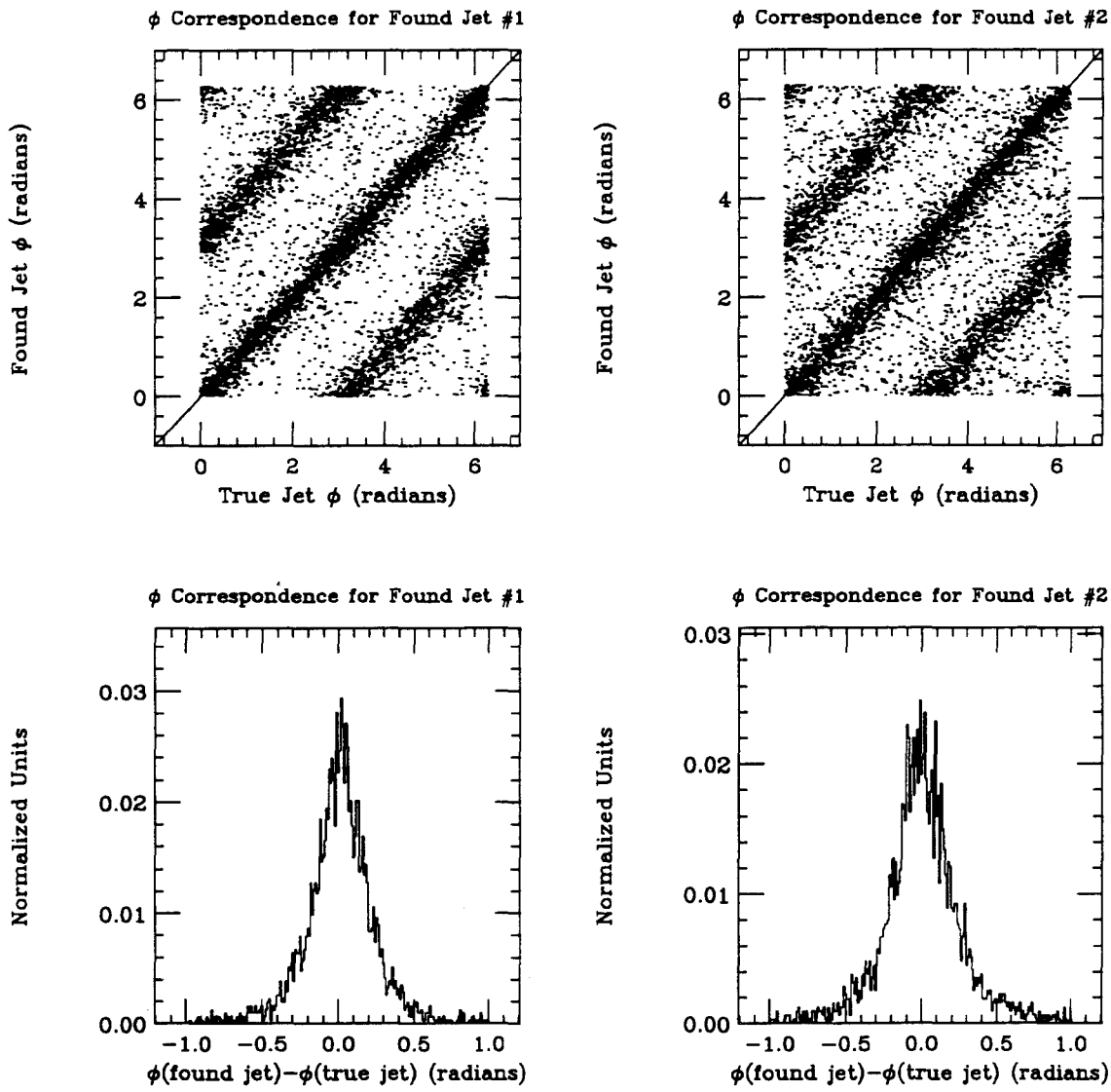

Figure 17: Shown is a comparison of the found jet ϕ with the true jet ϕ. The triple band structure in the scatter plots shows that the found jet #1 does not naturally correspond to true jet #1 (something not surprising since the numbering schemes are arbitrary.) However, the clear separation of the bands show how to ensure that you are comparing equivalent found and true jets (i.e. $|\phi_{\rm jet}^{\rm found} - \phi_{\rm jet}^{\rm true}| < 1$.) In the projection plots shown ($\phi_{\rm jet}^{\rm found} - \phi_{\rm jet}^{\rm true}$,) the correct found versus true jet assignment has been made. For this plot, both jets are required to have more than 2 GeV of $E_\perp$.

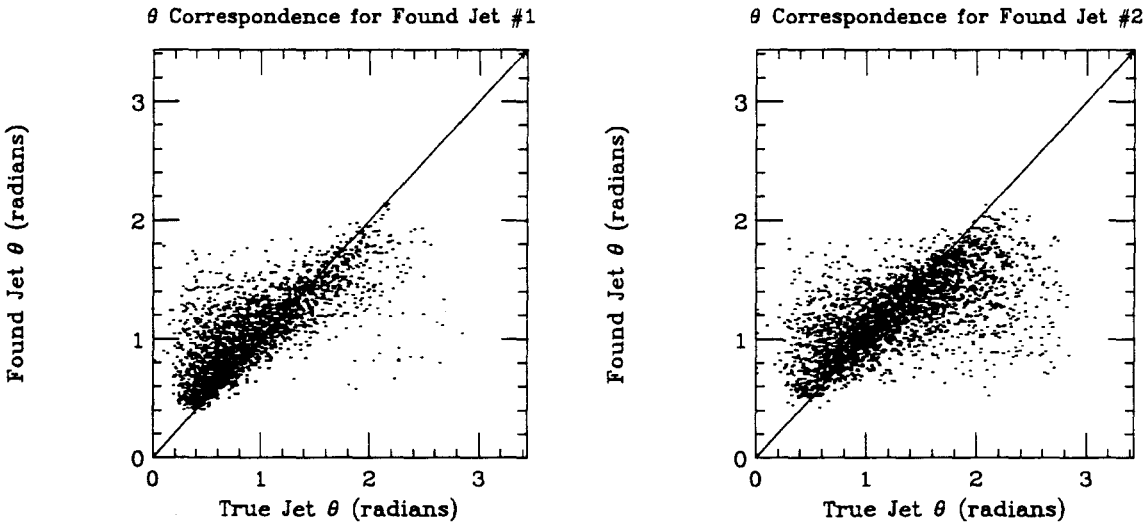

Figure 18: Comparison of the found jet θ with the true jet θ (CM frame.) In these plots, two reconstructed jets with $E_\perp > 2.0$ GeV are required. Both particles (beam and target) have flat structure functions.

the ϕ distribution is not seriously affected. However, since the 'clipping' occurs in the θ direction, a systematic offset occurs. The second reconstructed jet is worse on the average than the first, since it is typically in the backwards direction where the θ acceptance is worse. Figure (19 b) shows the only currently known correlation that solves the problem. What is shown is $\theta^{\rm true}_{\rm jet2} - \theta^{\rm found}_{\rm jet2}$ against $E^{\rm found}_{\perp \rm jet2}$. Intuitively the figure makes sense. High $E_\perp$ jets can not afford to lose energy and still remain high $E_\perp$. Insisting that both jets have an $E_\perp > 3.5 - 4$ GeV is clearly required to have good θ agreement. From this point on, unless otherwise specifically noted, a cut of both jets with $E_\perp > 4$ GeV is imposed.

Figure (20) is the first plot with the high $E_\perp$ cuts imposed and it shows the comparison between $\theta^{\rm real}$ and $\theta^{\rm found}$ for both jets 1 and 2. The correlation is much improved. One notable feature is there appears to be a slight slant with respect to the overlaid line. As usual, this overlaid line indicates perfect preservation. This slant opens the possibility of making a 'hard core'[11] Monte Carlo correction.

[11]Hard core means believing the Monte Carlo with a large level of faith and correcting the data

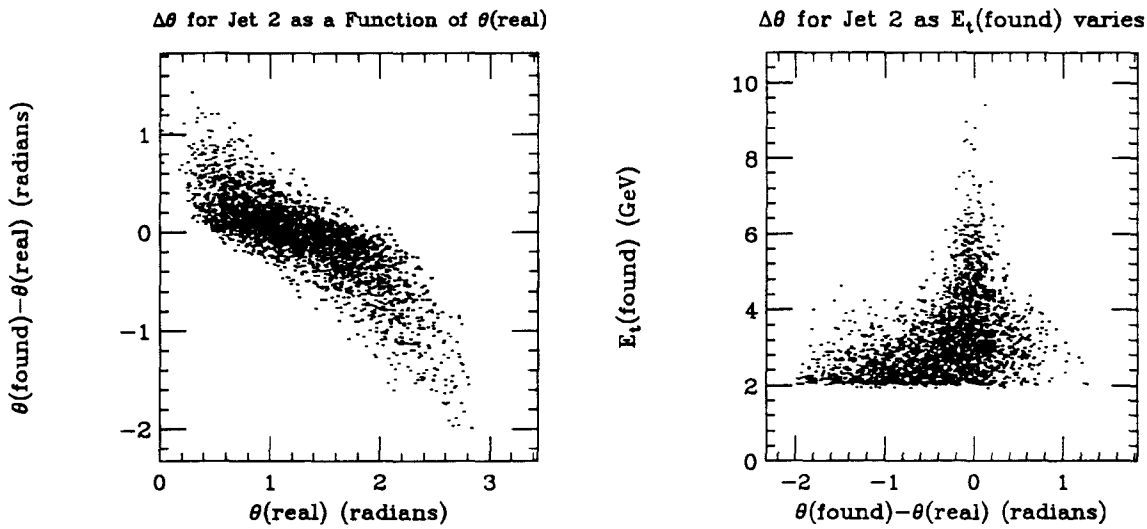

Figure 19: a.) The difference between found and true jet θ as a function of true jet θ (CM frame.) Recall that the edges of the main calorimeter are at (approximately) 0.45 and 1.75 radians. b.) The difference between found and true jet θ as a function of found jet $E_\perp$. Above a reconstructed jet $E_\perp$ threshold of approximately 4 GeV, the ability to reconstruct θ is much improved. For these plots, both jets are required to have more than 2 GeV of $E_\perp$

The cause of the slant stems from subtle consequences of calorimeter energy smearing and the Lorentz boosts. Recall that the formula for the center of mass angle (θ^*) of a particle (or jet) in terms of its lab angle (θ) is:

$$\tan\theta^* = \frac{\sin\theta}{\gamma(\cos\theta - \beta E/p)}$$

where β and γ are the Lorentz quantities describing the boost to the center of mass frame and E and p are the lab energy and momentum magnitude of the boosted particle or jet. The denominator is essentially $(1-1\cdot1)$, so one must be very careful about small variations in the various 1's. A lab jet has a certain ratio of energy and momentum. After the smearing of a calorimeter, the energy/momentum ratio is changed by the smearing process. This can be seen by the example of a single pion. After transverse energy deposition smearing, energy will appear in adjacent calorimeter modules. Taking a scalar and vector sum of the relevant modules, (and neglecting uninteresting energy resolution effects) one finds that the energy is unchanged, but the momentum has been reduced from lateral smearing.

The sensitivity to this effect is surprising. Consider a realistic lab angle of 3°, with a 250 GeV photon beam. Then $\cos\theta \sim 0.9986$ and $\beta \sim 0.9960$. If one considers a tiny 0.06% shift in the lab E/p ratio, and compares the $(\cos\theta - \beta E/p)$ term with E/p set to 1.0000 and 1.0006 respectively, one finds a 23% shift between the two extremes. A clearer, more dramatic example can be given by the comparison between the center of mass angle of a jet boosted with the correct E/p ratio and a jet boosted with a E/p ratio increased by 0.06%. The 'too heavy' jet θ is offset from the true jet by about 5°. Even more interesting is the fact that there is a distinct slant in a plot of these two quantities with the offset ranging from 4 to 6 degrees. Thus the mechanics of the slant appear to be understood. This offset appears in plots (24-28.)

This slant and offset can be dealt with by at least three methods: (1) Only work with lab frame jet measurement, (2) Invent an algorithm that combines the calorimeter energies in such a way to reproduce lab particles, or (3) Simply parameterize the offset and slope and correct for it. Certainly options (2) and (3) are comparable in how they affect the results, with option (1) being somewhat less satisfying.

for effects that can not be experimentally confirmed.

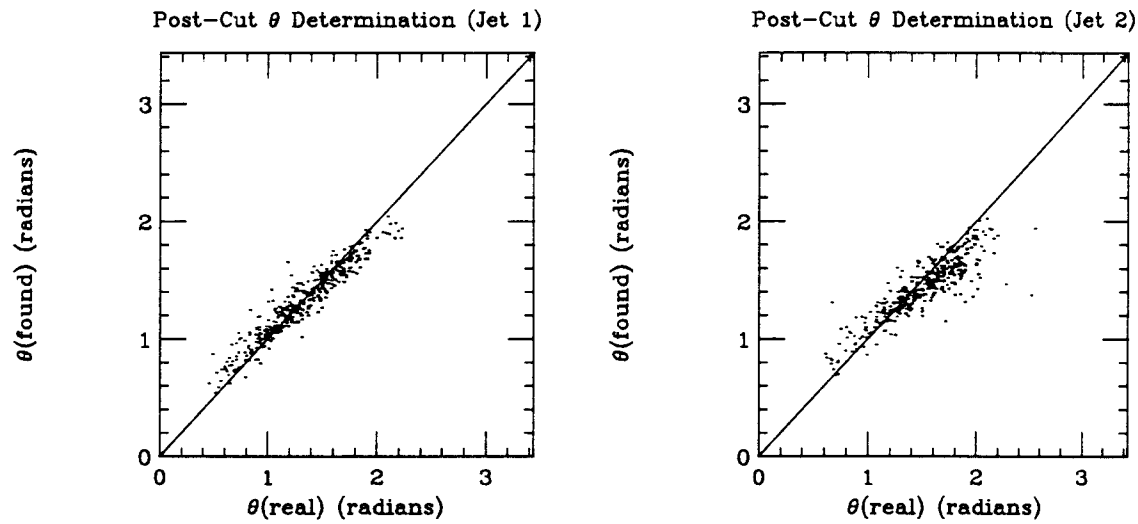

Figure 20: The correlation between θ_{found} and θ_{true} for both jet 1 and jet 2, with the requirement that both reconstructed jets have $E_\perp > 4$ GeV. The beam and target particles have uniform x probability distribution functions.

Since these slant and offset effects are small compared to other effects I will presently discuss, I have not made corrections for them.

Figure (21) plots $E_{\text{jet}}^{\text{found}}$ against $E_{\text{jet}}^{\text{true}}$ for both jets. A (poor) correlation is visible in both cases. Another feature to note is the underestimate of E for both jets. This is reasonable in part due to the high $E_\perp$ cut. As true jet energy goes up, energy conservation implies that there is less underlying event to compensate for any jet particles escaping from under the jet cone.

Using the ansatz of massless partons with jet mass arising primarily from final state interactions, equation (9) shows how to determine x_{beam} from final state CM kinematics. Figure (22) shows the correlations between $x_{\text{beam}}^{\text{real}}$ and $x_{\text{beam}}^{\text{found}}$. The found x is seen to be correlated with the true x, although not spectacularly well, with the smear coming primarily from the energy reconstruction. Since the high $E_\perp$ cut needed to clean up the data implicitly imposes a high x_{beam} cut, the behavior at high x is the most interesting and the most troubling. We see that above $x^{\text{actual}} \sim 0.7$ the x^{visible} is roughly invariant. Further, we recall that the structure function being probed is

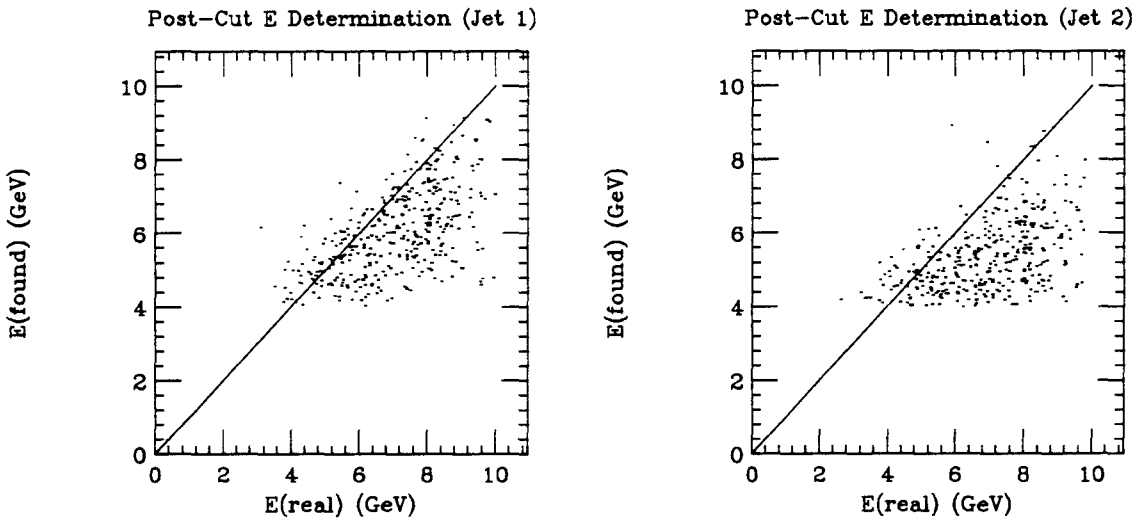

Figure 21: The correlation between E_{found} and E_{true} for both jet 1 and jet 2, with the requirement that both reconstructed jets have $E_\perp > 4$ GeV. The beam and target particles have uniform x probability distribution functions.

'flat' (i.e. all x's are equally likely.) The high $E_\perp$ cuts effectively require $x_{\text{beam}} > 0.5$, which precludes all low x (gluons for instance) measurements. This cut off is visible in figure (22) but can be seen from simple arguments. Since the center of mass energy for E683 is approximately 20 GeV, each incoming particle carries 10 GeV. Requiring 4 GeV jets, implies that x's are on the order of 0.4. Since it is further true that jets are typically not exactly at 90° in the center of mass frame, the x's must be slightly higher in order to allow θ deviations from 90°.

There is a feature of the jet finder, which I will outline here, that is potentially very useful for some investigations. In E683, we have used two different trigger types: 2HI (the two hottest towers in the MCAL both have an $E_\perp >$ a threshold (typically 0.75 GeV)) and Global (total MCAL $E_\perp > 8$ GeV.) If a normal trigger is applied (i.e. an OR of these two triggers) and a jet finder is applied ($E_\perp^{\text{minimum}} > 2$ GeV,) one may plot quantities such as $\phi_{\text{jet1}}^{\text{found}} - \phi_{\text{jet1}}^{\text{true}}$ & $\theta_{\text{jet1}}^{\text{found}} - \theta_{\text{jet1}}^{\text{true}}$ and look at the width of the resultant distributions. Upon doing so, one finds RMS widths $(\Delta\theta, \Delta\phi)$ of (0.23, 0.22) radians. However, if one applies solely the 2HI trigger (threshold of 0.75 GeV,)

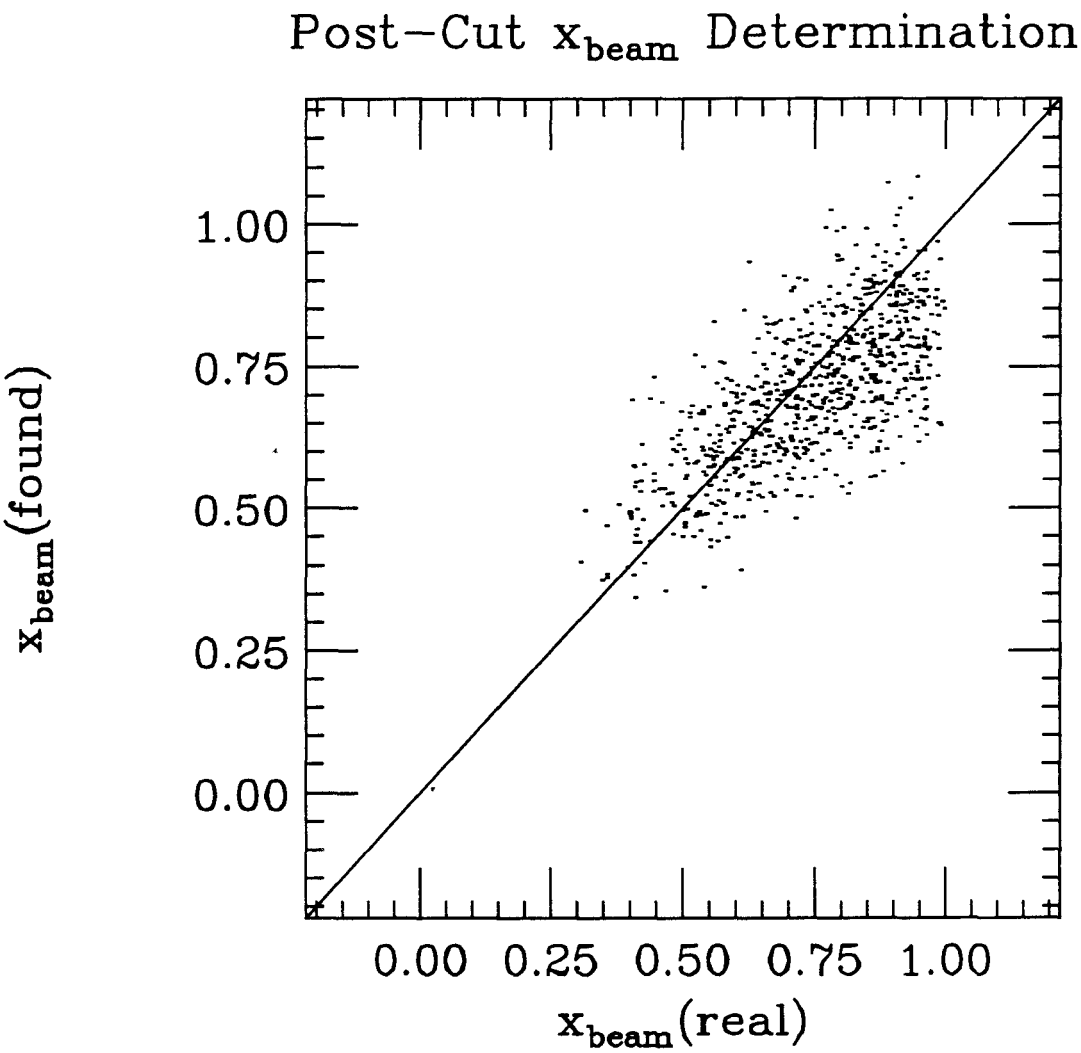

Figure 22: The $x_{\rm beam}$ correlations for events in which both reconstructed jets are required to have $E_\perp > 4$ GeV. The beam and target particles have uniform x probability distribution functions. $x_{\rm beam}^{\rm true}$ is the true naive x as reported by the Monte Carlo, $x_{\rm beam}^{\rm found}$ is determined from equation (9) using reconstructed jet kinematics.

one finds the widths have been reduced to (0.12, 0.15) radians. Keeping only the 2HI trigger, but raising the threshold to 1.00 GeV, yields widths (0.10, 0.11). A further threshold increase to 1.25 GeV improves the widths only slightly (0.08, 0.10) radians.

The numbers listed here are for found jet 1 (i.e. the easier to find jet.) Similar numbers for jet 2 would be subject to all the vagaries of minimum jet $E_\perp$ discussed above. The potentially useful point to be made is that there is a trigger effect on subsequent jet finding. This effect is sensible in that the 2HI trigger is more likely to trigger on events that either have low multiplicity jets, have a high fraction of the jet energy in the leading particle, or have the hottest particles in the jets nearly collinear. Such events would have more localized energy flow within the jet. It is possible that some E683 analyses can make use of this feature.

The previous discussion was concerned with hypothetical flat x distribution particles and the results were good enough to pursue further. Naively, we would expect that the results for real particles to be the same. Nonetheless, such an expectation needs to be checked. The three different types of photons (direct, VDM and QCD) are potentially different. The various perturbatively calculable QCD structure functions give similar results, so only QCD Duke and Owens [68] is shown here. I start by stating without proof that the ϕ finding ability of the jet finder is not uniform across beam particle types. Since the effect is much exacerbated in the reconstruction of θ, I defer for the moment the discussion of the cause of this variability. For a low reconstructed jet $E_\perp$ cut of 2 GeV (normal trigger,) the RMS of the distribution $\phi_{\rm jet}^{\rm found} - \phi_{\rm corresponding}^{\rm real}$ can range from as good as 0.22 radians to as bad as 0.39 radians. While bad, this RMS is sufficiently small to allow the criteria $|\phi_{\rm jet}^{\rm found} - \phi_{\rm corresponding}^{\rm real}| < 1$ radian to still effectively identify each reconstructed jet with its corresponding true jet.

As we will see, the θ determination is even worse. In figures (23) and (26) I present results equivalent to figure (19). All plots have $\theta^{\rm found} - \theta^{\rm real}$ plotted on the x axis and $E_\perp^{\rm found}$ along the y axis. For all structure functions, the results for both found jet 1 and found jet 2 are presented. Recall that found jet 1 is the one with the hotter seed tower.

Figure (23) illustrates the results for (a) direct photons and (b) VDM. The results

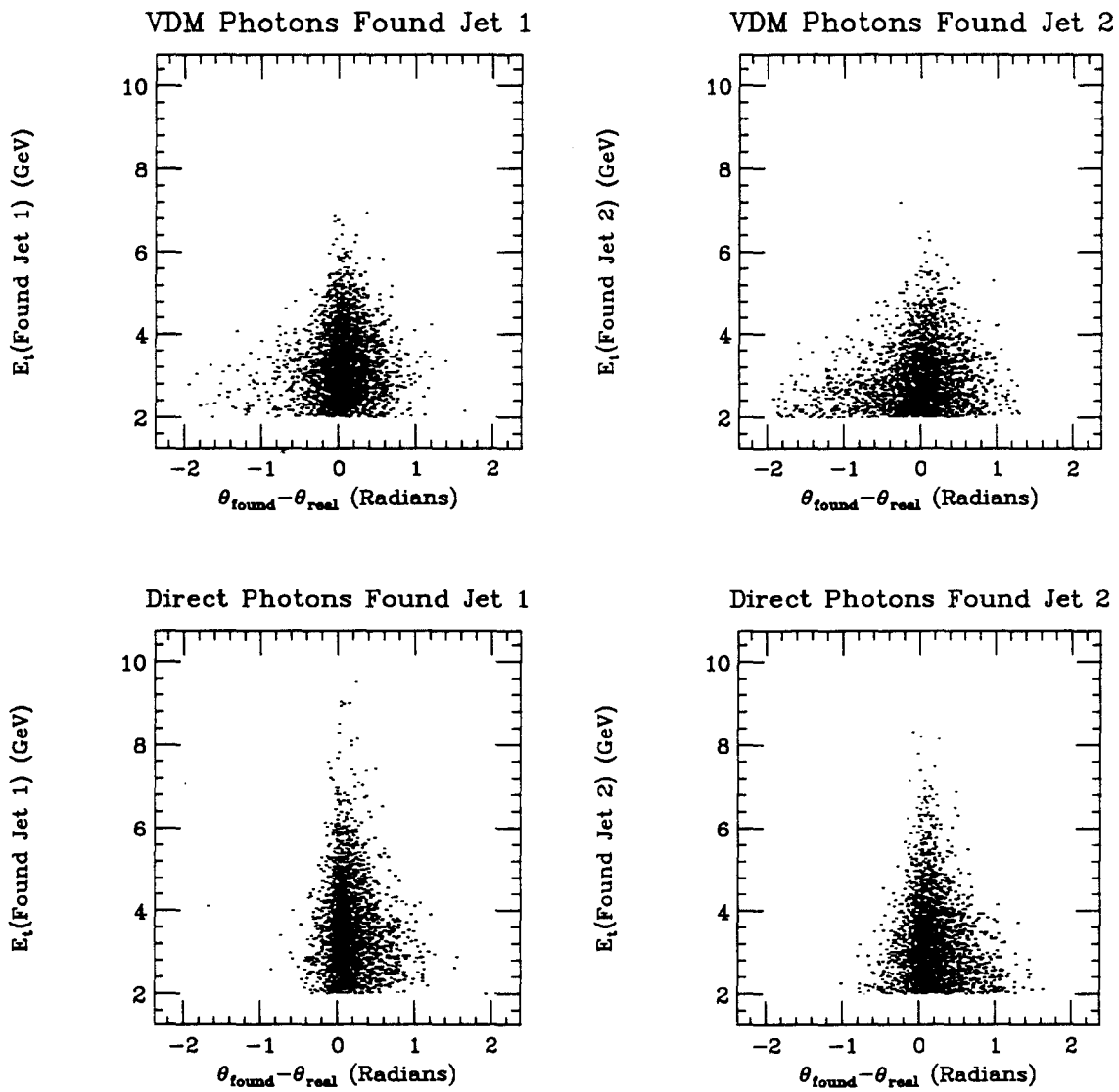

Figure 23: Shown is the correlations between $\theta^{\text{found}} - \theta^{\text{real}}$ and $E_{\perp}^{\text{found}}$ for both direct and VDM photons (CM frame.) The correlations for both jets are shown. Reconstructed jets are required to have $E_{\perp} > 2$ GeV.

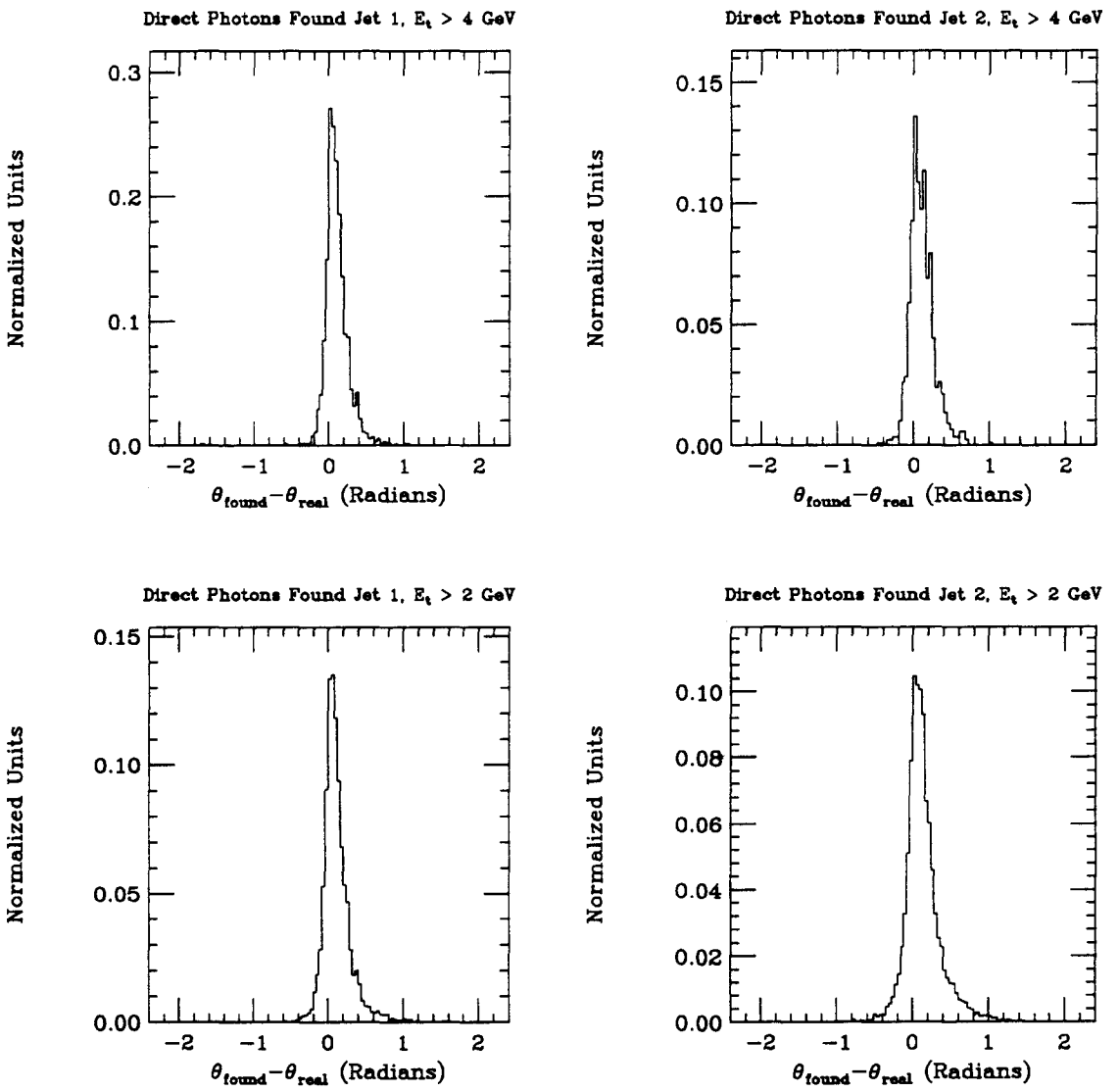

Figure 24: Shown is the quantity $\theta^{\text{found}} - \theta^{\text{real}}$ for direct photons (CM frame.) The reconstruction for both jets are shown. The bottom plots require that the reconstructed jet have $E_\perp > 2$ GeV, while the upper ones have the more stringent requirement $E_\perp > 4$ GeV.

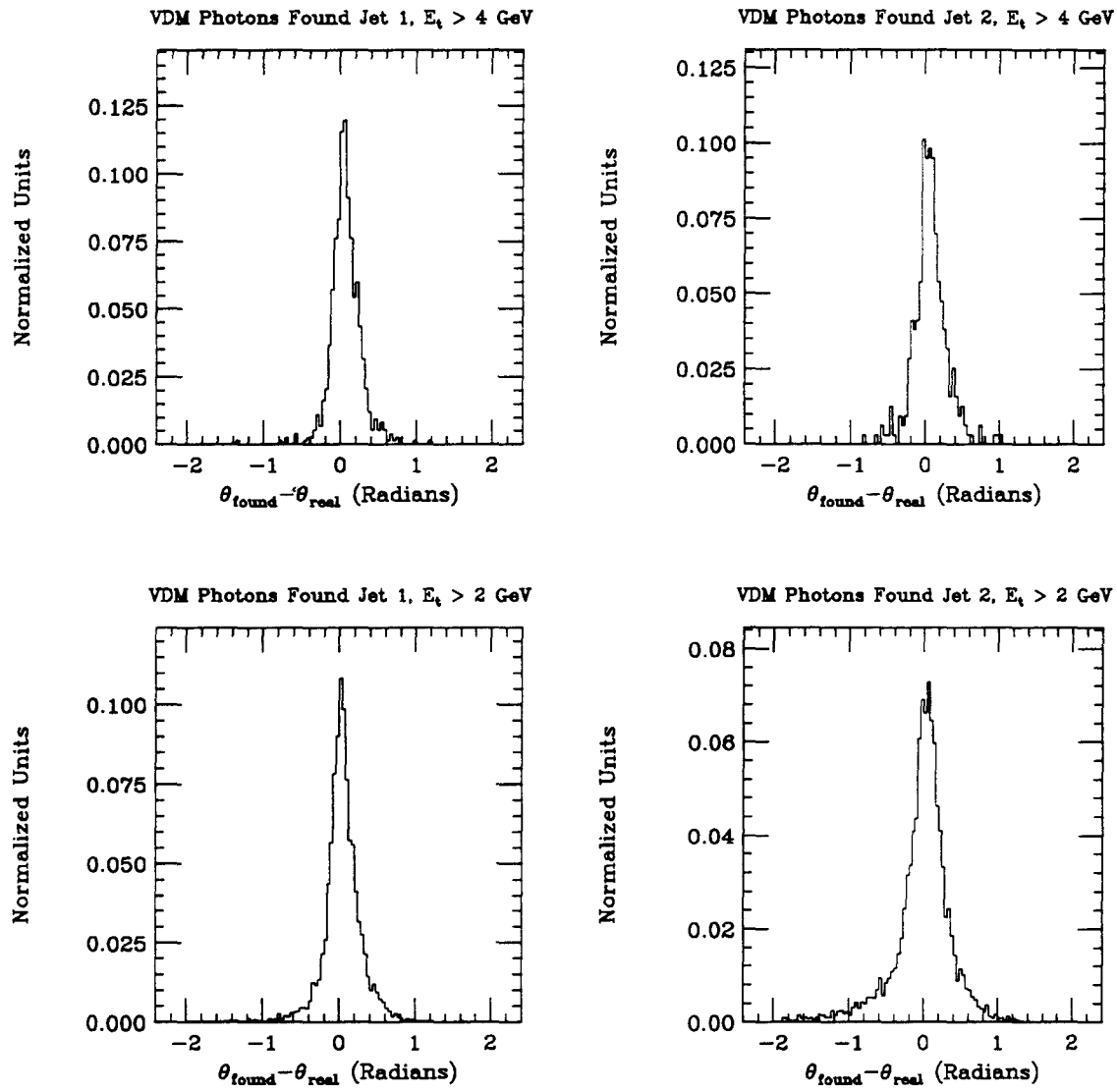

Figure 25: Shown is the quantity $\theta^{\text{found}} - \theta^{\text{real}}$ for VDM photons (CM frame.) The reconstruction for both jets are shown. The bottom plots require that the reconstructed jet have $E_\perp > 2$ GeV, while the upper ones have the more stringent requirement $E_\perp > 4$ GeV.

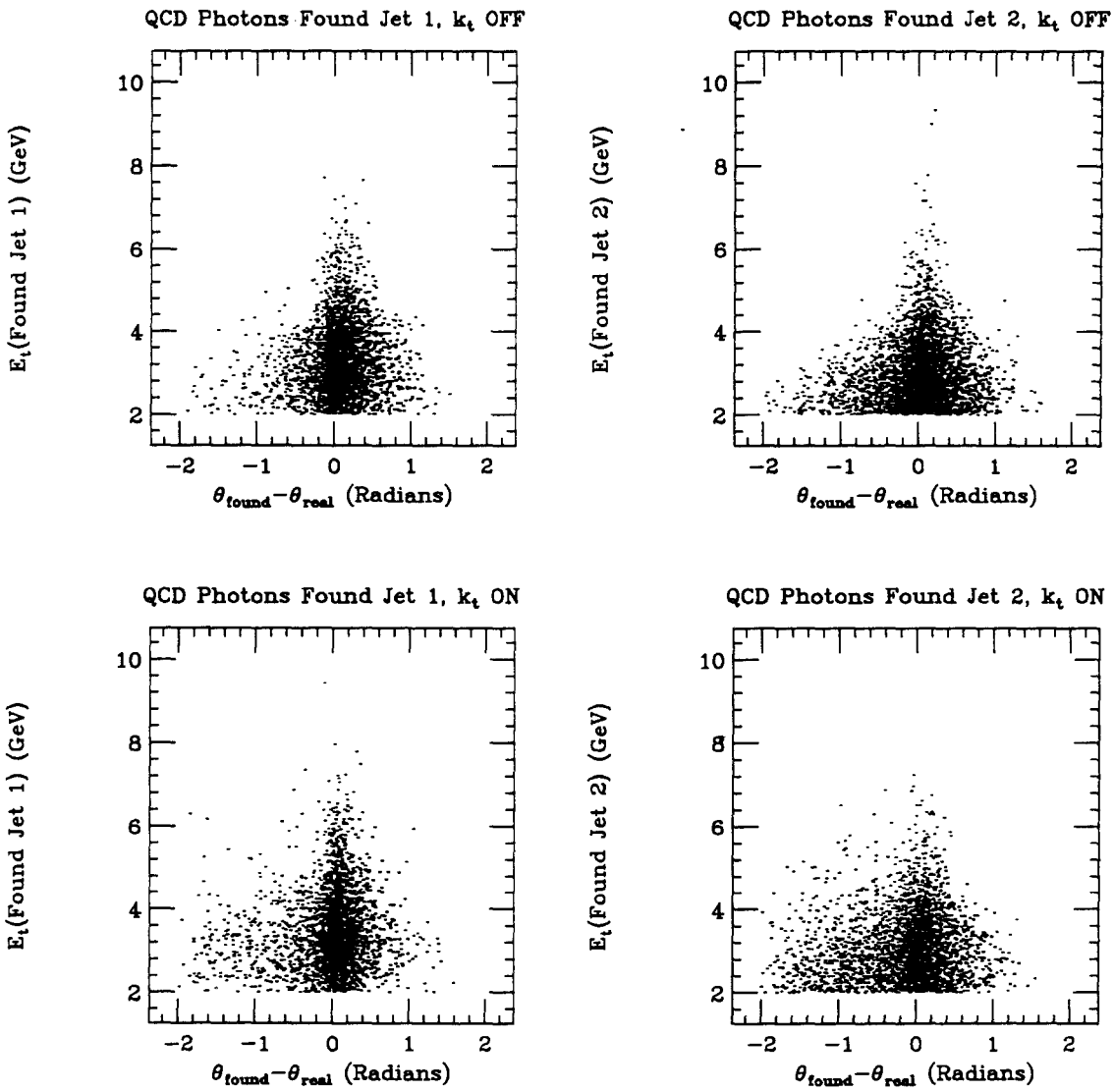

Figure 26: Shown is the correlations between $\theta^{\text{found}} - \theta^{\text{real}}$ and $E_{\perp}^{\text{found}}$ for extended photons with and without primordial $p_{\perp}$ (CM frame.) The correlations for both jets are shown. Reconstructed jets are required to have $E_{\perp} > 2$ GeV.

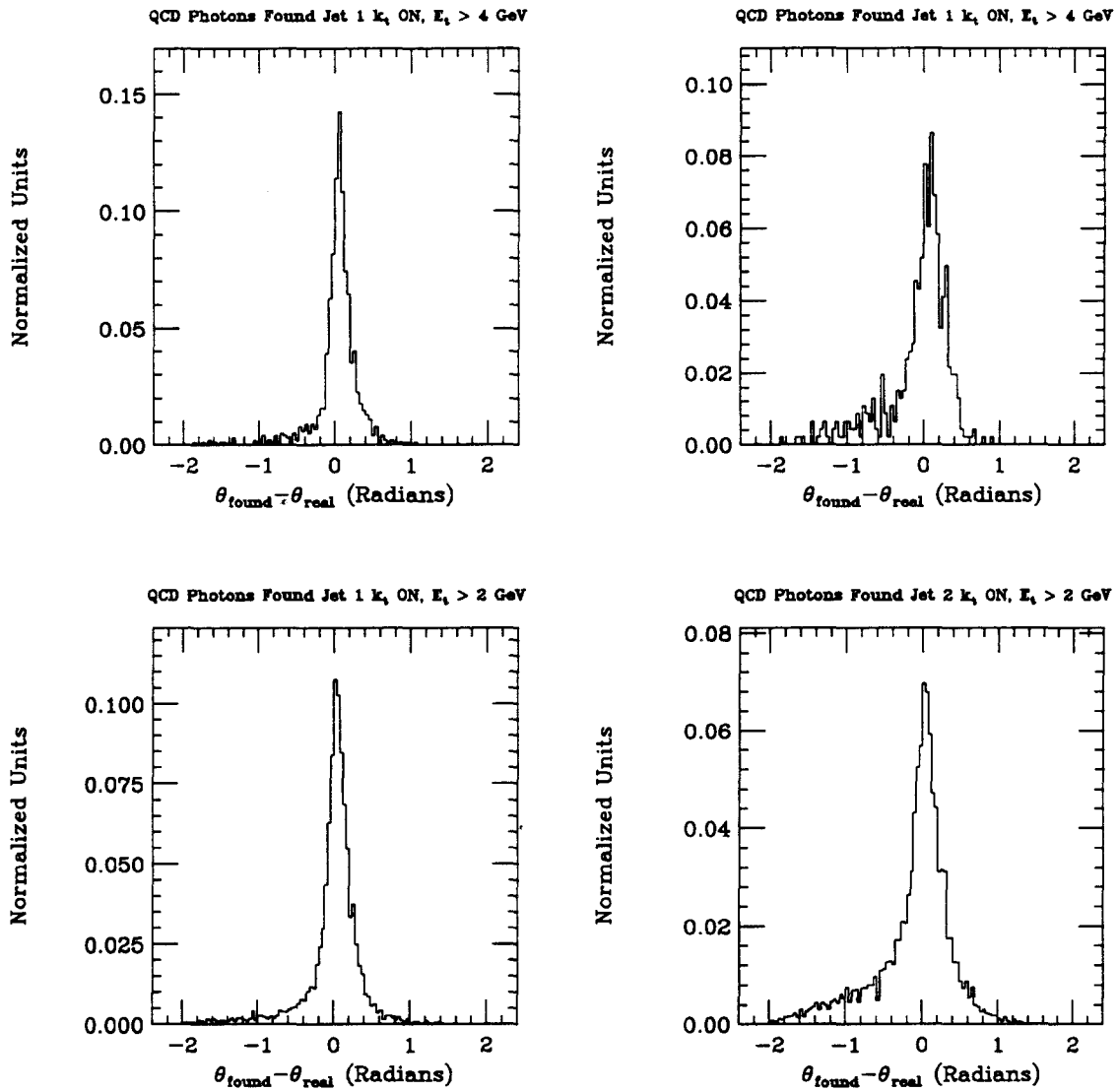

Figure 27: Shown is the quantity $\theta^{\text{found}} - \theta^{\text{real}}$ for extended photons (CM frame, $k_\perp$ ON.) The reconstruction for both jets are shown. The bottom plots require that the reconstructed jet have $E_\perp > 2$ GeV, while the upper ones have the more stringent requirement $E_\perp > 4$ GeV.

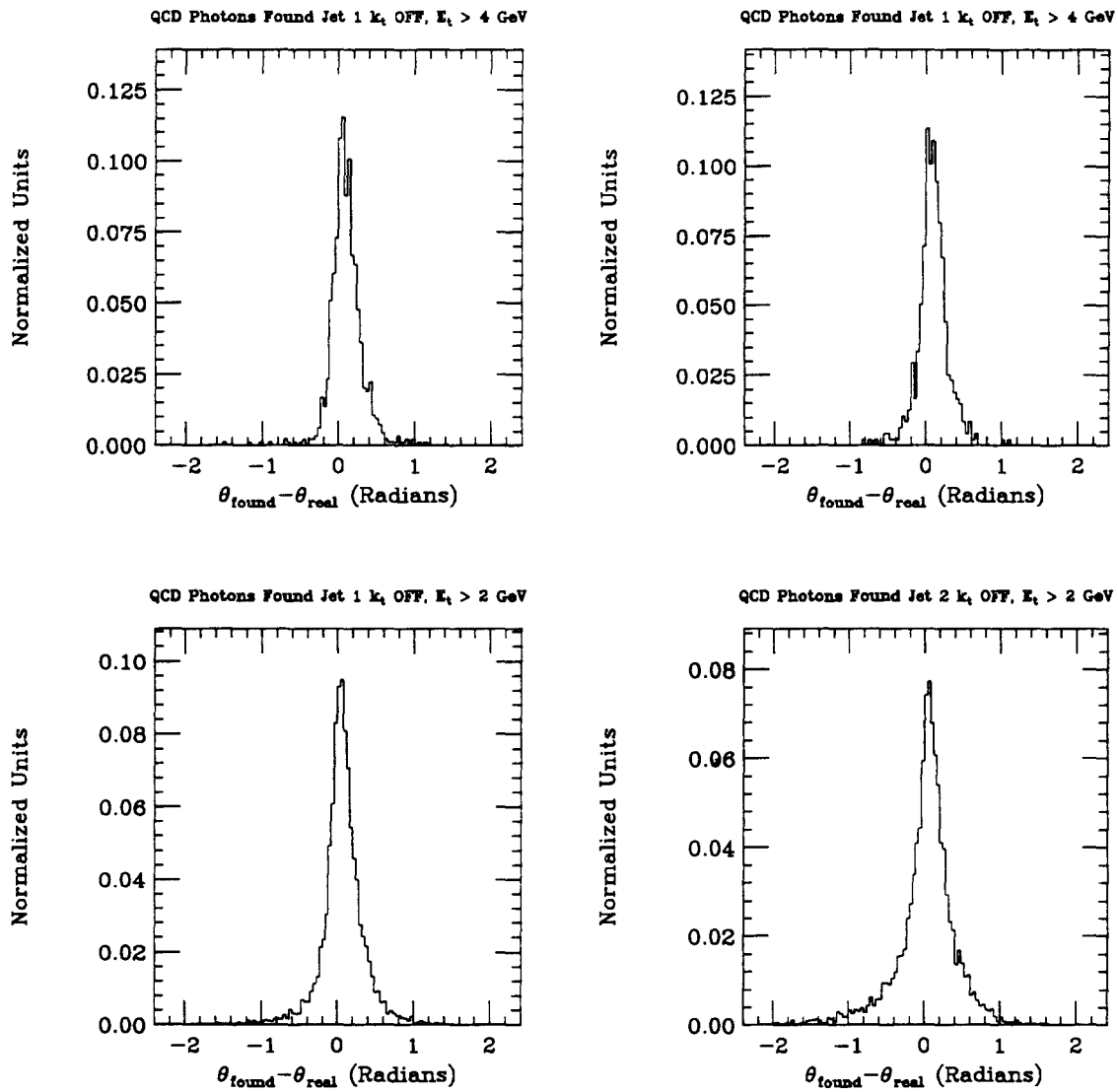

Figure 28: Shown is the quantity $\theta^{\text{found}} - \theta^{\text{real}}$ for extended photons (CM frame, $k_\perp$ OFF.) The reconstruction for both jets are shown. The bottom plots require that the reconstructed jet have $E_\perp > 2$ GeV, while the upper ones have the more stringent requirement $E_\perp > 4$ GeV.

for direct photons are amazing. The jet finder does a reasonable job for all found jet $E_\perp$'s, with a slightly worse job for jet 2. The VDM result is not as good. Jet 2 is somewhat worse than jet 1, especially in the region $E_\perp^{\text{found}}(\text{jet } 2) < 4$ GeV. However, above this cutoff, the ability to determine θ_2^{found} is improved. These points are further illustrated in figures (24) and (25).

Figures (26) and (27) show the θ reconstruction for QCD photons. Found jet 1 is similar to the previous figure with even a slight improvement over VDM. However jet 2 is more of a concern, since a long tail has appeared. Further, there is no reconstructed jet $E_\perp$ cut that removes the tail, in direct contradiction to the point demonstrated in figure (19). How can the QCD structure function result be so much worse than the other two aspects of the photon? The answer lies in the primordial $p_\perp$ of the perturbative QCD photon, which is of the order of 2 GeV (see figure (33),) much larger than the typical 400 MeV modelled in the case of pions or protons. Also demonstrated in figure (26) is the θ reconstruction for QCD photons when the $p_\perp$ caused by the perturbative splitting is turned off (see also (28).) The results are comparable to those of the VDM photons. The dependence of the jet finding capability on photon type, combined with the mixed nature of the beam make 'hard core' Monte Carlo jet finding corrections problematic.

One wonders why the $k_\perp$ of the photon has such a large effect on the jet finding, but the reason is not particularly mysterious. The $\hat{p}_\perp$ of a hard scattering is on the order of 3 GeV. The $k_\perp$ of the photon is (after trigger bias effects) approximately 2 GeV. Figure (29) shows an example of such an event. The two different $p_\perp$'s are added vectorially and the 'apparent' (i.e. $p_\perp$ carried by the outgoing partons even before jet formation) bears little resemblance to the hard scatter process we wish to observe. One jet has gained considerable $E_\perp$ at the expense of the other.

In figure (29), an interesting phenomenon is illustrated. A 2.8 GeV hard scatter is superimposed on a photon $k_\perp$ of 2 GeV. The result is that the two hard scatter partons now have very asymmetric $p_\perp$'s (in this example 1.4 and 4.7 GeV.) A parton that is not shown in the picture is the recoiling spectator parton from the photon, which carries 2 GeV. In this reasonably typical case, the spectator system carries

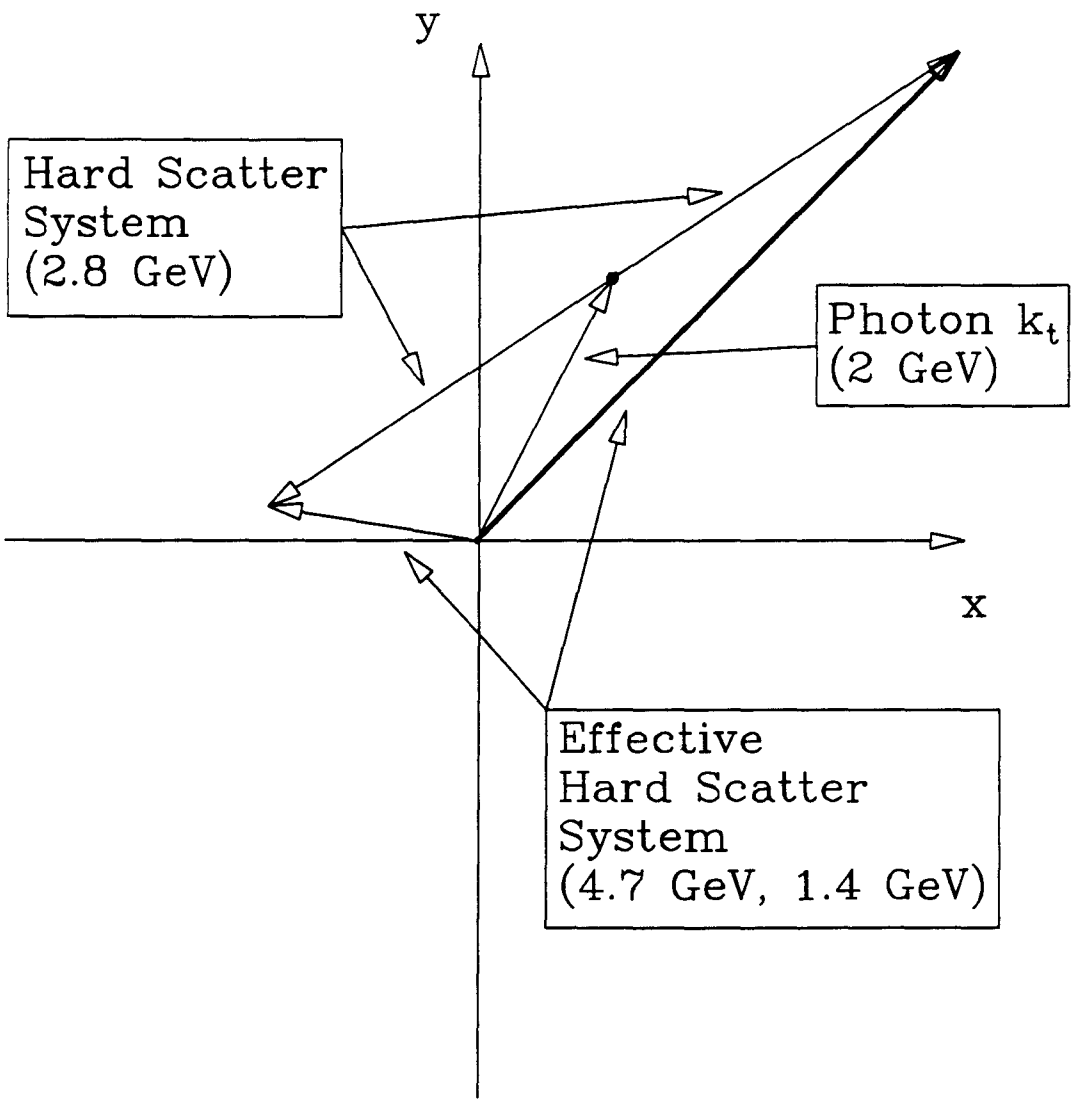

Figure 29: An example of the effect of $k_\perp$ on the scattering of a QCD type photon. A $k_\perp$ of 2 GeV is added to an event with a $\hat{p}_\perp$ of 2.8 GeV. The observable (if such things were possible) parton $E_\perp$'s are approximately 4.7 and 1.4 GeV respectively.

more $p_\perp$ than one of the two nominally more interesting hard scatter partons, and thus the definition of what is meant by 'hard scatter' comes into question. In the LUND Monte Carlo, the definition of hard scatter is relatively straightforward and I present the example of simple $q\overline{q}$ scattering by a single gluon exchange. In the limit of no $k_\perp$, the two quarks exiting the collision point are the hard scattered partons, with dynamics calculated from the simple Feynman tree diagram. When $k_\perp$ is added, those two quarks are still considered the hard scatter partons, since the addition of $k_\perp$ is taken to be a small perturbation to the simple calculation. However, in the case of TWISTER extended photon, $k_\perp$ is no longer a small effect. As shown above, it is possible for the recoil system to have comparable or greater $p_\perp$'s than at least one parton of the 'hard scatter' system.

For that reason, a new definition of hard scatter parton is considered. For the moment, we define the two hard scatter partons to be those two partons exiting the collision point that carry the highest $p_\perp$'s, regardless of their point of origin. This definition is a pragmatic experimental one, as opposed to a calculationally simple, theoretical one. Such a definition makes the biggest difference in the case of TWISTER extended photon, $k_\perp$ on. When this definition is made, the ability to reconstruct the kinematics of the second jet is vastly improved. Figure (30) corresponds to figure (27) with the primary difference being the change in definition of what is meant by hard scatter (the binning is also changed, but that does not affect the result.) The most fundamental difference between the two figures is the disappearance of the grossly asymmetric behavior for found jet 2. Initially the distribution $\theta_{\text{true}} - \theta_{\text{real}}$ for jet 1(2) had an RMS of 0.33(0.52) radians when the minimum found jet $E_\perp$ was 2.0 GeV and 0.23(0.57) radians for a minimum jet $E_\perp$ of 4.0 GeV. The θ correspondence has now improved to an RMS of 0.19(0.29) for the low cut off and 0.14(0.19) for the high $E_\perp$ jet cut off.

While a discussion of the implications of this result is deferred until section (10), certain things are readily apparent. First, it appears that it is possible to reconstruct the kinematics of the highest $E_\perp$ partons. Secondly, my investigations show that the highest $E_\perp$ parton is also one of the (nominally) hard scatter partons 97% of

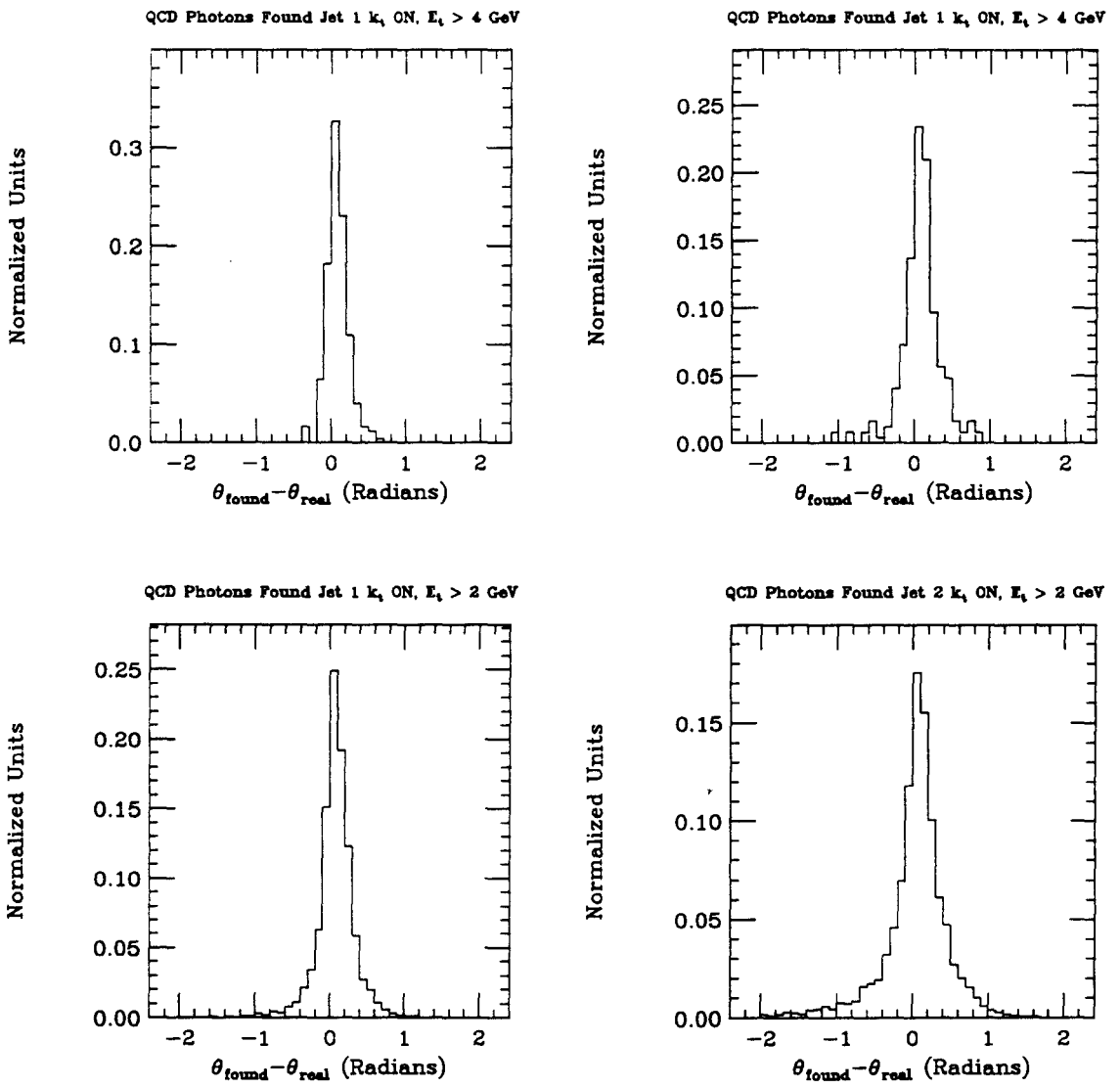

Figure 30: Shown is the quantity $\theta^{\text{found}} - \theta^{\text{real}}$ for extended photons (CM frame, $k_\perp$ ON.) The reconstruction for both jets are shown. The bottom plots require that the reconstructed jet have $E_\perp > 2$ GeV, while the upper ones have the more stringent requirement $E_\perp > 4$ GeV. In this plot, the reconstructed jets are being compared to the two highest $E_\perp$ partons, rather than the nominal 'hard scatter' partons.

the time, but the second highest $E_\perp$ parton is one of the (nominally) hard scatter partons only 67% of the time.[12] This implies that roughly one third of the time, the second highest $E_\perp$ parton comes from the recoiling spectator system. Together these facts paint a picture that is both refreshing and troubling. It appears that we are able to adequately reconstruct the kinematics of those partons that have the biggest $p_\perp$. However those partons are often not what we had thought. Collectively the experiment must either (1) learn to separate the two classes of events, or (2) choose to measure things for which the calculations have combined the two event types. Since $k_\perp$, if it actually exists as presented here, appears to be a significant stumbling block for reconstruction of 'hard scatter' parton kinematics, I devote the following section to looking to see if the $k_\perp$ suggested by the Monte Carlo is preserved as a final state observable. This is followed by a general data/Monte Carlo comparison, with the intent of investigating whether or not the predicted $k_\perp$ is present.

8.1 Possible $k_\perp$ Signatures

Since Monte Carlo results show that the $k_\perp$ of the photon appears to make an important contribution to the final state partons' kinematics, the simple question arises: 'Is there anything to this $k_\perp$ idea?' More cogently, is there a signal in the data that reveals the existence of the $k_\perp$ espoused in the Monte Carlo? I investigate this question in two stages. First I investigate the $k_\perp$'s predicted by two Monte Carlos: TWISTER/LUCIFER and HERWIG. In a later section, I compare Monte Carlo distributions with data to see if the Monte Carlo results are vaguely sensible.

As a prelude to the multi-Monte Carlo investigation of $k_\perp$, one must realize that while the parton from each parent hadron carries a $k_\perp$ of its own ($\vec{k}_\perp^1$ and $\vec{k}_\perp^2$ respectively,) the only thing that can be measured in an experiment is $\vec{k}_\perp^1 + \vec{k}_\perp^2$. As we shall see, the various Monte Carlos do deal with the individual parton's $k_\perp$'s quite differently, but the magnitude of the *total* $k_\perp$ is similar for various models.

In the LUND based models (TWISTER/LUCIFER,) the $k_\perp$ of the hadronic particles (pions and protons for instance) is given by a double Gaussian probability

[12] For TWISTER, extended photons, $k_\perp$ on, trigger and jet finding applied.

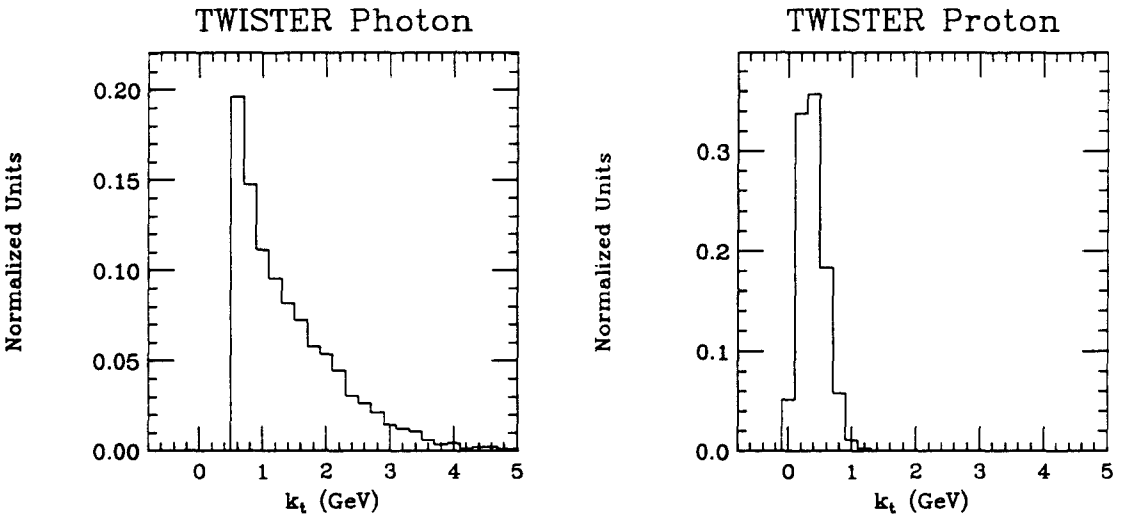

Figure 31: Shown is the $k_\perp$ used by the TWISTER Monte Carlo. On the left the $k_\perp$ of the extended photon is shown. On the right, the $k_\perp$ of the proton is shown. For this plot, the photon energy was 250 GeV.

distribution in k_x and k_y:

$$P(k_x, k_y) \propto e^{\frac{-(k_x^2+k_y^2)}{2\sigma_{k_\perp}^2}} ,$$

where $\sigma_{k_\perp}$ is taken to be the 300 MeV expected from confinement arguments. The direct gamma has no internal structure and therefore carries no $k_\perp$.

The extended photon in TWISTER is quite different and in keeping with its perturbative nature, gains its $k_\perp$ from Altarelli-Parisi evolution or more correctly from the ideas contained in equation (7) and in the discussion following it. The extended photon $k_\perp$ distribution goes as $1/k_\perp$ from an arbitrary 0.5 GeV to the kinematically determined maximum $\sqrt{\hat{s}}/2$. The sharp edge at 0.5 GeV is clearly unphysical and stems from the artificial distinction between VDM and QCD photons. The threshold is chosen to smooth the transition between these artificially separated states as much as possible. The two non-trivial types of $k_\perp$ (hadron and extended photon) are shown in figure (31.)

HERWIG implements hadron $k_\perp$'s very differently. Vanilla HERWIG does not implement primordial (i.e. confinement caused) $k_\perp$'s. Instead all $k_\perp$'s come from

initial state gluon radiation which is an integral part of the model and is governed by the Altarelli-Parisi equations. In E683's kinematic region, multiple splittings are infrequent and therefore the $k_\perp$ distribution when splittings occur look much like that evident in TWISTER extended photons.

Of course in the HERWIG model initial state gluon radiation does not always occur and in this case the partons carry no $k_\perp$, something very hard for this author to accept[13]. As an example, if the hard scatter parton is a valence parton (e.g. the u or $\overline{d}$ of a π^+, the u, u, or d of a proton, and most oddly, the u or $\overline{u}$ of an extended photon,) it is unlikely to have undergone initial state radiation and therefore has no $k_\perp$. In the case that the hard scatter parton is not a valence one (e.g. a gluon,) then a splitting must have occurred and the parton carries a $k_\perp$ governed by equation (7.) Figure (32) shows the $k_\perp$ distributions given by HERWIG to the partons of both the proton and the extended photon. Note that the two distributions are similarly shaped as compared to the differences seen in the TWISTER model.

Like the TWISTER extended photon $k_\perp$ distribution, what is seen in figure (32) is clearly unphysical. There is no physically defensible reason to expect that partons carry either no $k_\perp$ or more than 1 GeV. This split is broadly similar to the VDM/QCD split in TWISTER, but the analogy is not perfect, due to the differences in the structure functions of the two Monte Carlos.

Much of the unphysical characteristics of figure (32) can be reduced by adding primordial (or confinement) $k_\perp$ to the model. Such an extension is available in the model and can be easily implemented. Figure (32) also shows the $k_\perp$'s used by HERWIG if a double Gaussian 300 MeV primordial $k_\perp$ is added to both of the colliding partons.

Clearly the $k_\perp$'s of the partons are both very model and hadron type dependent. One might despair at the differences or perhaps hope to use the data to distinguish between the possibilities. However, the visible differences are smaller than one would think. If two partons 1 and 2 (each carrying a (k_x^i, k_y^i)) are scattered, the $k_\perp$ of the *total* event (which is the only thing that can be experimentally measured) may be

[13]Although we shall see that it doesn't make that much difference.

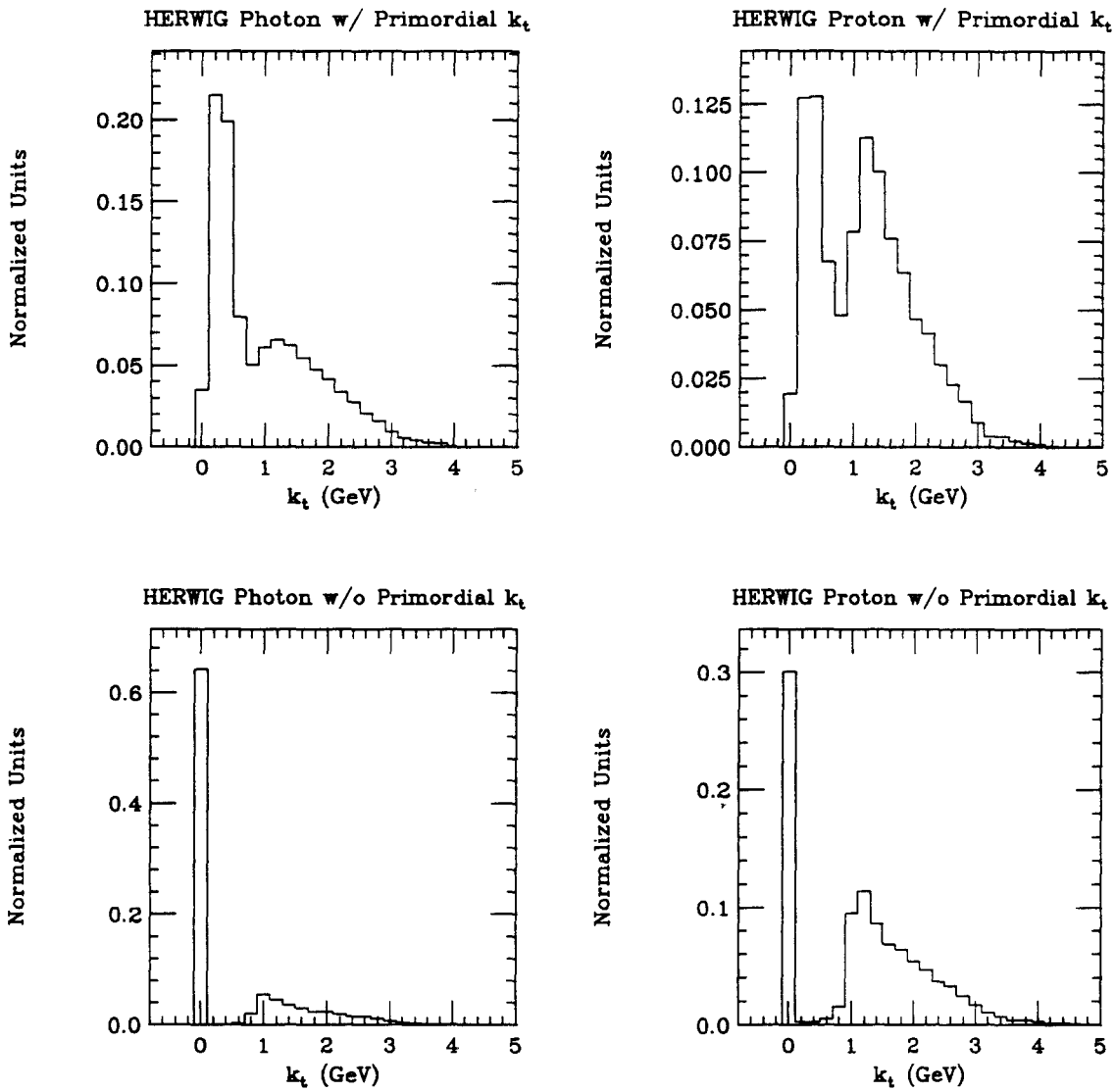

Figure 32: Shown is the $k_\perp$ used by the HERWIG Monte Carlo. On the left the $k_\perp$ of the extended photon is shown. On the right, the $k_\perp$ of the proton is shown. The top plots have an additional contribution of primordial (or confinement) $k_\perp$, while the bottom plots are for 'vanilla' HERWIG (i.e. default settings.) For this plot, the photon energy was 250 GeV.

defined:

$$k_\perp = \sqrt{(k_x^1 + k_x^2)^2 + (k_y^1 + k_y^2)^2}$$

Figure (33) shows the $k_\perp$ distribution for both the TWISTER and HERWIG extended photons. The most striking (and perhaps surprising) observation is that the two models have similar event $k_\perp$ distributions. This shows the $k_\perp$ in TWISTER is theoretically plausible and not a wild idiosyncrasy of the model. It also underscores that a 2 GeV-ish $k_\perp$ is thought to be present and one must account for it in one's ansatz. On the other hand, the TWISTER distribution is somewhat harder than that seen in HERWIG, primarily because HERWIG is allowed to have multiple gluon emission in the initial state and this has the effect of softening the $k_\perp$ distribution. The difference in $k_\perp$ fall off will have implications especially for the $p_\perp$ dependences of the cross section, but this difference is less important when one is simply discussing the jet finding ability.

Given this theoretical plausibility, the question of experimental signatures arises. Certainly the overall $k_\perp$ of the initial state is preserved in the final state and could be seen in the magnitude of the vector sum of the outgoing partons. For example, if two partons 1 and 2 exit the collision point with $p_\perp$'s given by (p_x^1, p_y^1) and (p_x^2, p_y^2), the $k_\perp$ of the initial state can also be written:

$$k_\perp = \sqrt{(p_x^1 + p_x^2)^2 + (p_y^1 + p_y^2)^2} \tag{10}$$

Such a quantity can be constructed from found jet quantities and it is hoped that the parton level $k_\perp$ is preserved across fragmentation and jet finding.

Another expected signature is the $\Delta\phi$ between the jets. As you might recall, ϕ is the azimuthal angle and measures the angular position in the xy plane. In the absence of $k_\perp$, conservation of transverse momentum dictates that the two exiting partons must have a ϕ angle between them of 180°. $k_\perp$ causes deviations of $\Delta\phi$ from 180°. So a $\Delta\phi$ measurement could be expected to shed light on the $k_\perp$ question.

An additional signature is the 'out of plane component' of the $k_\perp$ (called $k_{\perp\phi}$.) This measures the component of $k_\perp$ that causes the the two jets to have a $\Delta\phi < 180°$.

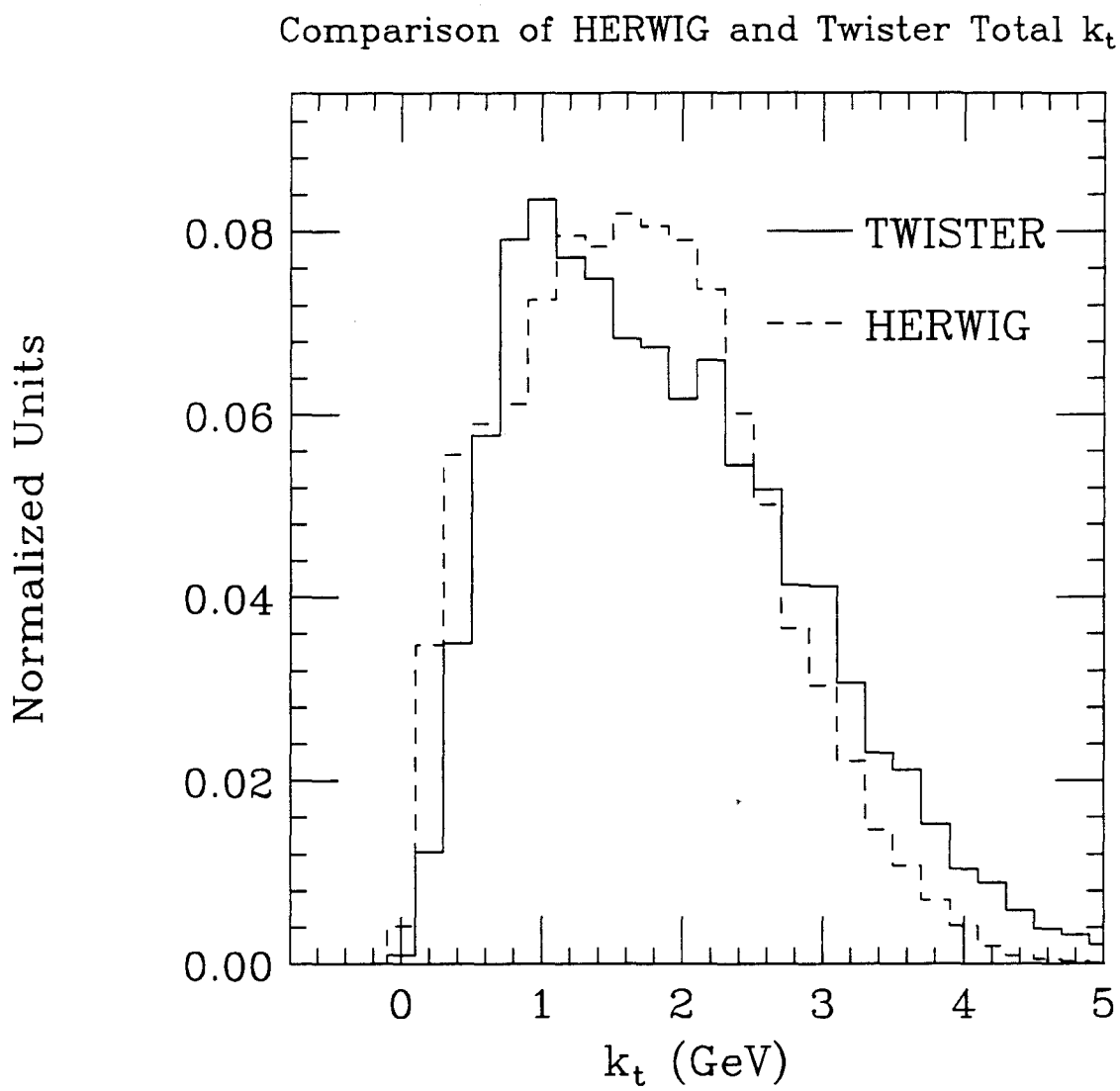

Figure 33: Shown is an overlay of the *total* $k_\perp$ used by the both the TWISTER and HERWIG Monte Carlos. TWISTER is shown by a solid curve, HERWIG by the dashed. The HERWIG curve has an additional 300 MeV primordial $k_\perp$ added that is not present in the default program configuration, TWISTER uses the program defaults. For this plot, the photon energy was 250 GeV.

Mathematically, this is expressed as

$$k_{\perp\phi} = <E_{\perp}^{\text{jet}}> \sin\Delta\phi \tag{11}$$

where $<E_{\perp}^{\text{jet}}>$ is defined to be the average jet $E_{\perp} = (E_{\perp}^{\text{jet1}} + E_{\perp}^{\text{jet2}})/2$ and $\Delta\phi$ is as specified above.

I investigated the three above quantities ($k_{\perp}, k_{\perp\phi}$, and $\Delta\phi$) for both direct and extended photons. I further separated my investigation into these quantities both using the 'hard scatter' partons and also those partons that explicitly have the highest post collision $p_{\perp}$. For reasons of space, I only give the $k_{\perp}$ results here, but the general conclusions are borne out by the $k_{\perp\phi}$ and $\Delta\phi$ investigations as well.

I investigate $k_{\perp}$ by comparing the $k_{\perp}$ of the true jets[14] with $k_{\perp}$'s measured by applying reconstructed jet quantities to equation (10) (inserting reconstructed jet $p_{\perp}$'s rather than true jet quantities.) I present the scatter plots of these two quantities for various cuts on the two jets $E_{\perp}$'s. Figure (34) shows the $k_{\perp}$ reconstruction capability for TWISTER extended photons ($k_{\perp}$ on) for the hard scatter partons and figure (35) shows the correlation between found $k_{\perp}$ and the true $k_{\perp}$ from the jets that came from the two highest $p_{\perp}$ partons. The scatter plots show that the found $k_{\perp}$ is at best very weakly correlated to the hard scatter $k_{\perp}$ and that the correlation between the $k_{\perp}$ of the jets from the high $p_{\perp}$ partons and the reconstructed $k_{\perp}$ is somewhat better (although still poor.) One obvious difference between the two plots is the range of true $k_{\perp}$ that is seen. The range of $k_{\perp}$ seen by using the hard scatter partons is greater than the range seen using the highest $p_{\perp}$ partons. This makes sense, given the possible asymmetry between the hard scatter partons shown in figure (29).

A final look at the $k_{\perp}$ reconstruction is shown in figure (36). In this figure, the quantity $k_{\perp}^{\text{found}} - k_{\perp}^{\text{true jet}}$ is made with the true jet defined first to be those jets that come from the 'hard scatter' system and then separately to be those jets that came from the highest $p_{\perp}$ partons. So, while the scatter plots show that the correlation is not strong, the difference plots in figure (36) show that the mean is accurately found,

[14]Note that this is not the same as the parton level $k_{\perp}$. Fragmentation has a distinct and significant effect in scrambling the parton $k_{\perp}$'s, but since the major effect is from the jet finding procedure, I have opted to present the results in this manner.

but with large event by event fluctuations.

One criticism of the above methods of investigating $k_\perp$ is that two jets are required to be found. Figure (29) underscores the possible asymmetry between the $p_\perp$'s of the hard scatter partons. Insisting that the second jet be above a certain threshold (say $p_\perp > 3$-4 GeV) essentially ensures that energy from the spectator system will be present under the jet cone. Increasing the $p_\perp$ threshold will exacerbate the problem. When one uses the more proper high $p_\perp$ partons, this problem is significantly reduced, but since I have so far not shown whether the large $k_\perp$ espoused by the Monte Carlo is actually present in the data, I wish to investigate methods of observing $k_\perp$ that are equally applicable to all reasonable models.

For this reason, a very different method was investigated. It is possible to take an event and define an arbitrary (x, y) direction. Then the $\Delta\phi$ of each particle (or tower) measured with respect to this arbitrary direction can be measured and entered into a histogram with a weight equal to the $E_\perp$ of the particle (or tower.) If instead of an arbitrary direction, one chooses the direction defined by a found jet and repeats this process for many events, the result is called an $E_\perp$ flow plot.

Since it appears that the first jet can be reconstructed with a reasonable degree of precision, I constructed $E_\perp$ plots in the following manner: (1) I applied the jet finding algorithm to Monte Carlo and data, (2) I required that at least one jet was found (but perhaps more,) (3) I then constructed an $E_\perp$ flow plot with the reference direction determined by the required reconstructed jet. Since no requirement was made on the second jet, biases introduced by the jet finding process are reduced. As this distribution is not one that lends itself to a scatter plot type of presentation, I defer the Monte Carlo/data comparison until later.

9 Monte Carlo/Data Comparison

In this section, I will outline the E683 specific details of the Monte Carlo, and then compare the data with both the LUCIFER/TWISTER (independent fragmentation) and HERWIG models.

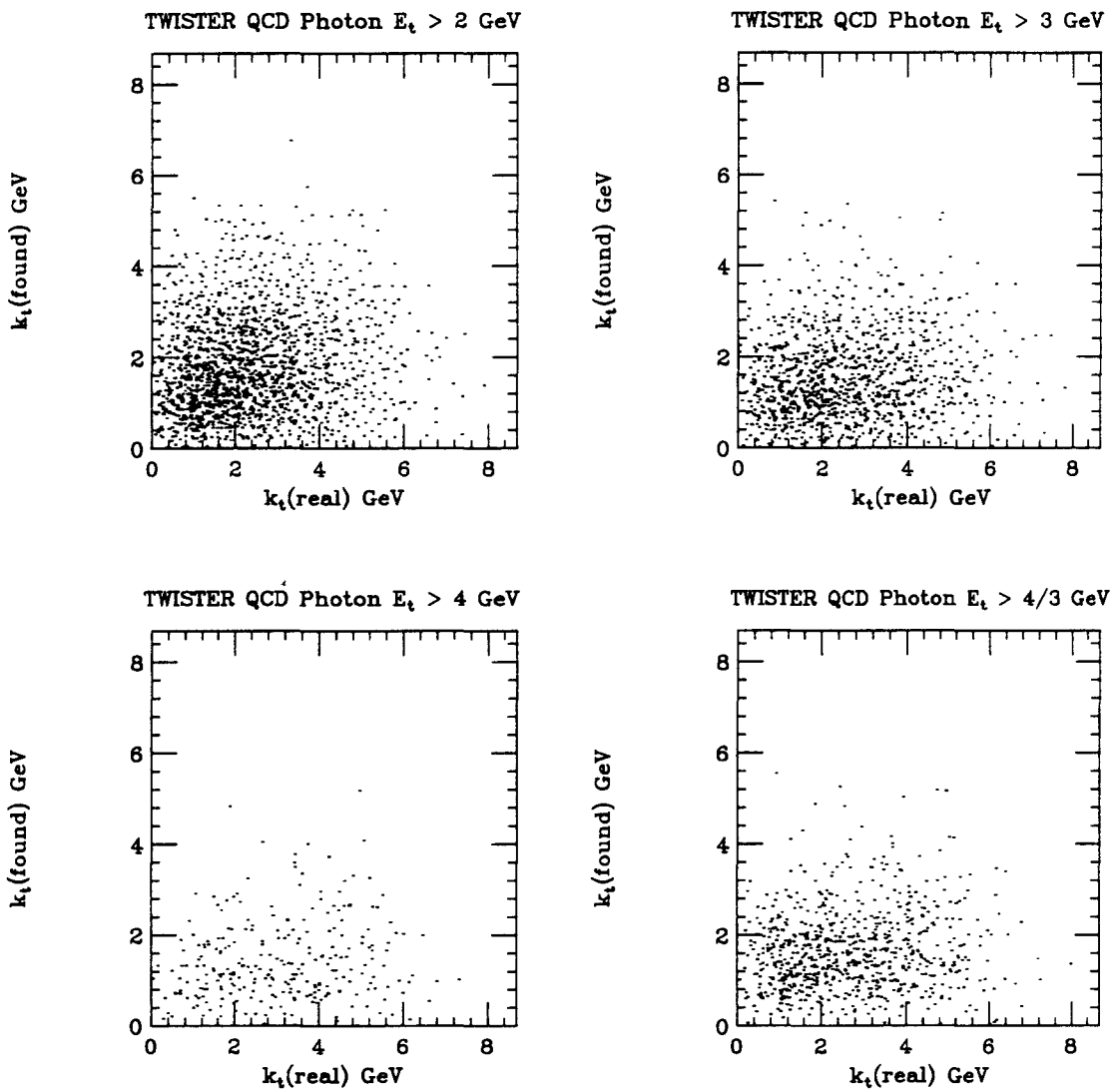

Figure 34: Shown is a scatter plot of the $k_\perp$ determined from reconstructed jets compared to true jet level $k_\perp$ for TWISTER extended photons ($k_\perp$ ON) for those jets coming from the 'hard scatter' system. The photon beam energy is drawn from the usual distribution, with a minimum $\hat{p}_\perp$ of 2 GeV. The title of each plot gives the minimum jet $E_\perp$ required of *each* reconstructed jet. The lower right hand plot is unique in that it has an asymmetric jet $E_\perp$ requirement, with $E_\perp$ requirements for jets 1 and 2 being 4 GeV and 3 GeV respectively.

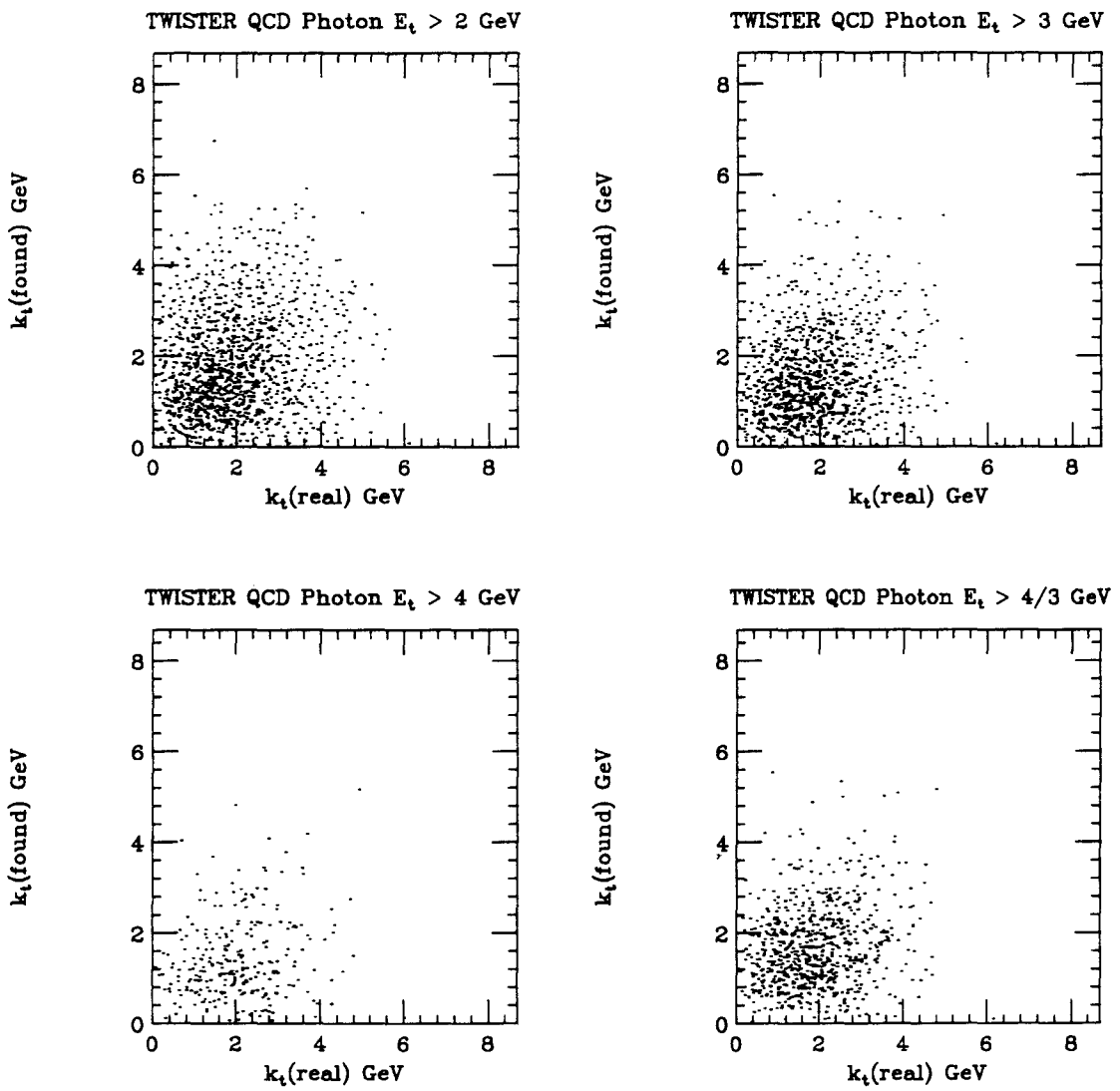

Figure 35: Shown is a scatter plot of the $k_\perp$ determined from reconstructed jets compared to true jet level $k_\perp$ for TWISTER extended photons ($k_\perp$ ON) for those jets coming from the high $p_\perp$ partons. The photon beam energy is drawn from the usual distribution, with a minimum $\hat{p}_\perp$ of 2 GeV. The title of each plot gives the minimum jet $E_\perp$ required of *each* reconstructed jet. The lower right hand plot is unique in that it has an asymmetric jet $E_\perp$ requirement, with $E_\perp$ requirements for jets 1 and 2 being 4 GeV and 3 GeV respectively.

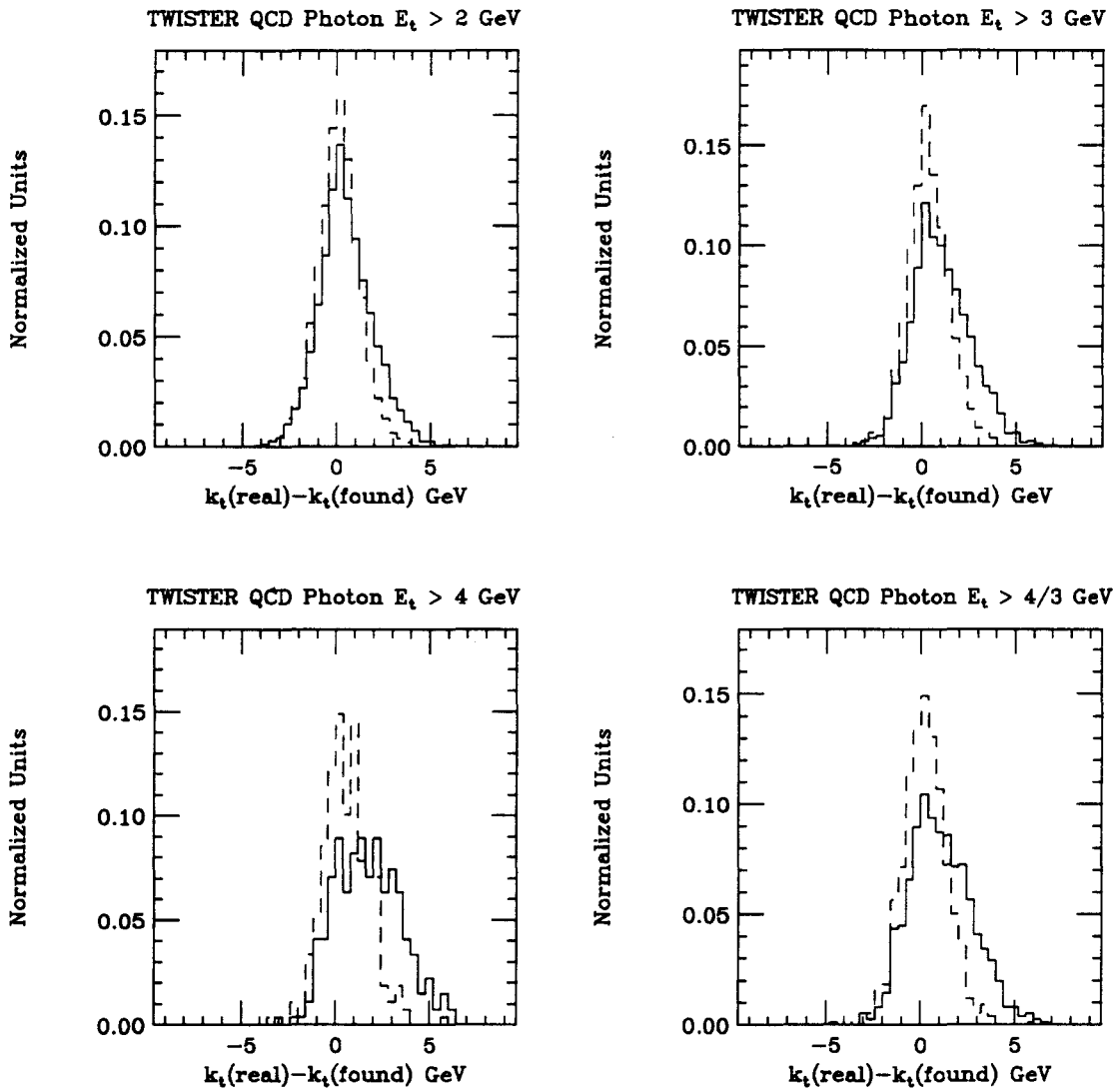

Figure 36: Shown is the distribution $k_\perp^{\text{found}} - k_\perp^{\text{truejet}}$ for TWISTER QCD extended photons. The solid line denotes a comparison to 'hard scatter' partons and the dashed line denotes 'high $E_\perp$' partons. The photon beam energy is drawn from the usual distribution, with a minimum $\hat{p}_\perp$ of 2 GeV. The title of each plot gives the minimum jet $E_\perp$ required of *each* reconstructed jet. The lower right hand plot is unique in that it has an asymmetric jet $E_\perp$ requirement, with $E_\perp$ requirements for jets 1 and 2 being 4 GeV and 3 GeV respectively.

9.1 Simulation of E683

When an experimental measurement is made and one wishes to compare it to a theoretical prediction, a problem arises. Since the experimental apparatus often distorts the distribution being measured, a direct theoretical and experimental comparison is generally not possible. At this point, a philosophical question arises: Does one try to de-convolve the detectors' effects from the experimental measurement?; or, Is it better to simulate the effects of the detector and distort the theoretical distribution? Ultimately, one probably would want to exercise the first option, as an experiment-free measurement is most useful to the physics community as a whole. Unfortunately, a successful attempt of this nature is predicated on a *thorough* understanding of all of the detector systematics, something not available at this time.

The second option is both safer and a necessary precursor to option 1. This option is safer, since the steps can be more naturally factorized (i.e. tested,) but even more fundamentally, the mathematics of de-convolving the response function are structurally unstable [64] and should be avoided if a reasonably correct Monte Carlo is available.

In order to simulate the data/experiment, many steps must be taken:

- The apparent beam energy distribution must be simulated.
- The event must be simulated. This is handled by the TWISTER/LUCIFER and HERWIG Monte Carlos.
- The various physics processes must be mixed in appropriate proportions (i.e. weighted by their cross-section.) This step is circumvented for reasons discussed below.
- The various detectors must be properly simulated.
- For E683, the case of multiple bremsstrahlung must be addressed.

The first step is handled by a straight parametrization of the data. The photon spectrum is measured for the triggered photon data (see figure (37).) The distribution

was separated into 25 bins from 0 to 500 GeV. When a Monte Carlo is run, the events are generated so that the each energy bin contributes the correct fraction of triggered events. One of the tests of the Monte Carlo is to investigate how the various jet cuts will affect the $E_\gamma^{\text{apparent}}$ distribution in both the Monte Carlo and the data.

The second step has been alluded to in section (1.6). LUCIFER [65] and TWISTER [66] are LUND JETSET 6.2 [67] based Monte Carlos which generate direct and extended photons respectively. They are incredibly easy to use and have many easily accessed hooks to tune all aspects of the event generation (hard scatter, fragmentation, structure functions, etc.) In this dissertation, with the exception of the variation of fragmentation models and structure functions, the defaults have been used. In the case of HERWIG [35], both direct and extended photons can be generated. When generating HERWIG events, I use the defaults, except that I turn the enhanced underlying event off as suggested by [42]. Throughout I use a minimum $p_\perp$ of the hard scatter system of 2.0 GeV. This was done after I discovered that events of a lower $p_\perp$ did not enter our data set.

Within TWISTER and LUCIFER separately, the different sub-processes that each Monte Carlo generates are mixed with the ratios of their respective cross sections. However there is no provision for mixing the events of the two Monte Carlos with the proper proportions and one must therefore combine them by hand with the ratio dictated by the relevant integrated cross section. The case is much the same for HERWIG.

While the Monte Carlos (and their underlying cross section calculations) make predictions of the relative mixing of direct and extended photons, one hope of this dissertation is to determine the mixing ratios present in the data. For this reason, each type of photon: TWISTER (QCD $k_\perp$ on, QCD $k_\perp$ off, VDM), LUCIFER, HERWIG (QCD, enhanced underlying event off), and HERWIG (direct, enhanced underlying event off) are compared separately with the data, with the hope that the mixing ratios can be determined. Section (9.6) discusses the predicted mixing ratios suggested by the TWISTER and LUCIFER Monte Carlos.

The fact that an event is generated does not ensure that we will see it. Each

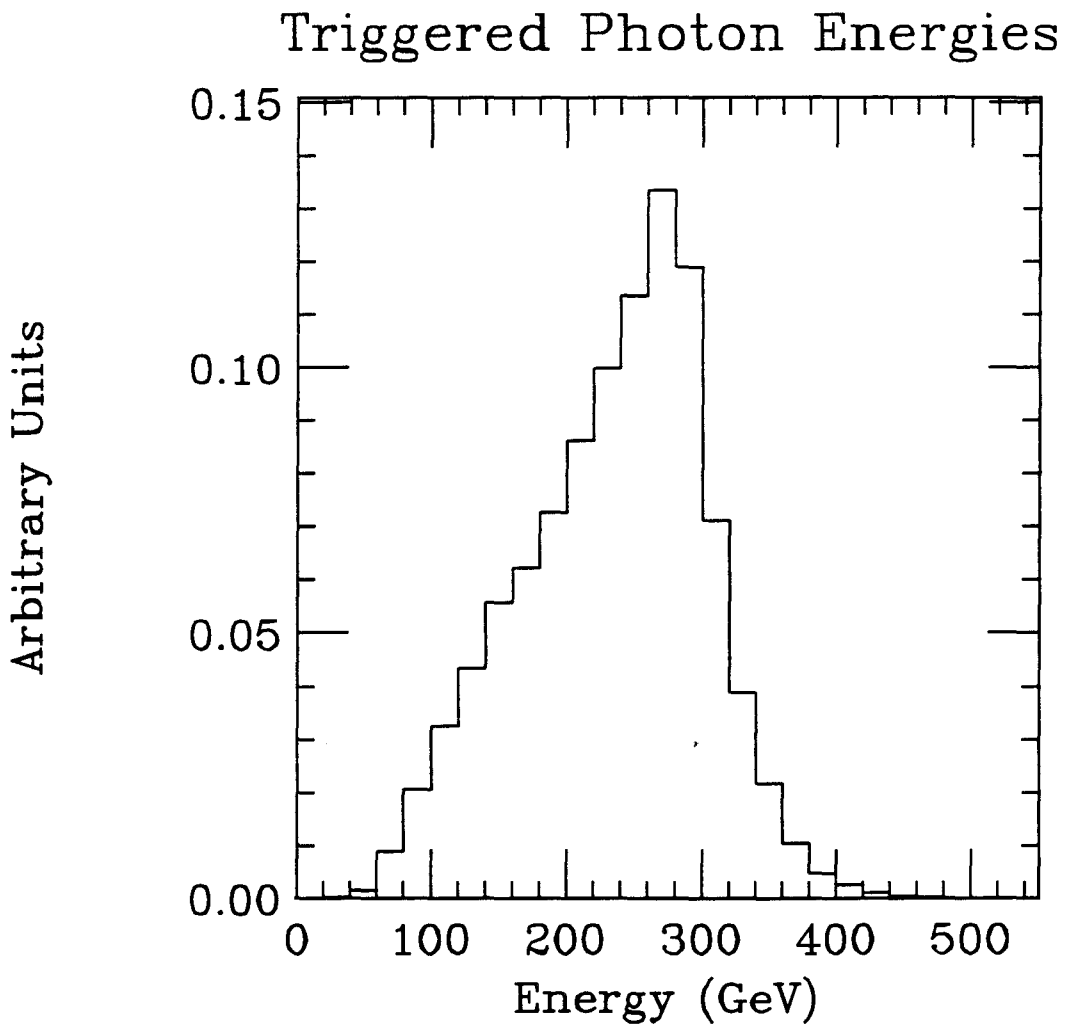

Figure 37: Measured E_γ spectrum for triggered events. The trigger consists of the following condition: (Total MCAL $E_\perp > 8$ Gev) OR (Both of the two hottest towers in the MCAL have $E_\perp > 0.75$ GeV.)

event is run through an experimental device simulator (see section (3.3)). All future talk of subsequent trigger and jet finding relate to experimentally simulated data which is nominally a close analog to the true data. E683 has a hardware high $E_\perp$ trigger that selects what are hoped to be interesting events. The hardware trigger has an $E_\perp$ dependent efficiency and so subsequent software triggers are applied to ensure that we are in the region of $\approx$ 100% acceptance. A good software trigger has been determined to be (total MCAL $E_\perp > 8$ GeV) logically OR'd with (the two hottest MCAL towers both have $E_\perp > 0.75$ GeV.)

In order to properly simulate E683 data, there is a beamline specific effect which is potentially troublesome. As mentioned in section (3.2), E683 suffers from the effect of multiple bremsstrahlung. That is, while we might measure an $E_\gamma^{\text{apparent}}$, the actual photon initiating the hard scatter usually has a lower energy. This is due to the fact that many photons are produced in any particular event and $E_\gamma^{\text{apparent}}$ is the sum of these photon's energy. Some of these photons are lost in their transport from production to the E683 target and the rest hit the BCAL. Since the equation used for x (equation (9)) has a $\sqrt{s}$ in the denominator, variations in E_γ^{real} will have an effect on measuring x. It will have a more general effect in any attempt to bin the data in (say) $\sqrt{s}$.

E683 collaborator Donna Naples has used GEANT to simulate our multiple bremsstrahlung behavior [69]. Mike Traynor, also a collaborator, has written a separate, nominally more sophisticated, simulator which gives essentially identical results [70]. I use only the Naples results here. I received an data file which contained (among other things) $E_\gamma^{\text{apparent}}$, the apparent photon energy, E_γ^{hard}, the energy of the hottest photon which makes it to E683's target unvetoed and E_γ^{soft}, the sum of the other lower energy photons that made it to our target. I plotted the distribution $E_\gamma^{\text{hard}}/E_\gamma^{\text{apparent}}$ (shown in figure (38)) and wrote a FORTRAN routine which generated events according to that probability density function.[15] The figure shows a peak at 1.0 with a long tail that shifts the mean of the distribution by $\sim$ 10%. Even more troubling

[15]Note that the mean and RMS of this distribution are very sensitive to binning effects—the mean of figure (38) can be shifted from 0.88 to 0.92 by changing the binning. Therefore, I have been careful to present all related histograms binned in the same way.

is the shape of the distribution which would indicate that the discrepancy in photon energy could occasionally exceed 50 GeV.

The effect of this uncertainty in the energy of the event-generating photon was accommodated by the following reasoning:

1. What is experimentally measured is $E_\gamma^{\text{apparent}}$. It is this distribution which must be reproduced.

2. Each time an $E_\gamma^{\text{apparent}}$ is measured, the true E_γ is chosen from the distribution of figure (38), multiplied by $E_\gamma^{\text{apparent}}$.

3. Since the energies of the outgoing partons scale with the center of mass hard scatter photon energy, an event is generated with $E_\gamma^{\text{apparent}}$ and then each outgoing particle has its energy and momentum scaled (in the CM frame) by the ratio $\sqrt{E_\gamma^{\text{hard}}/E_\gamma^{\text{apparent}}}$.[16]

4. This scaled event is then subsequently sent into the device simulator and the standard trigger is applied. If the event does not pass the trigger threshold, another is generated according to the above prescription until the desired number of events pass the trigger for that particular bin of $E_\gamma^{\text{apparent}}$ (i.e. the number of triggers you request, multiplied by the fractional distribution (figure (37).) By this method, the measured $E_\gamma^{\text{apparent}}$ (triggered) distribution can be generated, with the effect of multiple bremsstrahlung taken into account.

5. The remaining soft photon energy E_γ^{soft} (LAB) is sent as a single electromagnetic particle into the BCAL.

One must be extremely careful to use the proper Lorentz boosts. One must boost the scaled event from the CM frame to the lab using the boosts appropriate for the

[16]This point is often hard for people to understand. It depends on the fact that things like cross section, multiplicity and so forth vary only slowly with $\sqrt{s}$. Since the variation induced by the ratio $\sqrt{E_\gamma^{\text{hard}}/E_\gamma^{\text{apparent}}}$ is relatively small, the most quickly varying aspect of the scatter is due to center of mass energy conservation and the outgoing particles' energies scale linearly with $\sqrt{E_\gamma^{\text{LAB}}}$ (i.e. E_{CM}), with other aspects of the event essentially untouched.

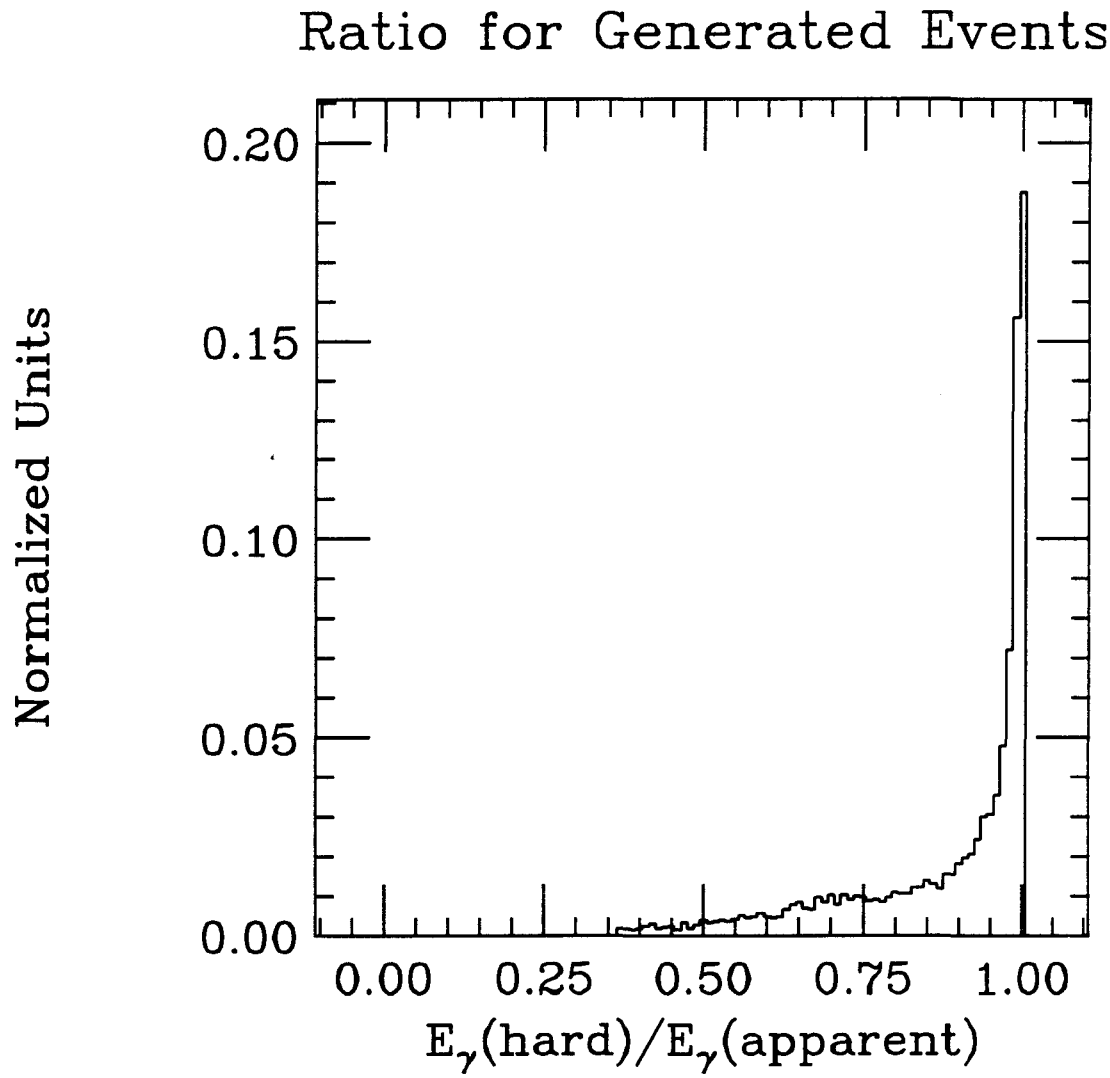

Figure 38: The Monte Carlo generated ratio $E_\gamma^{\text{hard}}/E_\gamma^{\text{apparent}}$ for photons at our target. This is for generated events, with no trigger or jet-finding restrictions imposed.

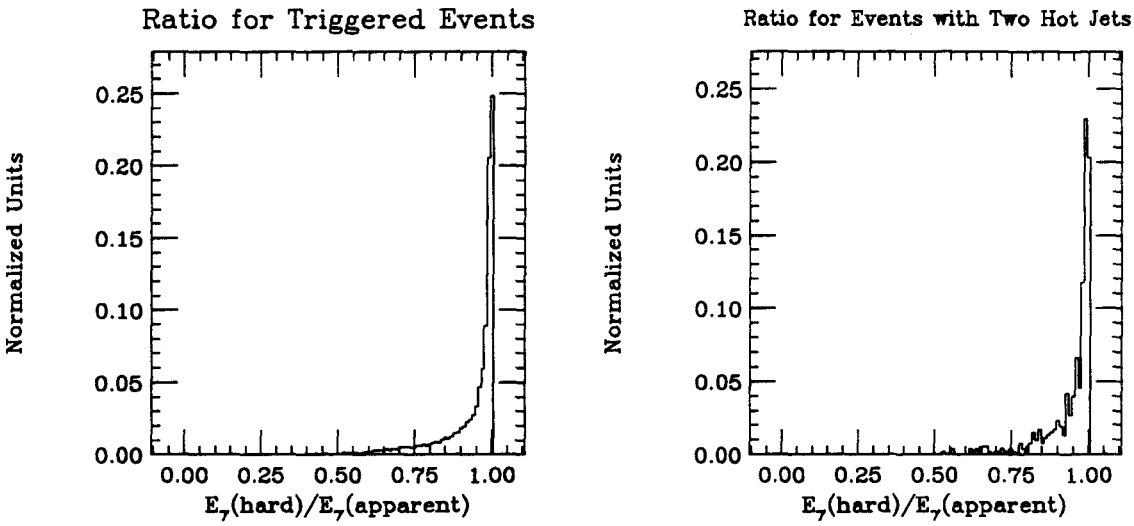

Figure 39: The TWISTER Monte Carlo determined ratio $E_\gamma^{\rm hard}/E_\gamma^{\rm apparent}$ for photons at our target (a) is triggered events, (b) is with 2 jets with $E_\perp > 4$ GeV.

real photon energy. However, the boosts from the lab to the CM for the purposes of jet finding must use the boosts appropriate for the apparent photon energy.

Figure (39 a) shows the distribution $E_\gamma^{\rm hard}/E_\gamma^{\rm apparent}$ for triggered events. One thing that is instantly notable is the reduction in the low energy tail. This is easier to understand when you consider that the MCAL $E_\perp$ distribution goes as $e^{-aE_\perp}$ (for our data $a \sim 1$.) This implies that most events are near the trigger threshold (roughly 56% of the triggers above an $E_\perp$ of 8.0 GeV are below 8.8 GeV (or a 10% shift.) A small drop in $E_\perp$ (or energy) will often drop that particular event below the trigger threshold. Figure (39 b) shows the same distribution with the additional cut that there were 2 jets found, both with $E_\perp > 4.0$ GeV. The low energy tail is ameliorated even more.

At this point, the Monte Carlo is complete. LUND and HERWIG events were generated as discussed above (i.e. normal events, adjusted for multiple bremsstrahlung, passed through the detector simulator (with a generously bad MCAL energy resolution,) and the normal MCAL based jet-finder.) In all cases, a sample of 10000 triggered events for each different photon type were generated. In the sections below,

I present the different types of photons for both LUND and HERWIG and compare the Monte Carlo results with the data. All the γp data was analyzed. The cuts of section (7.2) were applied and the PED_FIXER was turned on. The software trigger (MCAL $E_\perp > 8$ GeV) OR (Both of the two hottest MCAL towers had $E_\perp > 0.75$ GeV) was applied, as was the jet finder described in Appendix (B). The pileup cut was not applied except for BCAL distribution comparisons (see below) and neither was the POSH cut (but only after it was shown to be unimportant.)

The comparison is done in stages. I first compare the data and the Monte Carlo at the triggered level, with each trigger compared separately to underscore the similarities and the differences in the two. Since jets are not required to be found in the triggered data, the numbers of different kind of plots to be shown is necessarily small. I follow this section with a reasonably exhaustive presentation of kinematically oriented jet measurements. The section is concluded with a discussion of the expected mixture of extended and direct photons in our data sample as suggested by the LUND Monte Carlos. Prior to each data presentation, I discuss what is to be presented. The above notes on the data analysis are applicable throughout the following sections.

9.2 Triggered Data

As mentioned before, the triggers used in E683 are the 2HI trigger (Both of the two hottest MCAL towers had $E_\perp > 0.75$ GeV) and the Global trigger (MCAL $E_\perp > 8$ GeV). One would expect that the topology of these two triggers would strongly affect the shapes of the presented general kinematic distributions, with the Global trigger having on the whole more energy in the MCAL and probably distributed more uniformly. In plot (40) I show for 2HI triggers the MCAL energy and $E_\perp$, the planarity and the BCAL energy distributions for the LUCIFER and TWISTER Monte Carlos, overlaid with the data. All plots are normalized to have unit area. Shown in this figure is:

- LUCIFER direct photons, $k_\perp$ ON (open circles, long dash, long space line.)

- TWISTER QCD extended photons, $k_\perp$ OFF (open squares, short dash, short space line.)
- TWISTER QCD extended photons, $k_\perp$ ON (solid squares, short dash, long space line.)
- Data (solid circles, solid line.)

In figure (41) I show identical plots for the Global trigger.

In figure (42), I show the same plots for (mostly) the HERWIG Monte Carlo, 2HI triggers. Figure (43) I show HERWIG Monte Carlo, Global triggers. In these two plots the shown distributions are:

- HERWIG direct photons, $k_\perp$ ON, enhanced underlying event off, (open circles, long dash, long space line.)
- HERWIG QCD extended photons, $k_\perp$ ON, enhanced underlying event off, (open squares, short dash, short space line.)
- TWISTER VDM extended photons, $k_\perp$ ON (solid squares, short dash, long space line.)
- Data (solid circles, solid line.)

The presence of TWISTER VDM photons in this figure is arguably a little silly, but it is done because including it in the 'natural' figures (40) and (41) made the plots too difficult to read. This rather odd organization scheme is preserved throughout the following sections.

Inspection of figure (40) shows that with the exception of the BCAL energy plot, the data is not bracketted by the various photon types for 2HI triggers. The data is less planar, and contains less energy and $E_\perp$ in the MCAL. There is a smaller difference between the various photon types for the BCAL distribution, and the data fits among them, with TWISTER $k_\perp$ off favored.

The comparison of global triggers with data yields a better agreement. Taken in sum, figure (41) shows the global trigger data is best represented by TWISTER $k_\perp$

on, although it is only the BCAL energy distribution that excludes TWISTER $k_\perp$ off. With the exception of MCAL $E_\perp$, LUCIFER direct photons is strongly disfavored. Since the direct process is not expected to dominate until high $p_\perp$, this is not an unexpected result. At some level, the smaller differences between the various photons for global triggers is caused by the trigger itself. Global triggers require a minimum $E_\perp$ in the MCAL, with the strongly falling $E_\perp$ spectrum imposing the condition that most of the triggers come at or near the threshold. 2HI triggers do not have such a stringent restriction on overall event topology and so the various models are allowed to vary more.

The HERWIG 2HI plot (figure (42)) is much the same as seen for the LUND plot. With the exception of the BCAL energy plot, the data is not represented by any photon type or by any mixture of photon types. In figure (43) (the HERWIG global triggers), the data definitely does not appear to be well represented by HERWIG direct photons, and HERWIG extended photons is excluded by the planarity distribution, although this photon type is adequately supported by the rest of the presented distributions. The model in the 'HERWIG' plots that best represents the Global trigger data is, ironically, the TWISTER VDM model.

The disagreement between the data and the HERWIG Monte Carlos for the planarity distribution of global triggers shows that the LUND Monte Carlo/data agreement for planarity is not kinematically forced. The high planarity of HERWIG events suggest a too planar structure. 'Vanilla' HERWIG originally was a hadron event generator, which modelled the spectator system by overlaying a representation of UA5 minimum bias data [36]. This mechanism for generating the underlying event has been shown to be excessive for photon data, although is required to reproduce our pion data [42]. In this simulation, the enhancement mechanism has been turned off. So, where in hadronic data the HERWIG spectator system algorithm has been tuned to give good agreement, this has not been done for photon data. For pion data, the enhancement degraded the event planarity and the too high planarity of HERWIG for global triggers presumably indicates the need for a subdued enhancement for photon data. In order to investigate this in a somewhat related way, I present in table (2)

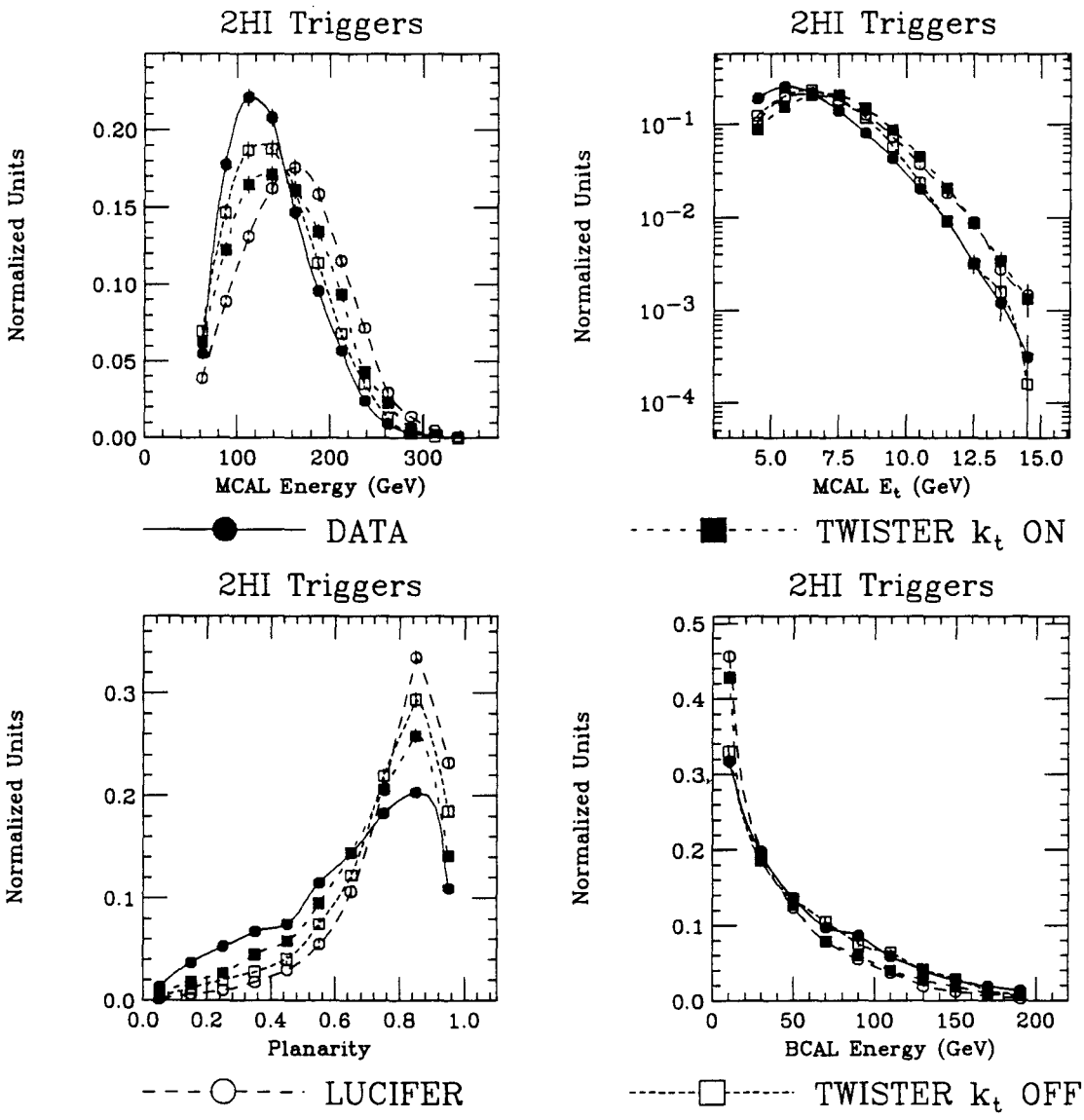

Figure 40: Shown is a comparison between LUND Monte Carlos and data for 2HI triggers. Plots of event planarity, BCAL energy, MCAL energy and MCAL $E_\perp$ are shown. The meaning of the symbols is shown on the plot. Note that the MCAL $E_\perp$ is on a logarithmic scale.

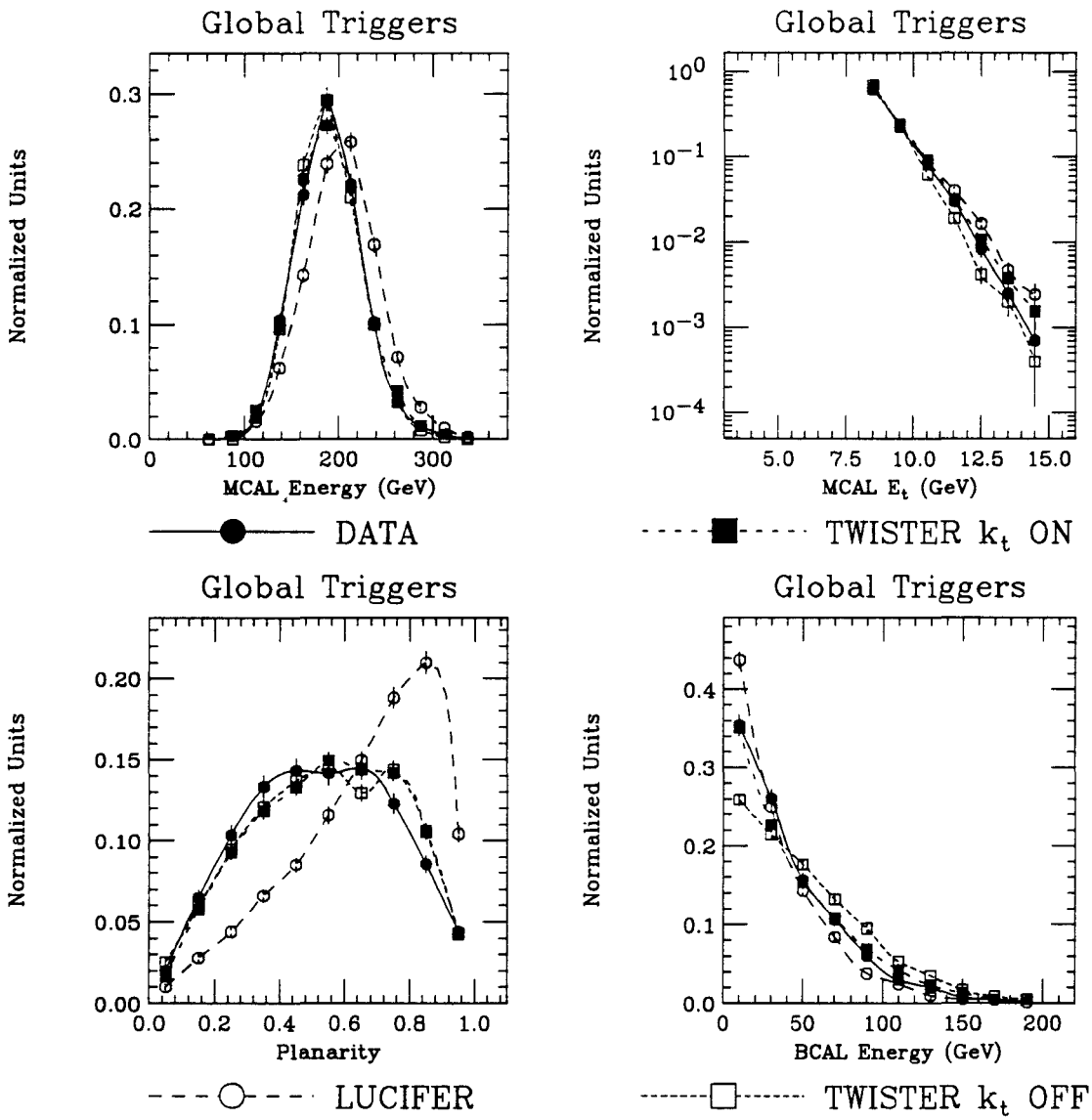

Figure 41: Shown is a comparison between LUND Monte Carlos and data for Global triggers. Plots of event planarity, BCAL energy, MCAL energy and MCAL $E_\perp$ are shown. The meaning of the symbols is shown on the plot. Note that the MCAL $E_\perp$ is on a logarithmic scale.

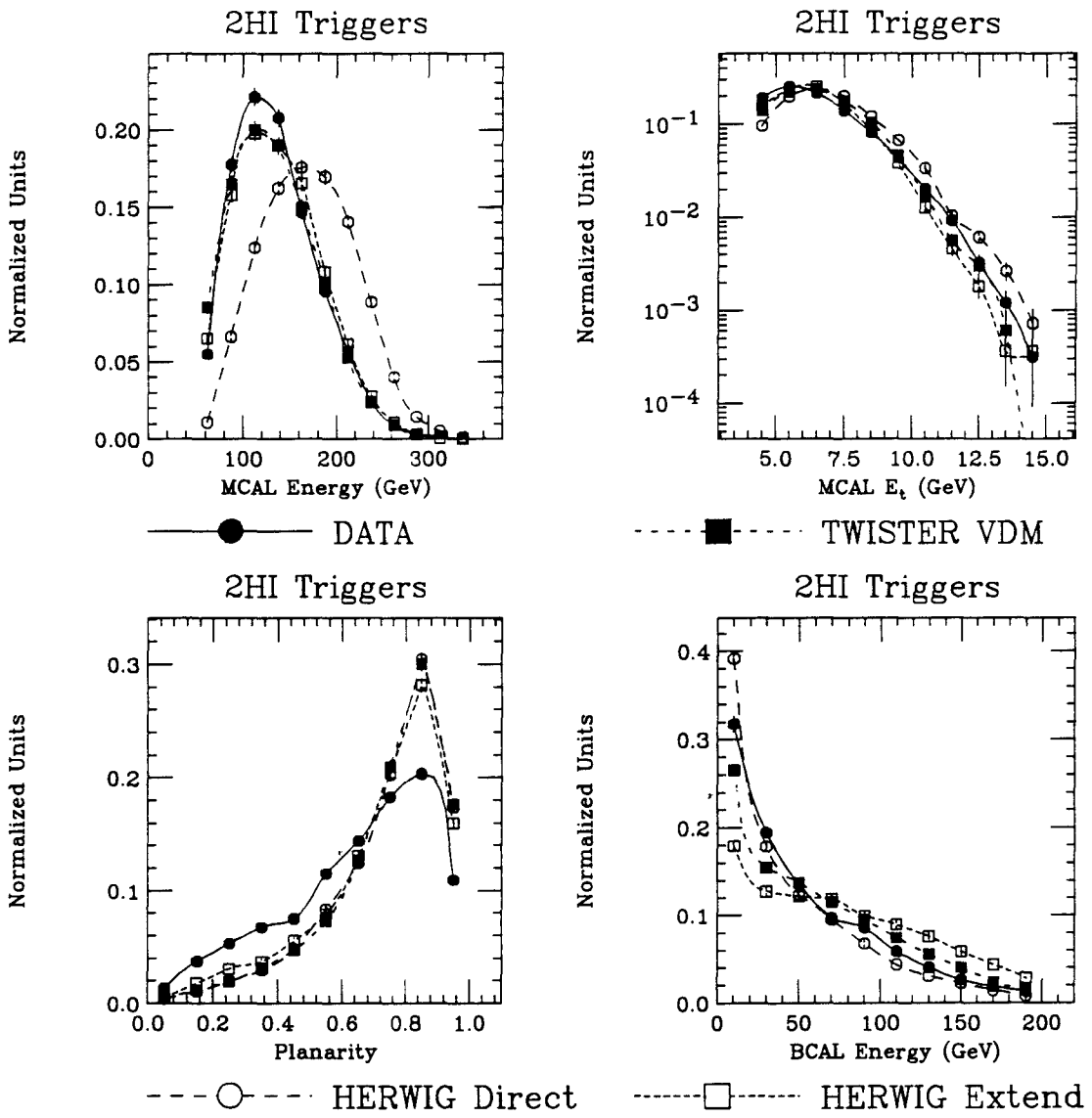

Figure 42: Shown is a comparison between the HERWIG Monte Carlo and data for 2HI triggers. Plots of event planarity, BCAL energy, MCAL energy and MCAL $E_\perp$ are shown. The meaning of the symbols is shown on the plot. For aesthetic reasons, TWISTER VDM is shown on this plot. Note that the MCAL $E_\perp$ is on a logarithmic scale.

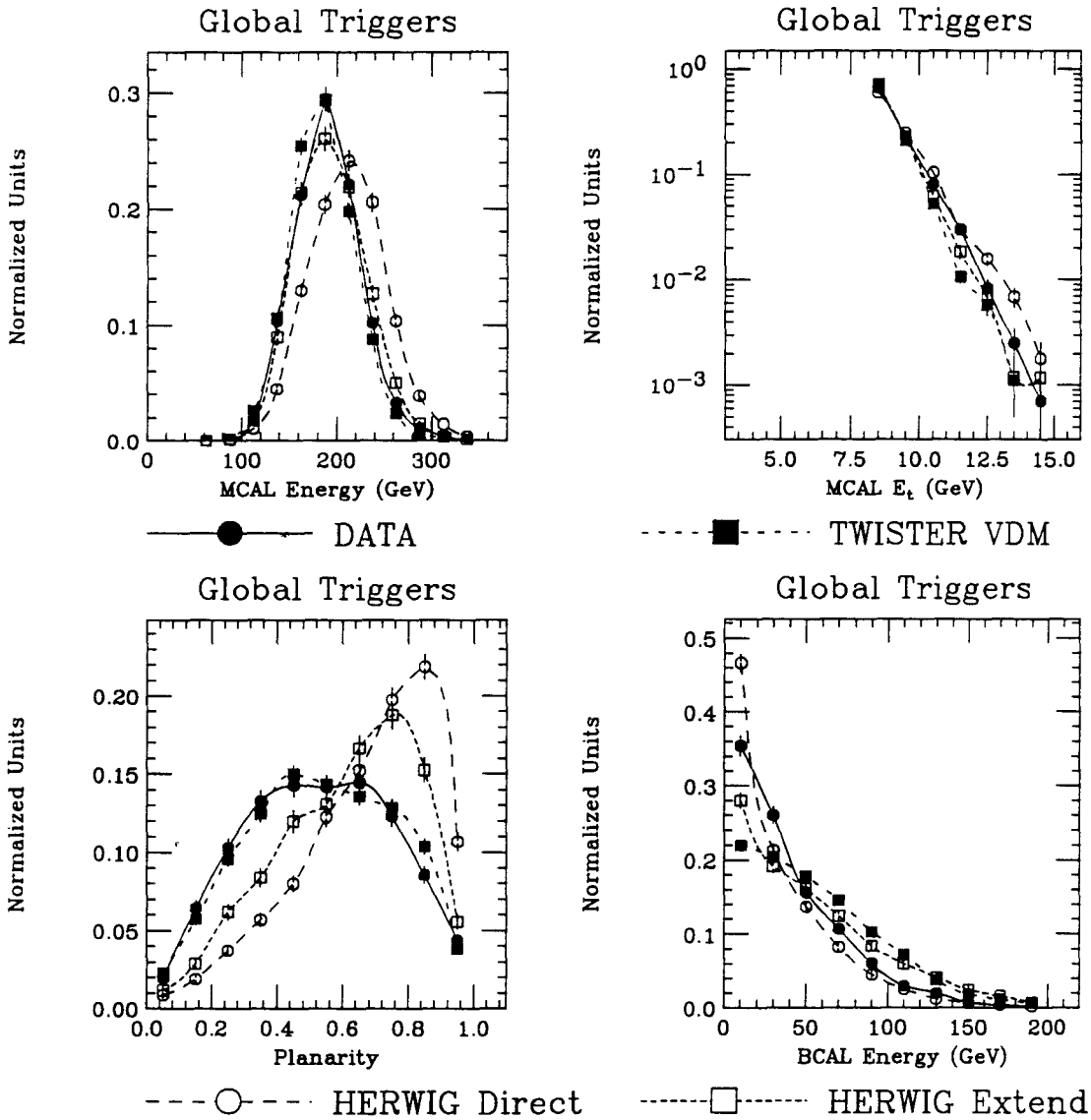

Figure 43: Shown is a comparison between the HERWIG Monte Carlo and data for Global triggers. Plots of event planarity, BCAL energy, MCAL energy and MCAL $E_\perp$ are shown. The meaning of the symbols is shown on the plot. For aesthetic reasons, TWISTER VDM is shown on this plot. Note that the MCAL $E_\perp$ is on a logarithmic scale.

Photon Type	2HI	Global	Both
TWISTER QCD $k_\perp$ OFF	62.9 ± 0.8 %	50.5 ± 0.7 %	13.4 ± 0.4 %
TWISTER QCD $k_\perp$ ON	61.0 ± 0.8 %	58.2 ± 0.8 %	19.2 ± 0.4 %
TWISTER VDM $k_\perp$ ON	66.5 ± 0.8 %	45.3 ± 0.7 %	11.7 ± 0.3 %
HERWIG direct (UE OFF)	83.0 ± 0.9 %	25.5 ± 0.5 %	8.5 ± 0.3 %
HERWIG extended (UE OFF)	83.2 ± 0.9 %	33.6 ± 0.6 %	16.8 ± 0.4 %
LUCIFER direct $k_\perp$ ON	75.7 ± 0.9 %	44.9 ± 0.7 %	20.5 ± 0.5 %
Data	76.2 ± 0.7 %	36.4 ± 0.7 %	12.5 ± 0.3 %

Table 2: Shown is the fraction of total triggers caused by the 2HI and Global trigger for both the Monte Carlo and the data. As suggested by figure (43), the HERWIG Monte Carlo sample has a heavy contribution of 2HI triggers. Presumably even those HERWIG events which only fired the Global trigger still retained their overall higher planarity structure. The errors shown above are statistical only.

the fraction of the triggers caused by the 2HI trigger, the Global trigger and by both.

As suggested in section (3.3), the MCAL simulator has not been tuned to specifically reproduce E683 calibration data and for this reason, is a potentially weak point in the Monte Carlo/data comparison. In order to definitively believe the simulator one must check it against the calibration data, which is being done but is not available as of this writing. One could imagine, for example, that the simulator simply does not adequately transversely smear the energy to account for calorimeter showering. For this reason, I investigated something which would tell if the simulator was returning completely silly results. I did this by simply counting the number of towers above various energy and $E_\perp$ thresholds for the simulated data. If, for example, the Monte Carlo says that there are double the number of MCAL towers above 10 GeV than seen in the data, we would be correct to be worried.

I histogrammed the number of towers with a lab frame energy greater than 1, 3, 5, and 10 GeV and those towers with an $E_\perp$ greater than 0.50, 0.75, 1.00, and 1.25 GeV. This was done separately for 2HI and Global triggers, as well as for HERWIG and LUND Monte Carlos. For reasons of length, I do not present them all here. In figures (44 & 45) I show the agreement for the 2HI triggers for the LUND Monte Carlo, the other results are quite similar. While the Monte Carlo/data

agreement is not perfect, it is rather impressive. In addition, the differences between the different photon types and Monte Carlos show that the simulator does have some sensitivity to the distribution of particles incident on it. As jet finding cuts are applied, these distributions change, but the relative Monte Carlo/data agreement is preserved. I conclude that the simulator is basically correct and do not expect an improved simulator will significantly affect any results presented in this thesis.

9.3 Emergence of the Dominance of the Hard Scattering Signal

While the existence of jets are nearly universally conceded at center of mass energies exceeding 100 GeV, historically demonstrating the existence of jets in the energy regime accessible by todays hadron fixed target programs ($20 < \sqrt{s} < 30$ GeV) has been more difficult. A number of methods have been proposed to demonstrate the existence of low $E_\perp$ jets. Many have been rejected as having potential or blatant biases which cloud the interpretation of the data. One method for showing the existence of jets that appears to have survived the process of proposal and criticism is to observe the mean planarity of events for different bins of total $E_\perp$ in the detector.

Planarity is a measure of the 'jettiness' of an event. For each event, a reference vector is chosen in the transverse plane. A dot product is formed between the $\vec{p}_\perp$ of each particle (or detector module) and the reference vector and a sum of these projections is constructed. The reference vector is varied until the sum is maximized. When this direction is found, a sum of the dot products of all the particles (or detector modules) and the vector perpendicular to the reference vector is also done (all this takes place in the transverse plane.) This sum corresponds to the minimum projection. The planarity P is then just

$$P = \frac{\sum \text{max} - \sum \text{min}}{\sum \text{max} + \sum \text{min}}$$

Planarity has the property that an event that is symmetric in the transverse plane has $P = 0$. Two identically back to back particles have $P = 1$. High planarity is therefore expected to reflect jet-like behavior.

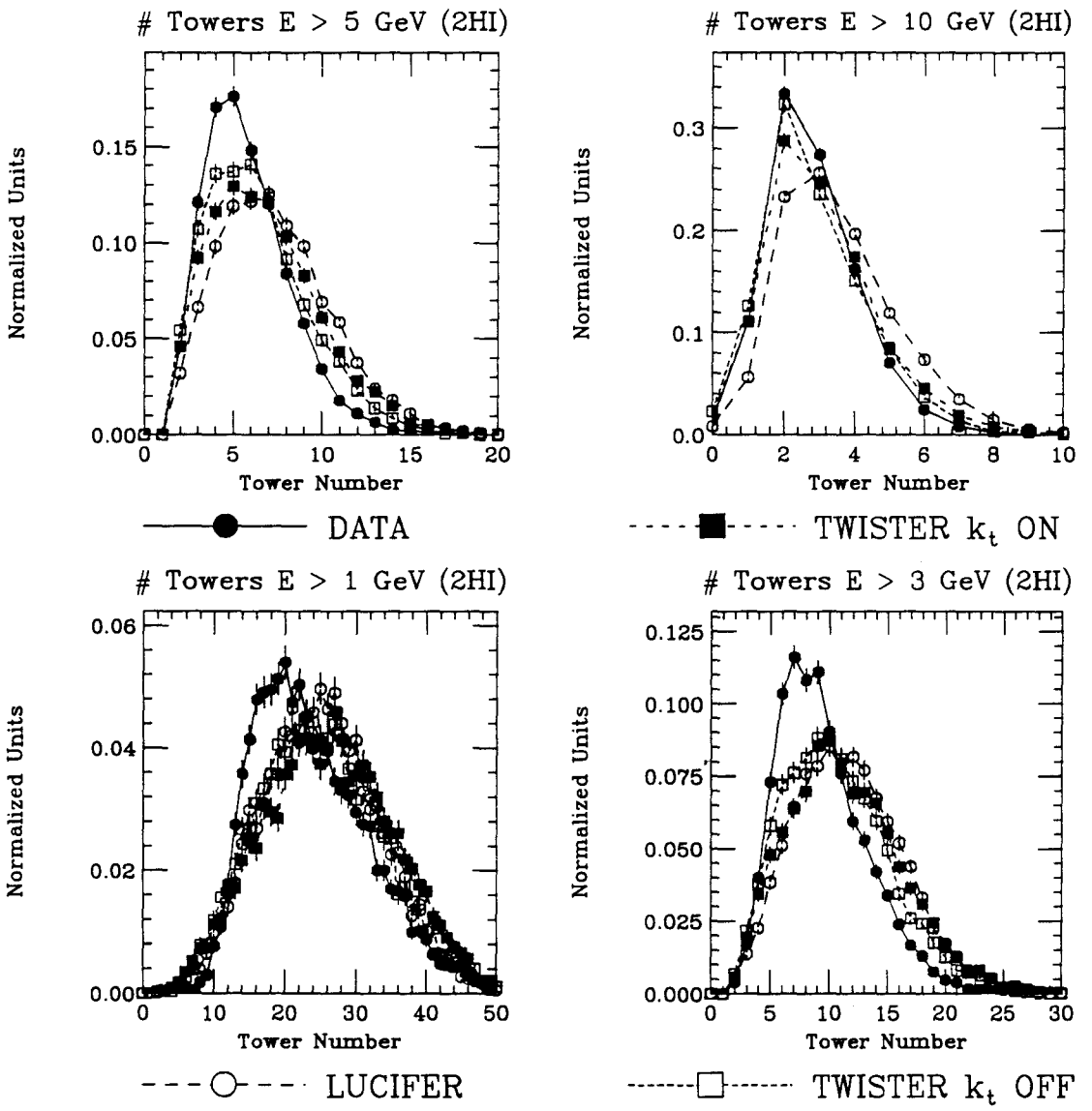

Figure 44: Shown is a comparison between the LUND Monte Carlos and data for 2HI triggers. The variable being displayed is the number of MCAL towers above the energy thresholds 1, 3, 5, and 10 GeV. The meaning of the symbols is shown on the plot. Note that the horizontal scale changes between plots.

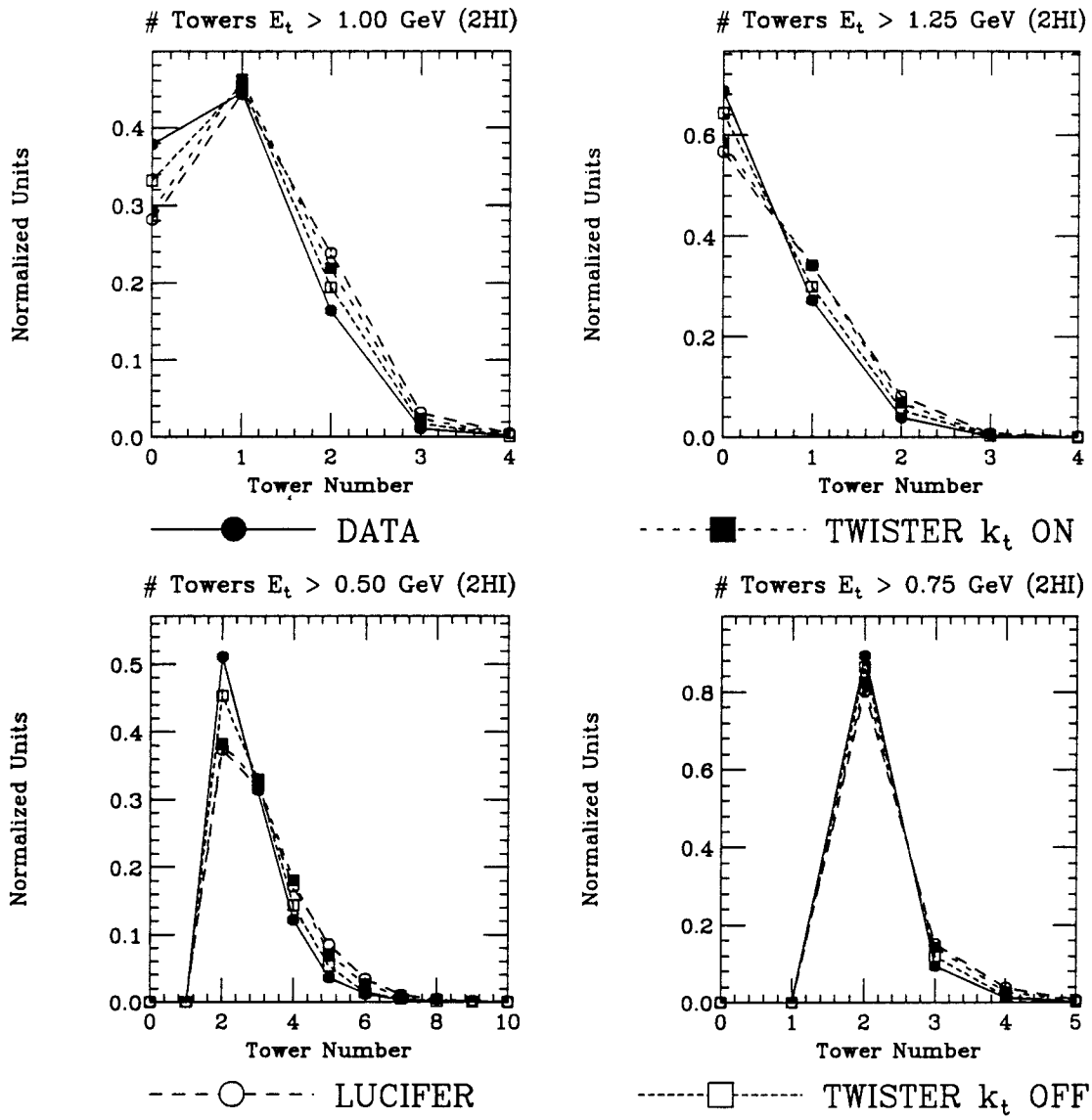

Figure 45: Shown is a comparison between the LUND Monte Carlos and data for 2HI triggers. The variable being displayed is the number of MCAL towers above the $E_\perp$ thresholds 0.50, 0.75, 1.00, and 1.25 GeV. The meaning of the symbols is shown on the plot. Note that the horizontal scale changes between plots.

If jets are a dominant signal, planarity should increase as total event $E_\perp$ increases. It is very important that the triggers be a simple threshold on the global $E_\perp$. A trigger with a restrictive geometry (like our 2HI) can be criticized as manufacturing a jet signal, because of the requirement of a lot of localized $E_\perp$.

Such a technique has been applied in earlier pp and πp experiments [74, 75, 76]. E557, E609, and NA5 all had average planarities in the range of 0.4-0.5 and in all cases the planarity was independent of total $E_\perp$. In contrast, when these experiments used a type of geometrically restrictive trigger, mean planarity increased with total $E_\perp$.

The AFS collaboration [73] did a similar analysis of their data for different center of mass energies ($\sqrt{s}$ = 30, 45, 63 GeV.) For the first two energies, the results of the previously mentioned experiments were corroborated. However for the 63 GeV bin, average planarity was shown to increase dramatically for the highest $E_\perp$'s; thus showing the eventual dominance of the jet signal in hadron-hadron interactions.

E683 is the first experiment to do an investigation of this sort for γp data. It is hoped that a jet signal will be easier to observe due to the expected reduced underlying event. Earlier, I defined a Global trigger which was formed by summing the $E_\perp$'s of all of the MCAL towers and imposing a threshold. In the data, two different hardware Global thresholds were concurrently used and I shall call them Global low and Global high respectively. The Global low hardware threshold was not fully efficient below an MCAL $E_\perp$ of 4 GeV and so a software cut of 4 GeV was applied. For the Global high threshold, a software MCAL $E_\perp$ cut of 8 GeV was applied.[17]

Because the beam available to E683 is a broadband beam, average planarity might not increase with $E_\perp$, due to the fact that one would expect that high $E_\perp$ events would be at least somewhat correlated with high beam energies. This effect

[17]The Global high threshold becomes fully efficient at perhaps 7 GeV. The cut of 8 GeV was applied in order to maintain continuity with other analyses. The 8 GeV cut is necessary when one desires to compare hydrogen to nuclear and (especially) deuterium data. Reducing the MCAL software $E_\perp$ cut does not affect the following results.

can be removed by plotting $x_\perp$

$$x_\perp = \frac{E_\perp^{\mathrm{MCAL}}}{\sqrt{s}}$$

which is the fraction of the total available event energy seen as MCAL $E_\perp$. Figure (46) shows the planarity distributions for different bins of $x_\perp$.[18] At low $x_\perp$ the average planarity is quite low, however above an $x_\perp$ of about 0.55, the character of the planarity curve changes dramatically, reflecting the signature expected when jet production starts to dominate. Figure (47) shows the average planarity plotted as a function of $x_\perp$. Overlaid are similar plots from Monte Carlo.

The Monte Carlo $x_\perp$ dependence of average event planarity is shown to have the same basic shape as the data, with obvious differences. Within the statistics, the roll over at $x_\perp \sim 0.6$ is present in the data and all the Monte Carlos, with TWISTER extended photon $k_\perp$ on having the best overall agreement. The fact that the planarity has a marked increase for the higher $E_\perp$ bins shows the dominance of the hard scatter signal over minimum bias background. This behavior is in striking contrast to the behavior seen in the above described experiments.

9.4 Monte /Data Comparison, General Jet Kinematic Variables

When one makes the transition from triggered data to reconstructed jet data, one is handed a double edged sword. While it is true that at its simplest level the point of QCD calculations is to understand the dynamics of two body parton scatters (and nominally the dynamics of the ensuing jets,) the fact that a jet (by some definition) is found necessarily restricts the type of data one can see. If two jets are required above a certain threshold, one will not see events in which there is no concentration of energy (or $E_\perp$) in the detector. Unless one is in a kinematic region where only hard scatter (and jet production) physics can be found, one must always keep in mind the possibility that the data seen is heavily selected by the cuts. When one looks at normalized kinematic event distributions (as I shall do presently,) the possibility

[18]Note that the standard Global trigger (MCAL $E_\perp > 8$ GeV) corresponds to an $x_\perp$ of 0.37 at a beam energy of 250 GeV.

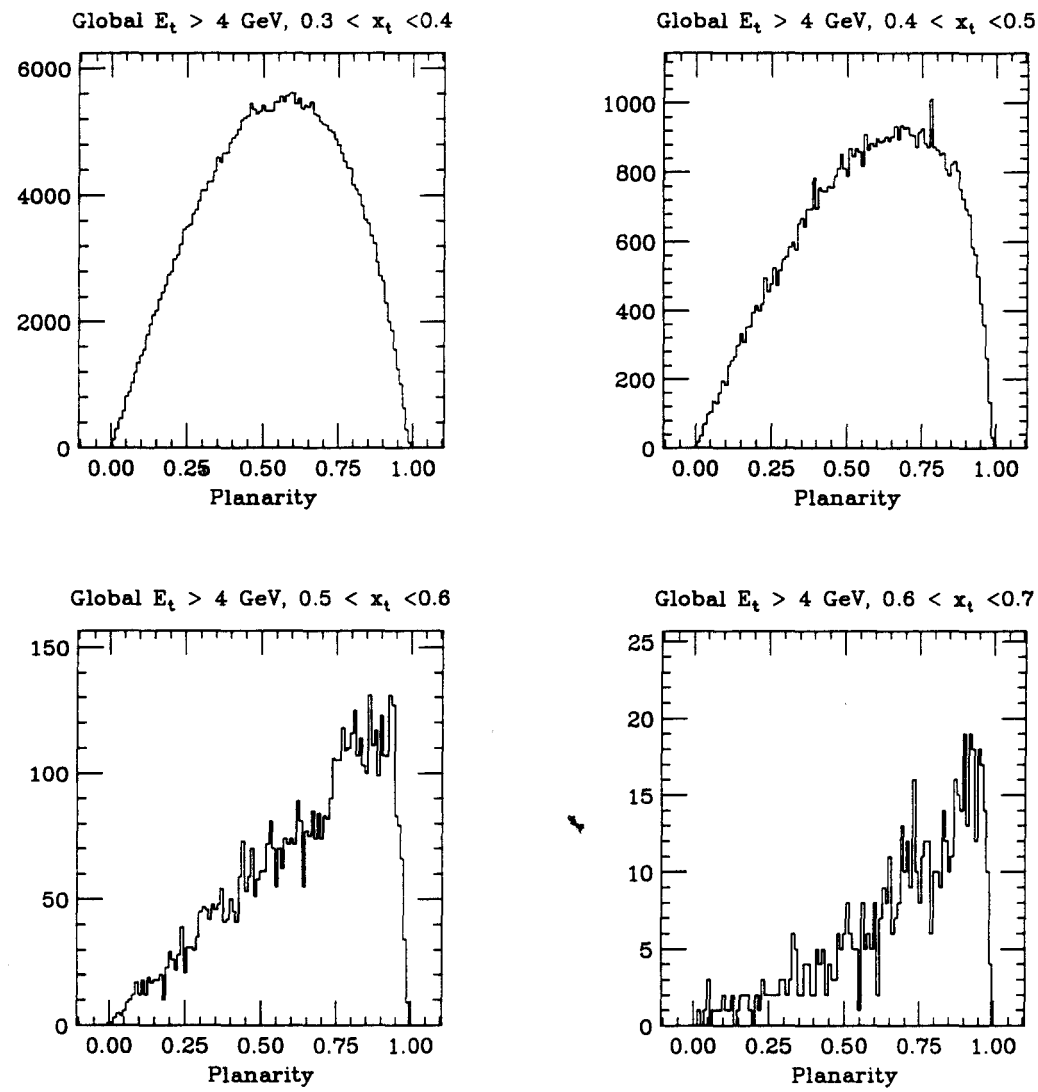

Figure 46: Shown are planarity distributions for Global triggers (MCAL $E_\perp > 4$ GeV) for different $x_\perp$ bins. The beginning of the dominance of the jet signal is clearly evident.

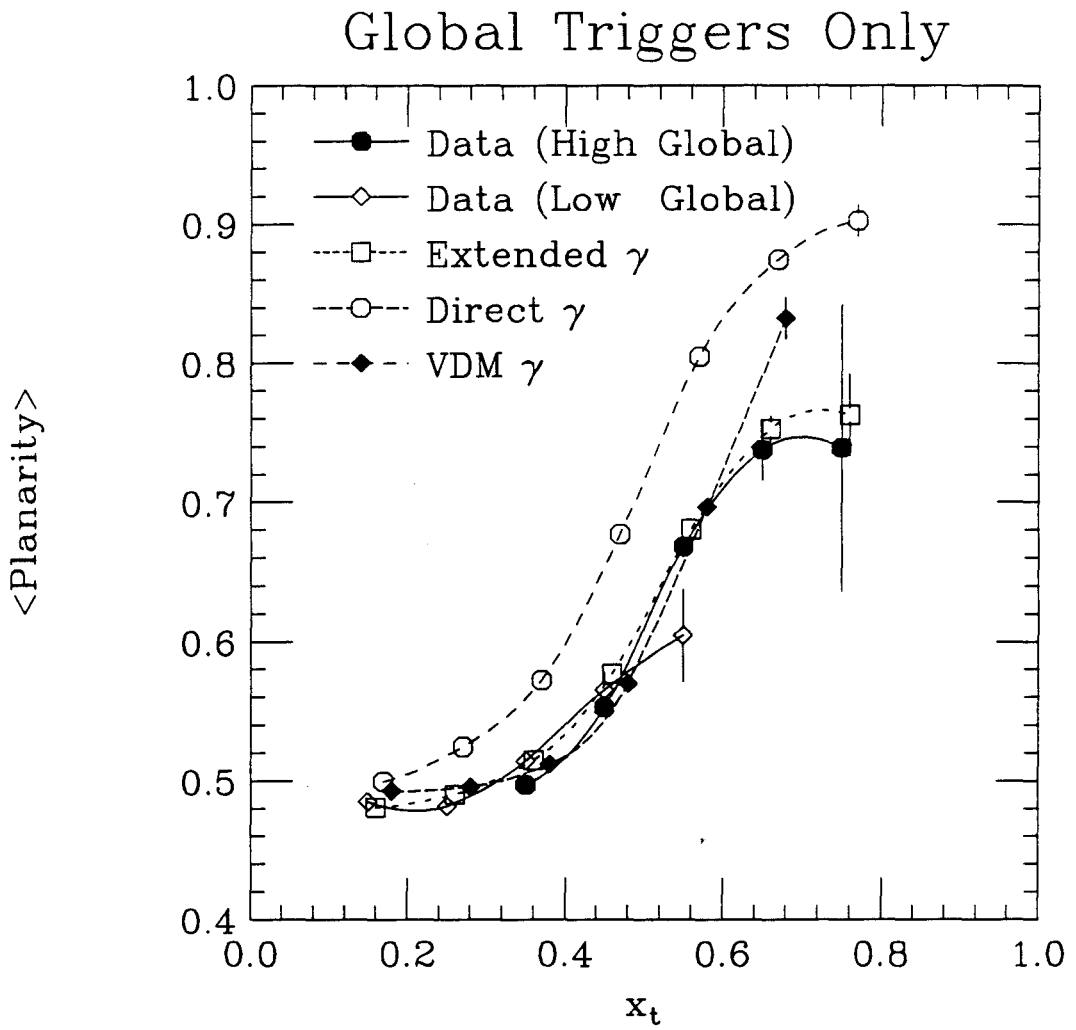

Figure 47: Shown is the average planarity as a function of $x_\perp$ for low Global triggers (MCAL $E_\perp > 4$ GeV). TWISTER QCD extended photons $k_\perp$ on, LUCIFER, and TWISTER VDM photons are compared with data. HERWIG is not compared because figure (43) shows that it does not get planarity correct, even for higher $E_\perp$ thresholds. While LUCIFER has a similar problem, it is included for completeness. In the above plot, the symbols are offset slightly to hilite the error bars. They should be taken as being plotted without the offset, with the data points being placed correctly.

exists that the cuts select only the topologies that are requested. Ultimately we will also ask the question: 'How many events of this topology are present per unit of photon flux?' This is in essence a cross-section question, which will not be addressed here. As we shall see, there is a significant amount of information accessible simply by exploring the shapes of the various distributions.

Below I present an extensive number of plots for the various Monte Carlos. I present the HERWIG/Data and LUND/Data Comparison separately. Within each Monte Carlo, I separate the two different types of triggers (2HI and Global). On each page, the events are separated into the (overlapping) 4 categories: the $E_\perp$ of *both* jets is greater than (2.0, 3.0, 4.0, 5.0) GeV respectively. As we shall see, this organization is somewhat clumsy and wasteful of space, but it allows the reader to observe the evolution of the distributions for each trigger type as the jet $E_\perp$ thresholds are increased. In order to compare the effect of the trigger, I present on consecutive pages the different trigger types for a particular distribution for a particular Monte Carlo. In this section, the following figures are shown:

Figure (48) LUND Apparent Photon Energy 2HI Trigger

Figure (49) LUND Apparent Photon Energy Global Trigger

Figure (50) LUND MCAL Energy 2HI Trigger

Figure (51) LUND MCAL Energy Global Trigger

Figure (52) LUND MCAL Planarity 2HI Trigger

Figure (53) LUND MCAL Planarity Global Trigger

Figure (54) LUND BCAL Energy 2HI Trigger

Figure (55) LUND BCAL Energy Global Trigger

Figure (56) LUND MCAL $E_\perp$ 2HI Trigger

Figure (57) LUND MCAL $E_\perp$ Global Trigger

Figure (79) HERWIG BCAL Energy Global Trigger

Figure (80) HERWIG MCAL $E_\perp$ 2HI Trigger

Figure (81) HERWIG MCAL $E_\perp$ Global Trigger

Figure (82) HERWIG Average Jet $E_\perp$ 2HI Trigger

Figure (83) HERWIG Average Jet $E_\perp$ Global Trigger

Figure (84) HERWIG $|E_\perp^{\text{jet1}} - E_\perp^{\text{jet2}}|$ 2HI Trigger

Figure (85) HERWIG $|E_\perp^{\text{jet1}} - E_\perp^{\text{jet2}}|$ Global Trigger

Figure (86) HERWIG MCAL $E_\perp$ not in Jets 2HI Trigger

Figure (87) HERWIG MCAL $E_\perp$ not in Jets Global Trigger

Figure (88) HERWIG $k_\perp$ 2HI Trigger

Figure (89) HERWIG $k_\perp$ Global Trigger

Figure (90) HERWIG $\Delta\phi$ Between Jets 2HI Trigger

Figure (91) HERWIG $\Delta\phi$ Between Jets Global Trigger

Figure (92) HERWIG $k_{\perp\phi}$ 2HI Trigger

Figure (93) HERWIG $k_{\perp\phi}$ Global Trigger

Figure (94) HERWIG x_{BEAM} 2HI Trigger

Figure (95) HERWIG x_{BEAM} Global Trigger

Specifically, in the LUND/data comparison, the data is compared with TWISTER $k_\perp$ on, TWISTER $k_\perp$ off, and LUCIFER. In all cases, the fragmentation scheme is independent fragmentation. For the HERWIG/data comparisons, the data is compared with HERWIG extended photons enhanced underlying event off, HERWIG direct photons, enhanced underlying event off, and TWISTER VDM photons. This odd

combination was forced by the aesthetics of the plots. It was simply ugly to put five different data sets on the plots. I did most of the event generation with a minimum $\hat{p}_\perp$ of 2.0 GeV. In order to get better statistics for the higher reconstructed jet $E_\perp$ bins, I generated additional events with a minimum $\hat{p}_\perp$ of 3.3 GeV. These events appear only in the plots which require both reconstructed jets to have $E_\perp$'s exceeding 4.0 and 5.0 GeV. The threshold of 3.3 GeV was chosen by first generating events with a 2.0 GeV threshold and determining what the minimum $\hat{p}_\perp$ was for these kind of events. A threshold of 3.3 GeV was conservative. For events with two reconstructed jets each having an $E_\perp$ exceeding 5.0 GeV, a minimum $\hat{p}_\perp$ threshold of 4.0 GeV would have been acceptable. For all data distributions, the target empty contributions were subtracted bin by bin and what is presented is nominally solely from γp scattering.

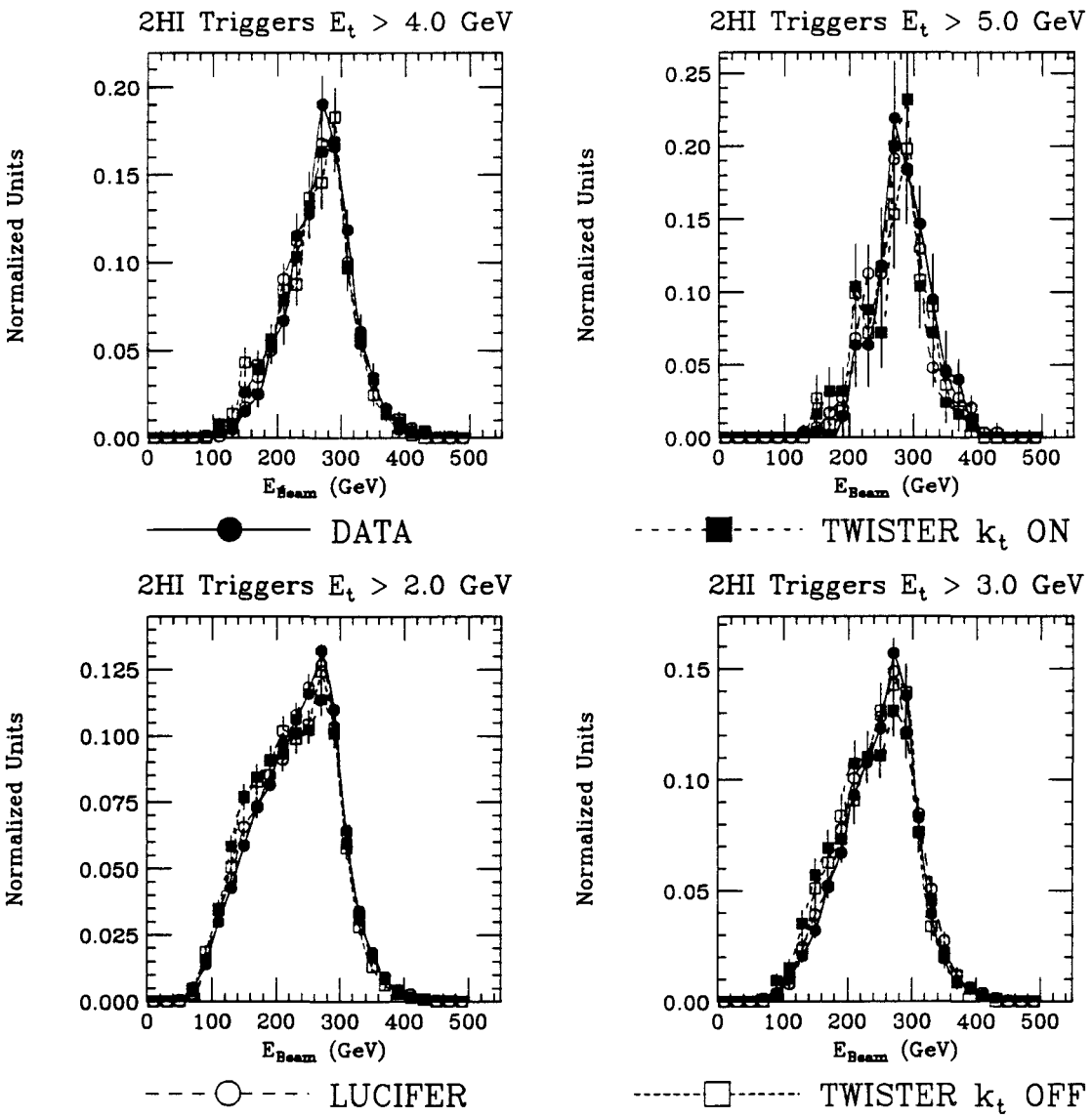

Figure 48: Shown is a comparison between the LUND Monte Carlos and data for 2HI triggers. The variable being displayed is beam energy E_γ for different reconstructed jet thresholds. The thresholds apply to *both* jets and are listed on the plot, as are the meaning of the symbols used.

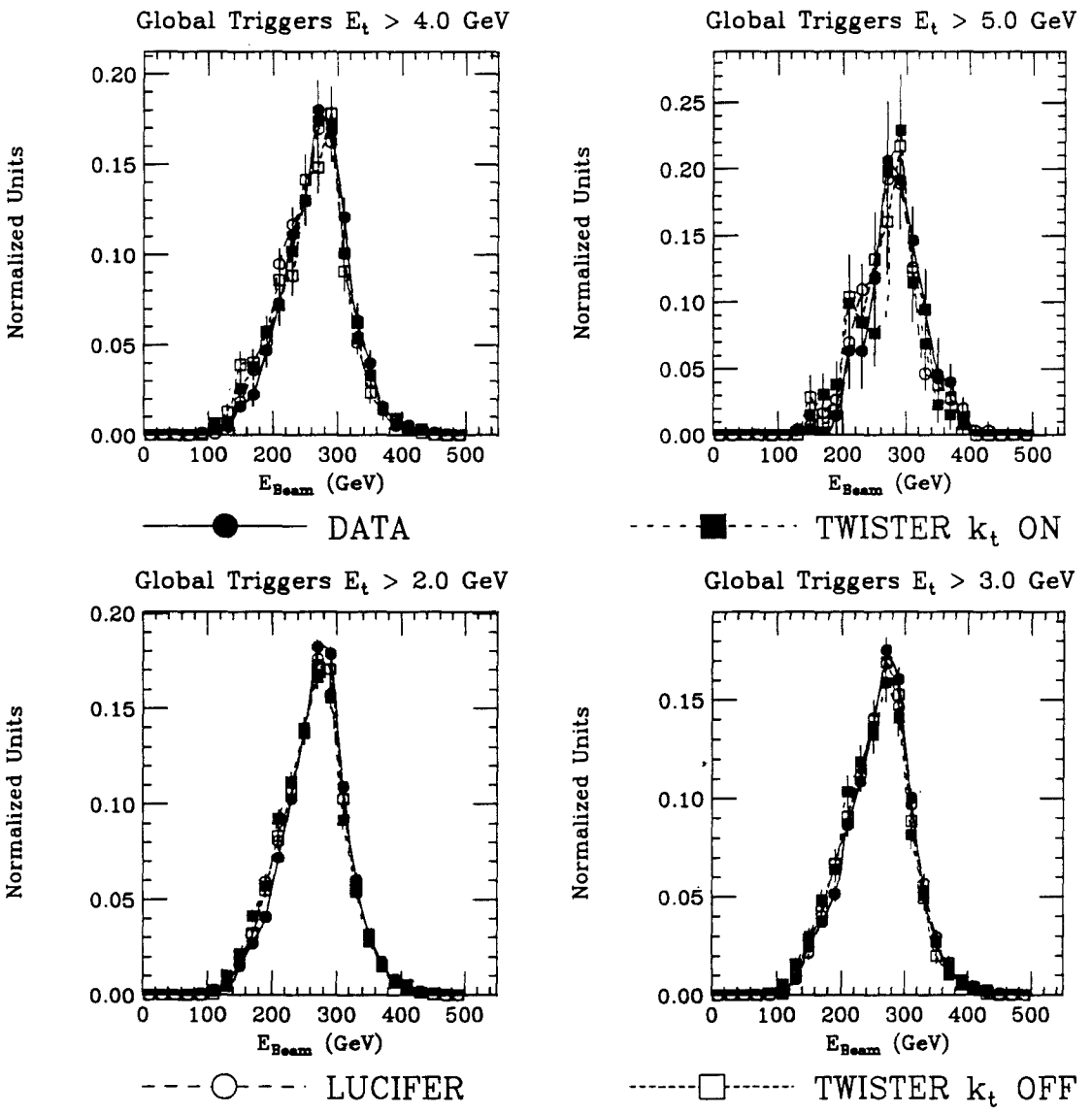

Figure 49: Shown is a comparison between the LUND Monte Carlos and data for Global triggers. The variable being displayed is beam energy E_γ for different reconstructed jet thresholds. The thresholds apply to *both* jets and are listed on the plot, as are the meaning of the symbols used.

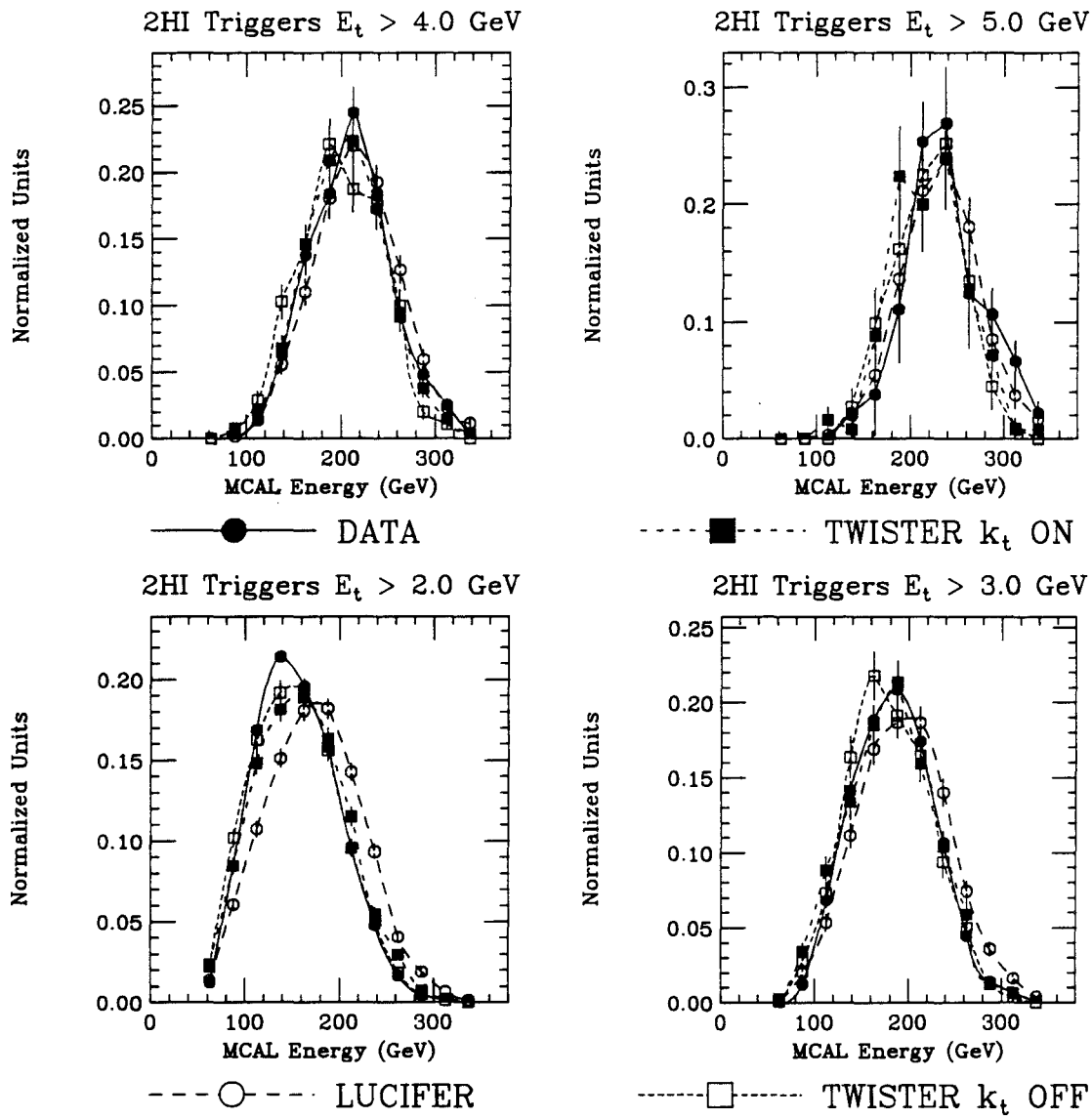

Figure 50: Shown is a comparison between the LUND Monte Carlos and data for 2HI triggers. The variable being displayed is the MCAL energy E_{MCAL} for different reconstructed jet thresholds. The thresholds apply to *both* jets and are listed on the plot, as are the meaning of the symbols used.

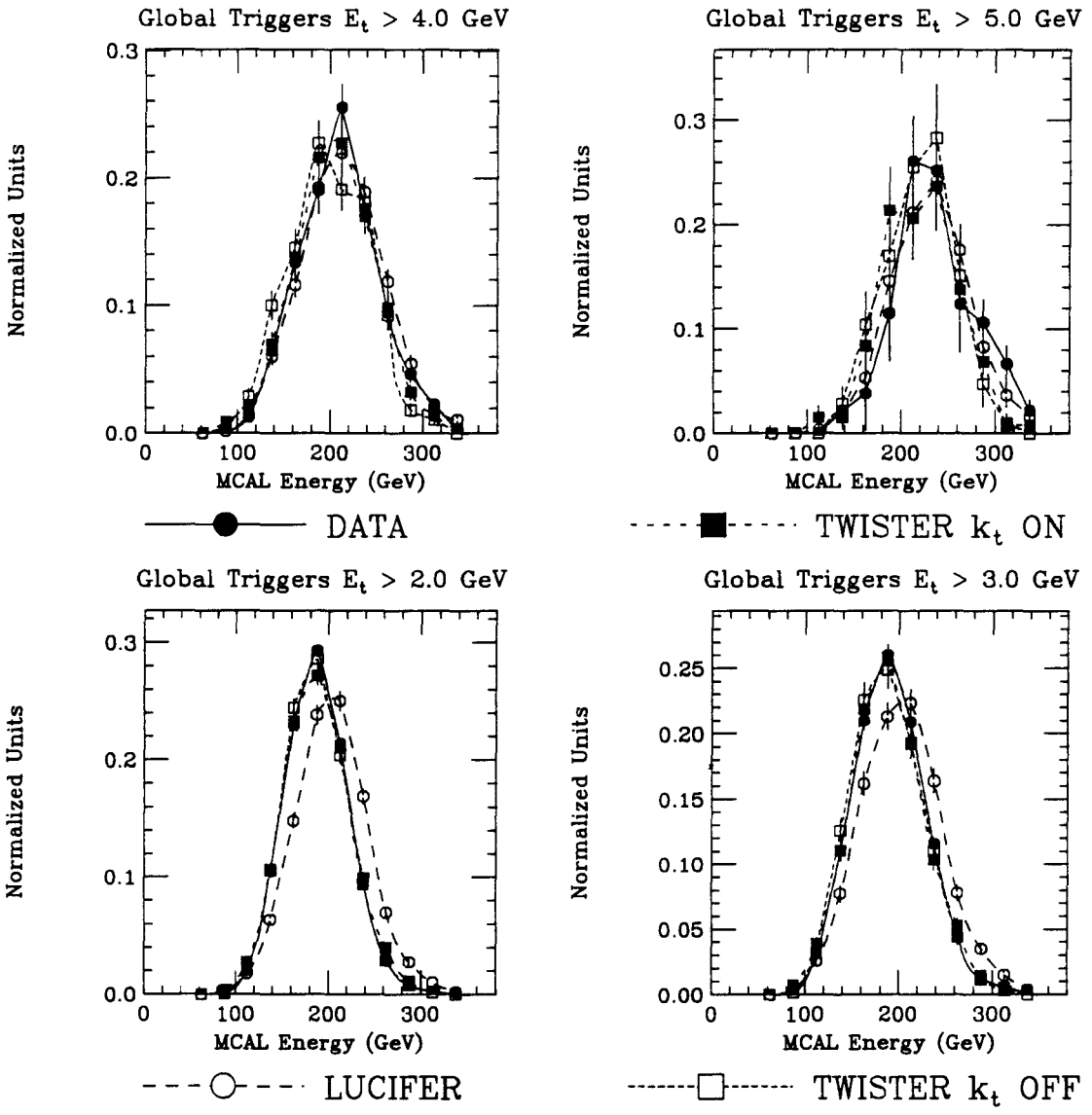

Figure 51: Shown is a comparison between the LUND Monte Carlos and data for Global triggers. The variable being displayed is the MCAL energy E_{MCAL} for different reconstructed jet thresholds. The thresholds apply to *both* jets and are listed on the plot, as are the meaning of the symbols used.

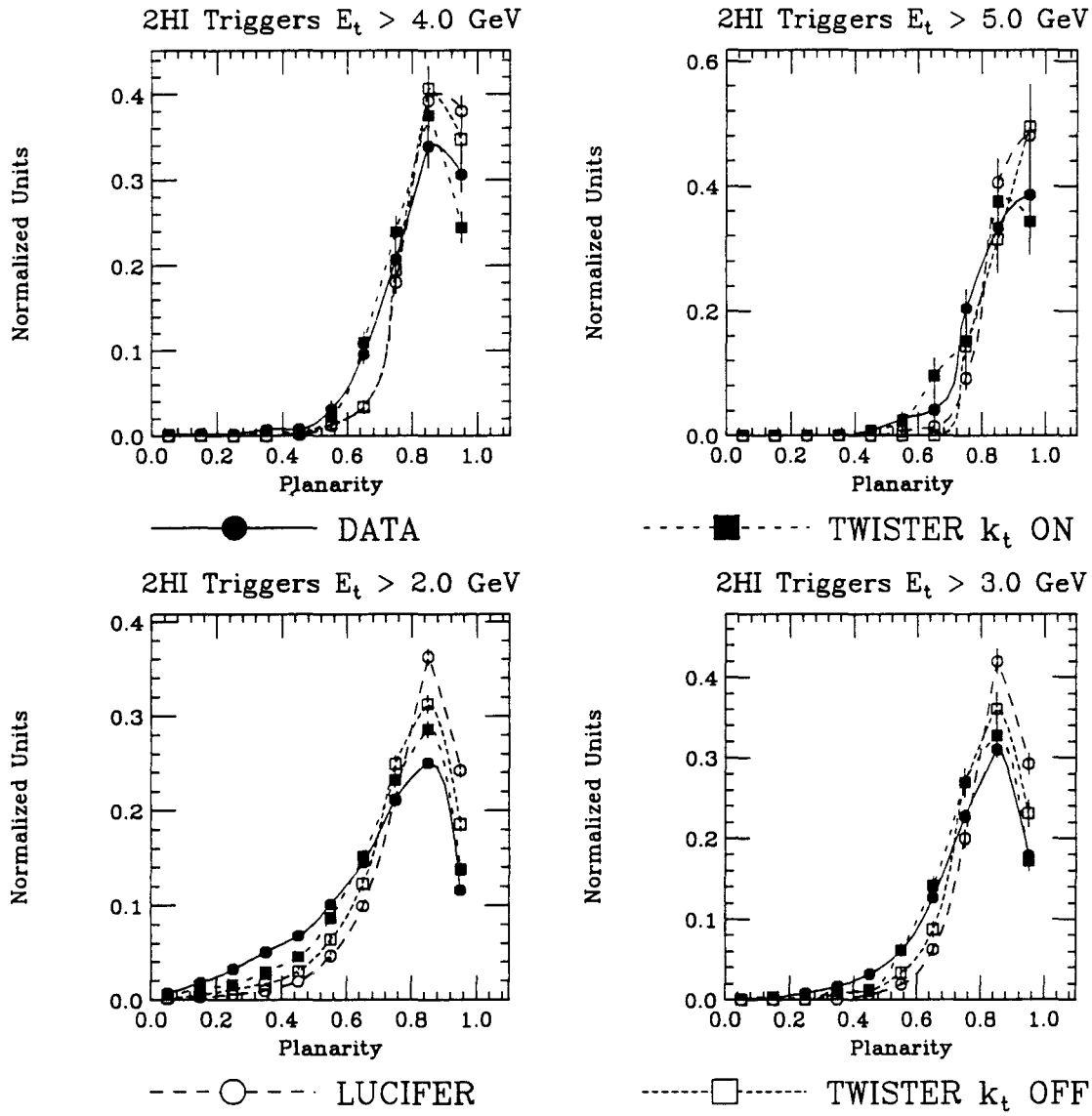

Figure 52: Shown is a comparison between the LUND Monte Carlos and data for 2HI triggers. The variable being displayed is the MCAL Planarity for different reconstructed jet thresholds. The thresholds apply to *both* jets and are listed on the plot, as are the meaning of the symbols used.

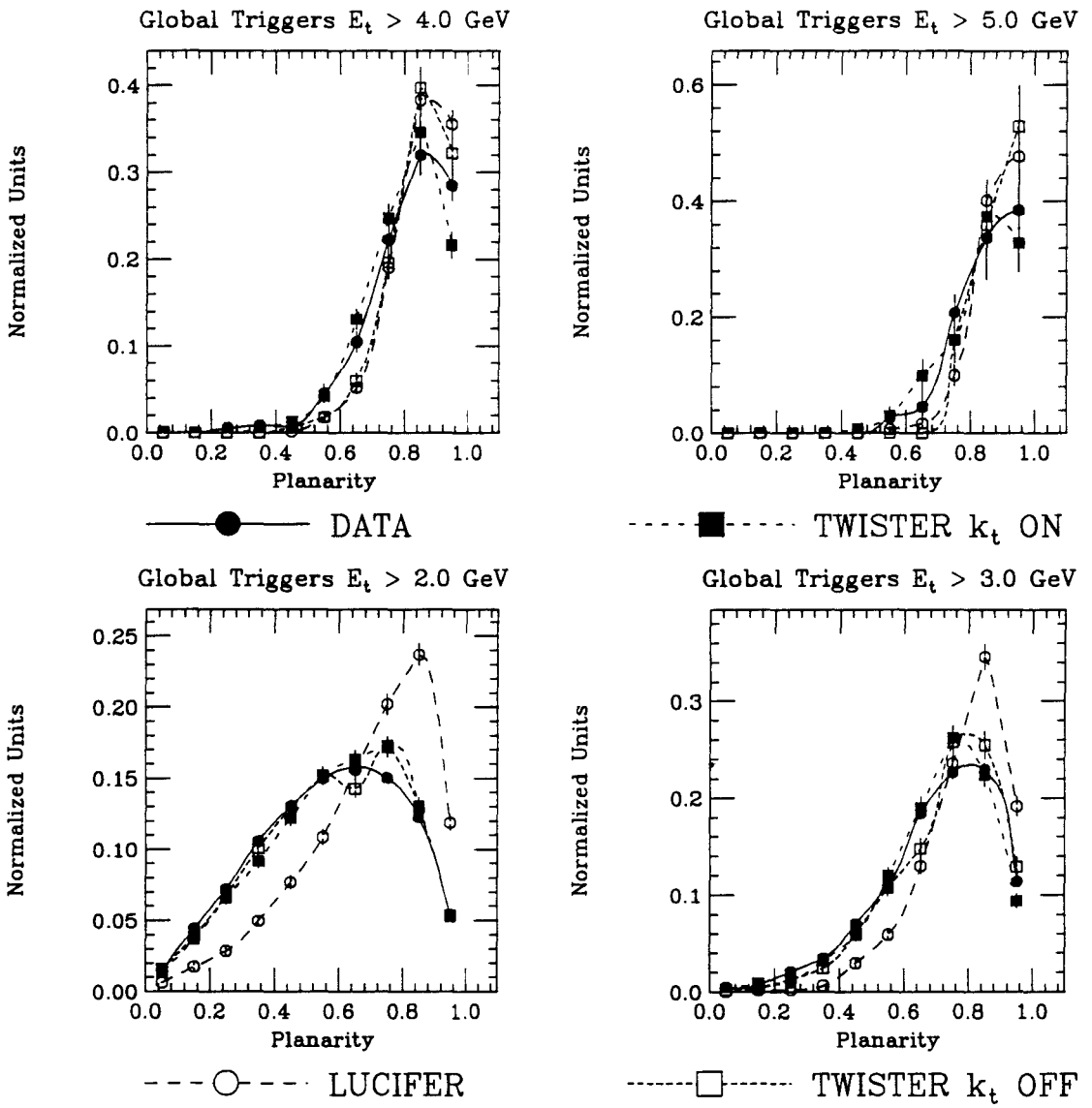

Figure 53: Shown is a comparison between the LUND Monte Carlos and data for Global triggers. The variable being displayed is the MCAL Planarity for different reconstructed jet thresholds. The thresholds apply to *both* jets and are listed on the plot, as are the meaning of the symbols used.

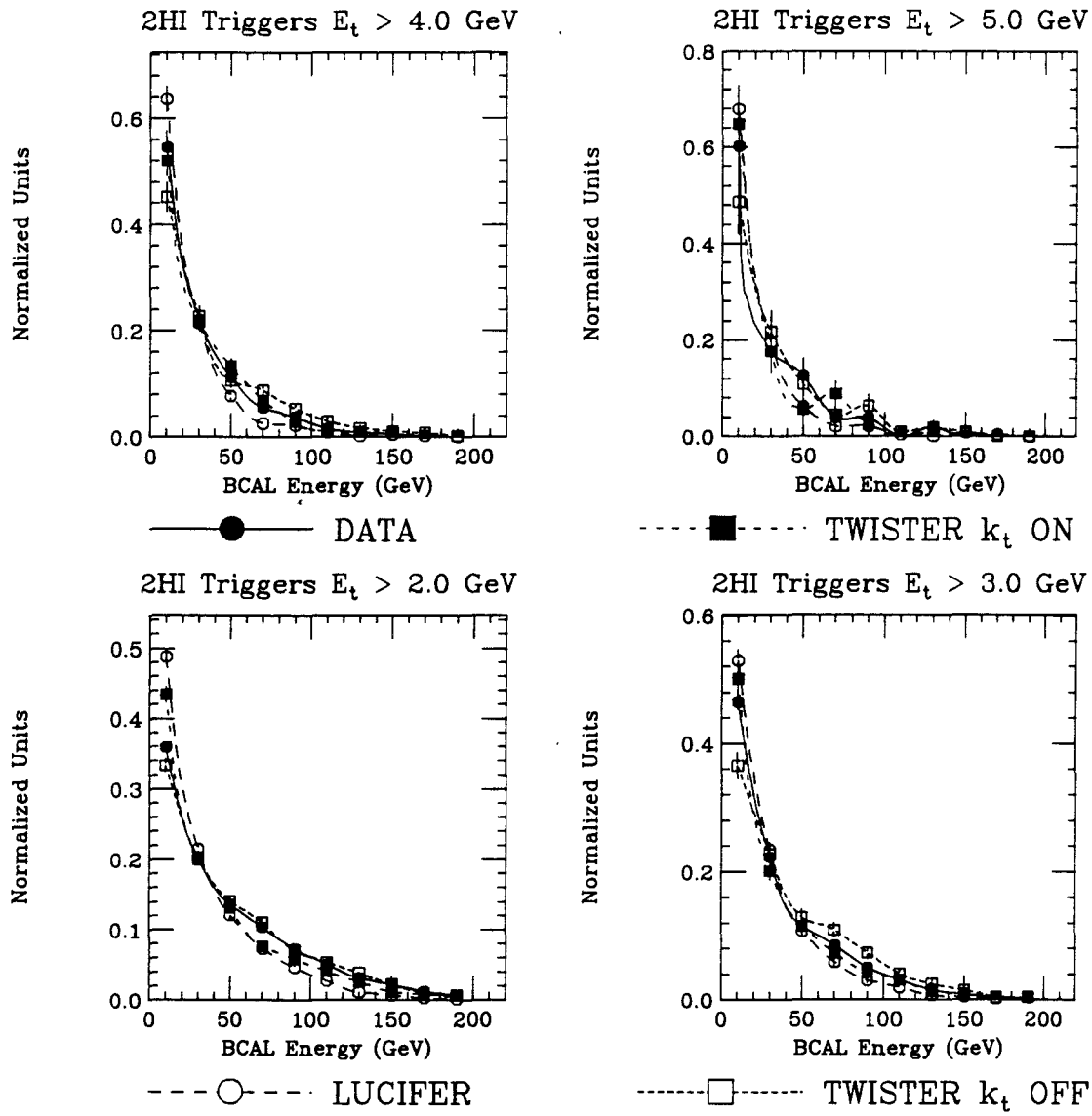

Figure 54: Shown is a comparison between the LUND Monte Carlos and data for 2HI triggers. The variable being displayed is the BCAL energy E_{BCAL} for different reconstructed jet thresholds. The thresholds apply to *both* jets and are listed on the plot, as are the meaning of the symbols used.

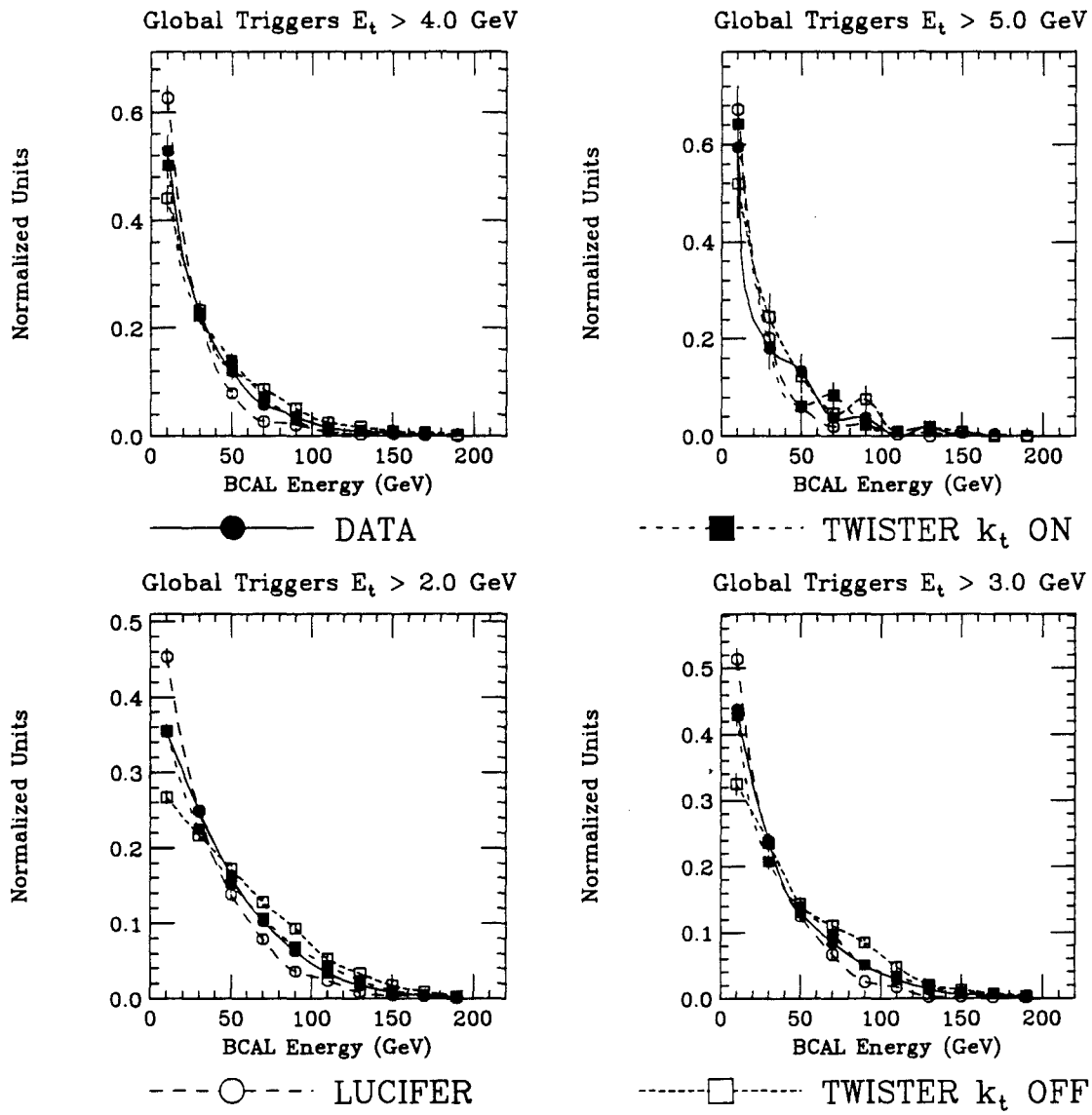

Figure 55: Shown is a comparison between the LUND Monte Carlos and data for Global triggers. The variable being displayed is the BCAL energy E_{BCAL} for different reconstructed jet thresholds. The thresholds apply to *both* jets and are listed on the plot, as are the meaning of the symbols used.

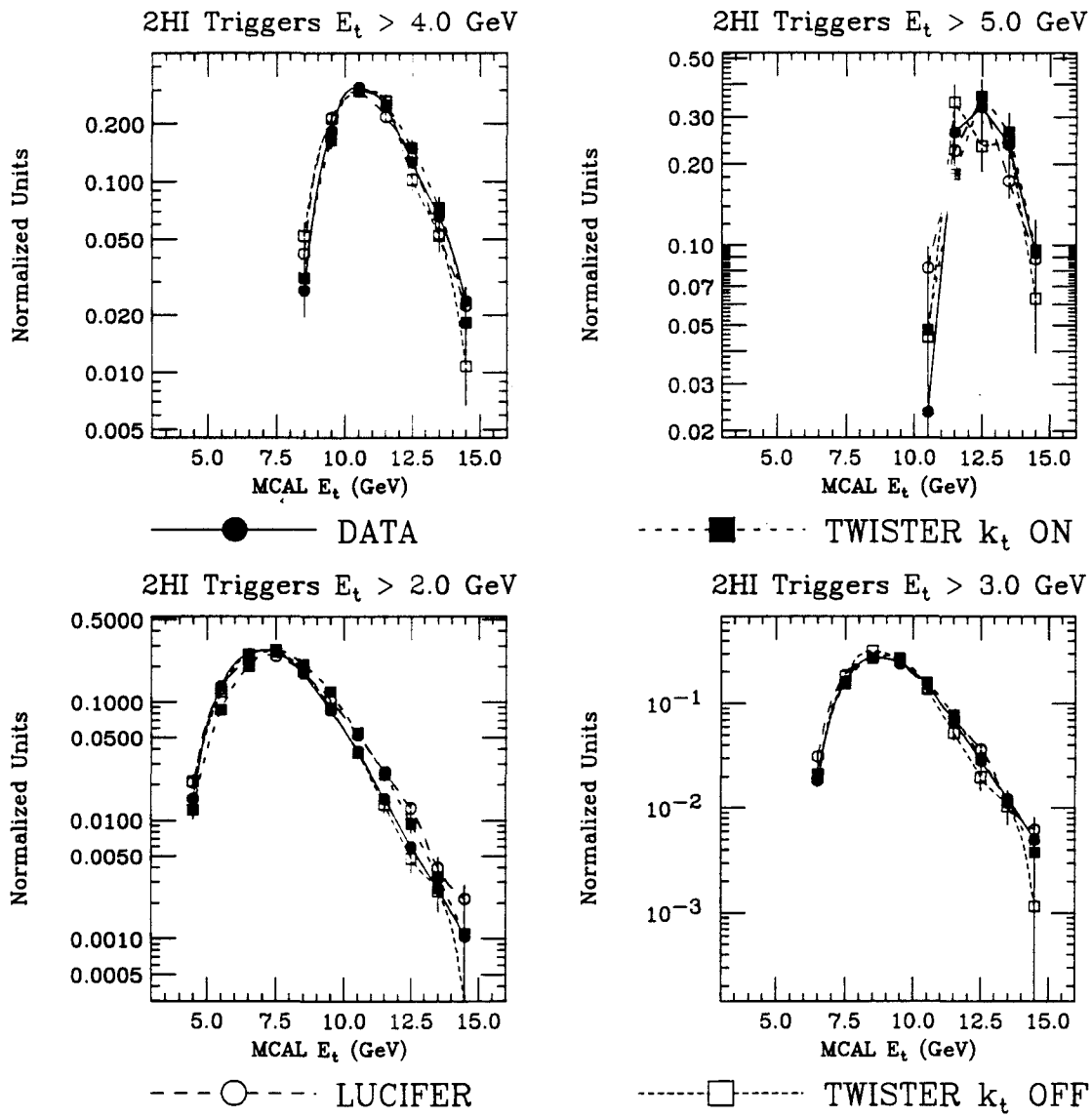

Figure 56: Shown is a comparison between the LUND Monte Carlos and data for 2HI triggers. The variable being displayed is the MCAL $E_\perp$ for different reconstructed jet thresholds. The thresholds apply to *both* jets and are listed on the plot, as are the meaning of the symbols used. Note that these plots are on logarithmic scales.

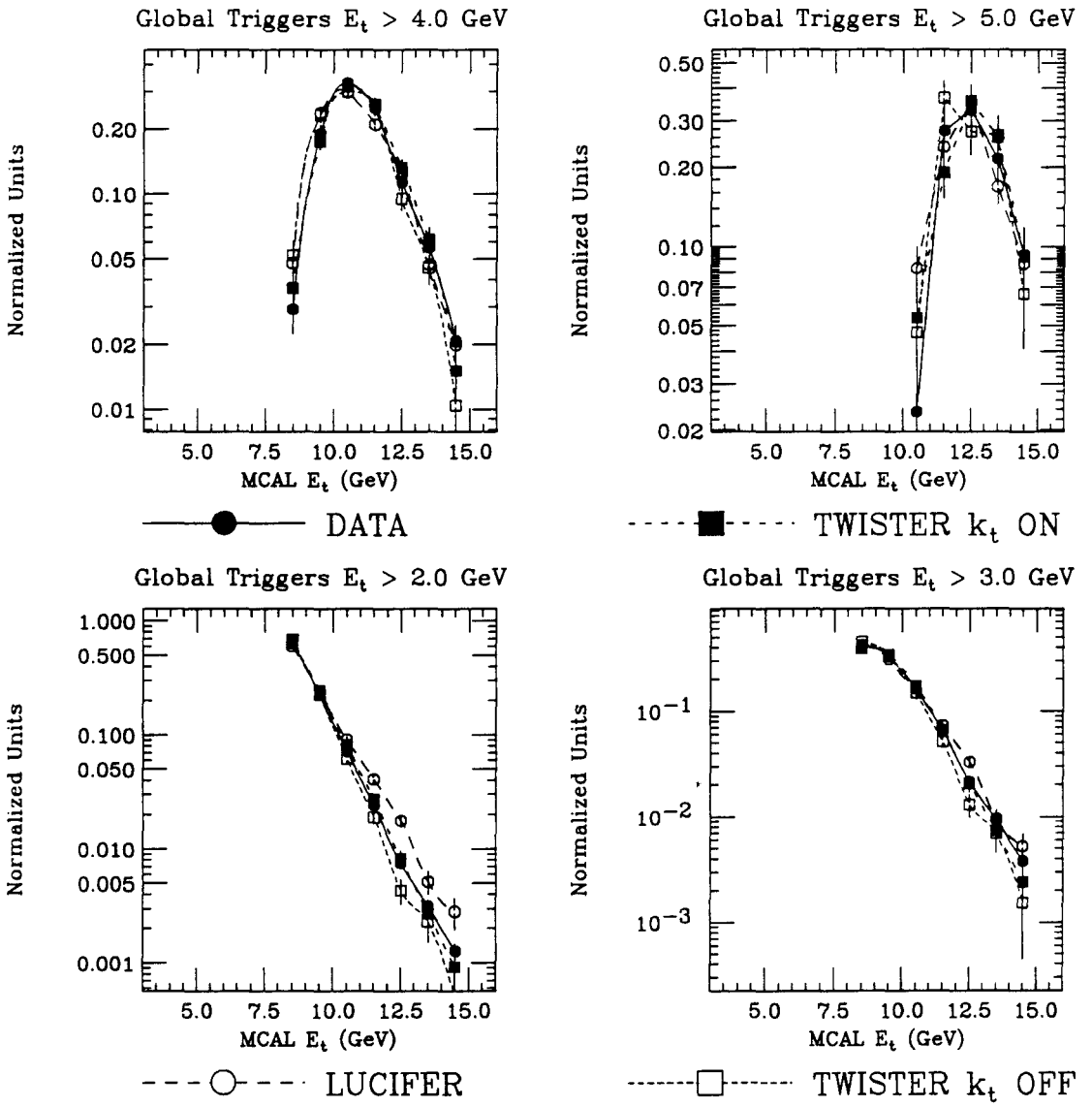

Figure 57: Shown is a comparison between the LUND Monte Carlos and data for Global triggers. The variable being displayed is the MCAL $E_\perp$ for different reconstructed jet thresholds. The thresholds apply to *both* jets and are listed on the plot, as are the meaning of the symbols used. Note that these plots are on logarithmic scales.

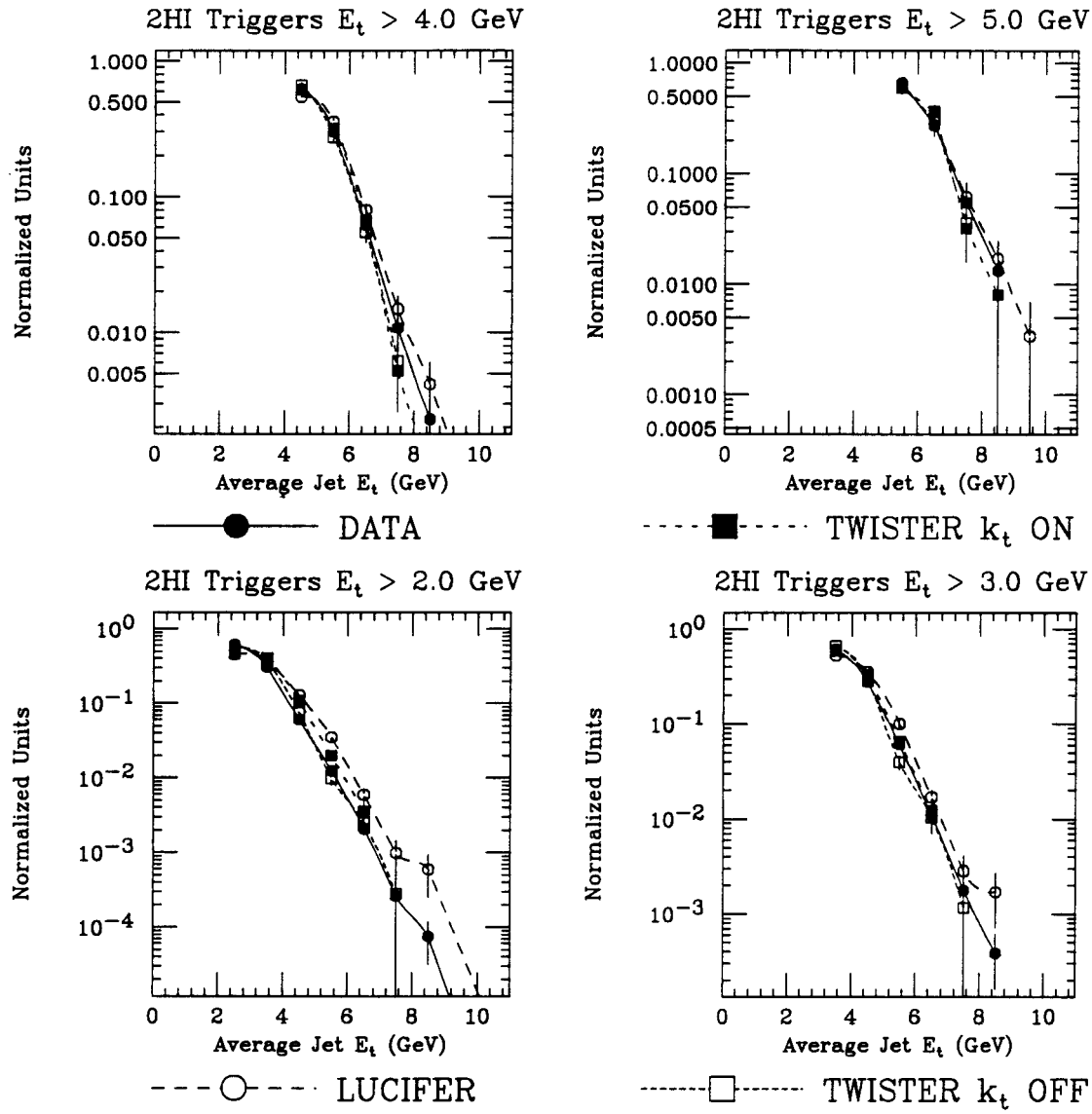

Figure 58: Shown is a comparison between the LUND Monte Carlos and data for 2HI triggers. The variable being displayed is the average jet $E_\perp$ for different reconstructed jet thresholds. The thresholds apply to *both* jets and are listed on the plot, as are the meaning of the symbols used. Note that these plots are on logarithmic scales.

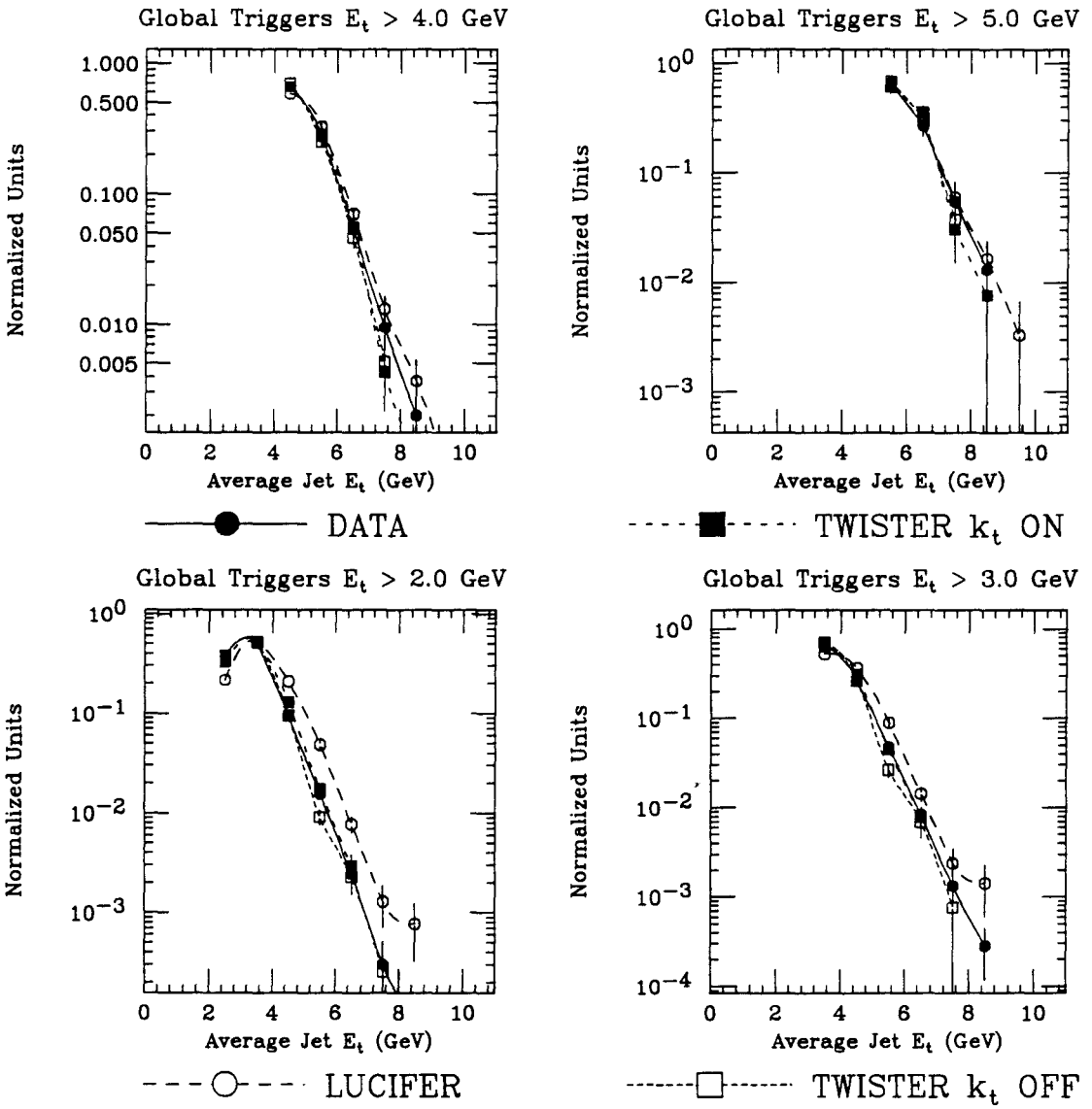

Figure 59: Shown is a comparison between the LUND Monte Carlos and data for Global triggers. The variable being displayed is the average jet $E_\perp$ for different reconstructed jet thresholds. The thresholds apply to *both* jets and are listed on the plot, as are the meaning of the symbols used. Note that these plots are on logarithmic scales.

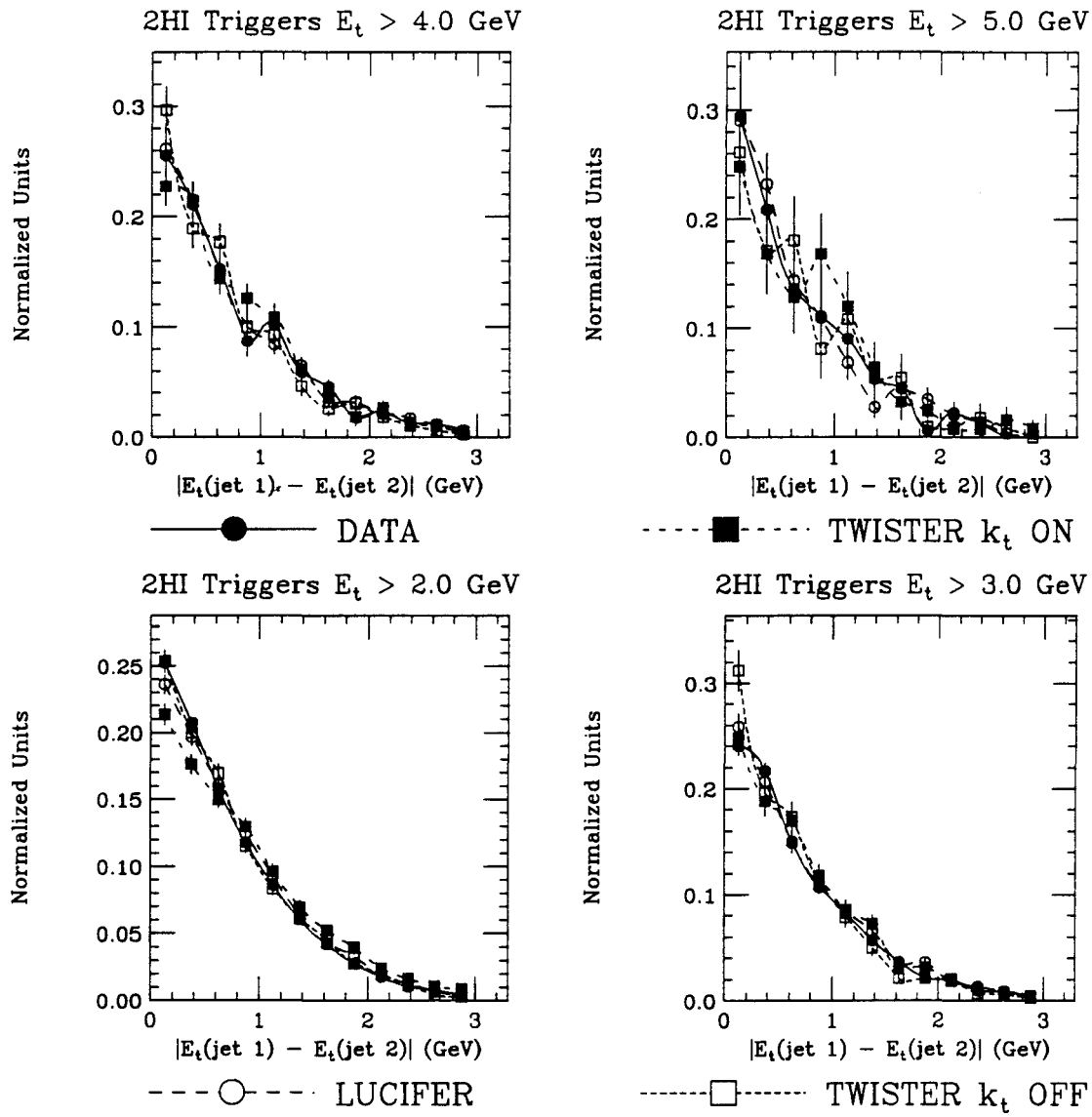

Figure 60: Shown is a comparison between the LUND Monte Carlos and data for 2HI triggers. The variable being displayed is $|E_\perp^{\text{jet1}} - E_\perp^{\text{jet2}}|$ for different reconstructed jet thresholds. The thresholds apply to *both* jets and are listed on the plot, as are the meaning of the symbols used.

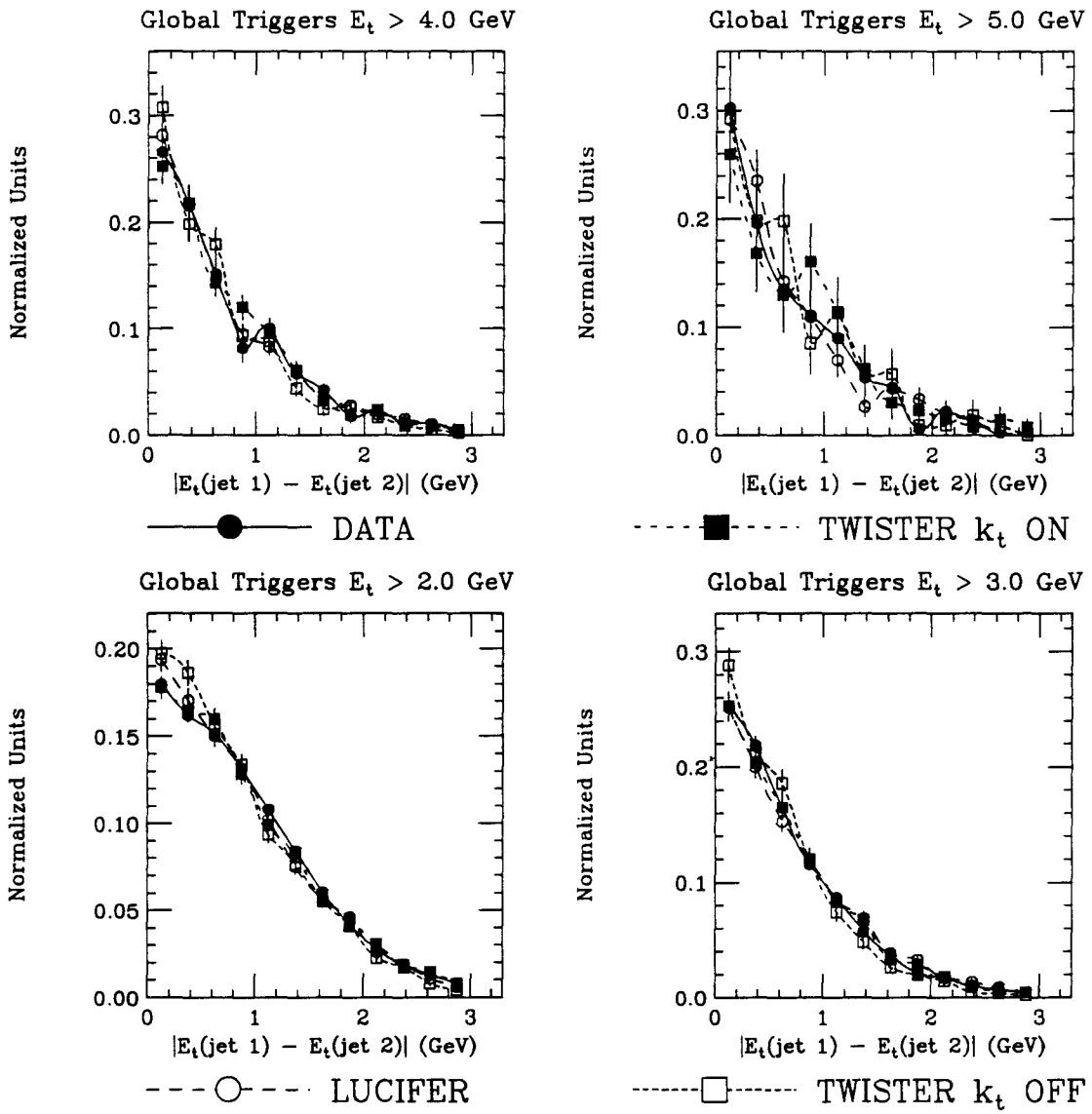

Figure 61: Shown is a comparison between the LUND Monte Carlos and data for Global triggers. The variable being displayed is $|E_\perp^{\text{jet1}} - E_\perp^{\text{jet2}}|$ for different reconstructed jet thresholds. The thresholds apply to *both* jets and are listed on the plot, as are the meaning of the symbols used.

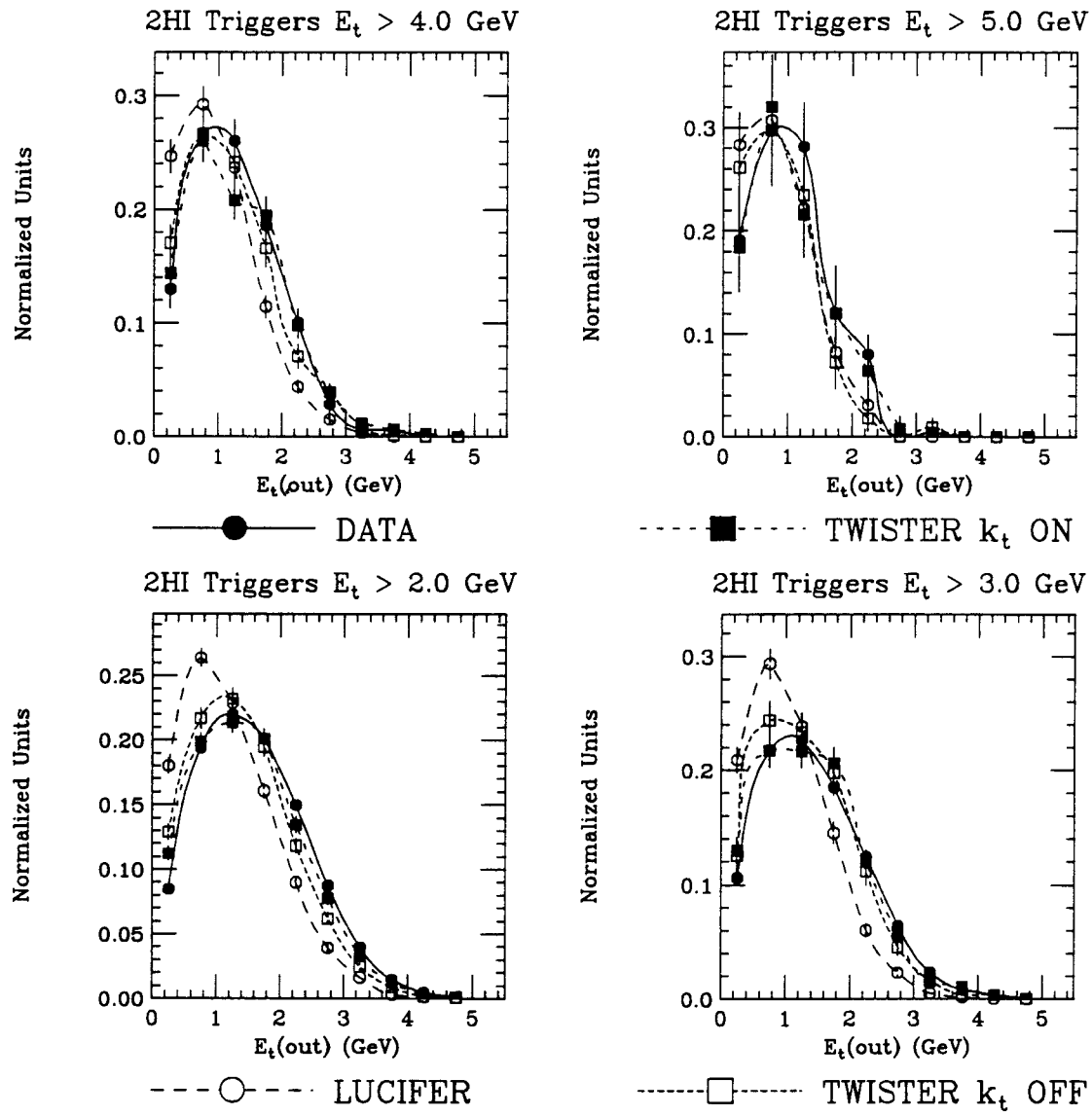

Figure 62: Shown is a comparison between the LUND Monte Carlos and data for 2HI triggers. The variable being displayed is MCAL $E_\perp$ not in the jet cone for different reconstructed jet thresholds. The thresholds apply to *both* jets and are listed on the plot, as are the meaning of the symbols used.

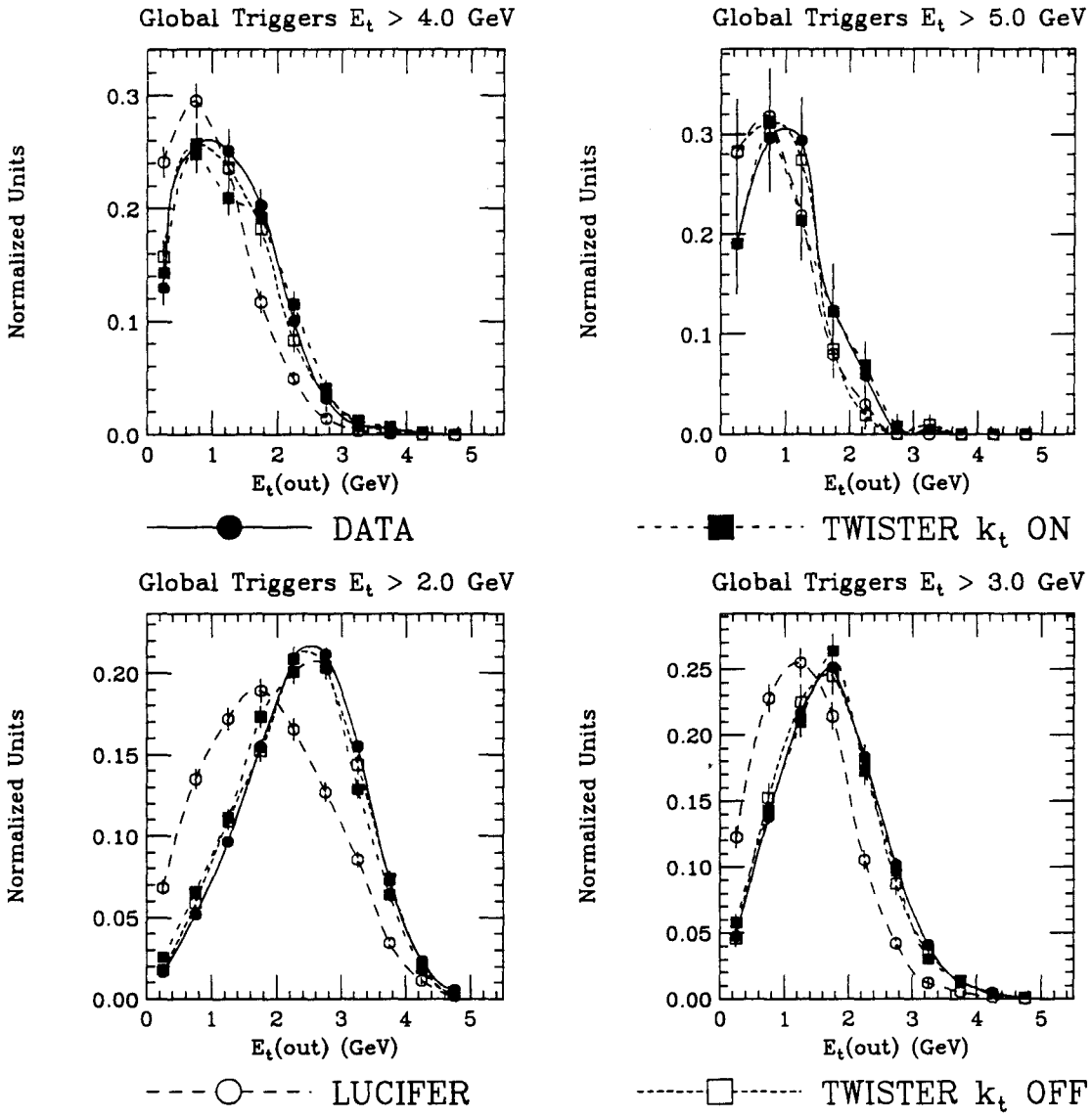

Figure 63: Shown is a comparison between the LUND Monte Carlos and data for Global triggers. The variable being displayed is MCAL $E_\perp$ not in the jet cone for different reconstructed jet thresholds. The thresholds apply to *both* jets and are listed on the plot, as are the meaning of the symbols used.

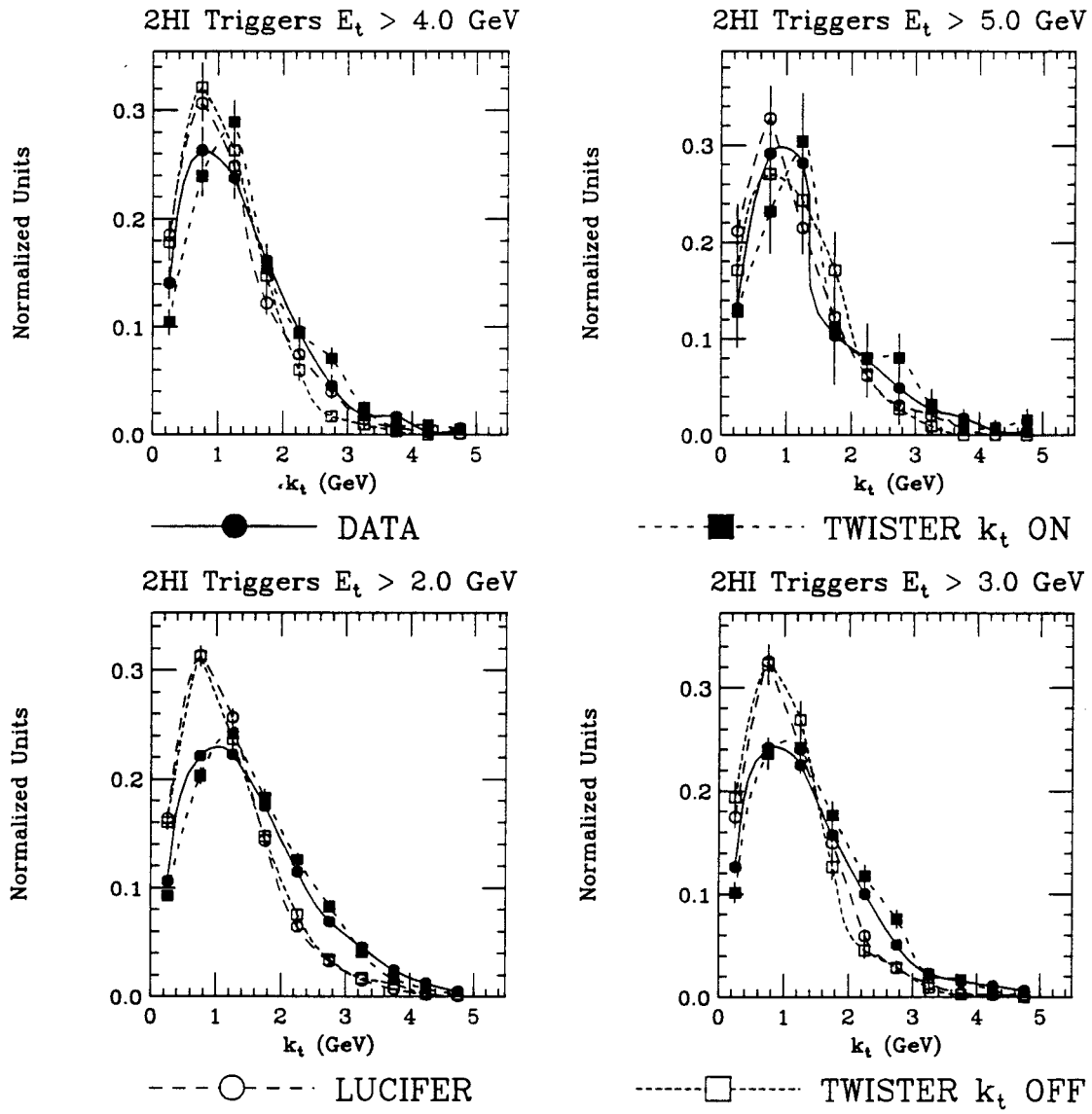

Figure 64: Shown is a comparison between the LUND Monte Carlos and data for 2HI triggers. The variable being displayed is $k_\perp$, as defined by equation (10), for different reconstructed jet thresholds. The thresholds apply to *both* jets and are listed on the plot, as are the meaning of the symbols used.

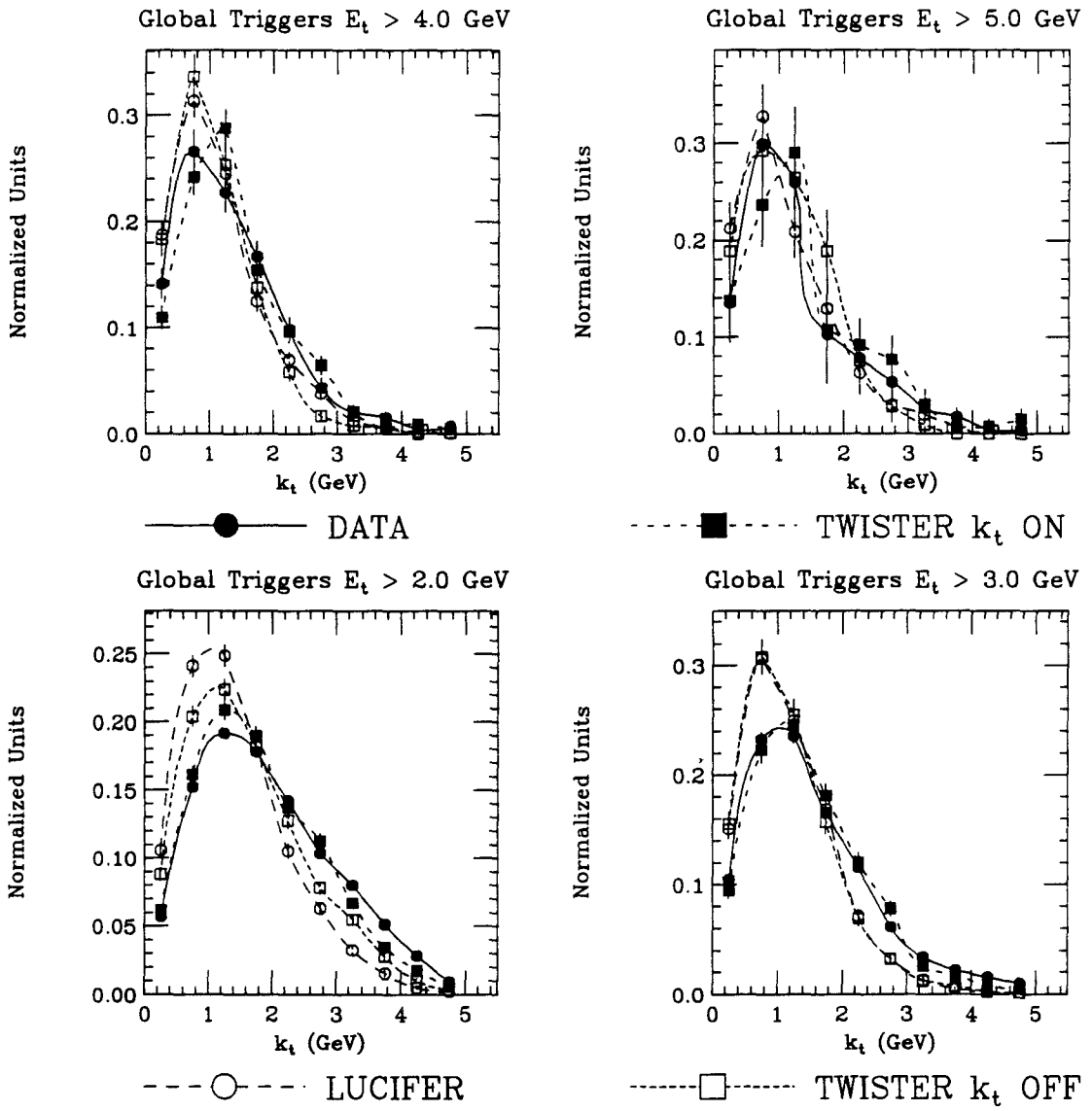

Figure 65: Shown is a comparison between the LUND Monte Carlos and data for Global triggers. The variable being displayed is $k_\perp$, as defined by equation (10), for different reconstructed jet thresholds. The thresholds apply to *both* jets and are listed on the plot, as are the meaning of the symbols used.

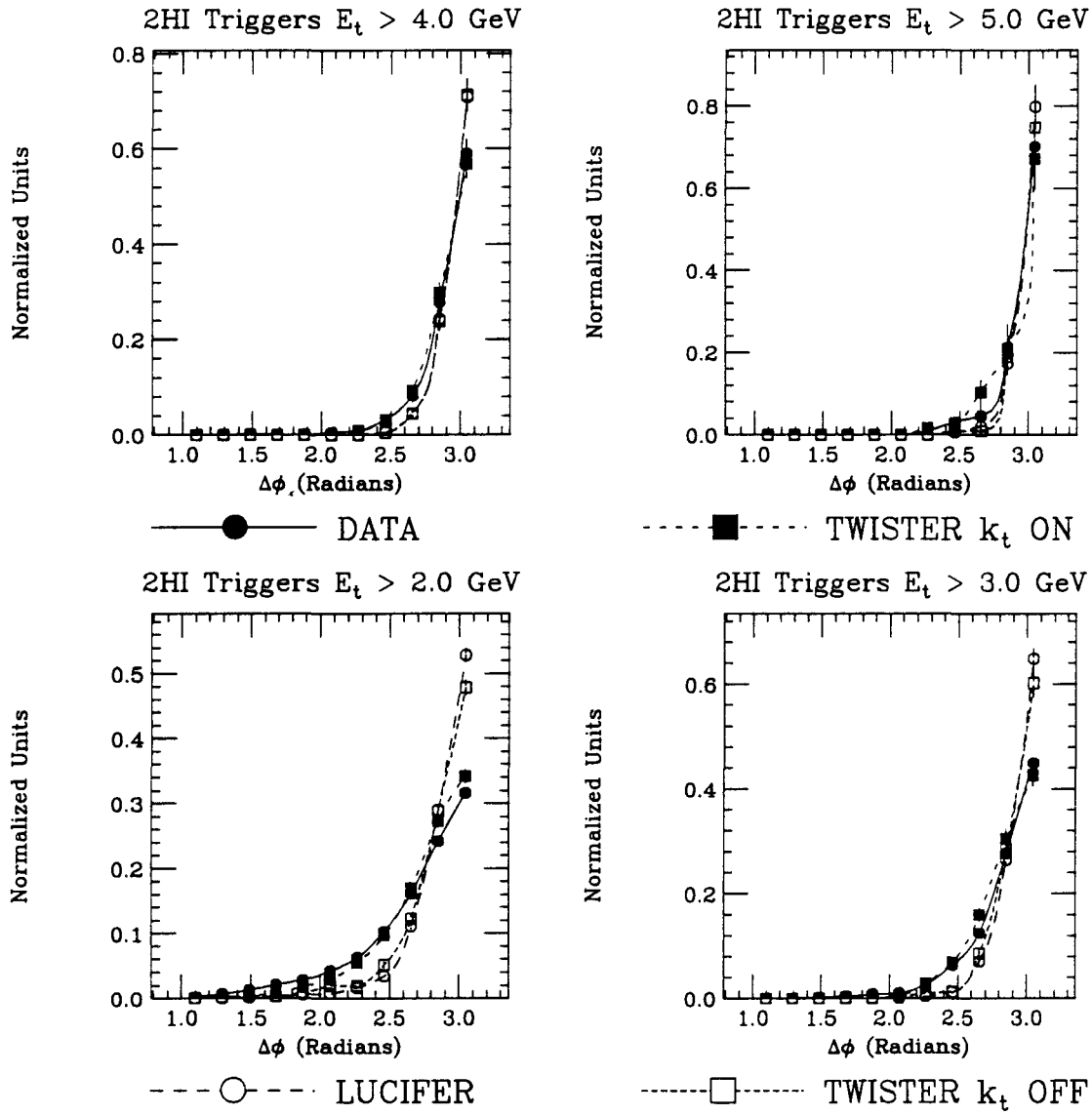

Figure 66: Shown is a comparison between the LUND Monte Carlos and data for 2HI triggers. The variable being displayed is $\Delta\phi$ between the two jets for different reconstructed jet thresholds. The thresholds apply to *both* jets and are listed on the plot, as are the meaning of the symbols used.

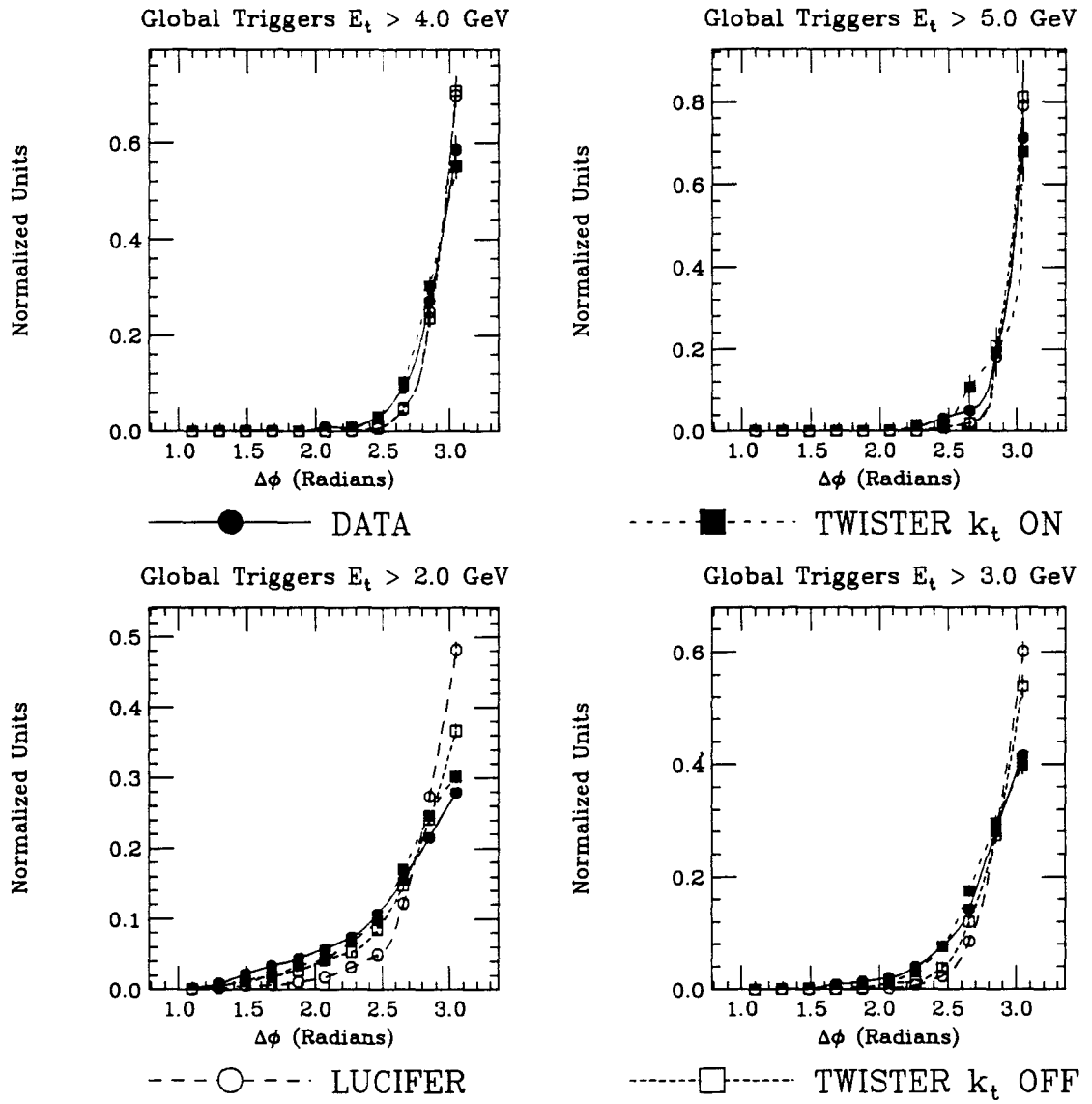

Figure 67: Shown is a comparison between the LUND Monte Carlos and data for Global triggers. The variable being displayed is $\Delta\phi$ between the two jets for different reconstructed jet thresholds. The thresholds apply to *both* jets and are listed on the plot, as are the meaning of the symbols used.

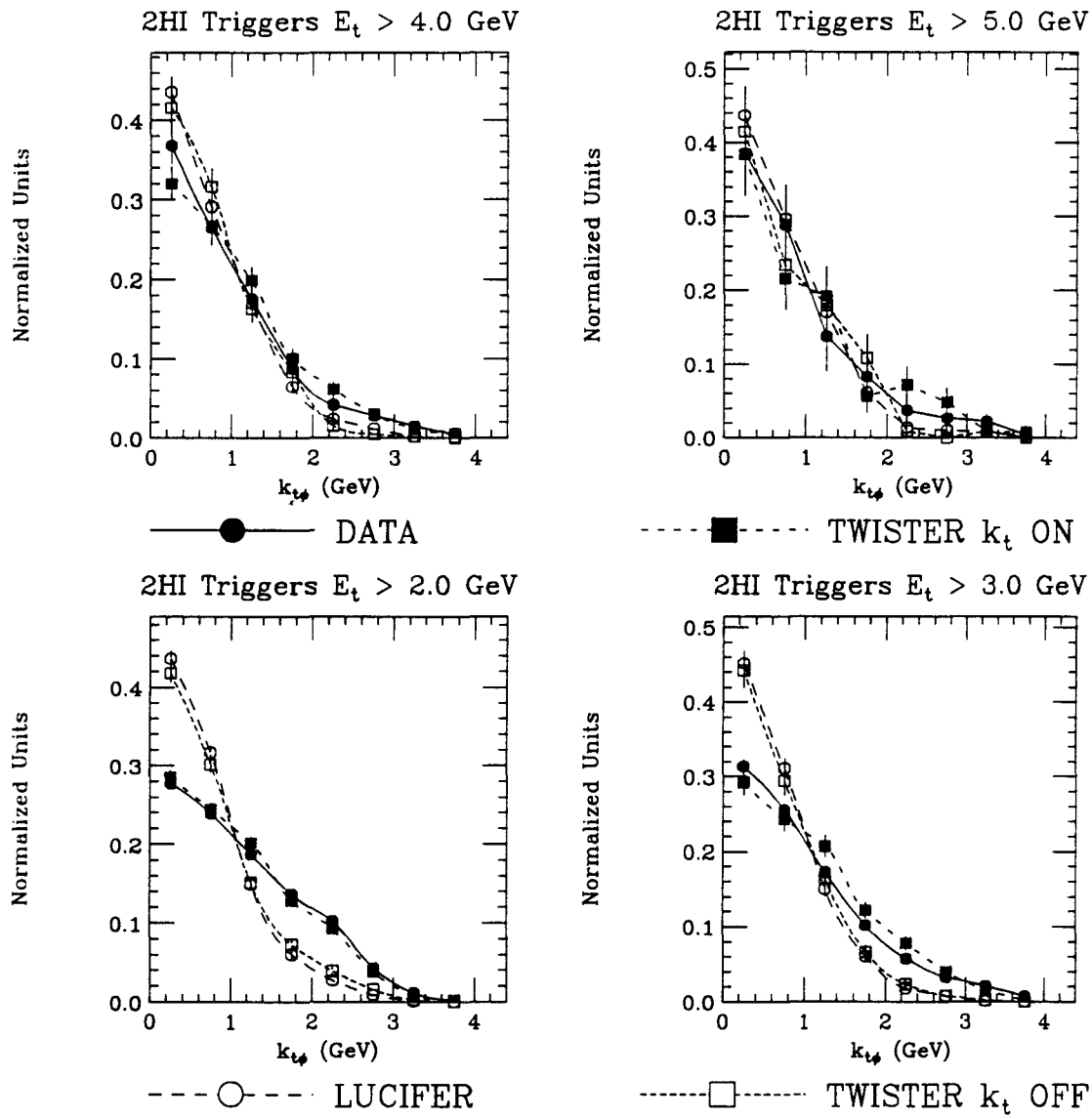

Figure 68: Shown is a comparison between the LUND Monte Carlos and data for 2HI triggers. The variable being displayed is $k_{\perp\phi}$, as defined by equation (11), for different reconstructed jet thresholds. The thresholds apply to *both* jets and are listed on the plot, as are the meaning of the symbols used.

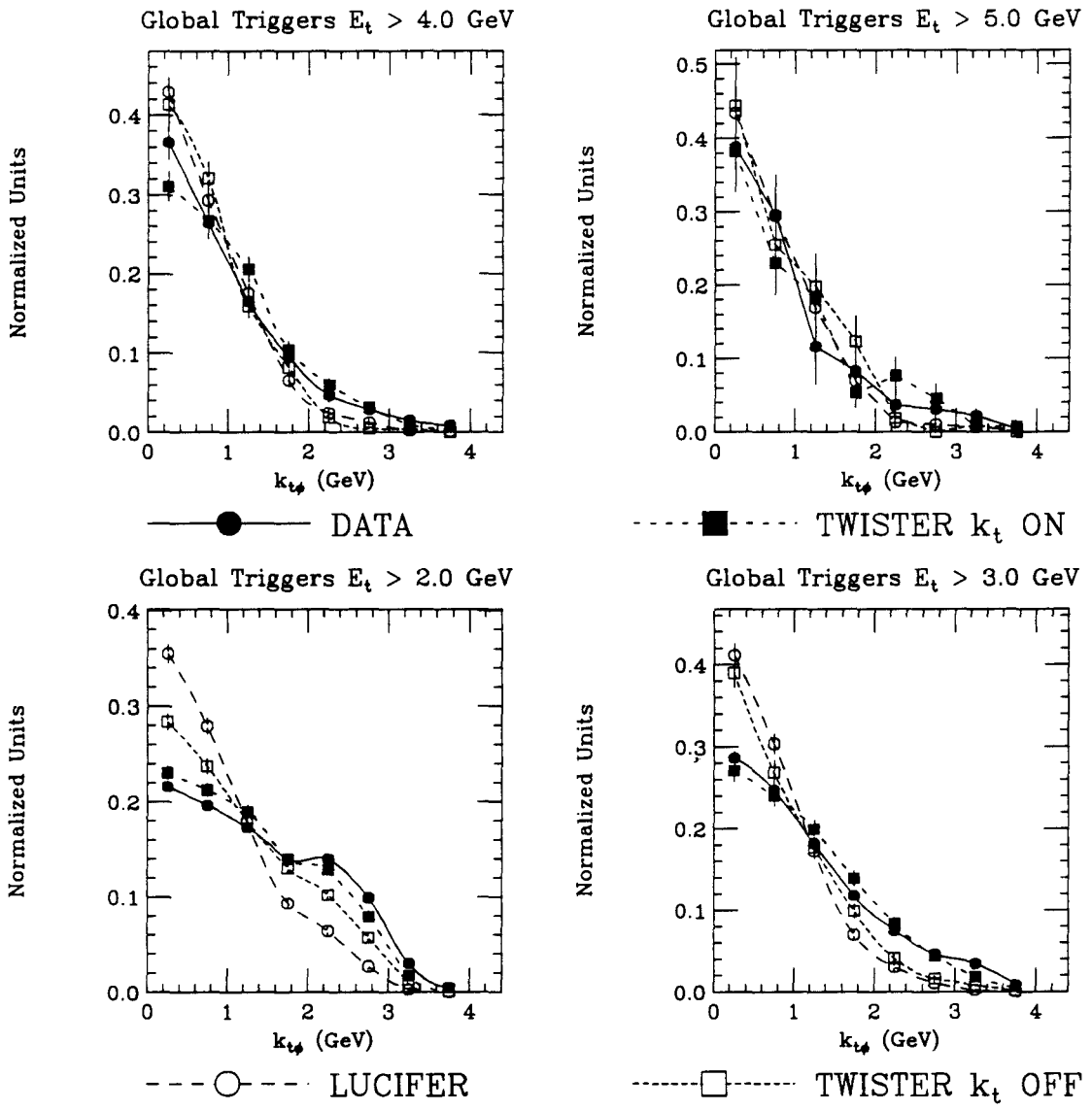

Figure 69: Shown is a comparison between the LUND Monte Carlos and data for Global triggers. The variable being displayed is $k_{\perp\phi}$, as defined by equation (11), for different reconstructed jet thresholds. The thresholds apply to *both* jets and are listed on the plot, as are the meaning of the symbols used.

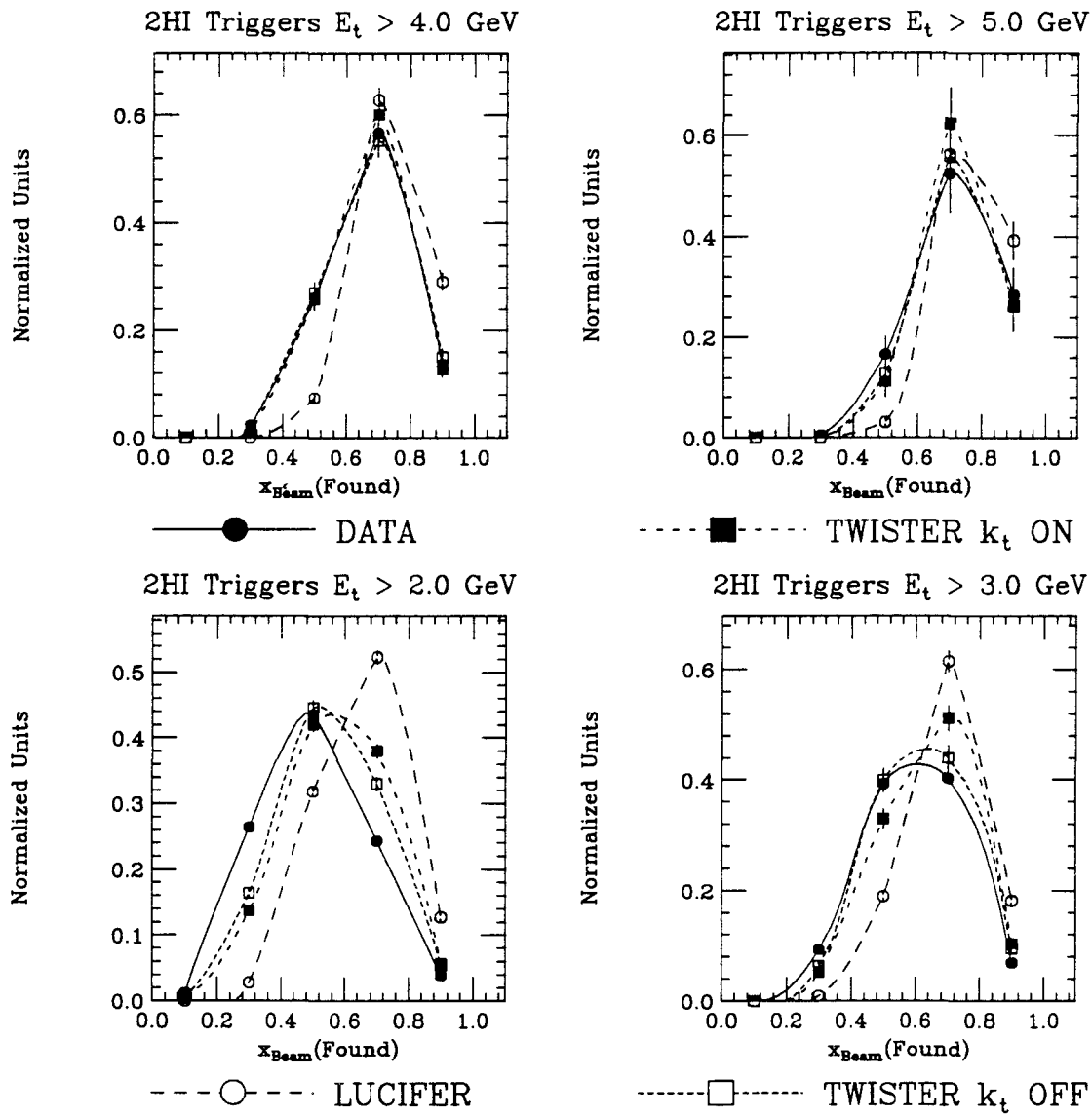

Figure 70: Shown is a comparison between the LUND Monte Carlos and data for 2HI triggers. The variable being displayed is x_{BEAM}, as defined by equation (9) and reconstructed jet kinematics, for different reconstructed jet thresholds. The thresholds apply to *both* jets and are listed on the plot, as are the meaning of the symbols used.

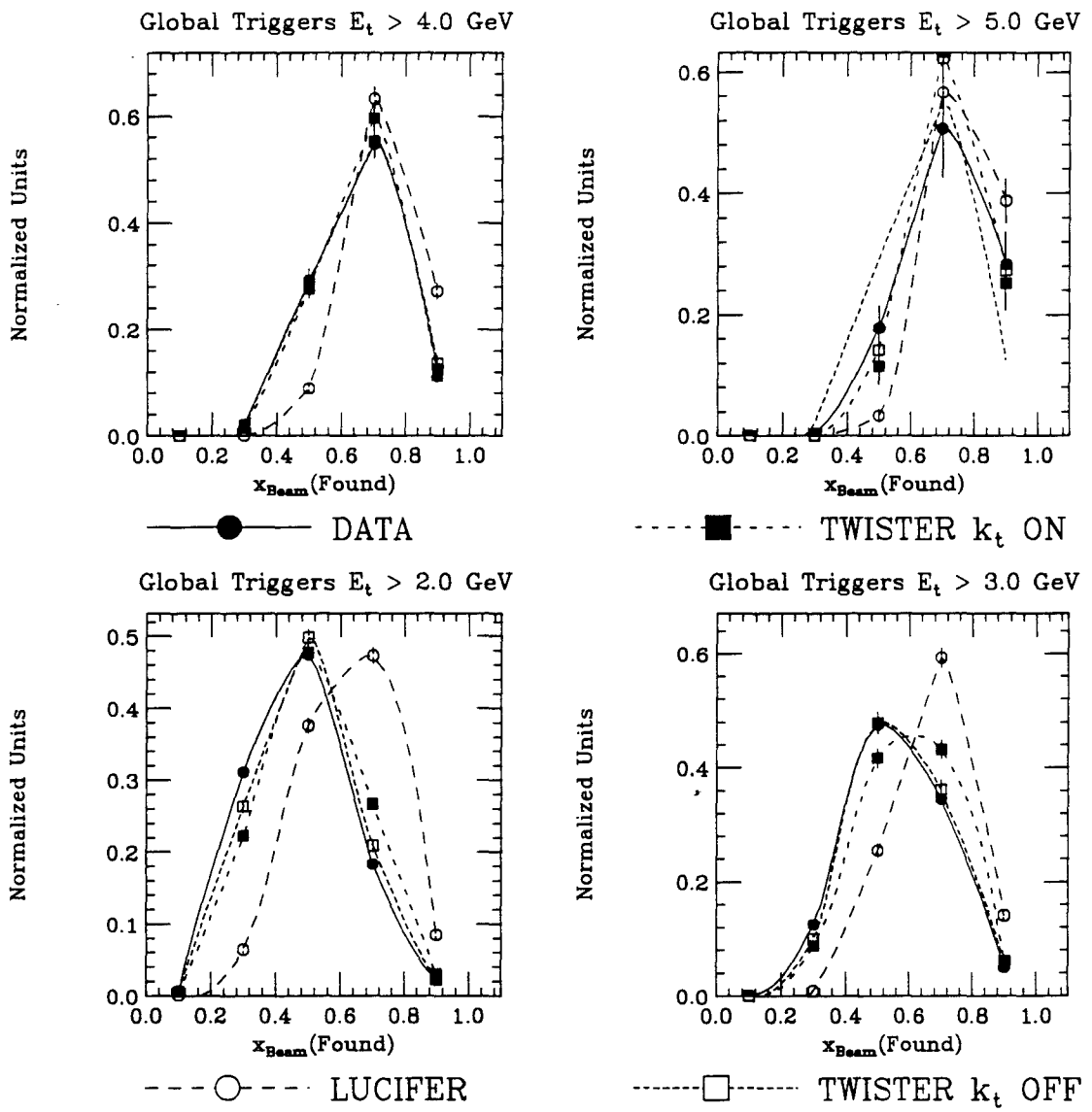

Figure 71: Shown is a comparison between the LUND Monte Carlos and data for Global triggers. The variable being displayed is x_{BEAM}, as defined by equation (9) and reconstructed jet kinematics, for different reconstructed jet thresholds. The thresholds apply to *both* jets and are listed on the plot, as are the meaning of the symbols used.

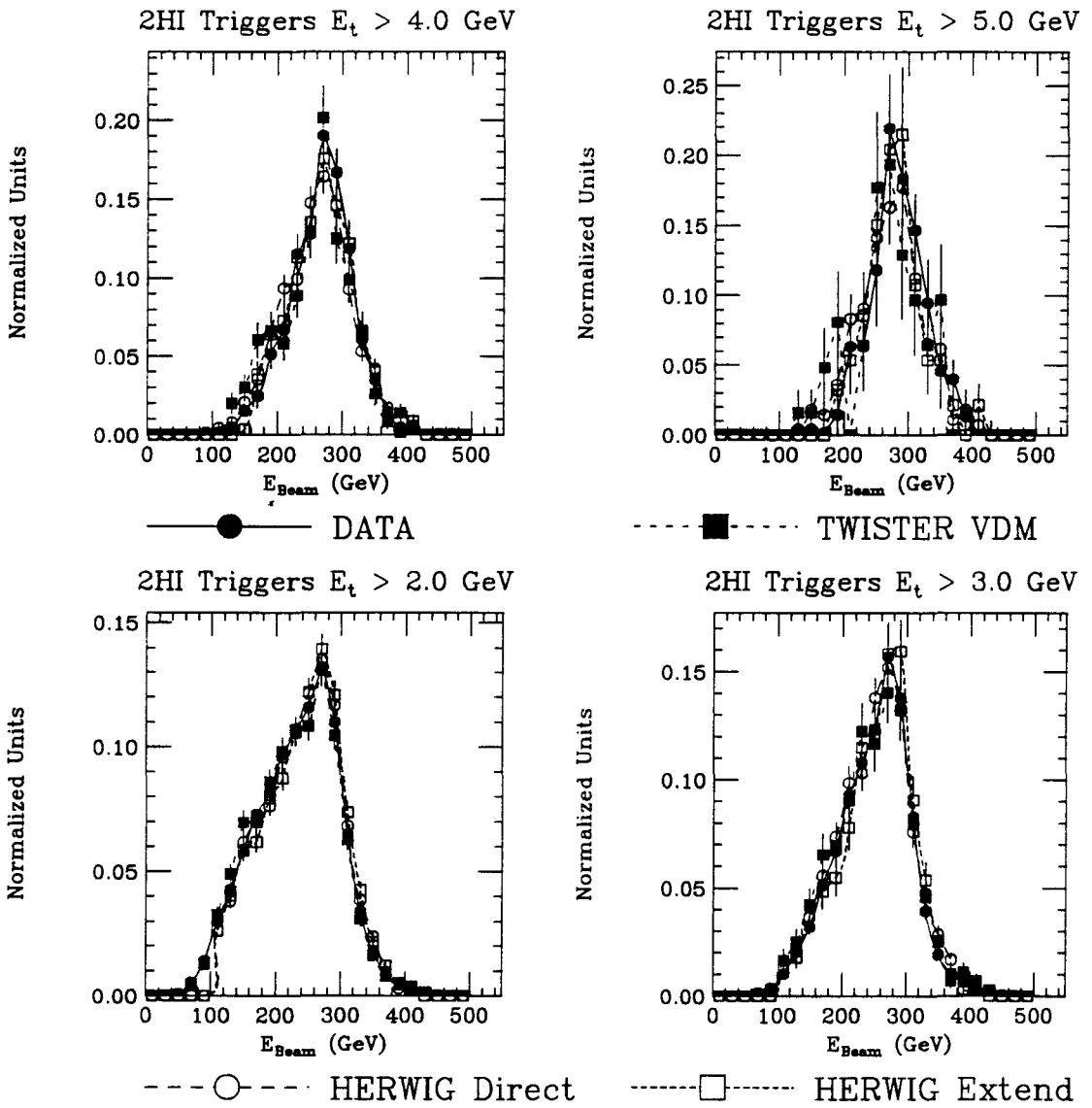

Figure 72: Shown is a comparison between the HERWIG Monte Carlo and data for 2HI triggers. The variable being displayed is beam energy E_γ for different reconstructed jet thresholds. The thresholds apply to *both* jets and are listed on the plot, as are the meaning of the symbols used.

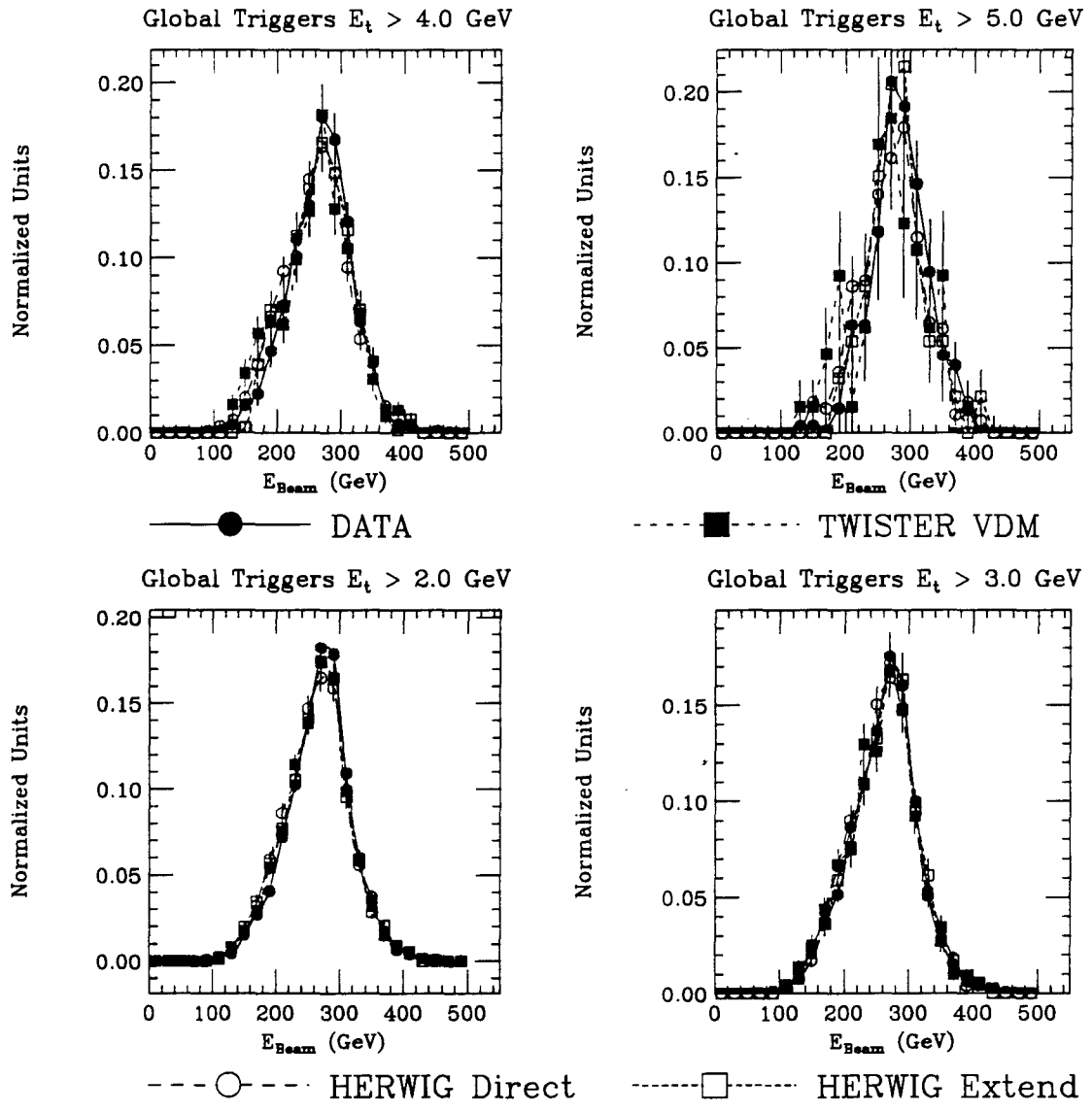

Figure 73: Shown is a comparison between the HERWIG Monte Carlo and data for Global triggers. The variable being displayed is beam energy E_γ for different reconstructed jet thresholds. The thresholds apply to *both* jets and are listed on the plot, as are the meaning of the symbols used.

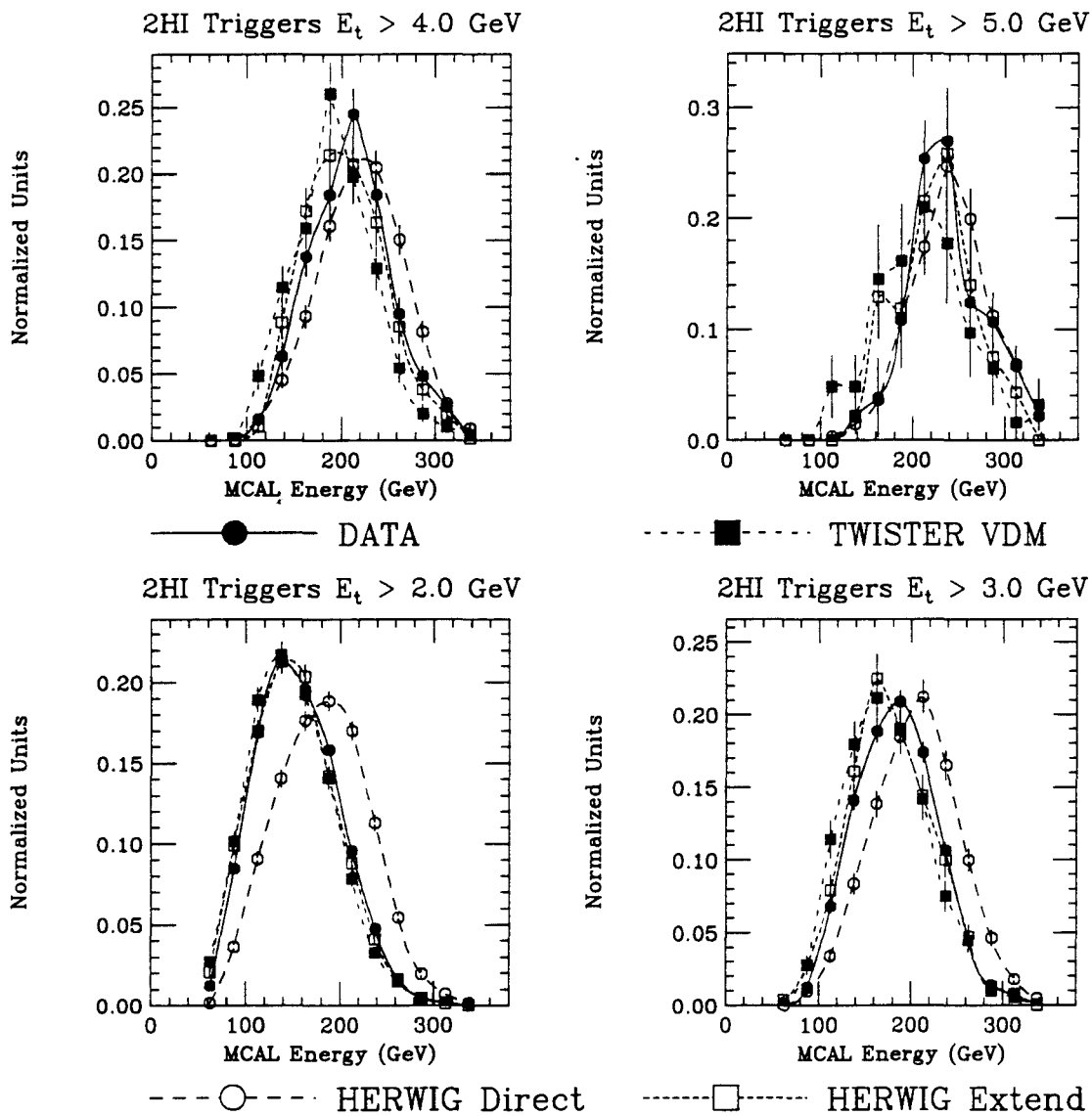

Figure 74: Shown is a comparison between the HERWIG Monte Carlo and data for 2HI triggers. The variable being displayed is the MCAL energy E_{MCAL} for different reconstructed jet thresholds. The thresholds apply to *both* jets and are listed on the plot, as are the meaning of the symbols used.

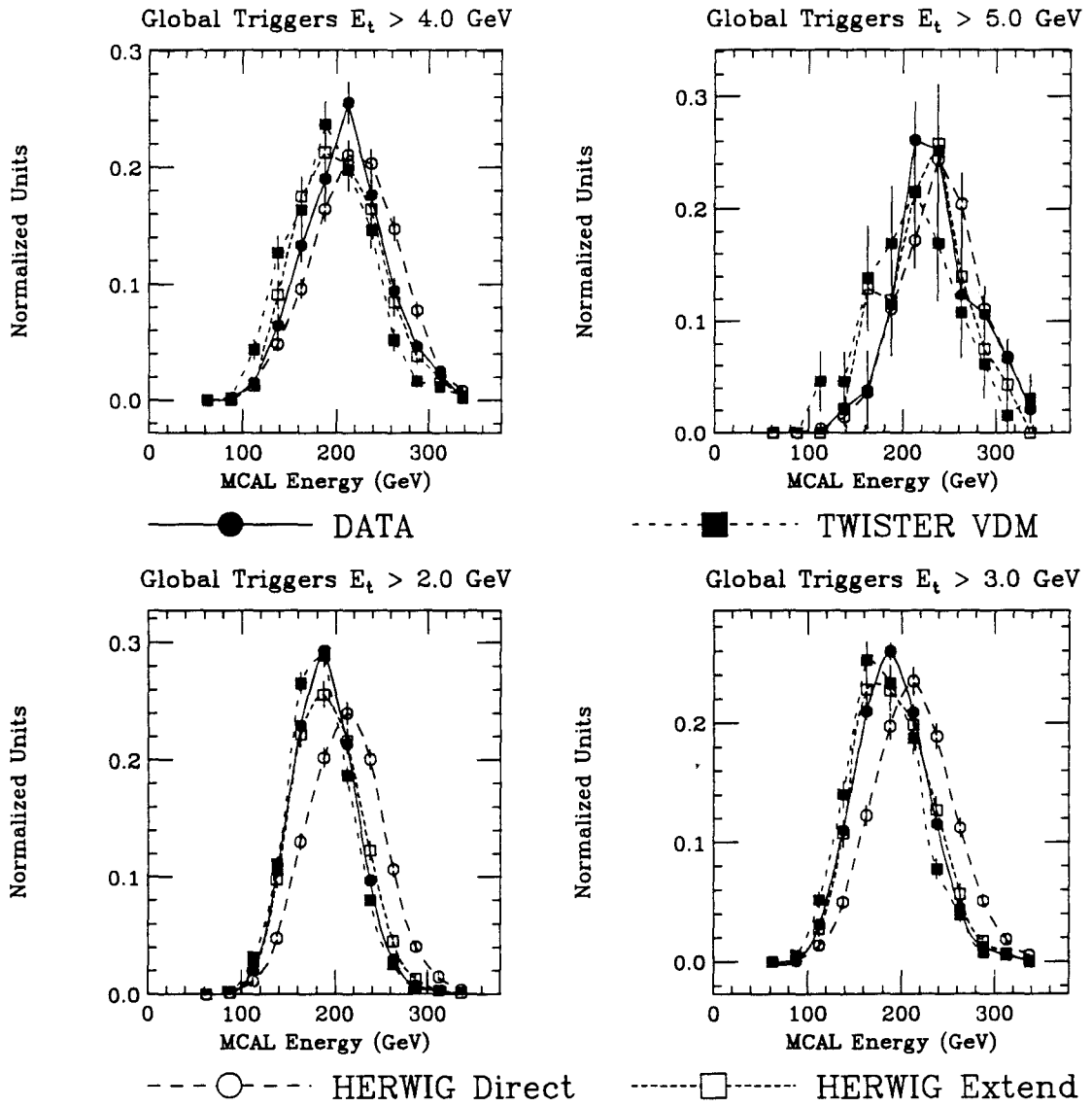

Figure 75: Shown is a comparison between the HERWIG Monte Carlo and data for Global triggers. The variable being displayed is the MCAL energy E_{MCAL} for different reconstructed jet thresholds. The thresholds apply to *both* jets and are listed on the plot, as are the meaning of the symbols used.

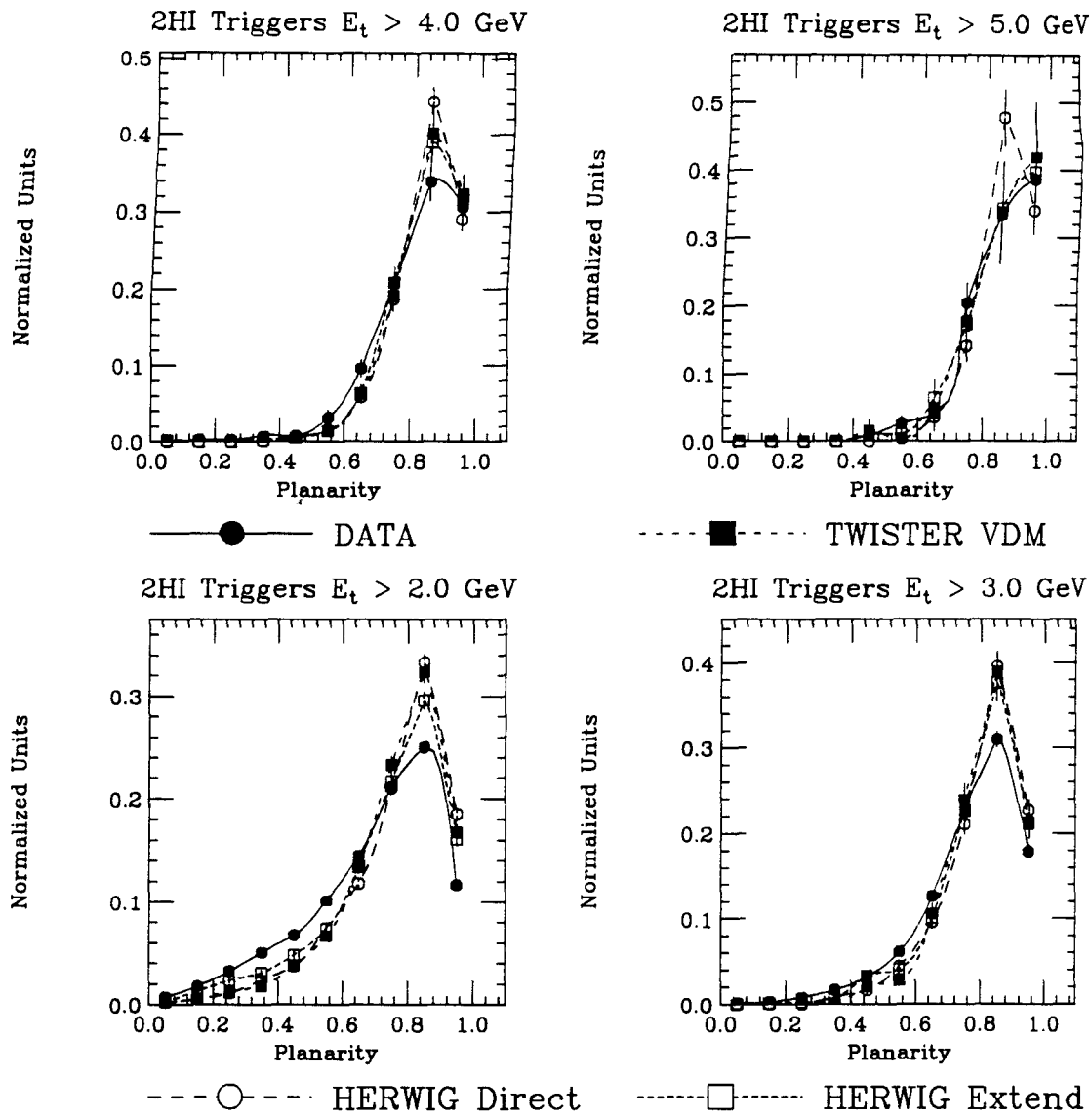

Figure 76: Shown is a comparison between the HERWIG Monte Carlo and data for 2HI triggers. The variable being displayed is the MCAL Planarity for different reconstructed jet thresholds. The thresholds apply to *both* jets and are listed on the plot, as are the meaning of the symbols used.

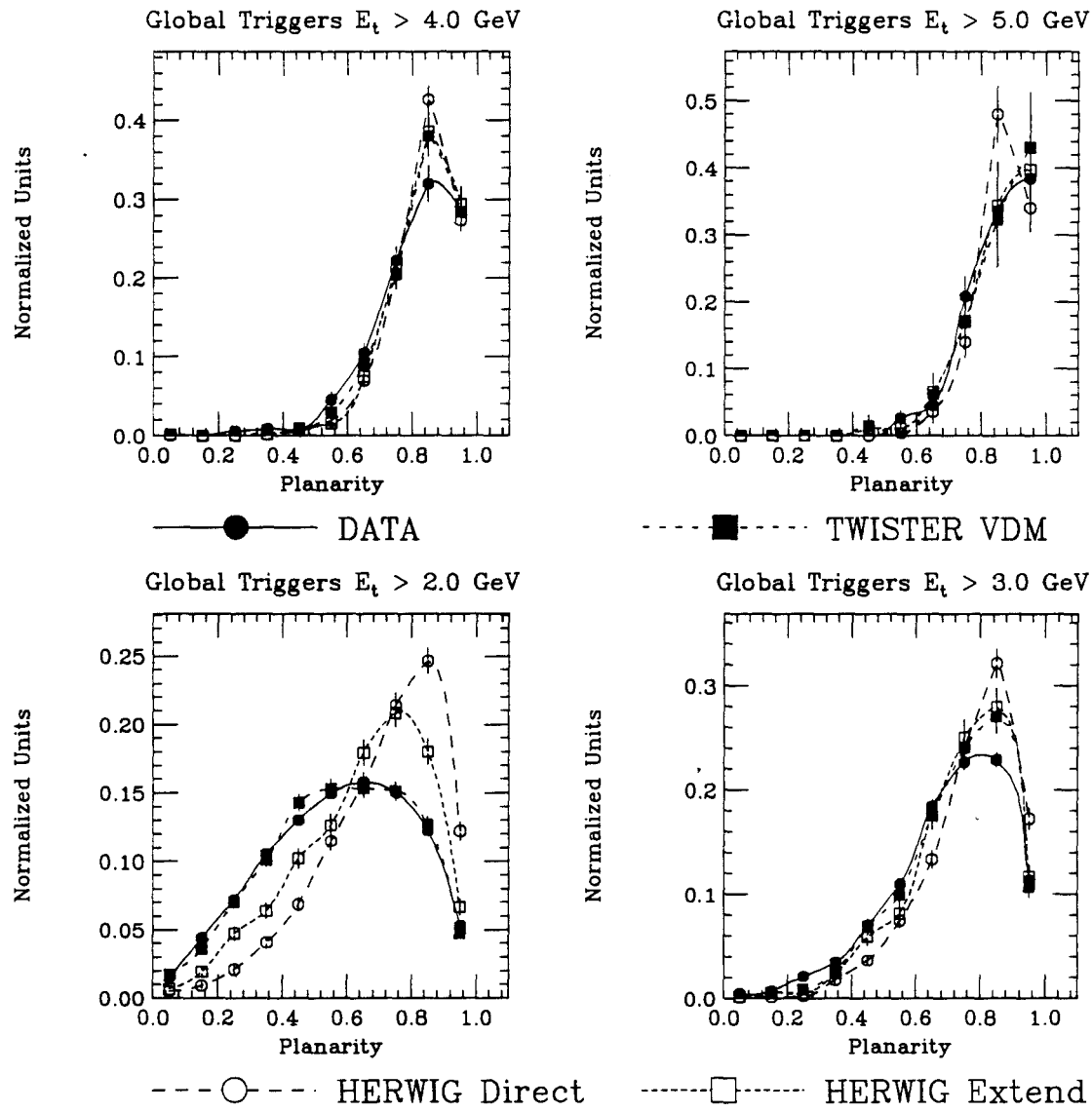

Figure 77: Shown is a comparison between the HERWIG Monte Carlo and data for Global triggers. The variable being displayed is the MCAL Planarity for different reconstructed jet thresholds. The thresholds apply to *both* jets and are listed on the plot, as are the meaning of the symbols used.

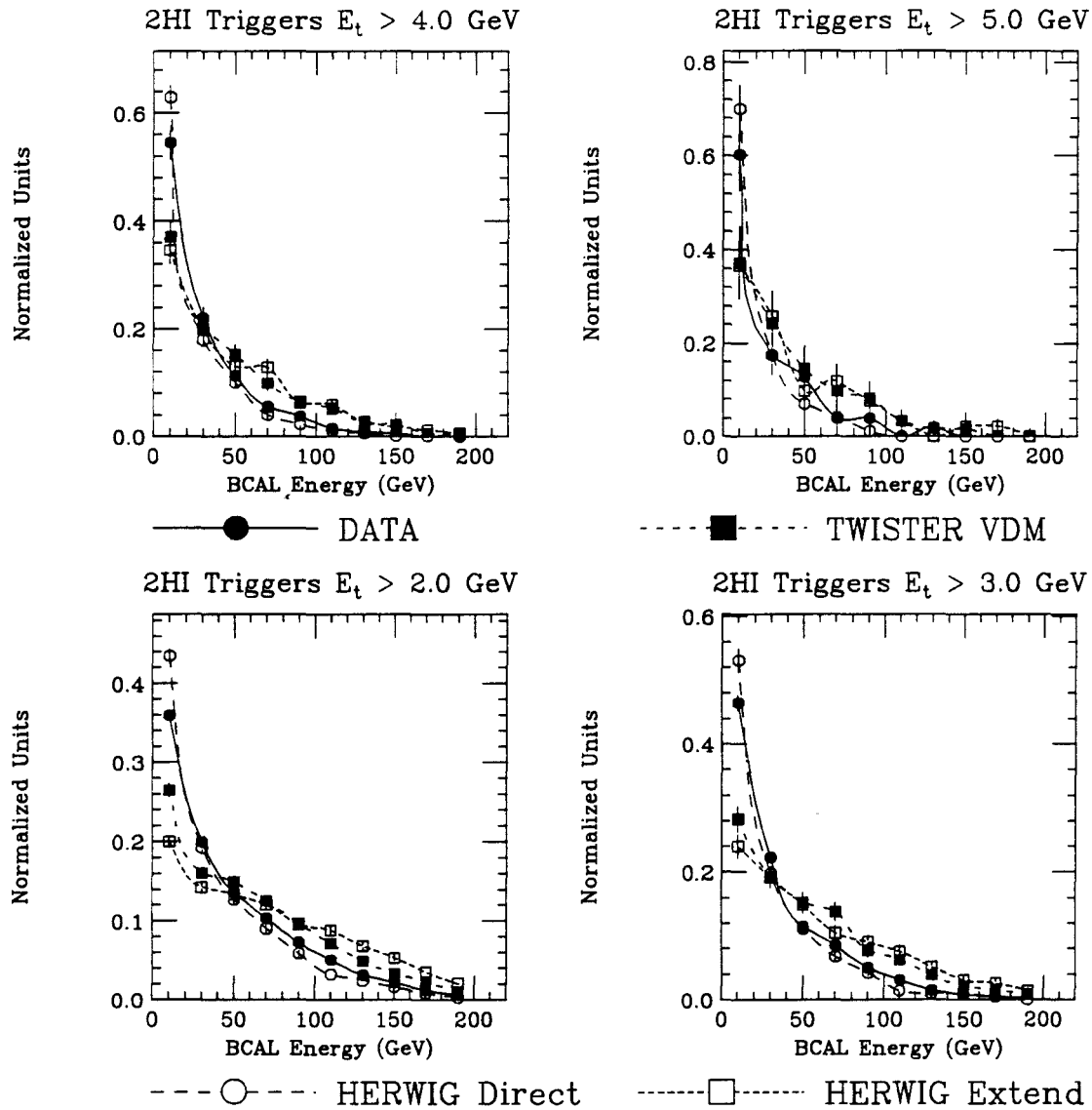

Figure 78: Shown is a comparison between the HERWIG Monte Carlo and data for 2HI triggers. The variable being displayed is the BCAL energy E_{BCAL} for different reconstructed jet thresholds. The thresholds apply to *both* jets and are listed on the plot, as are the meaning of the symbols used.

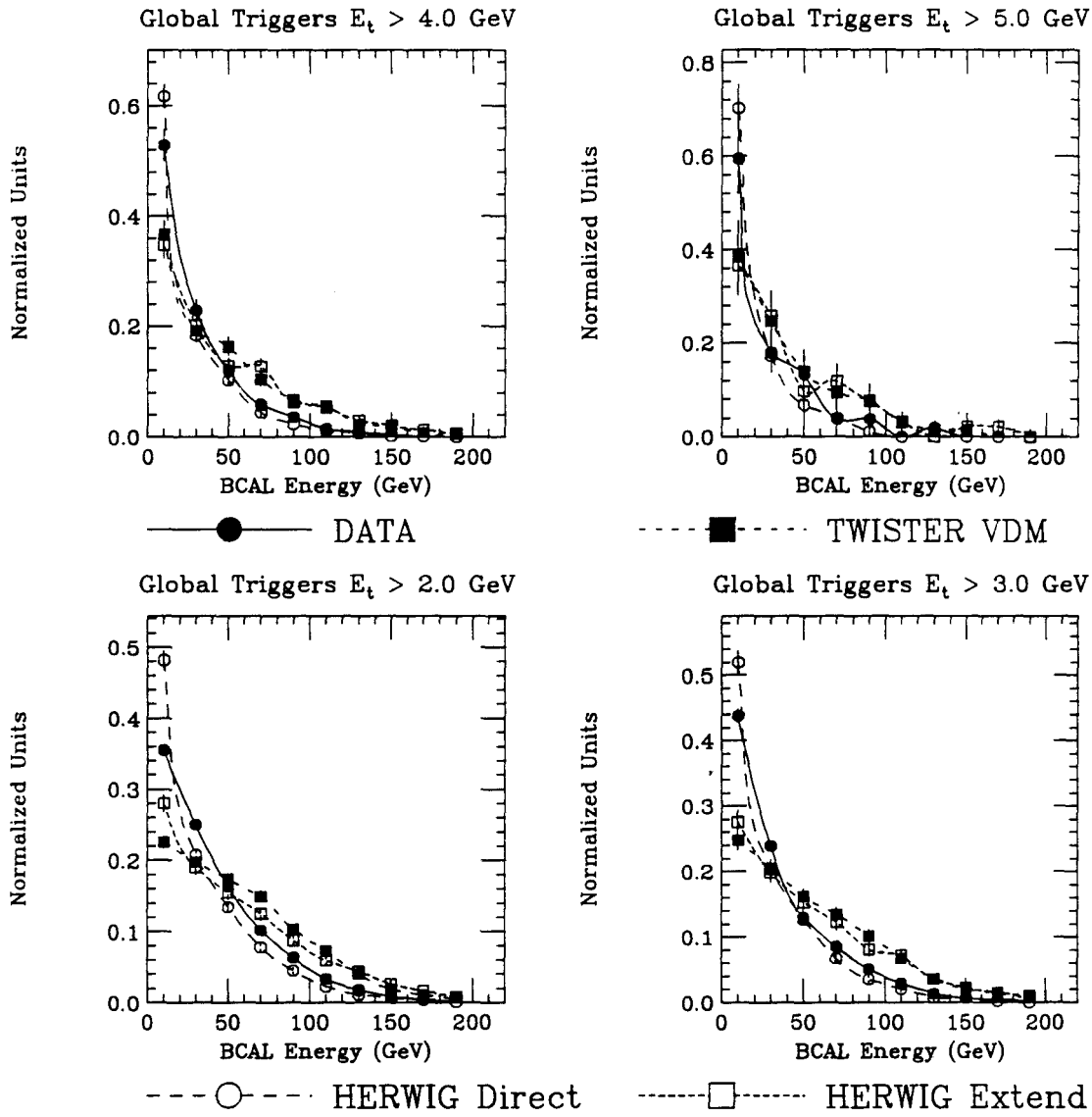

Figure 79: Shown is a comparison between the HERWIG Monte Carlo and data for Global triggers. The variable being displayed is the BCAL energy E_{BCAL} for different reconstructed jet thresholds. The thresholds apply to *both* jets and are listed on the plot, as are the meaning of the symbols used.

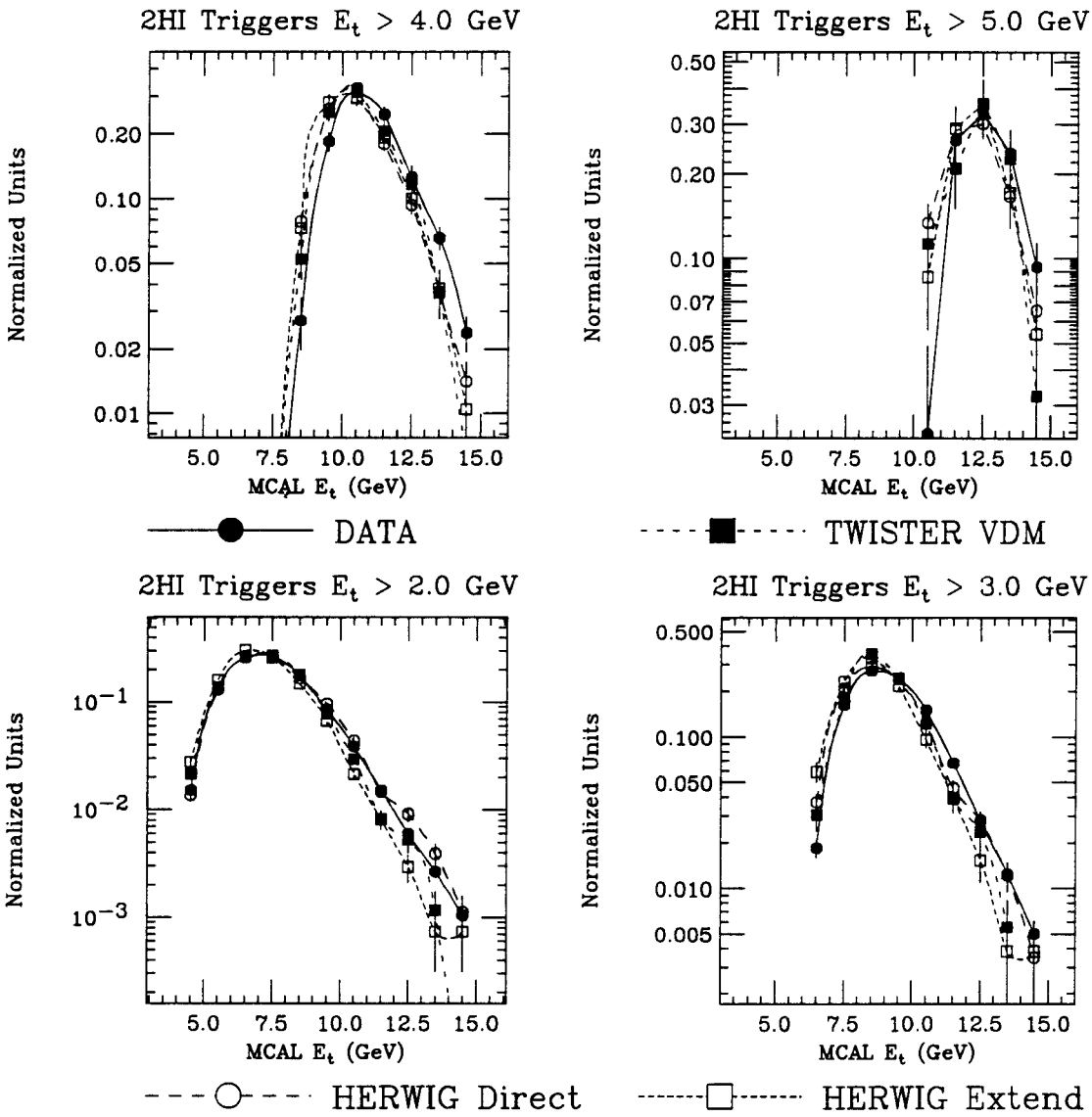

Figure 80: Shown is a comparison between the HERWIG Monte Carlo and data for 2HI triggers. The variable being displayed is the MCAL $E_\perp$ for different reconstructed jet thresholds. The thresholds apply to *both* jets and are listed on the plot, as are the meaning of the symbols used. Note that these plots are on logarithmic scales.

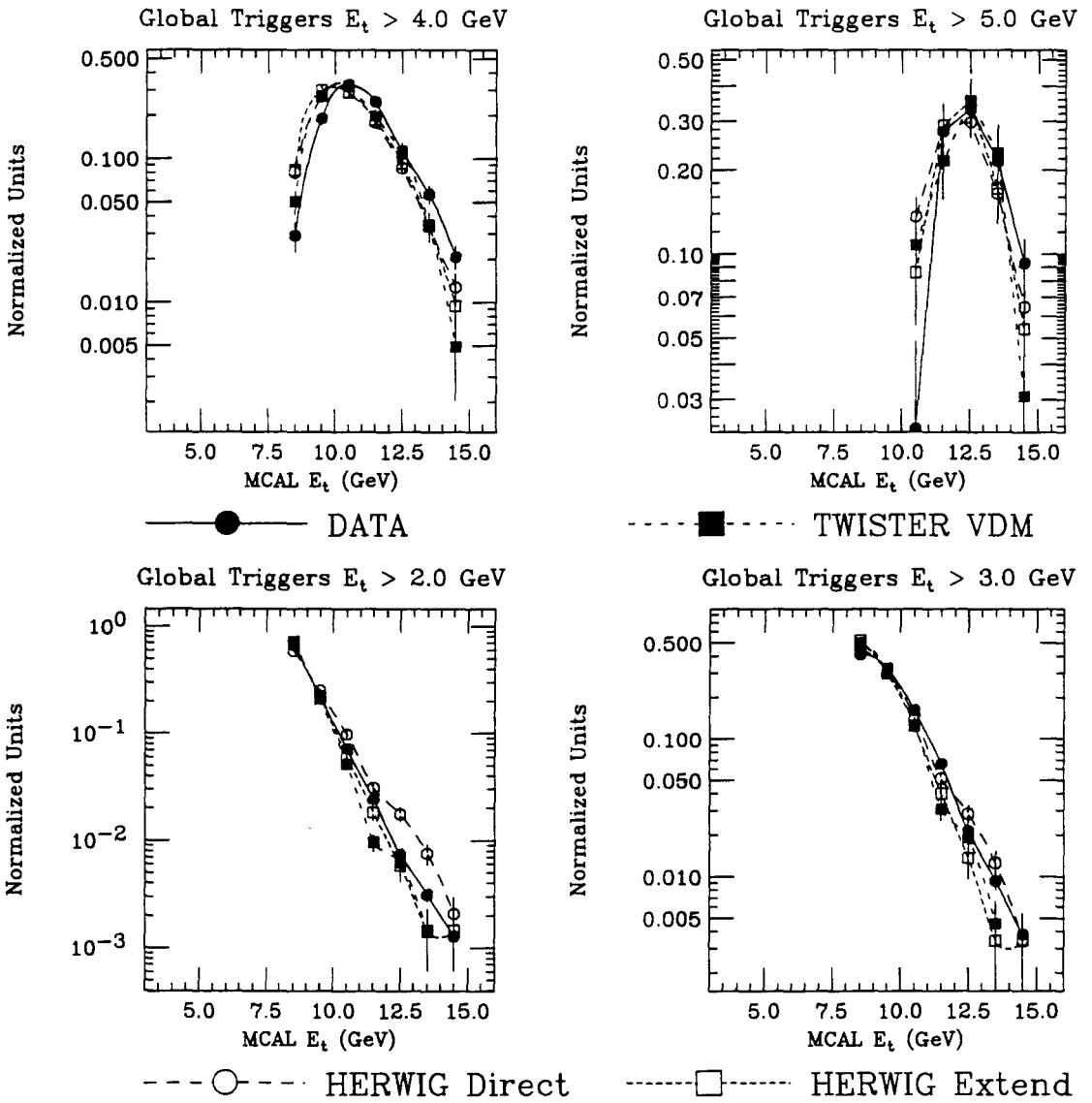

Figure 81: Shown is a comparison between the HERWIG Monte Carlo and data for Global triggers. The variable being displayed is the MCAL $E_\perp$ for different reconstructed jet thresholds. The thresholds apply to *both* jets and are listed on the plot, as are the meaning of the symbols used. Note that these plots are on logarithmic scales.

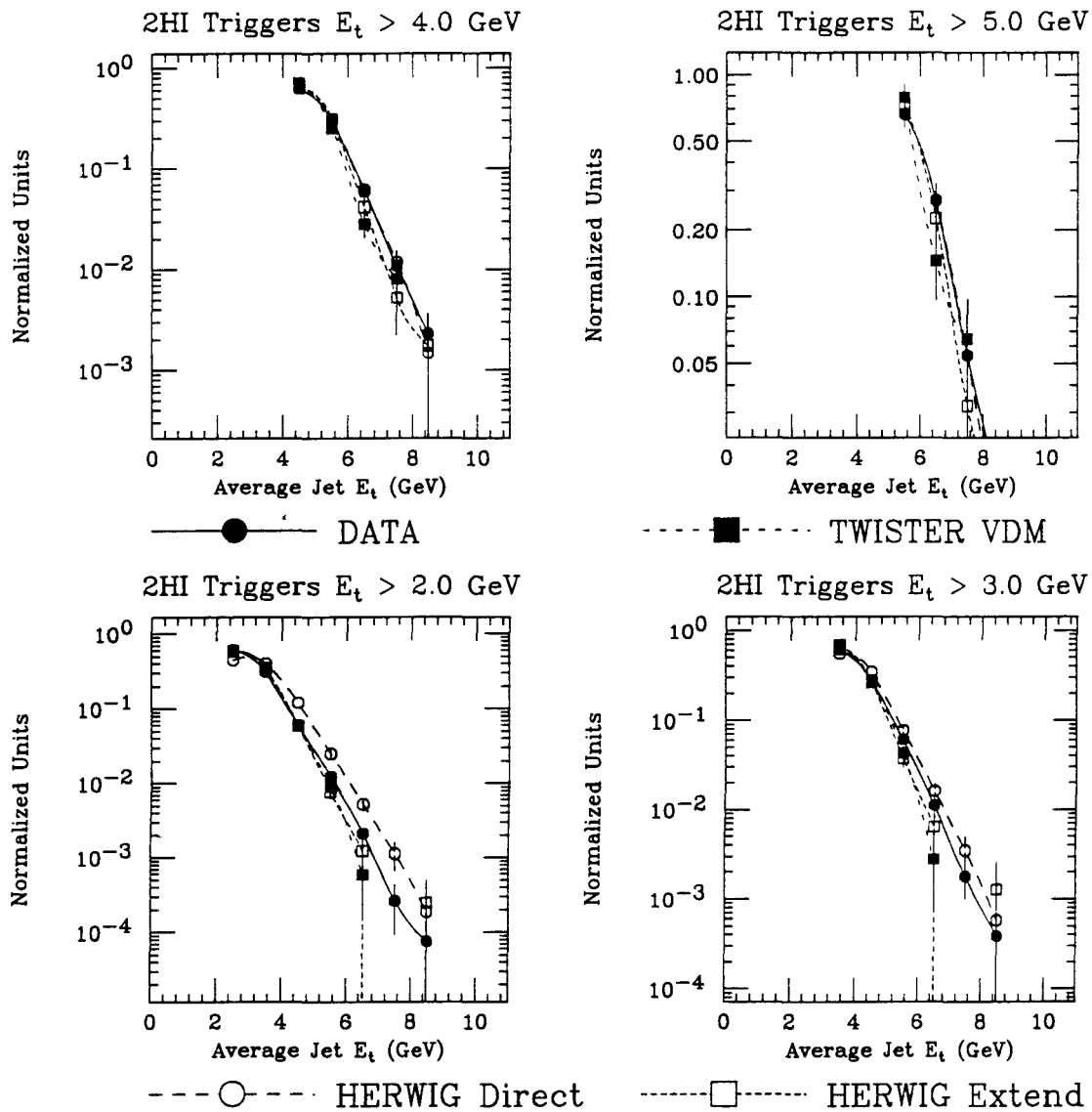

Figure 82: Shown is a comparison between the HERWIG Monte Carlo and data for 2HI triggers. The variable being displayed is the average jet $E_\perp$ for different reconstructed jet thresholds. The thresholds apply to *both* jets and are listed on the plot, as are the meaning of the symbols used. Note that these plots are on logarithmic scales.

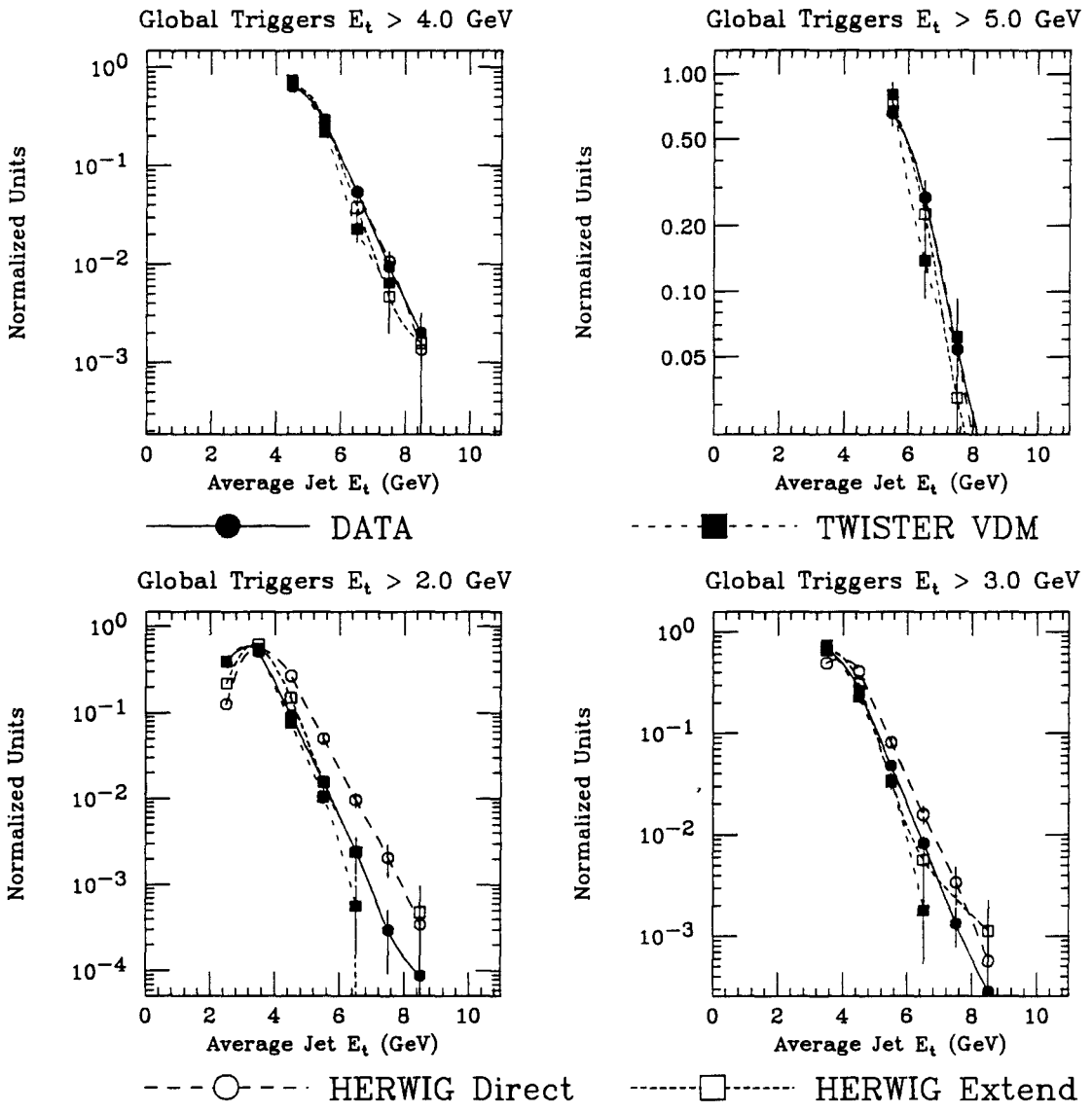

Figure 83: Shown is a comparison between the HERWIG Monte Carlo and data for Global triggers. The variable being displayed is the average jet $E_\perp$ for different reconstructed jet thresholds. The thresholds apply to *both* jets and are listed on the plot, as are the meaning of the symbols used. Note that these plots are on logarithmic scales.

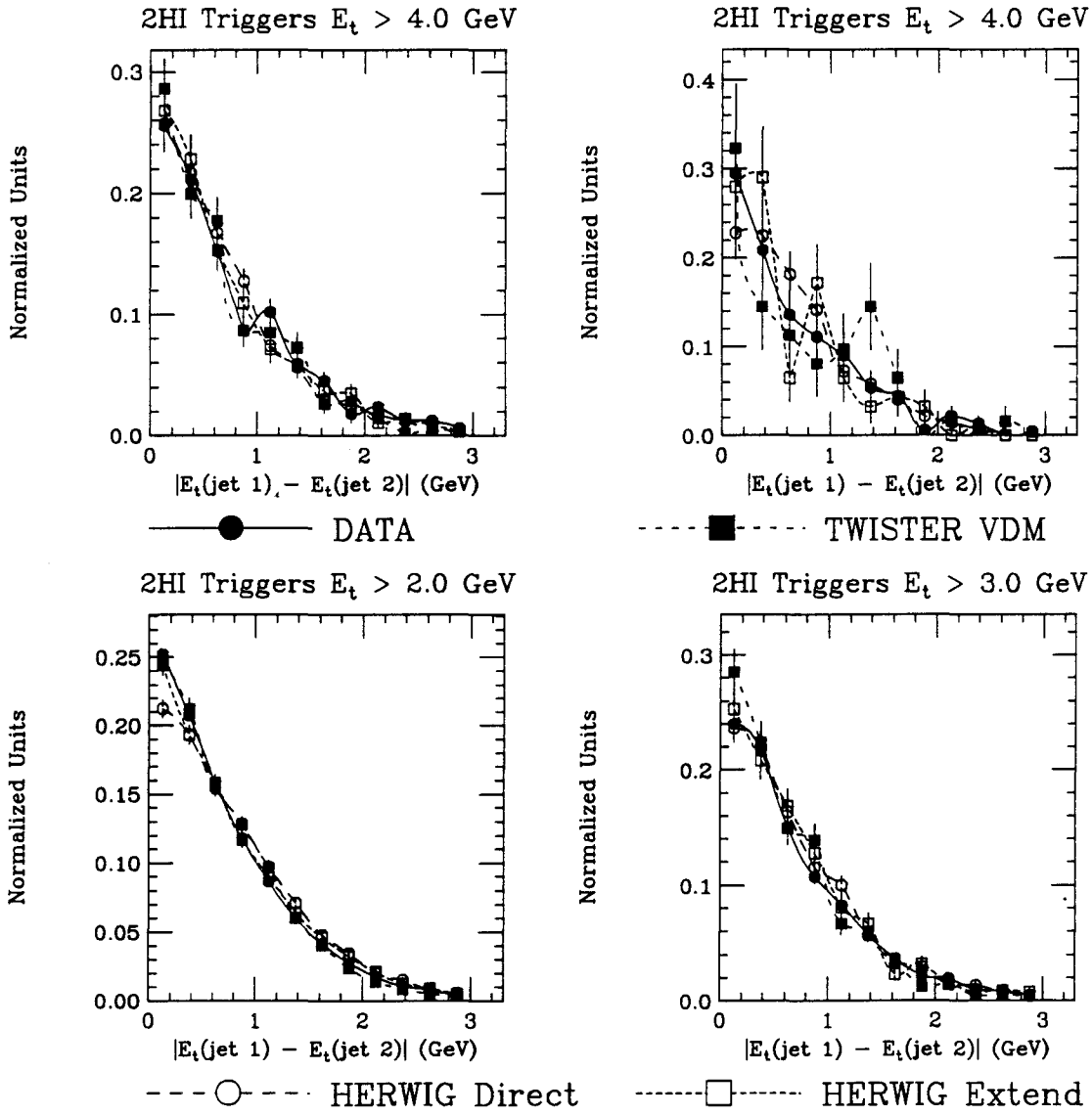

Figure 84: Shown is a comparison between the HERWIG Monte Carlo and data for 2HI triggers. The variable being displayed is $|E_\perp^{\text{jet1}} - E_\perp^{\text{jet2}}|$ for different reconstructed jet thresholds. The thresholds apply to *both* jets and are listed on the plot, as are the meaning of the symbols used.

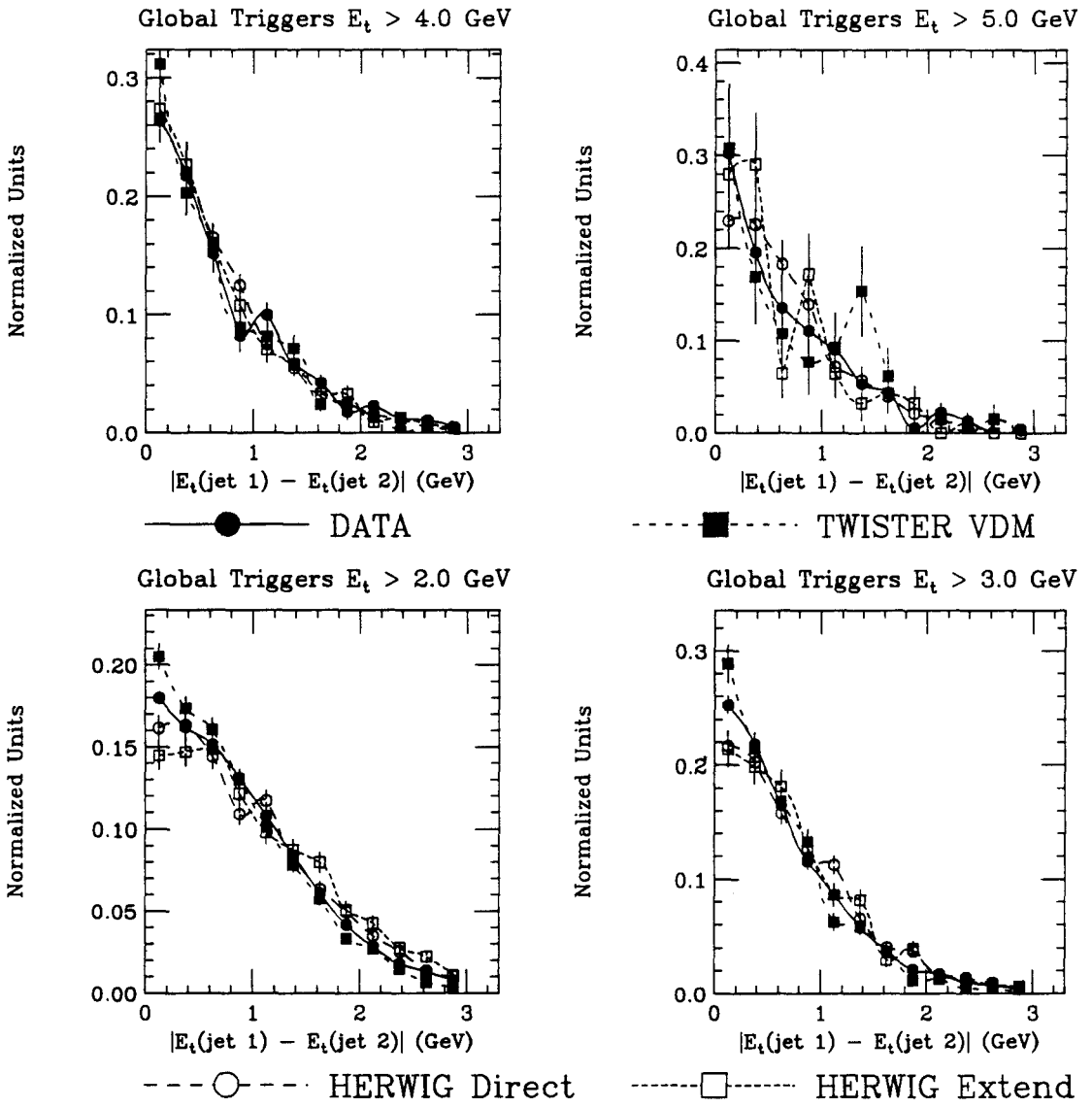

Figure 85: Shown is a comparison between the HERWIG Monte Carlo and data for Global triggers. The variable being displayed is $|E_\perp^{\text{jet1}} - E_\perp^{\text{jet2}}|$ for different reconstructed jet thresholds. The thresholds apply to *both* jets and are listed on the plot, as are the meaning of the symbols used.

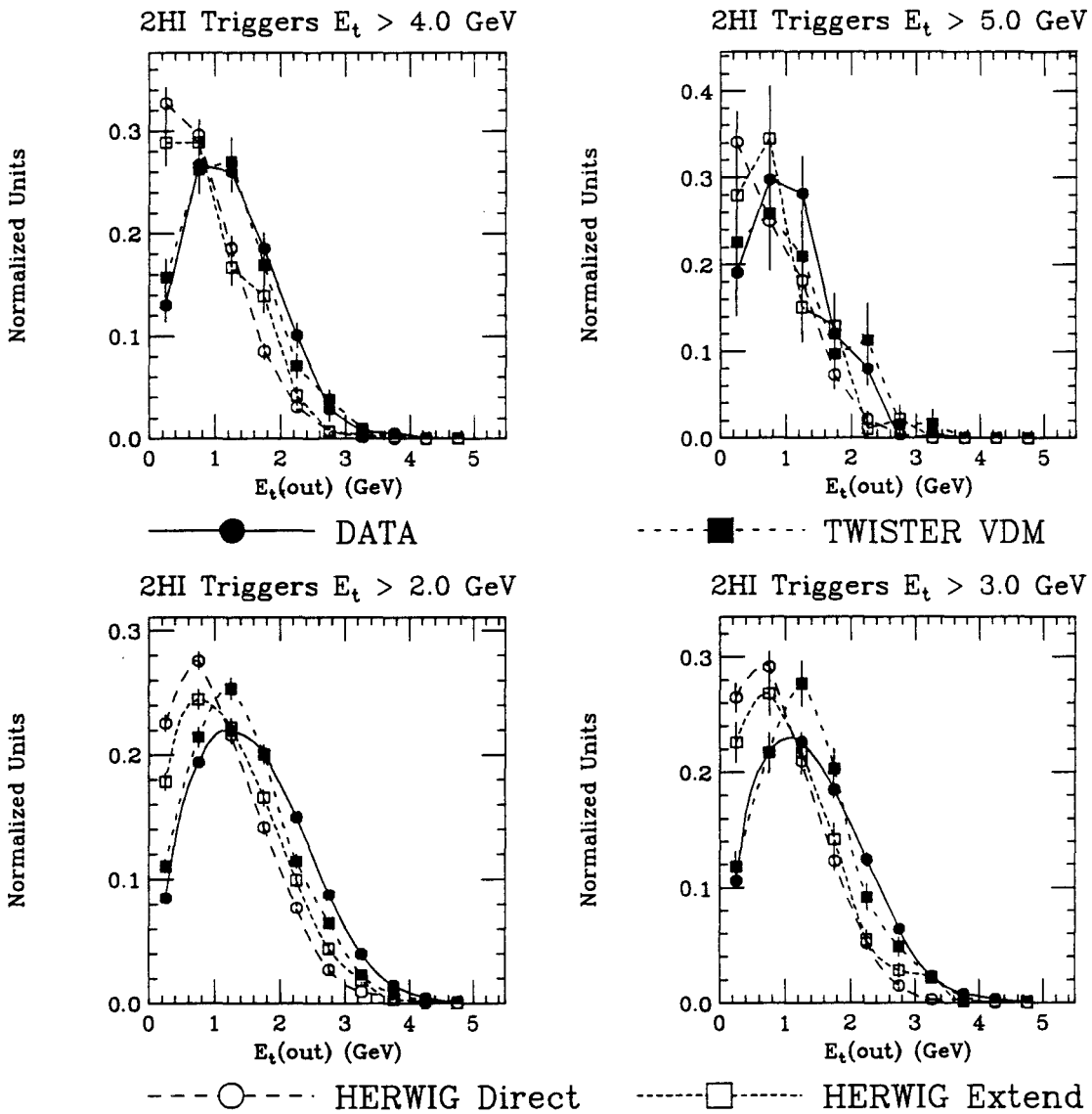

Figure 86: Shown is a comparison between the HERWIG Monte Carlo and data for 2HI triggers. The variable being displayed is MCAL $E_\perp$ not in the jet cone for different reconstructed jet thresholds. The thresholds apply to *both* jets and are listed on the plot, as are the meaning of the symbols used.

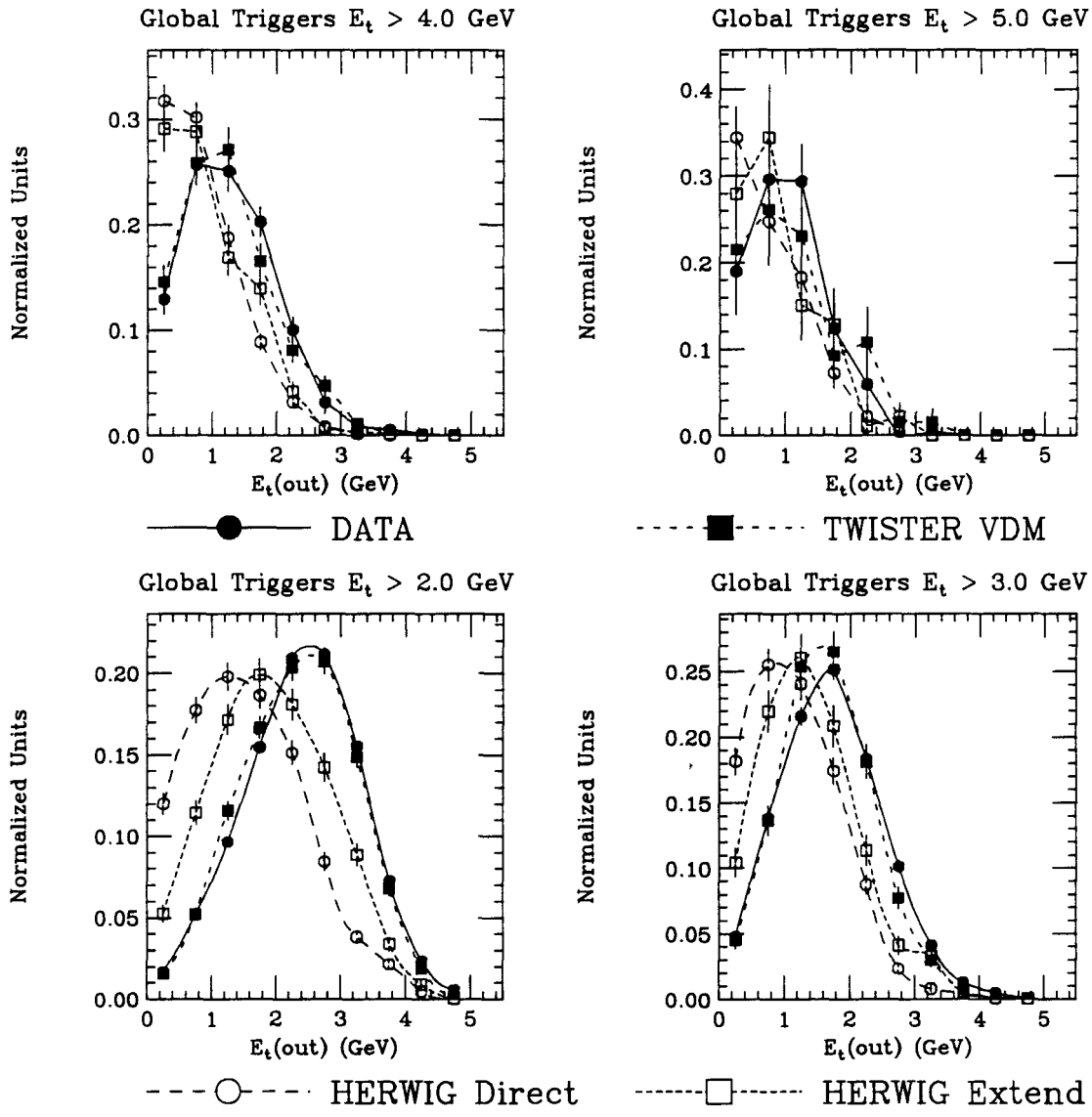

Figure 87: Shown is a comparison between the HERWIG Monte Carlo and data for Global triggers. The variable being displayed is MCAL $E_\perp$ not in the jet cone for different reconstructed jet thresholds. The thresholds apply to *both* jets and are listed on the plot, as are the meaning of the symbols used.

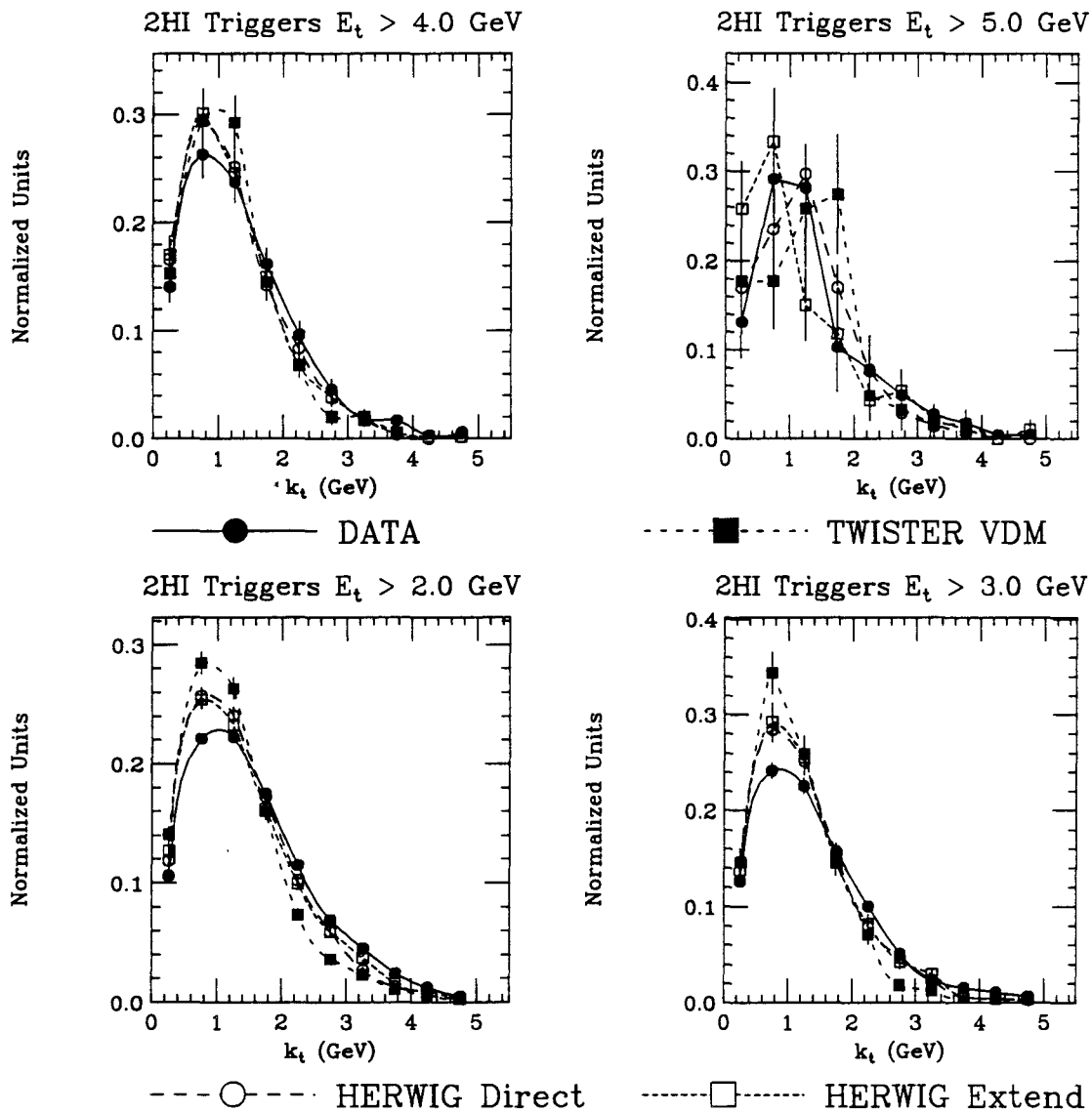

Figure 88: Shown is a comparison between the HERWIG Monte Carlo and data for 2HI triggers. The variable being displayed is $k_\perp$, as defined by equation (10), for different reconstructed jet thresholds. The thresholds apply to *both* jets and are listed on the plot, as are the meaning of the symbols used.

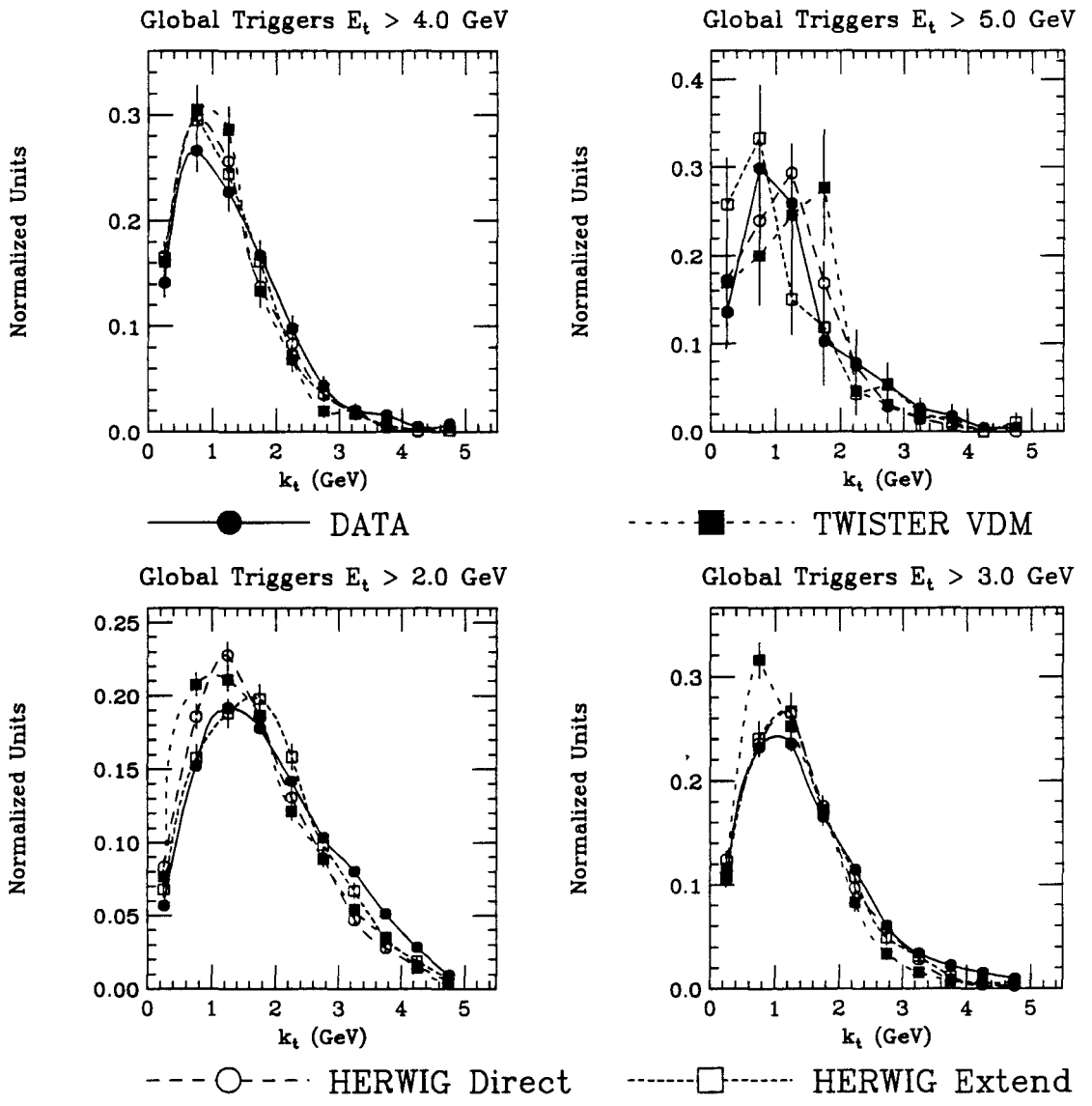

Figure 89: Shown is a comparison between the HERWIG Monte Carlo and data for Global triggers. The variable being displayed is $k_\perp$, as defined by equation (10), for different reconstructed jet thresholds. The thresholds apply to *both* jets and are listed on the plot, as are the meaning of the symbols used.

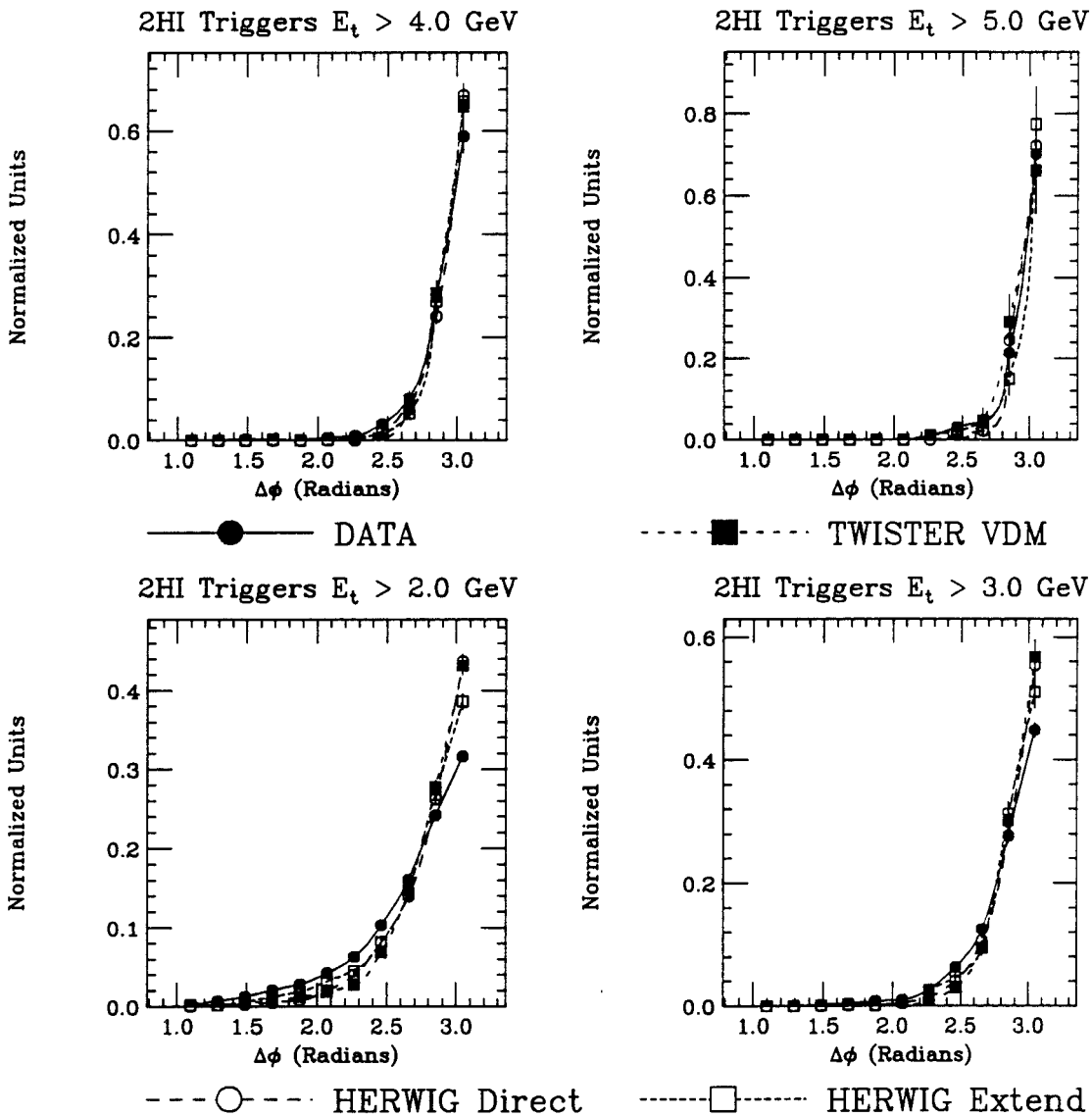

Figure 90: Shown is a comparison between the HERWIG Monte Carlo and data for 2HI triggers. The variable being displayed is $\Delta\phi$ between the two jets for different reconstructed jet thresholds. The thresholds apply to *both* jets and are listed on the plot, as are the meaning of the symbols used.

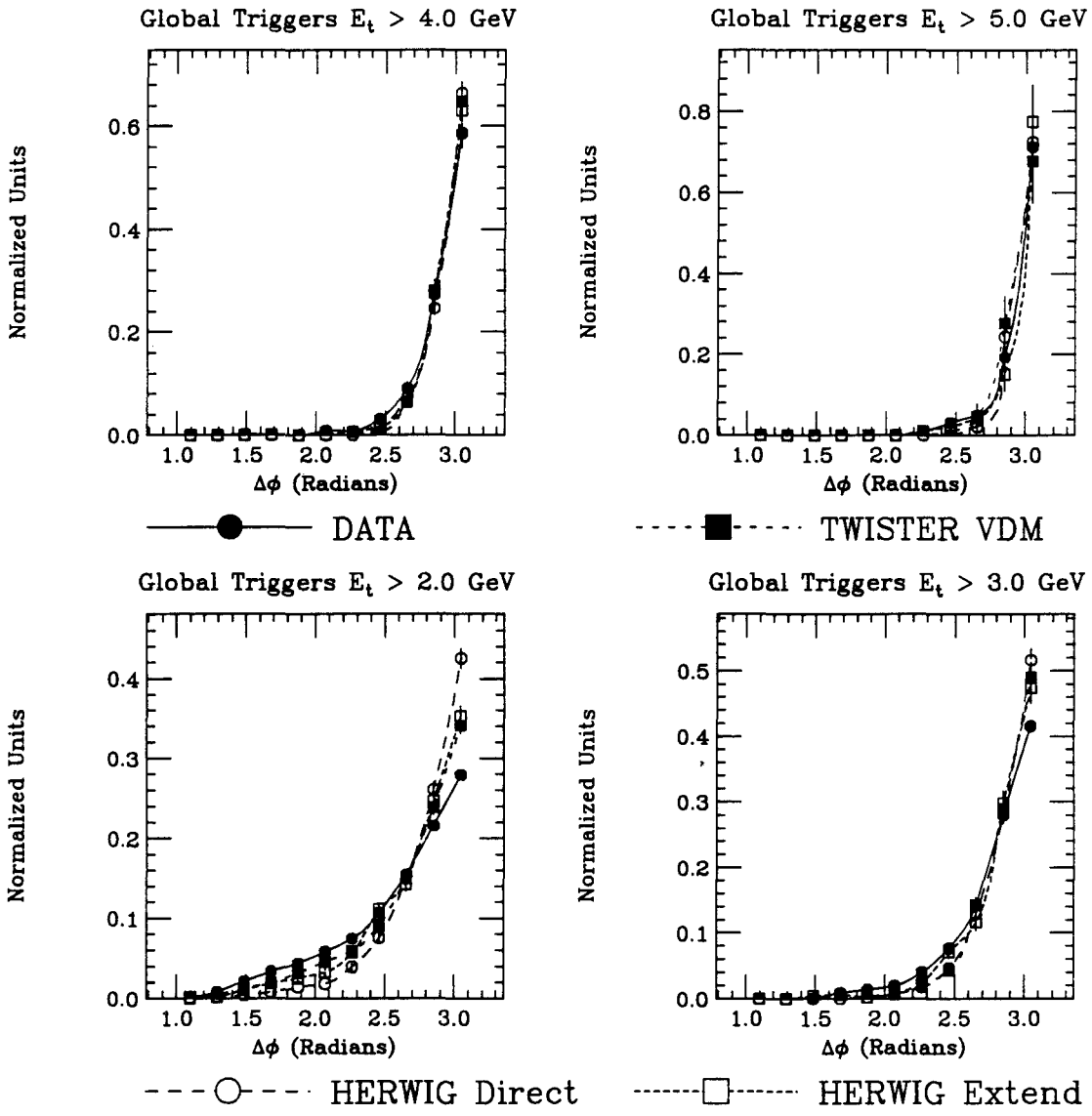

Figure 91: Shown is a comparison between the HERWIG Monte Carlo and data for Global triggers. The variable being displayed is $\Delta\phi$ between the two jets for different reconstructed jet thresholds. The thresholds apply to *both* jets and are listed on the plot, as are the meaning of the symbols used.

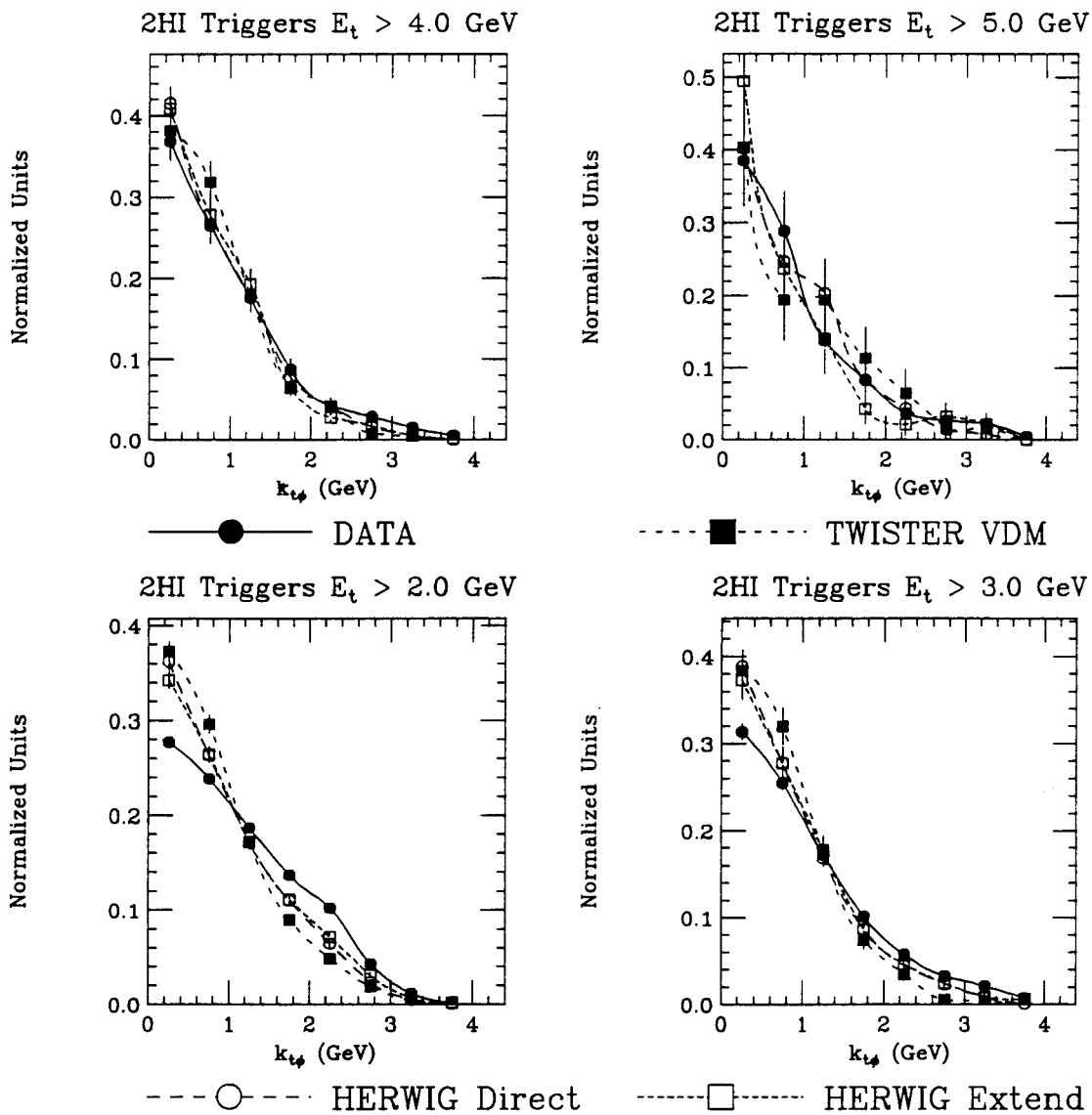

Figure 92: Shown is a comparison between the HERWIG Monte Carlo and data for 2HI triggers. The variable being displayed is $k_{\perp\phi}$, as defined by equation (11), for different reconstructed jet thresholds. The thresholds apply to *both* jets and are listed on the plot, as are the meaning of the symbols used.

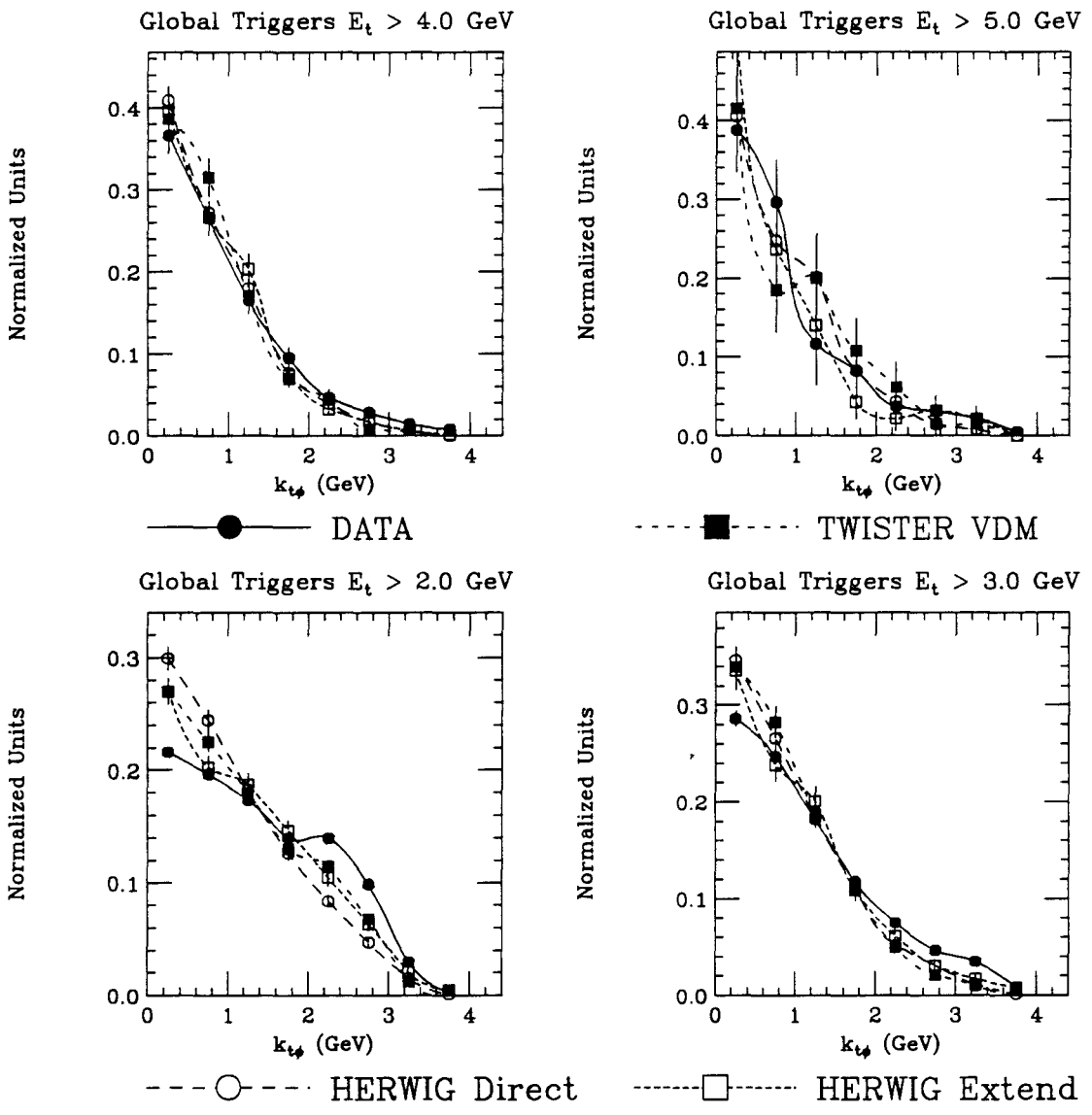

Figure 93: Shown is a comparison between the HERWIG Monte Carlo and data for Global triggers. The variable being displayed is $k_{\perp\phi}$, as defined by equation (11), for different reconstructed jet thresholds. The thresholds apply to *both* jets and are listed on the plot, as are the meaning of the symbols used.

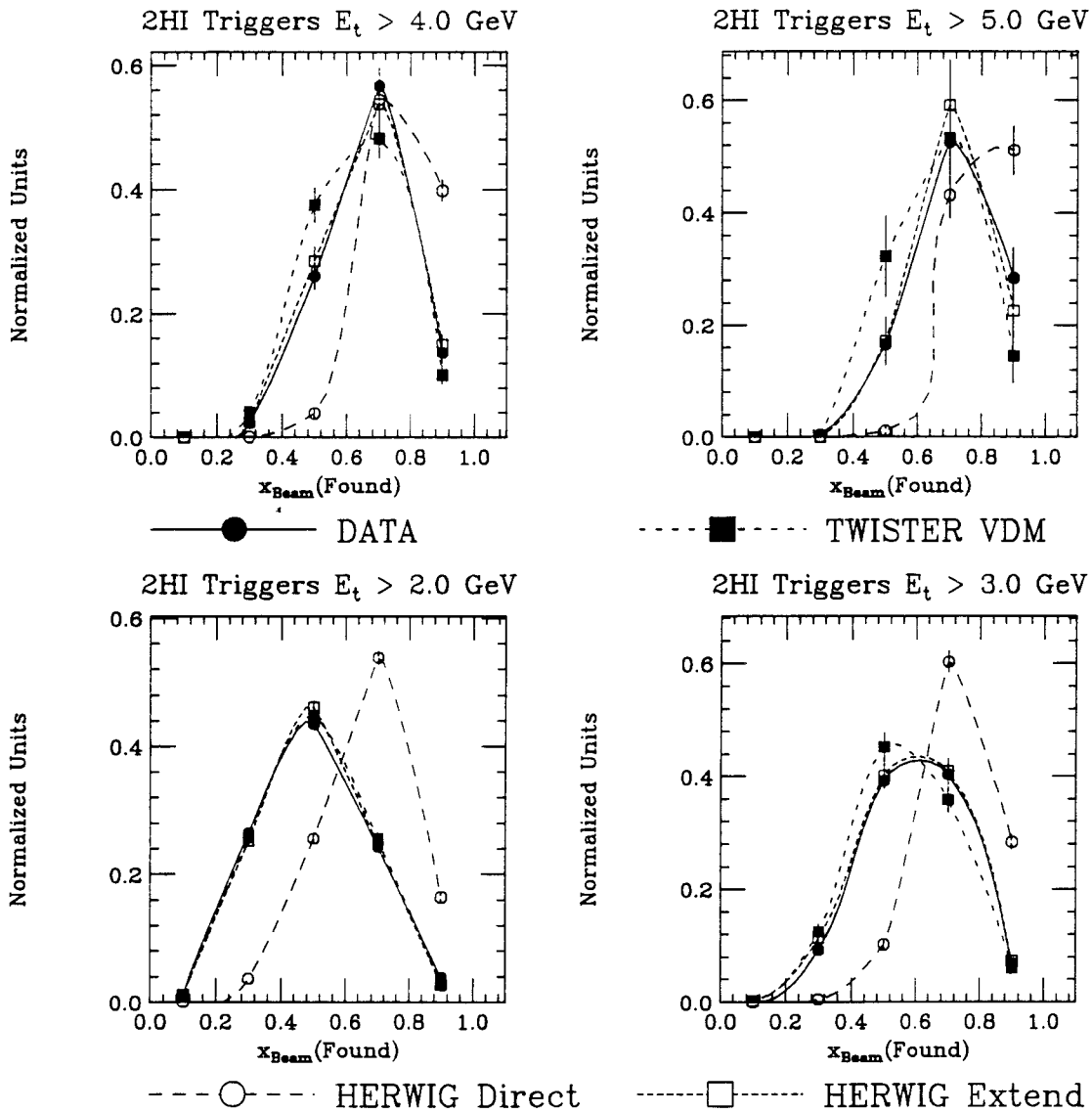

Figure 94: Shown is a comparison between the HERWIG Monte Carlo and data for 2HI triggers. The variable being displayed is x_{BEAM}, as defined by equation (9) and reconstructed jet kinematics, for different reconstructed jet thresholds. The thresholds apply to *both* jets and are listed on the plot, as are the meaning of the symbols used.

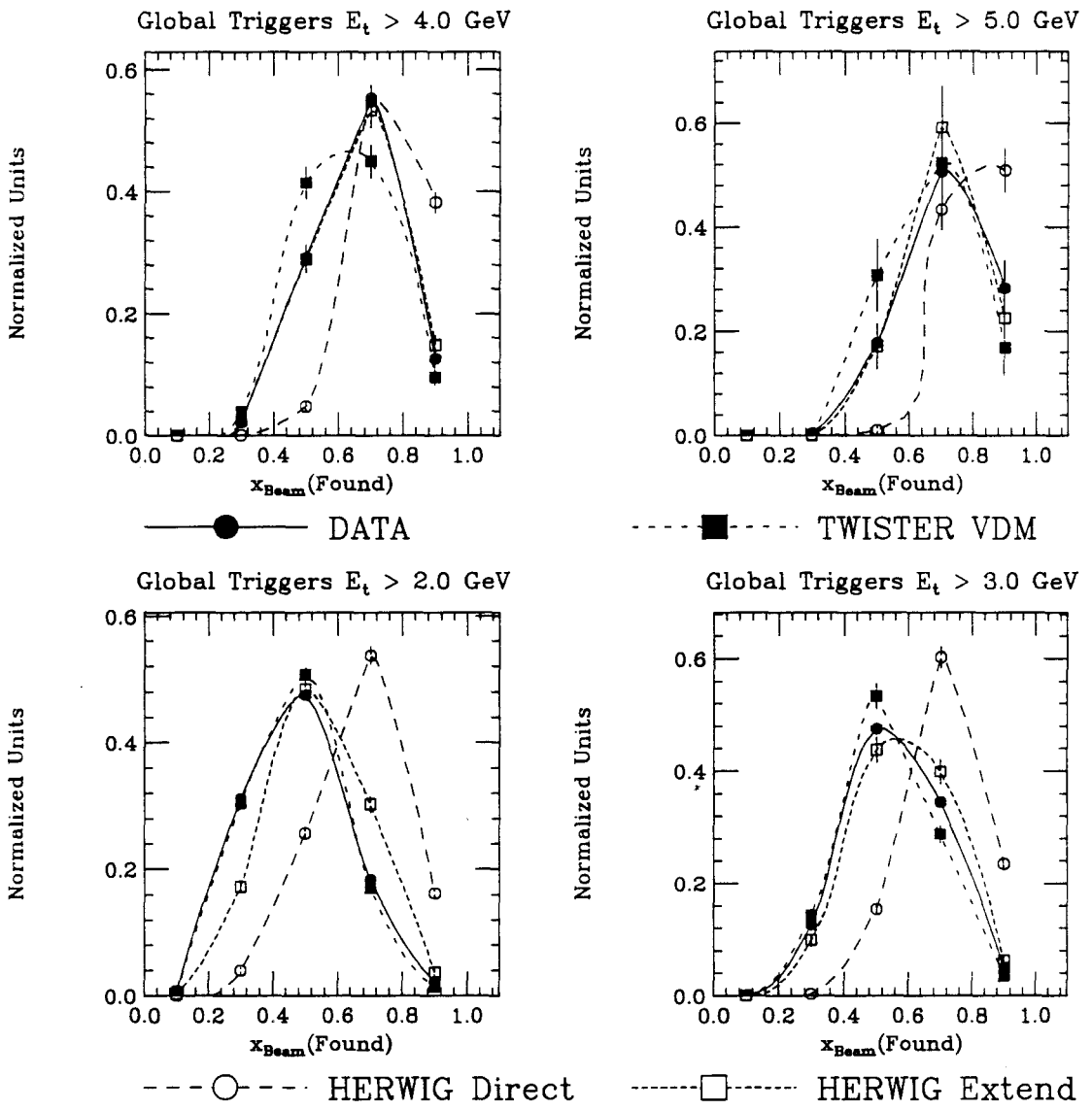

Figure 95: Shown is a comparison between the HERWIG Monte Carlo and data for Global triggers. The variable being displayed is x_{BEAM}, as defined by equation (9) and reconstructed jet kinematics, for different reconstructed jet thresholds. The thresholds apply to *both* jets and are listed on the plot, as are the meaning of the symbols used.

Such a huge number of plots must obviously be absorbed slowly, but many things can be easily seen. To start with, there are plots that do not distinguish between the different photon types. An example of this is the E_γ plots, which look much the same for all Monte Carlo runs and the data. While the Monte Carlo gets the correct *triggered* E_γ distribution by construction, there is no fundamental reason why it must be correct for reconstructed jet data. In fact, for the lowest jet thresholds, the two different trigger types are caused by photons from slightly different energy distributions.

However, other plots do distinguish between various photon types. For instance, for the low jet $E_\perp$ thresholds the direct photon is excluded in plots like MCAL planarity (especially for 2HI triggers,) or the $E_\perp$ out of the jet cone for Global triggers.

A very interesting observation to be made is the evolution of data/Monte Carlo agreement as jet $E_\perp$ thresholds are varied. While the various distributions can be quite different for the low $E_\perp$ thresholds, they become more alike as the thresholds are raised. This could be interpreted as the cuts starting to force the shapes of the observed distributions. Such an effect must occur at some level, but is probably not the entire cause.

A related observation is the fact that while at a jet threshold of $E_\perp > 2$ GeV, the two trigger types often yield very different shapes, by the time the jet threshold has been raised to $E_\perp > 4$ GeV, the shapes are generally identical. This stems from an interplay between the definitions of the various triggers and between the jet thresholds:

1. The Global threshold requires an MCAL Global $E_\perp$ exceeding 8 GeV.

2. The 2HI threshold requires two towers both with an $E_\perp$ exceeding 0.75 GeV.

3. Two jets are required, both must exceed an $E_\perp$ of 4 GeV.

If one starts with a 2HI trigger sample, requirement (3) above requires a minimum of 8 GeV $E_\perp$ in the MCAL, which is synonymous with the Global trigger. If one starts with a Global trigger, the effect is not as blatant. However, a requirement of 4 GeV $E_\perp$ in a jet makes it likely that there is at least one hot tower under the jet cone,

which often exceeds 0.75 GeV. This is the reason for the increased overlap between the two trigger types at high $E_\perp$ thresholds for the reconstructed jets.

9.5 Data/Monte Carlo $E_\perp$ Flow Comparison

In principle, this comparison could easily be tucked in the previous section. However, since there is a new twist in some of the plots, I shall present them separately.

An $E_\perp$ flow plot is generally generated in the following way. Two jets are found above some threshold algorithm (e.g. both jets above an $E_\perp$ threshold, or both jets above a threshold, with the average $E_\perp$ of the two jets above a more stringent threshold, etc.) The direction of one of the jets (typically the one with the higher $E_\perp$) is chosen to be the base direction. The azimuthal angle of each tower (or particle) measured from that point is determined and an entry is placed in a histogram with a weight equal to the $E_\perp$ of the tower. After many events are processed in this manner, a shape emerges that illustrates the average event topology. I discuss figure (96) in a general way to give the reader an idea of what the distribution teaches us.

To begin with, there is a concentration of $E_\perp$ both at 0 and π radians. This is consistent with the signature expected from jet production (i.e. two partons exiting a collision with an azimuthal separation of approximately 180°.) Also, the peak at π radians appears less pronounced than the one at 0. An obvious conclusion that can be drawn is that the softer jet is less collimated and more spread out. While obvious, that conclusion is wrong. If the softer jet is used to define the origin, it also gives a more pronounced peak. The actual mechanism for the broadening of the π peak is the variation in $\Delta\phi$ event to event. Recall that the distribution is an ensemble of many events. For any particular event, there is an azimuthal angle between the jets that is different than π radians. If two identical jets were entered into a histogram, with the only difference between consecutive events being a variation in azimuthal angle, the resultant would be an $E_\perp$ plot with a smeared out peak at π radians.

In figures (96-107) I present the $E_\perp$ flow data/Monte Carlo comparison. The plots are separated into 2HI and Global triggers and are separated by Monte Carlo type. In order to be able to compare the Monte Carlo with the data, I have presented each

Monte Carlo separately. While bulky, this approach makes the comparison easier. As one would expect, after the results of the previous section, the low $E_\perp$ thresholds have poorer agreement between the data and the Monte Carlo. Also, low jet $E_\perp$ Global triggers have more overall $E_\perp$ than the 2HI triggers, but it is distributed such that the two peaks are more smeared out. By the time the jet threshold reaches 4 GeV, the differences are much less marked.

As you might recall, in section (8.1), it was suggested that the $E_\perp$ flow plot might be able to distinguish between different ideas about the $k_\perp$'s of the scattering partons. However, in section (8) I also showed the difficulties associated in understanding the second jet caused by the $k_\perp$ if it is there. For that reason, I also explore a '1 jet' $E_\perp$ flow plot. For this plot, I insist that there be at least one jet (although there may be more) and use the direction of the first jet found to define the origin. Since it appears that the first jet found appears to be unambiguous (i.e. according to the Monte Carlo the first jet found corresponds to both a 'hard scatter' and a 'high $p_\perp$' parton) it is expected that any possible biases caused by inclusion of the underlying event underneath the second jet cone will be avoided. I present in figures (108-113) these distributions. Note that unlike previous distributions, both triggers are included in these plots. While similar to the previous $E_\perp$ plots, the data always has a suppressed peak at π radians, compared to the $E_\perp$ flow plots which have two reconstructed jets required. This does lend support to the idea that the choice of triggers and jet reconstruction cuts is quite restrictive and is an important factor in determining the shapes of the distributions that have been presented.

9.6 Predicted Ratios of Direct and Extended Photons

A natural question to be posed to an experiment like E683 with a beam that has different aspects (direct photon, extended photon, VDM) is: 'What are the various fractions of the different beam particle types present in your data?' One way to ascertain this is to take a particular distribution (say the MCAL energy distribution) and determine the shape that (say) direct photons produce. If one determines the shape of the MCAL energy distribution of the extended photon and it is found to be

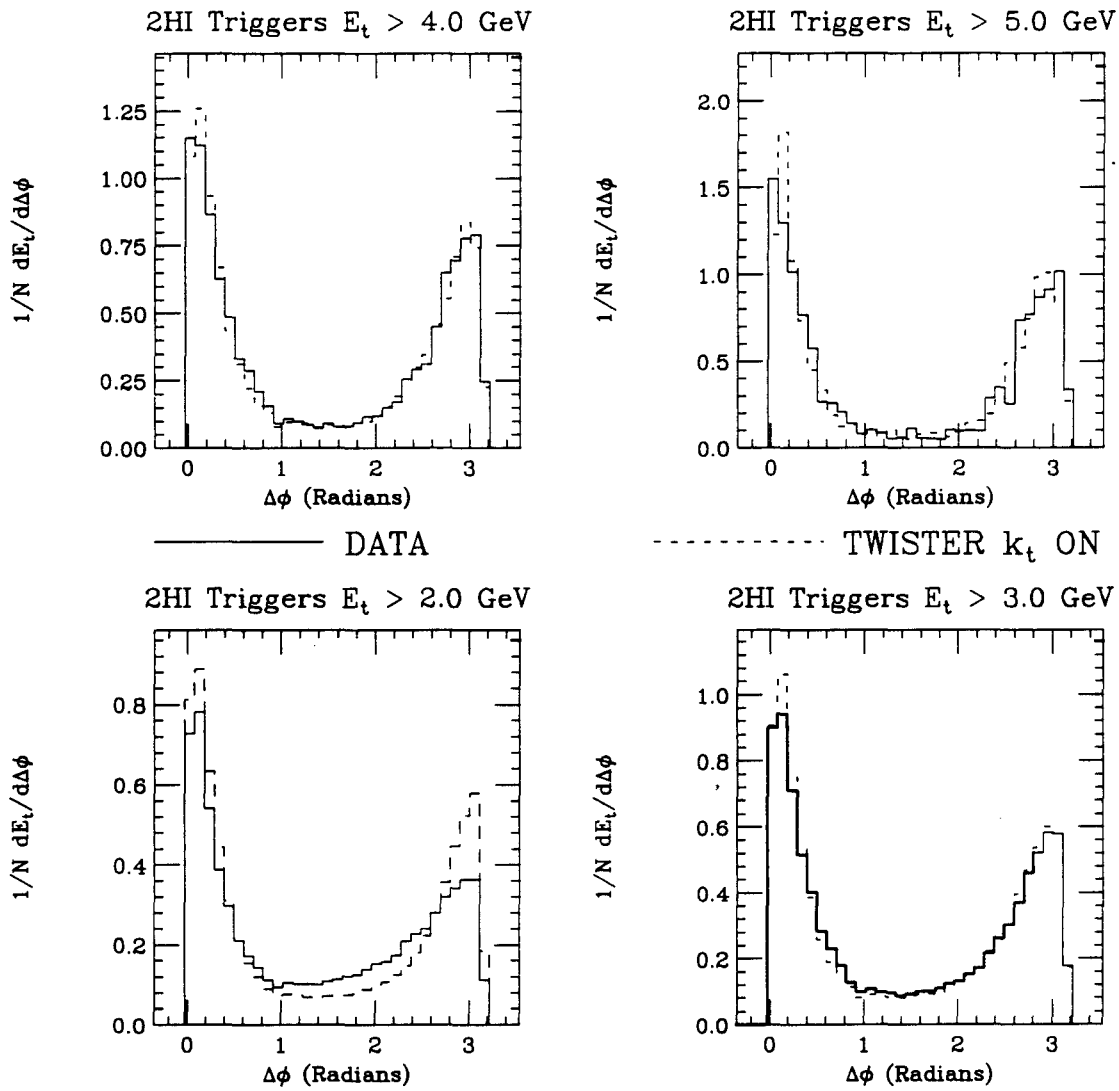

Figure 96: Shown is a comparison between TWISTER $k_\perp$ ON and data for 2HI triggers. The distribution being displayed is $E_\perp$ flow plot, for different reconstructed jet thresholds. The thresholds apply to *both* jets and are listed on the plot, as are the meaning of the lines used.

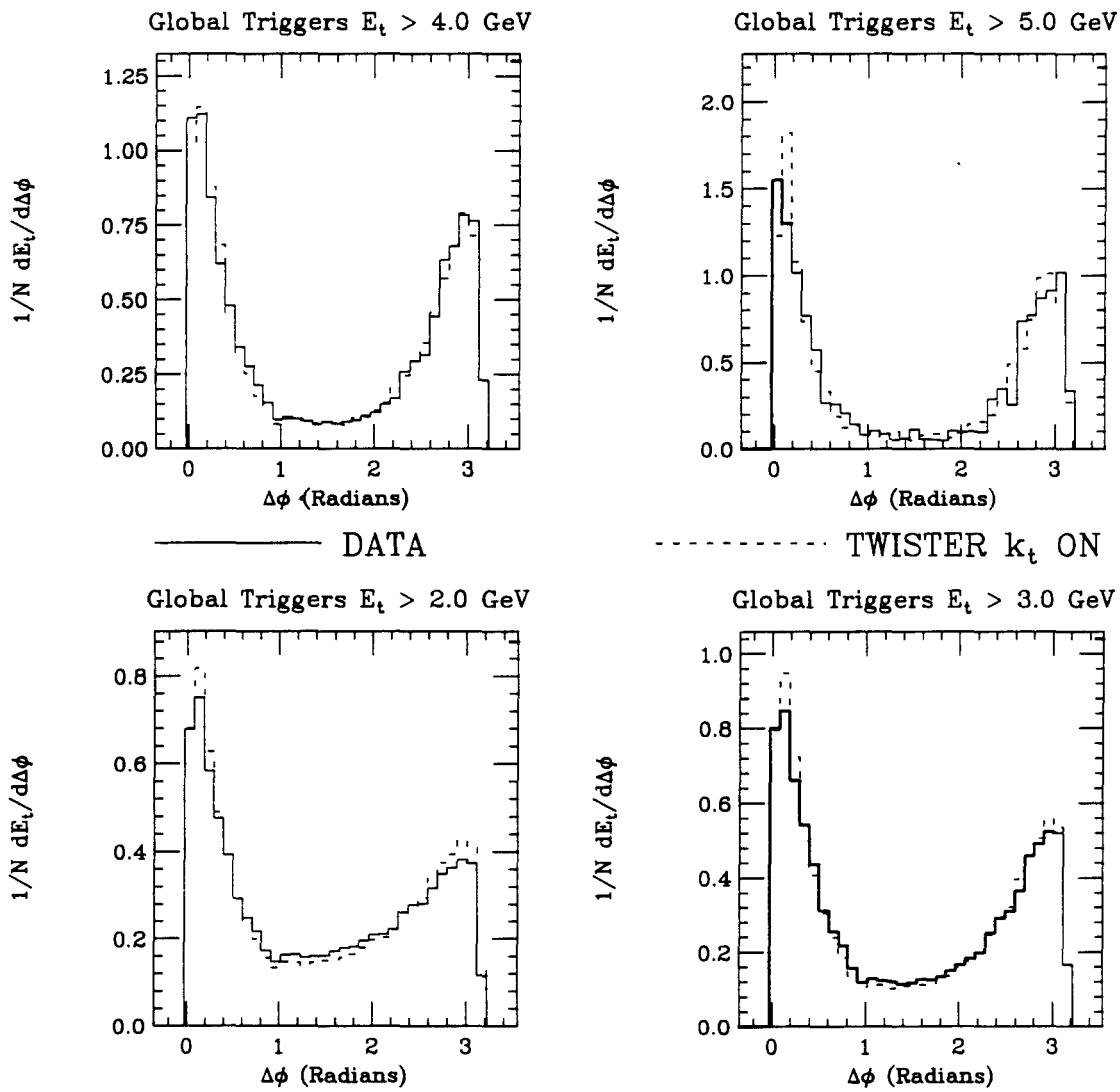

Figure 97: Shown is a comparison between TWISTER $k_\perp$ ON and data for Global triggers. The distribution being displayed is $E_\perp$ flow plot, for different reconstructed jet thresholds. The thresholds apply to *both* jets and are listed on the plot, as are the meaning of the lines used.

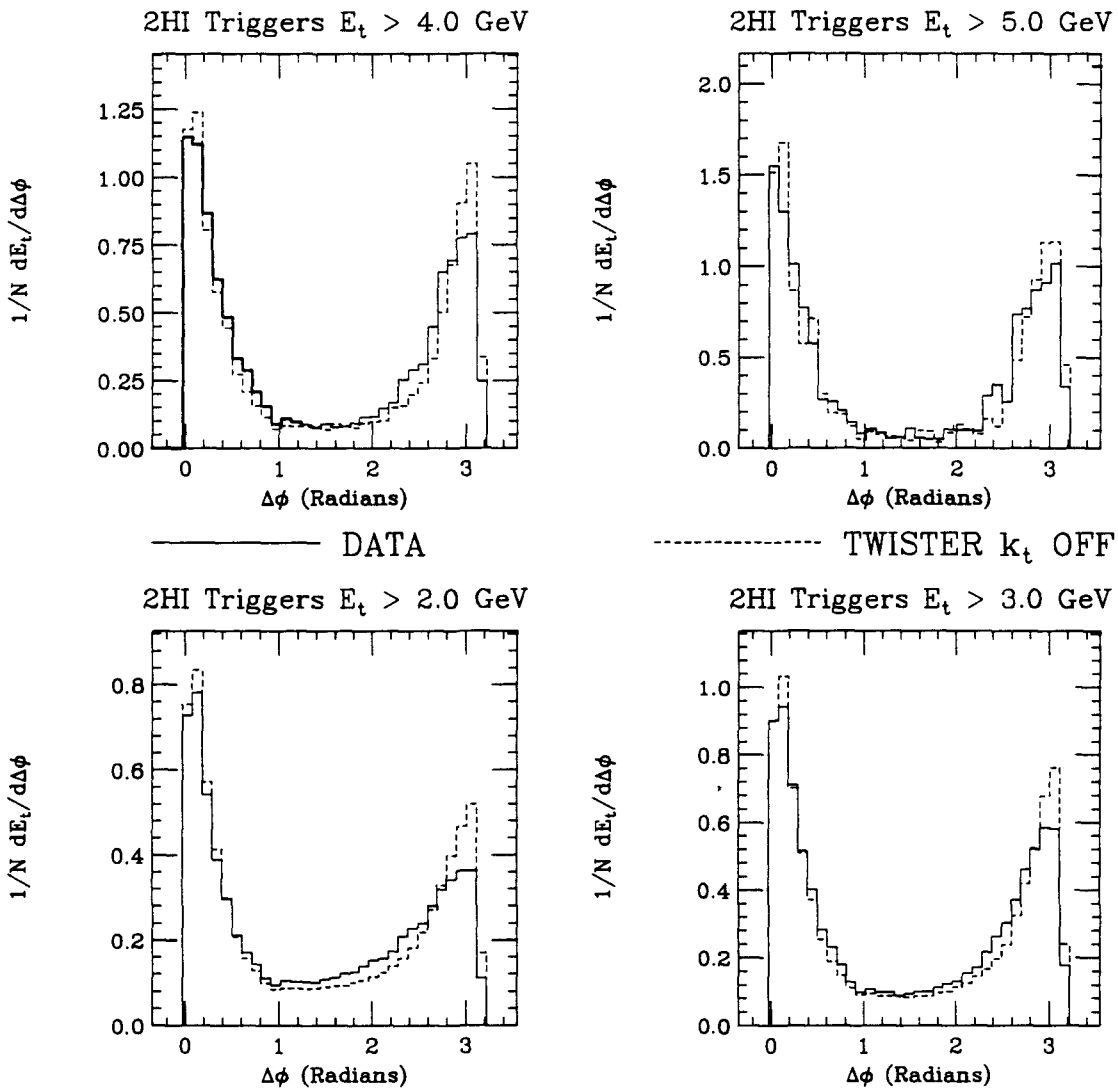

Figure 98: Shown is a comparison between TWISTER $k_\perp$ OFF and data for 2HI triggers. The distribution being displayed is $E_\perp$ flow plot, for different reconstructed jet thresholds. The thresholds apply to *both* jets and are listed on the plot, as are the meaning of the lines used.

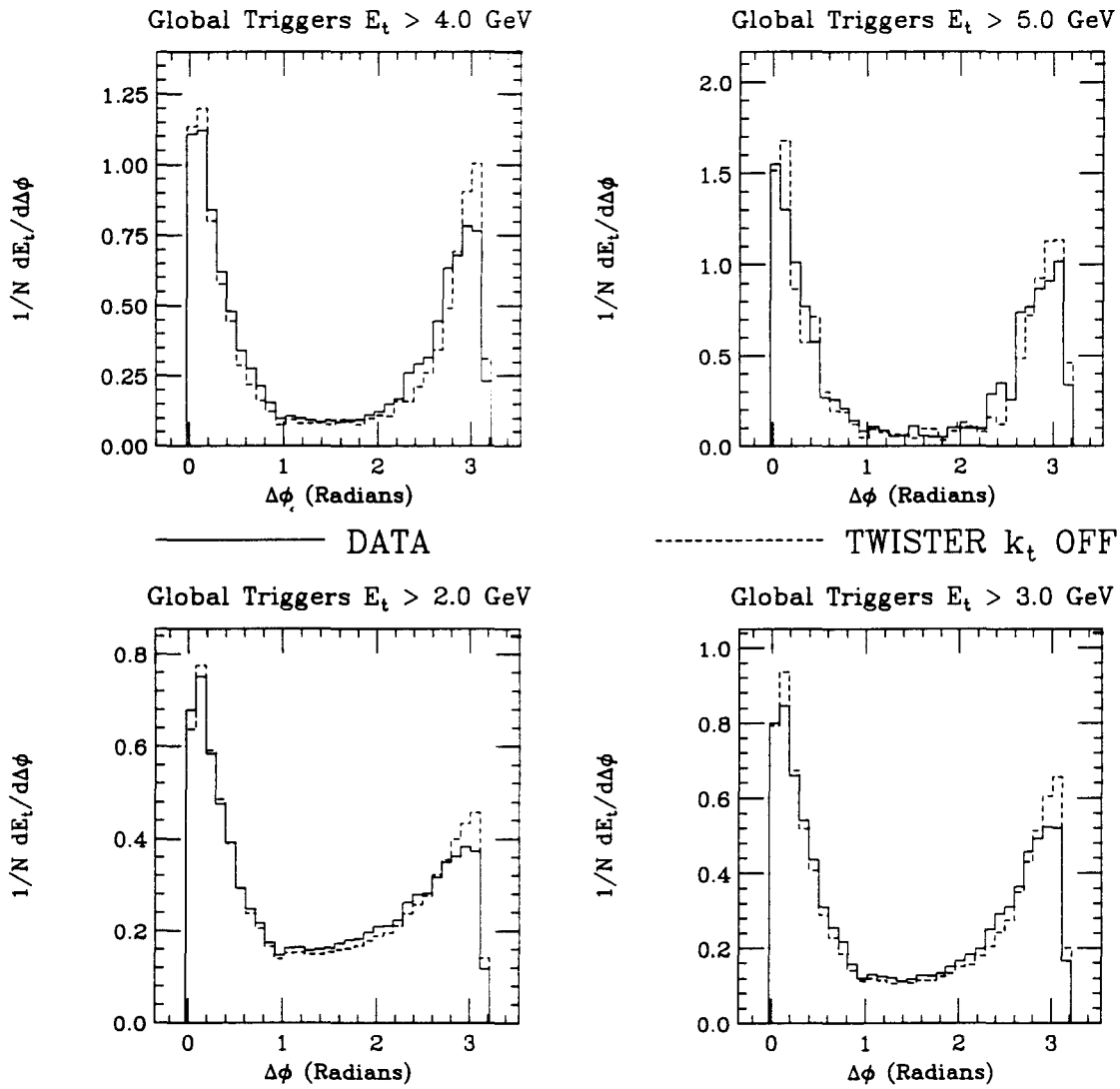

Figure 99: Shown is a comparison between TWISTER $k_\perp$ OFF and data for Global triggers. The distribution being displayed is $E_\perp$ flow plot, for different reconstructed jet thresholds. The thresholds apply to *both* jets and are listed on the plot, as are the meaning of the lines used.

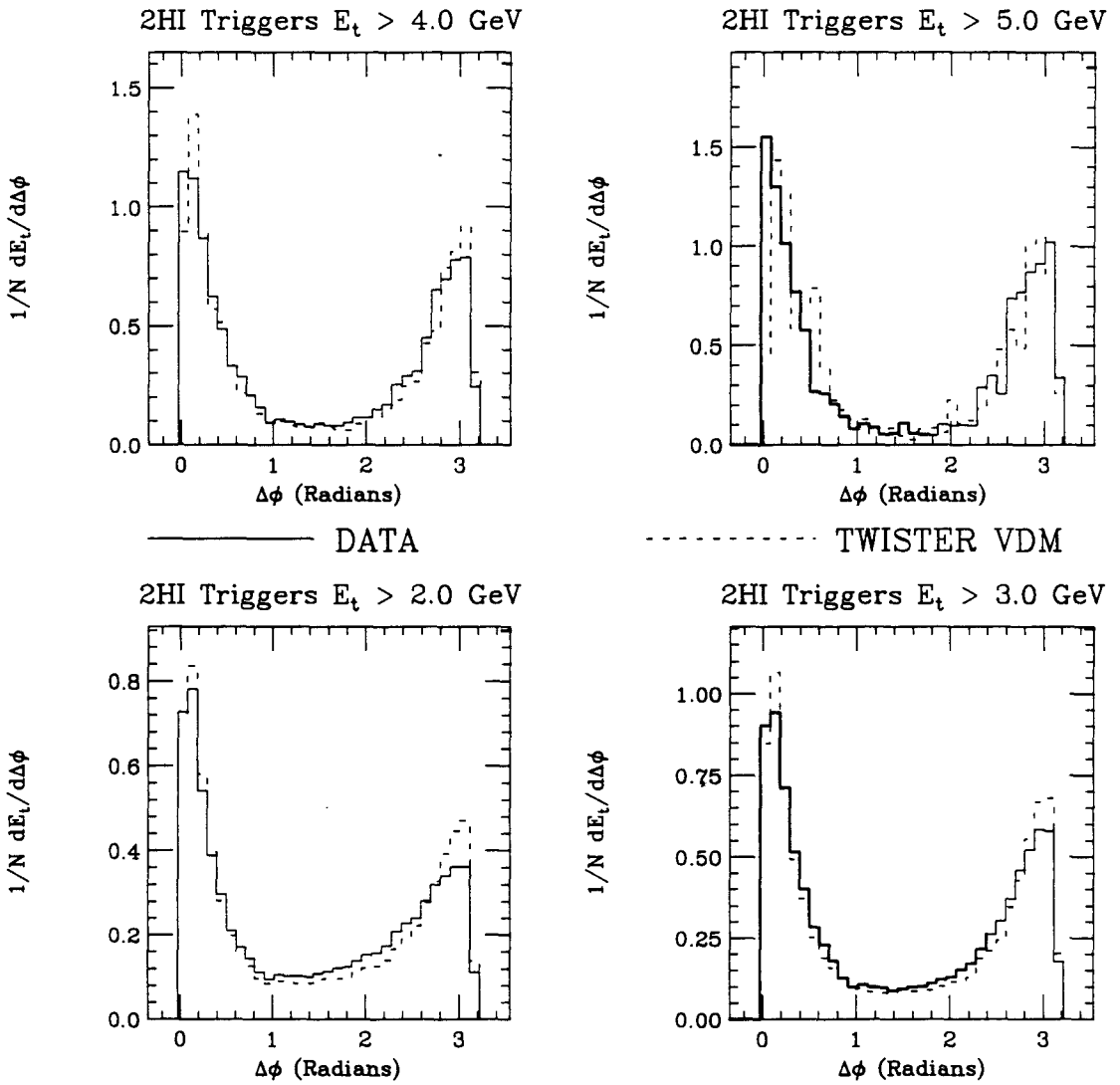

Figure 100: Shown is a comparison between TWISTER VDM and data for 2HI triggers. The distribution being displayed is $E_\perp$ flow plot, for different reconstructed jet thresholds. The thresholds apply to *both* jets and are listed on the plot, as are the meaning of the lines used.

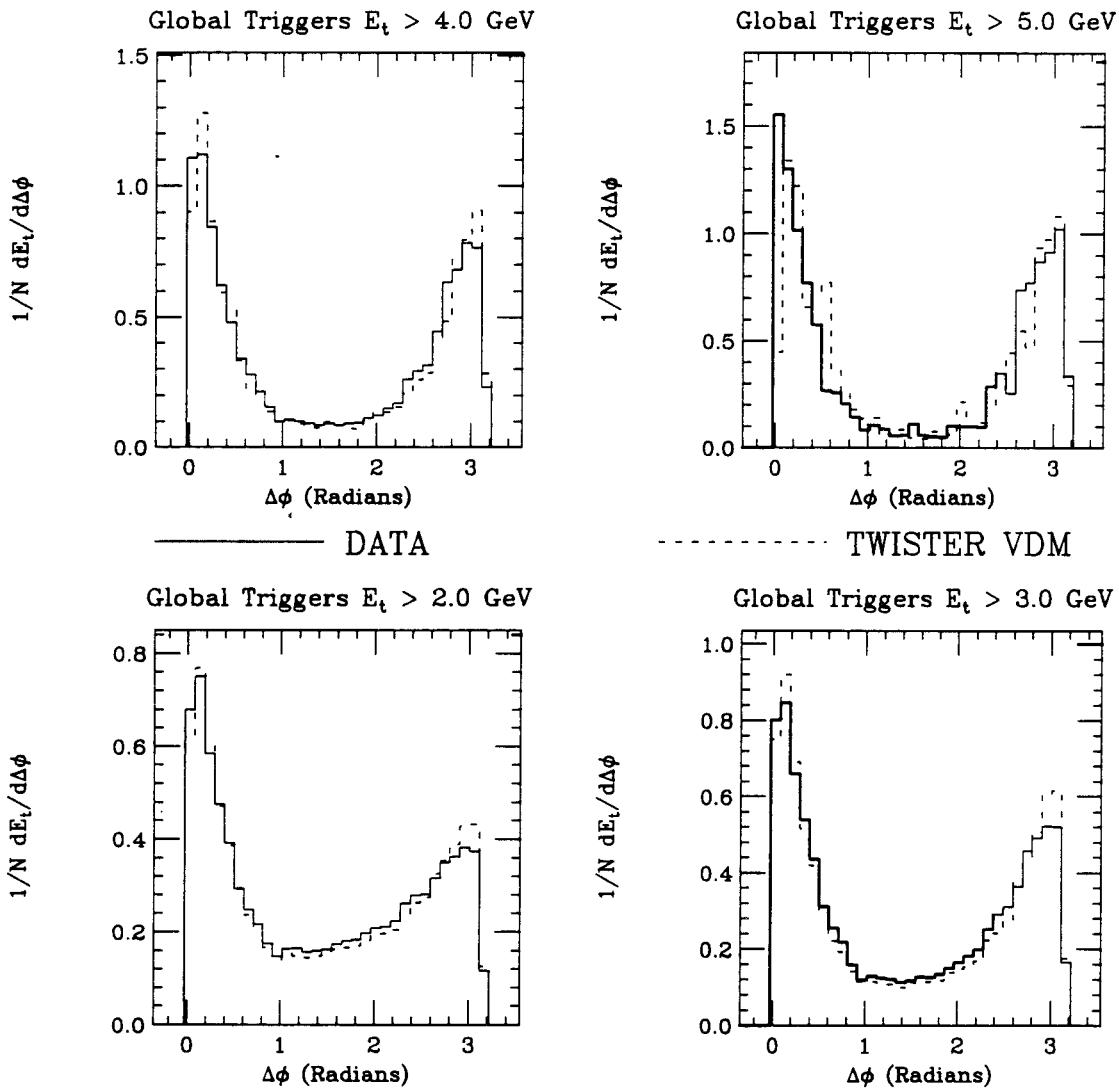

Figure 101: Shown is a comparison between TWISTER VDM and data for Global triggers. The distribution being displayed is $E_\perp$ flow plot, for different reconstructed jet thresholds. The thresholds apply to *both* jets and are listed on the plot, as are the meaning of the lines used.

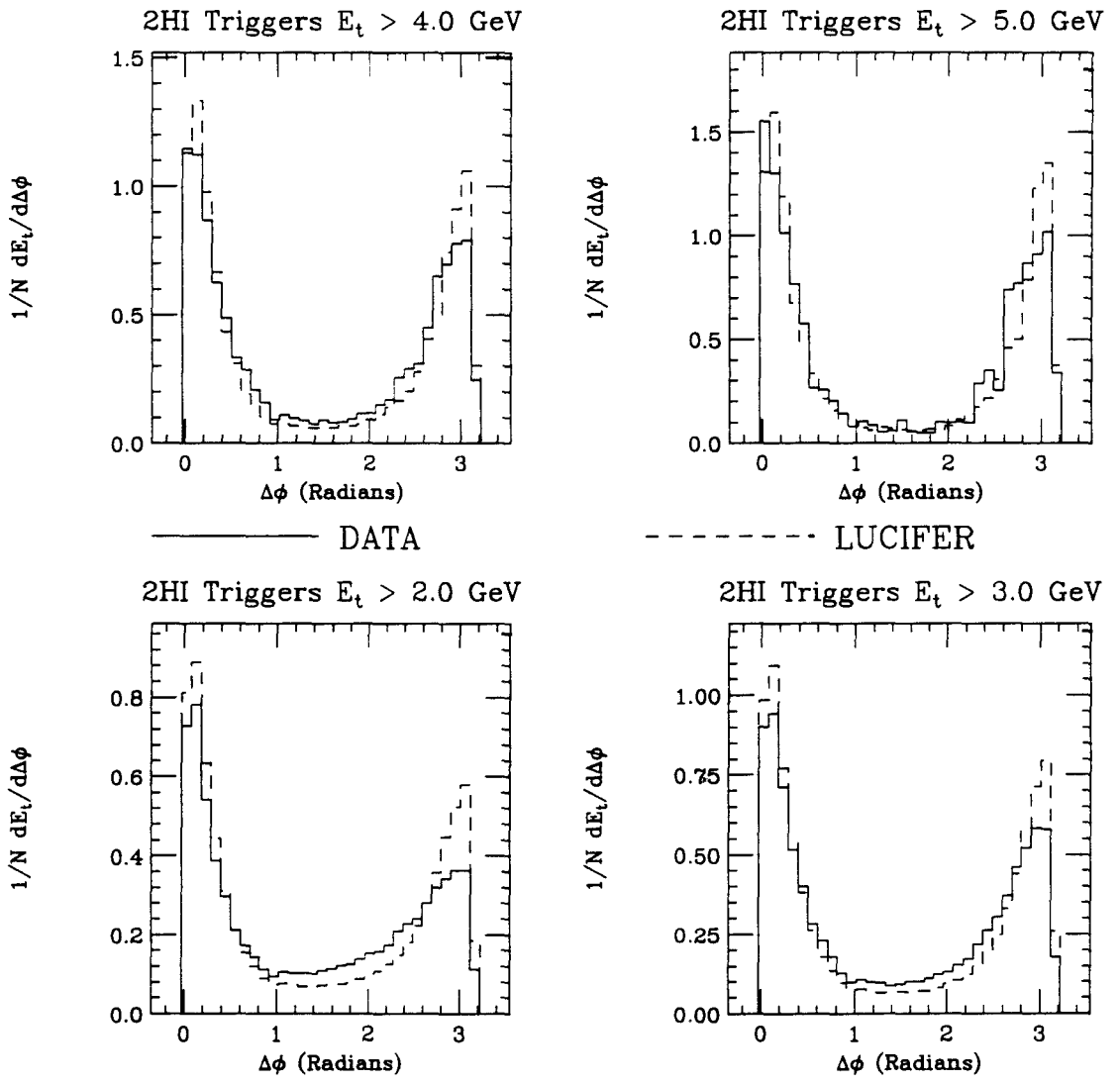

Figure 102: Shown is a comparison between LUCIFER and data for 2HI triggers. The distribution being displayed is $E_\perp$ flow plot, for different reconstructed jet thresholds. The thresholds apply to *both* jets and are listed on the plot, as are the meaning of the lines used.

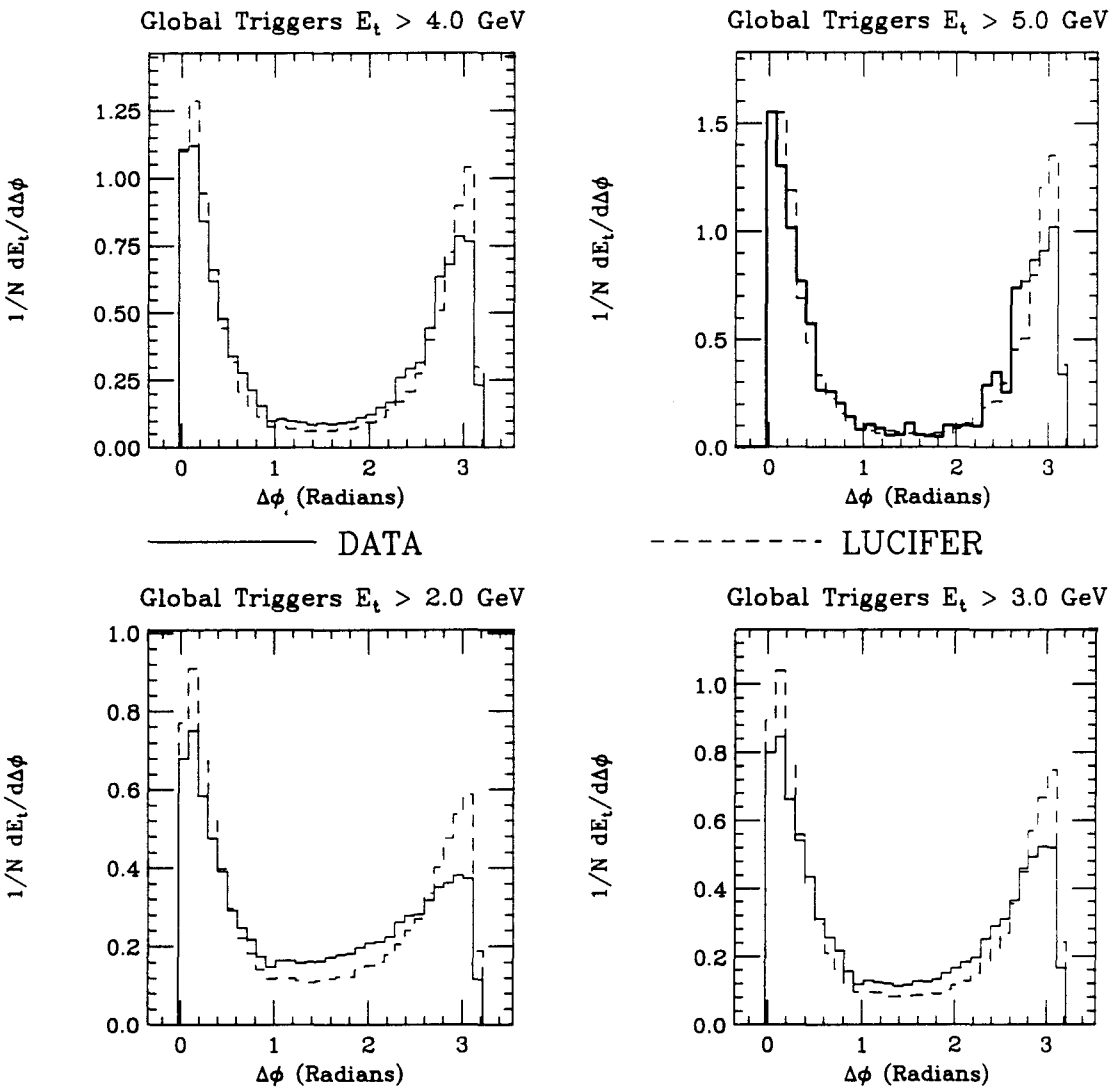

Figure 103: Shown is a comparison between LUCIFER and data for Global triggers. The distribution being displayed is $E_\perp$ flow plot, for different reconstructed jet thresholds. The thresholds apply to *both* jets and are listed on the plot, as are the meaning of the lines used.

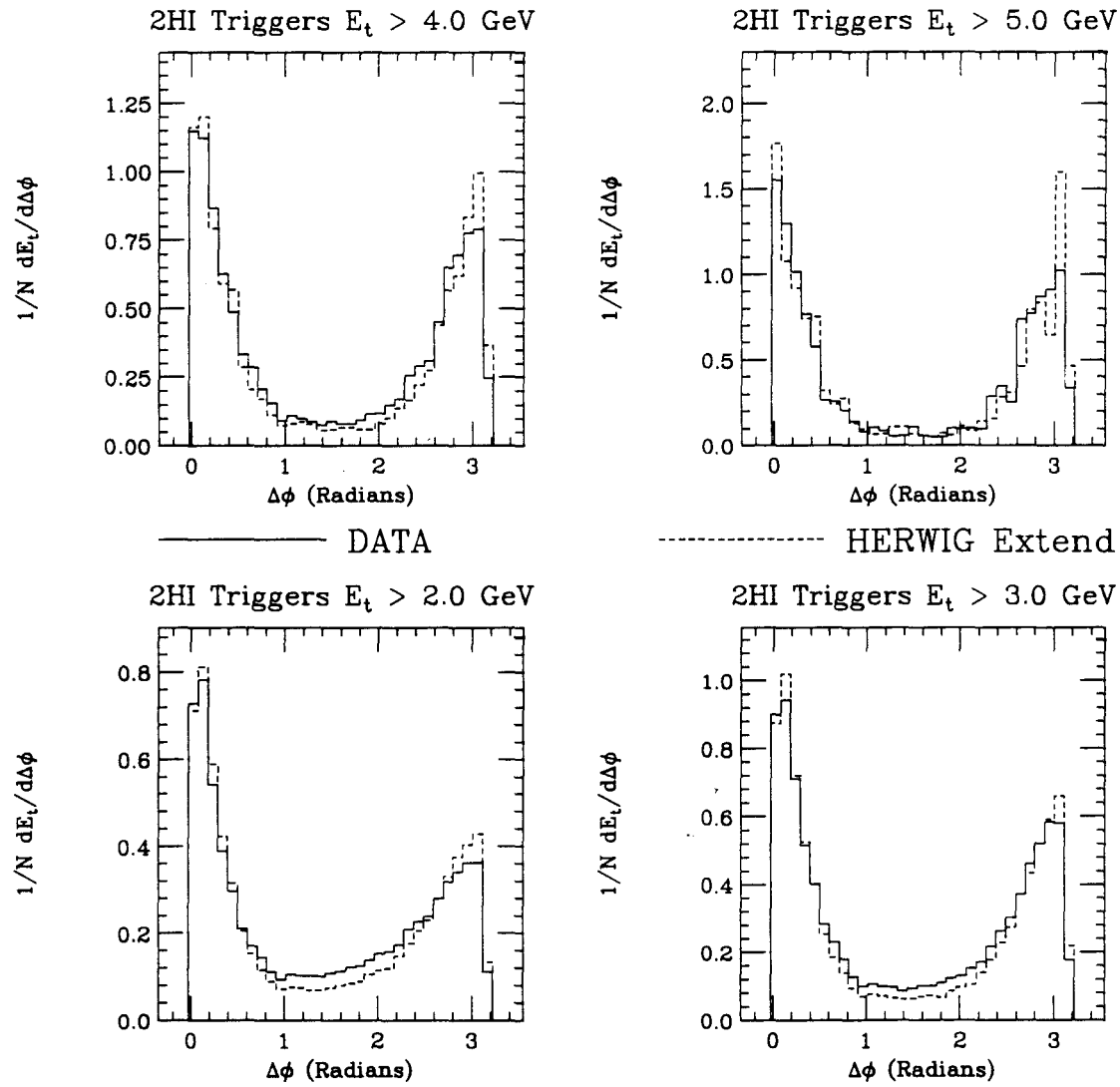

Figure 104: Shown is a comparison between HERWIG extended photons and data for 2HI triggers. The distribution being displayed is $E_\perp$ flow plot, for different reconstructed jet thresholds. The thresholds apply to *both* jets and are listed on the plot, as are the meaning of the lines used.

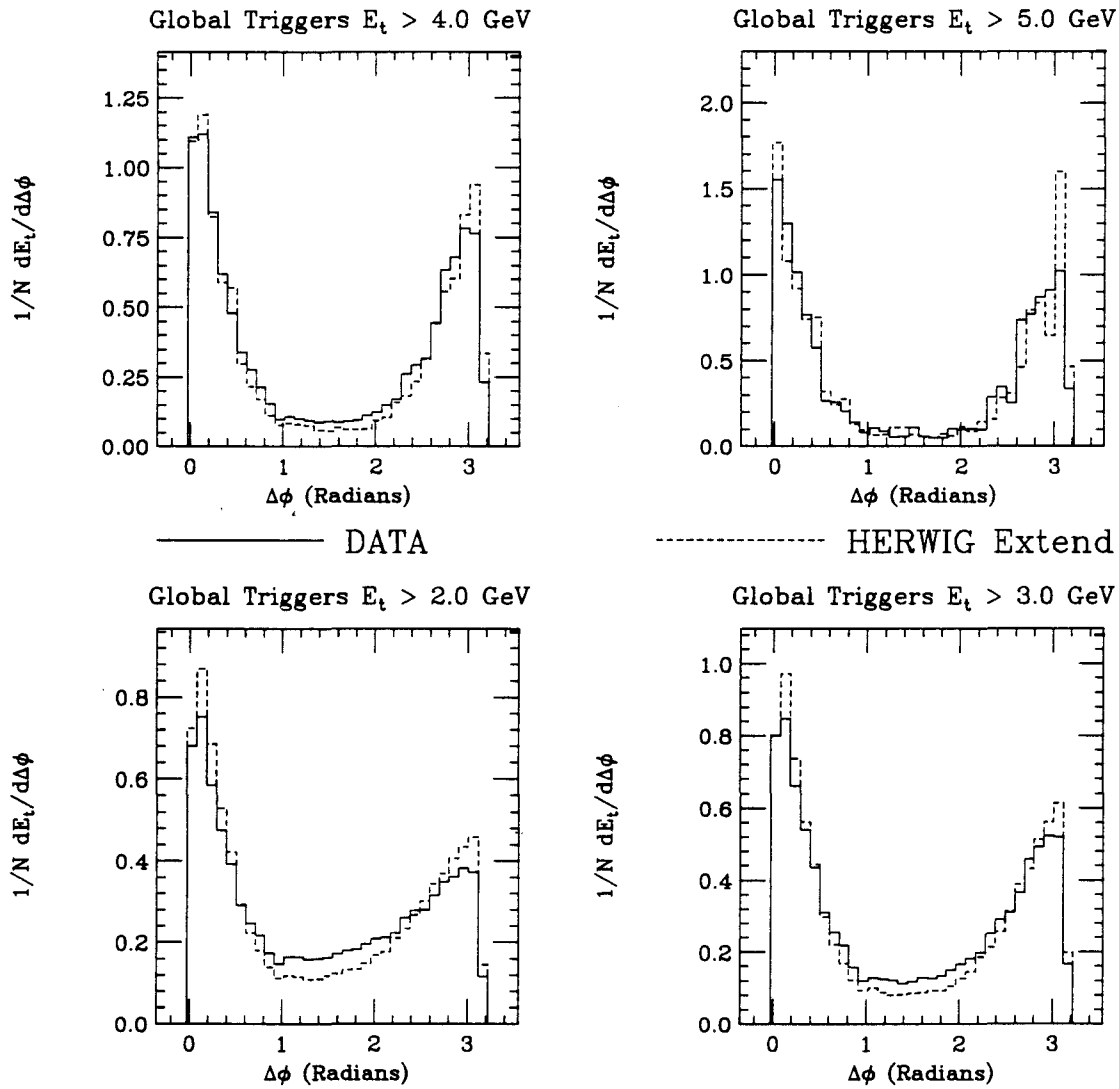

Figure 105: Shown is a comparison between HERWIG extended photons and data for Global triggers. The distribution being displayed is $E_\perp$ flow plot, for different reconstructed jet thresholds. The thresholds apply to *both* jets and are listed on the plot, as are the meaning of the lines used.

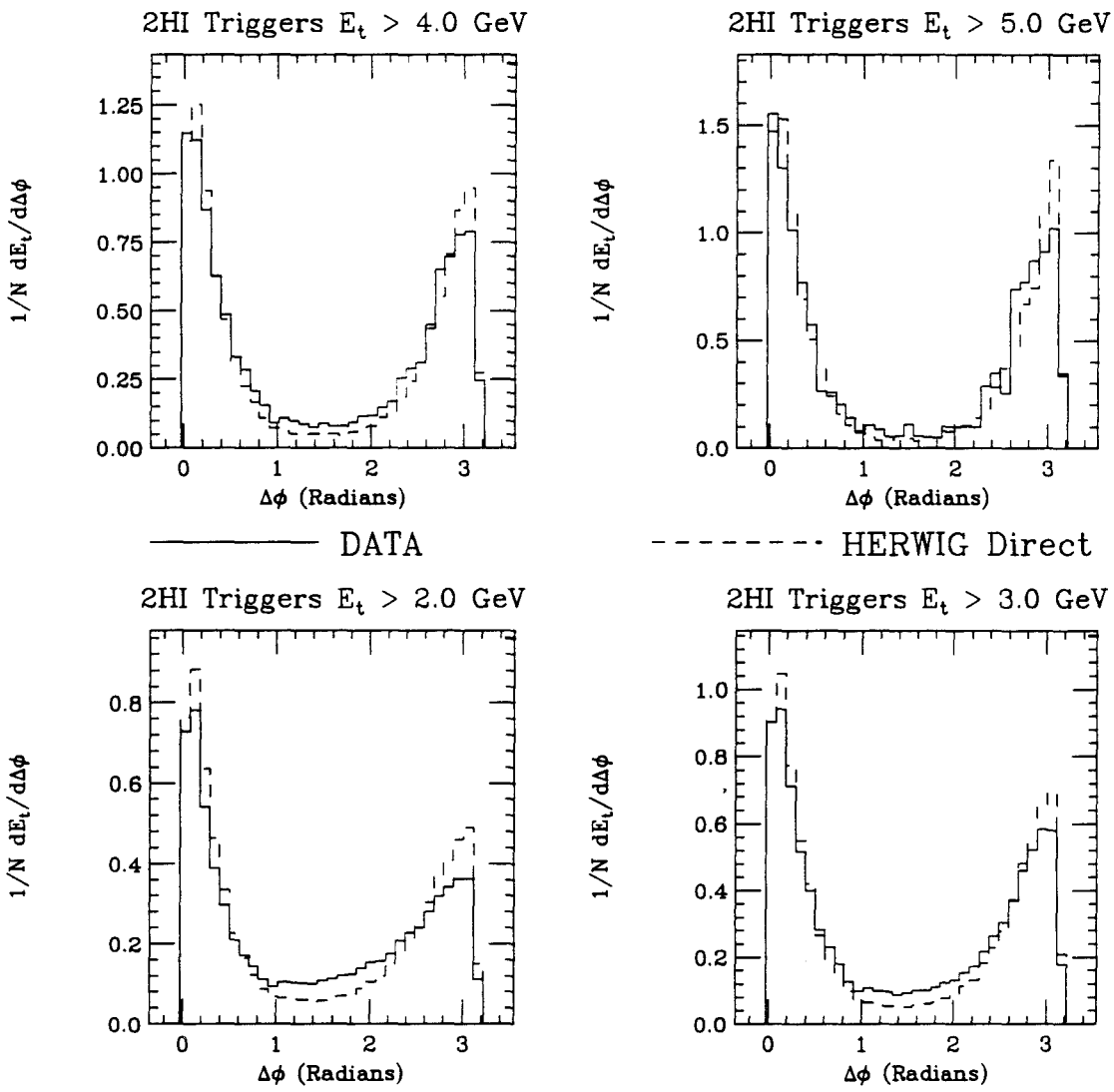

Figure 106: Shown is a comparison between HERWIG direct photons and data for 2HI triggers. The distribution being displayed is $E_\perp$ flow plot, for different reconstructed jet thresholds. The thresholds apply to *both* jets and are listed on the plot, as are the meaning of the lines used.

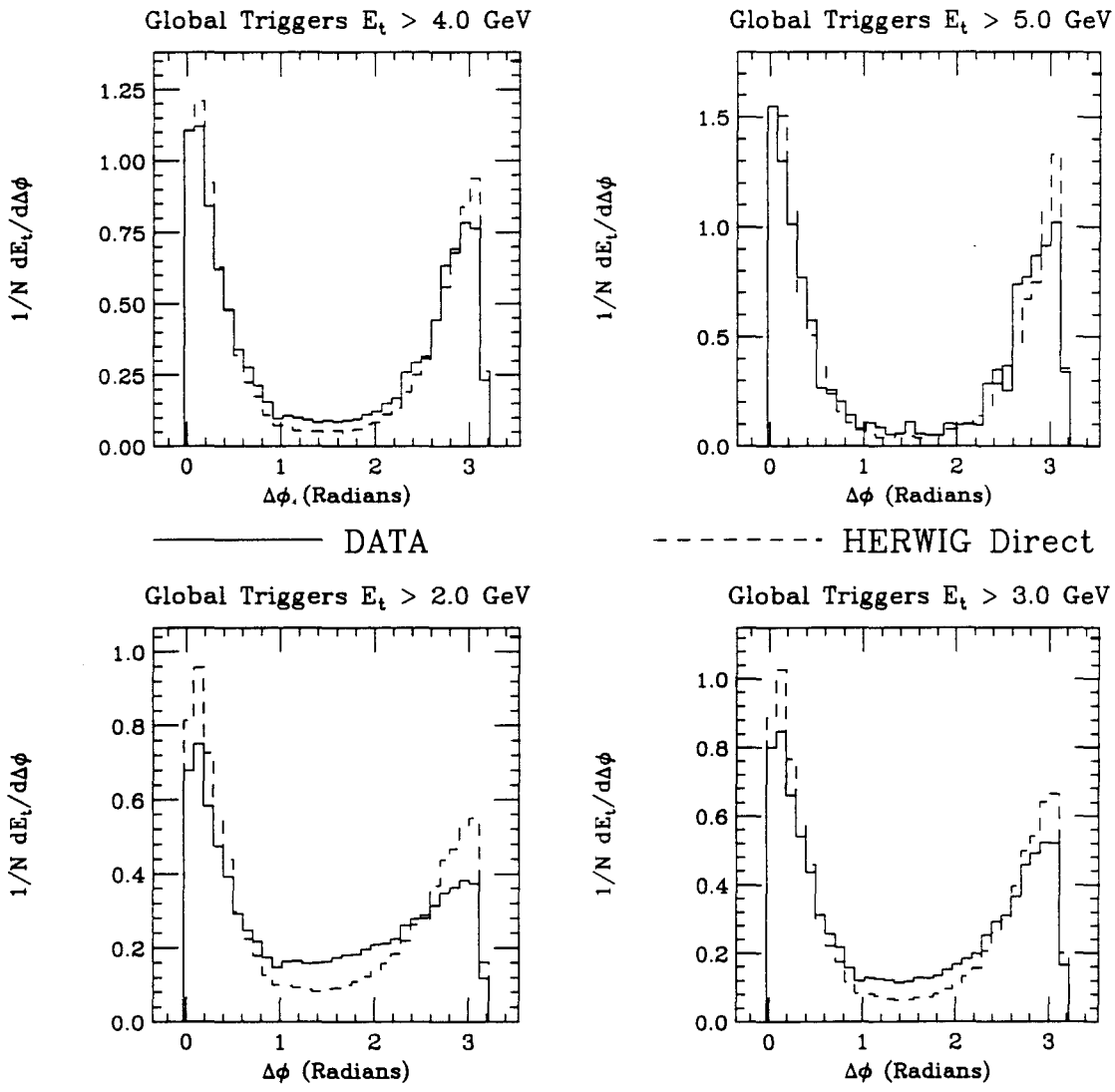

Figure 107: Shown is a comparison between HERWIG direct photon and data for Global triggers. The distribution being displayed is $E_\perp$ flow plot, for different reconstructed jet thresholds. The thresholds apply to *both* jets and are listed on the plot, as are the meaning of the lines used.

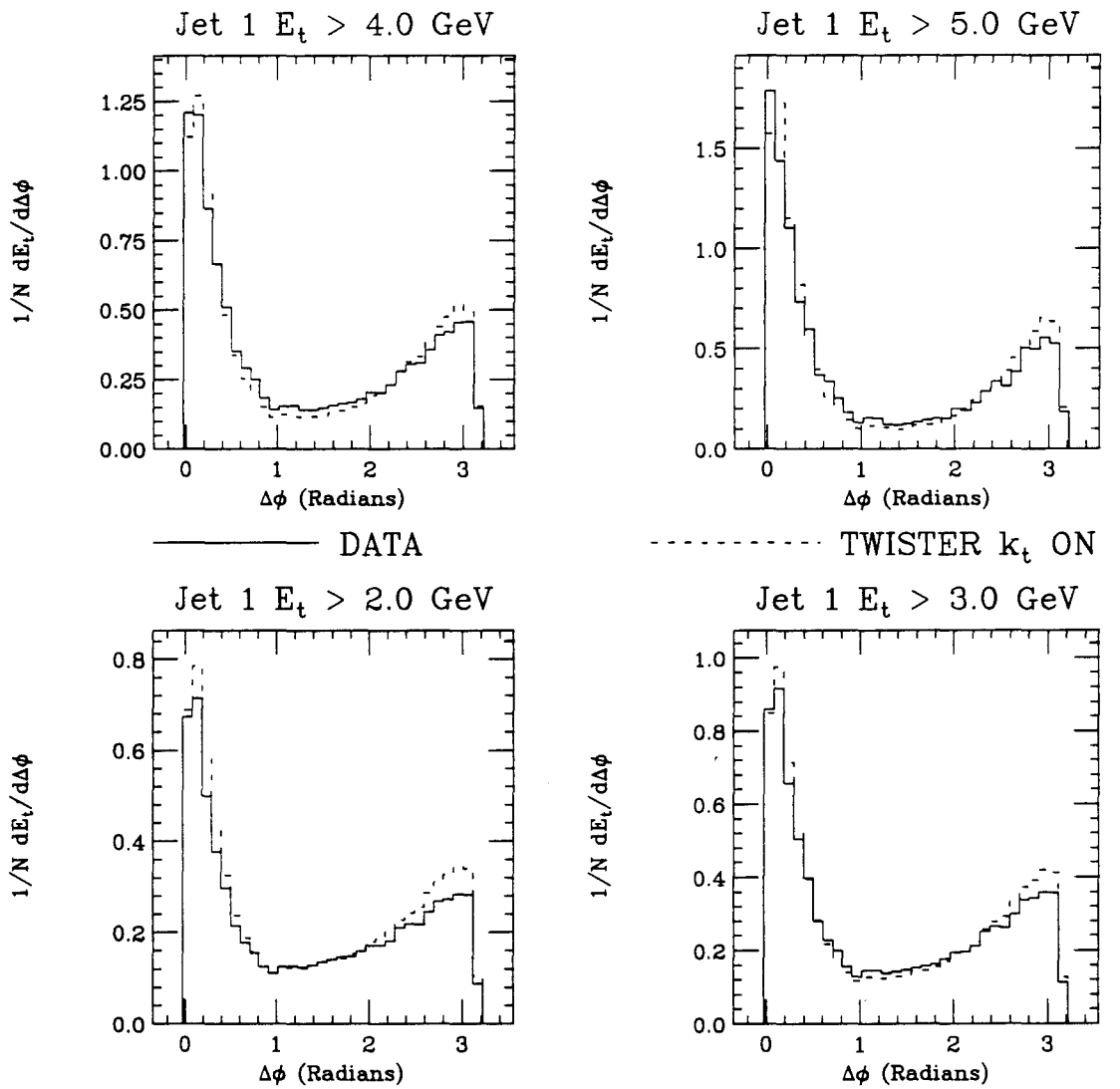

Figure 108: Shown is a comparison between TWISTER $k_\perp$ ON and data of an $E_\perp$ flow plot, for different reconstructed jet thresholds. The thresholds apply to *only to the one required jet* and are listed on the plot, as are the meaning of the lines used.

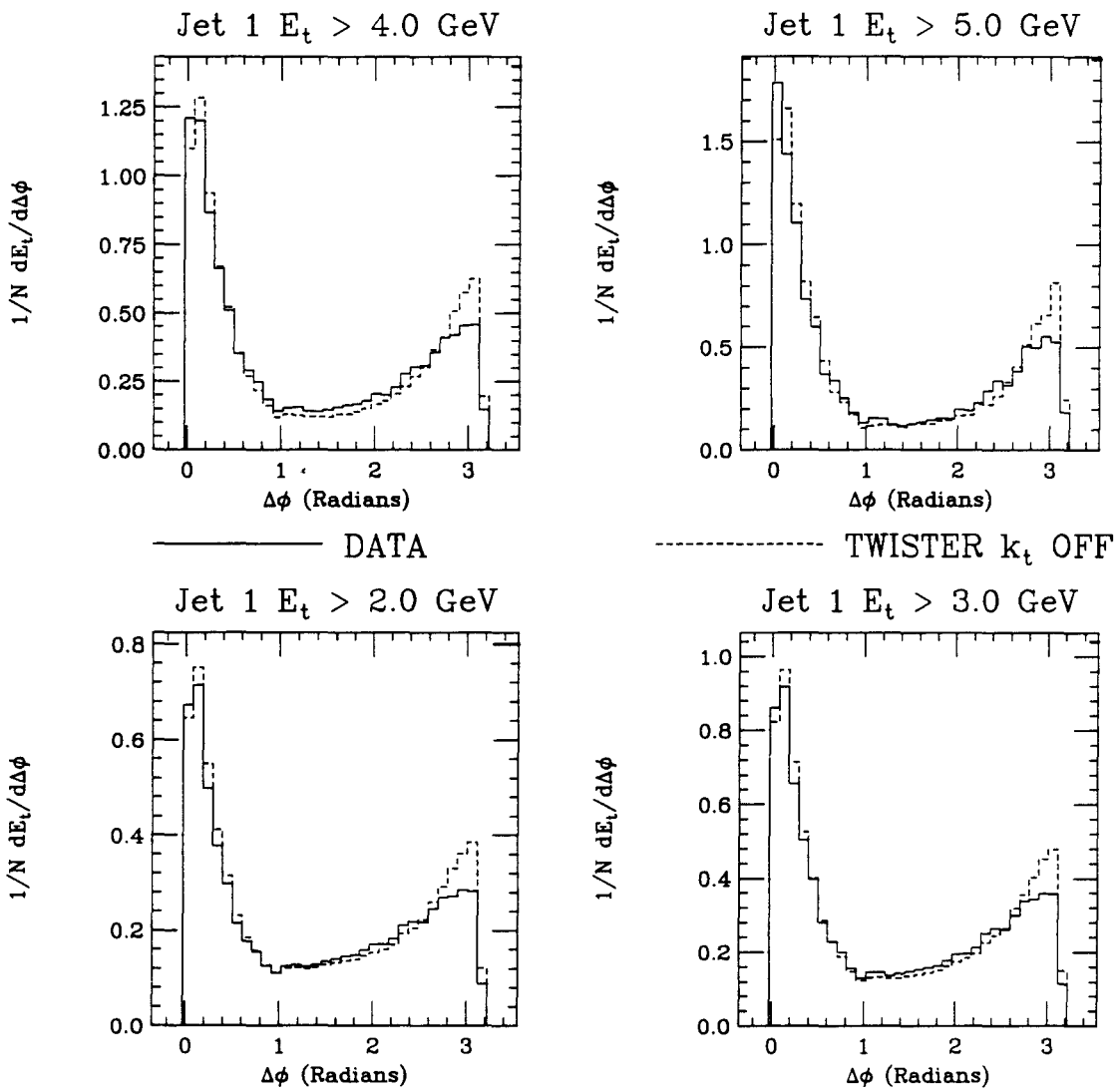

Figure 109: Shown is a comparison between TWISTER $k_\perp$ OFF and data of an $E_\perp$ flow plot, for different reconstructed jet thresholds. The thresholds apply to *only to the one required jet* and are listed on the plot, as are the meaning of the lines used.

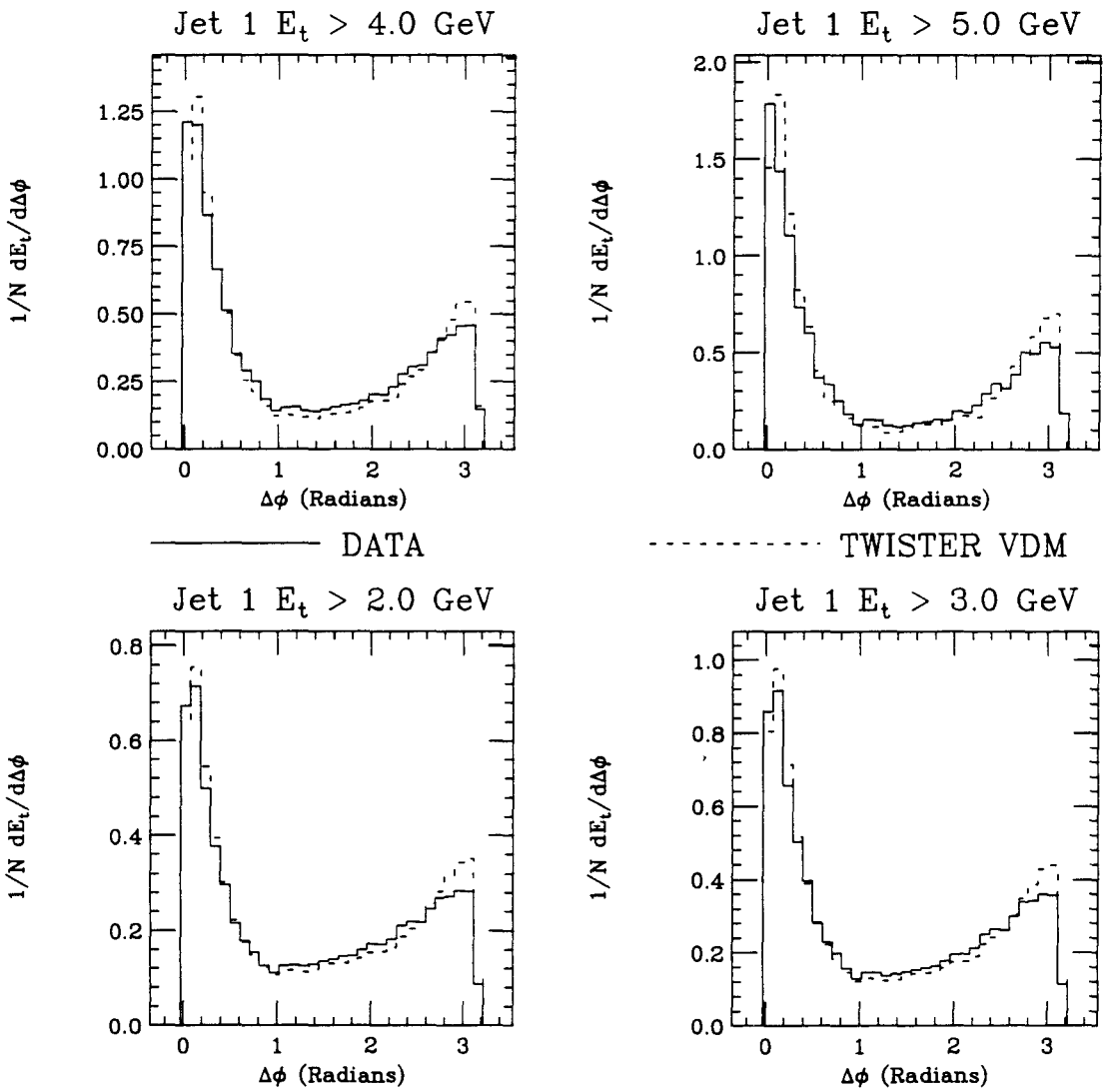

Figure 110: Shown is a comparison between TWISTER VDM and data of an $E_\perp$ flow plot, for different reconstructed jet thresholds. The thresholds apply to *only to the one required jet* and are listed on the plot, as are the meaning of the lines used.

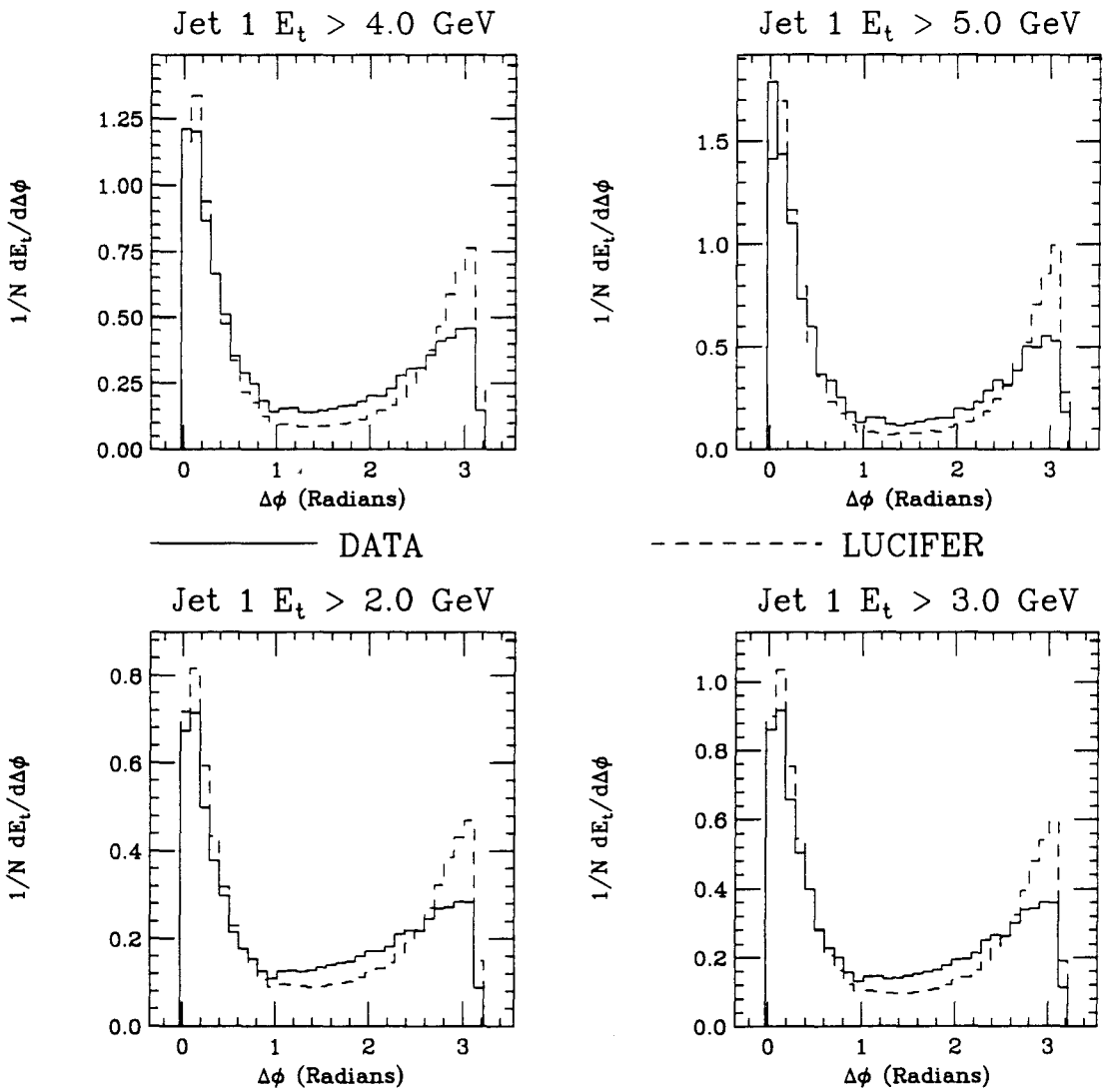

Figure 111: Shown is a comparison between LUCIFER and data of an $E_\perp$ flow plot, for different reconstructed jet thresholds. The thresholds apply to *only to the one required jet* and are listed on the plot, as are the meaning of the lines used.

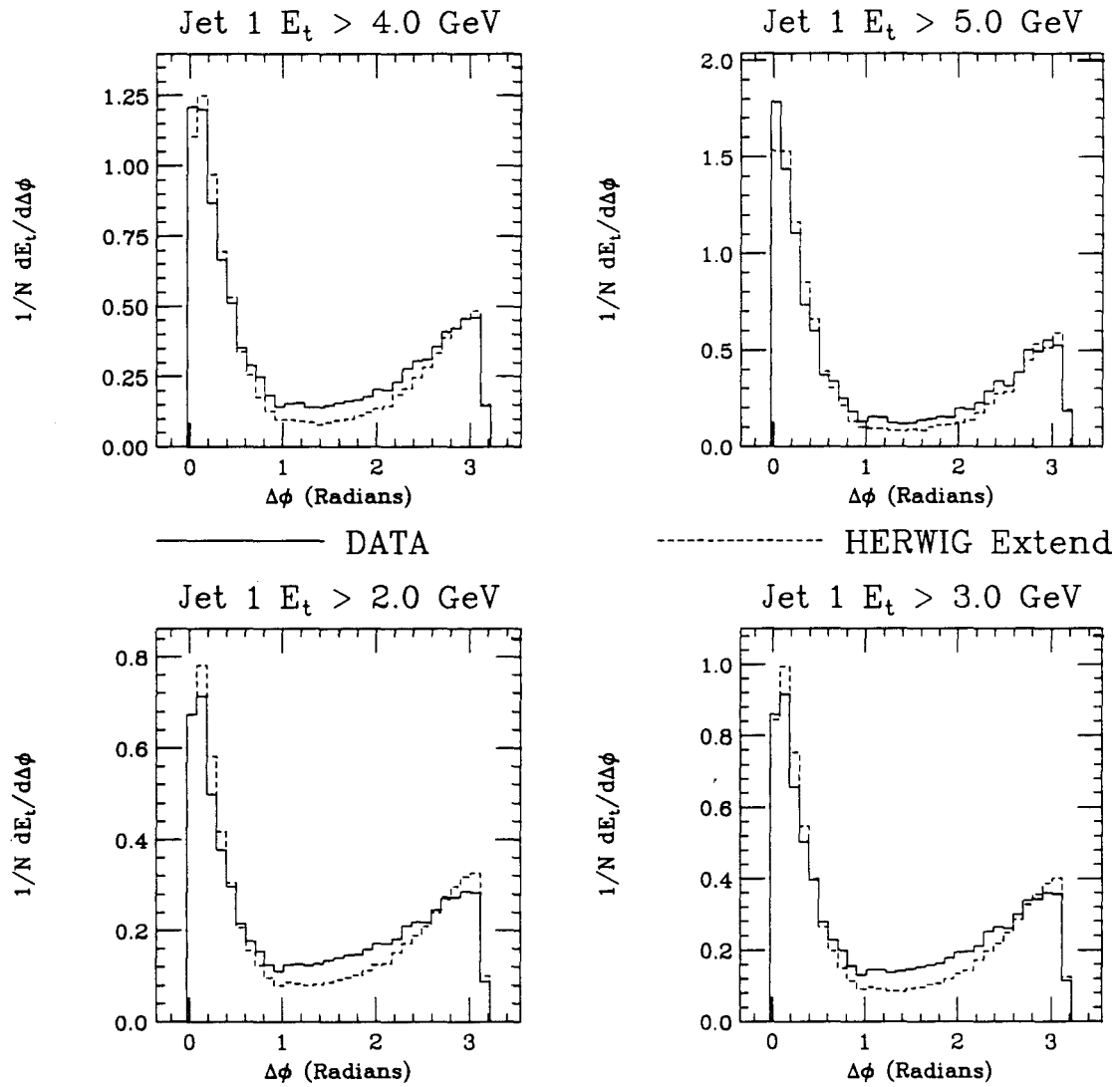

Figure 112: Shown is a comparison between HERWIG extended photons and data of an $E_\perp$ flow plot, for different reconstructed jet thresholds. The thresholds apply to *only to the one required jet* and are listed on the plot, as are the meaning of the lines used.

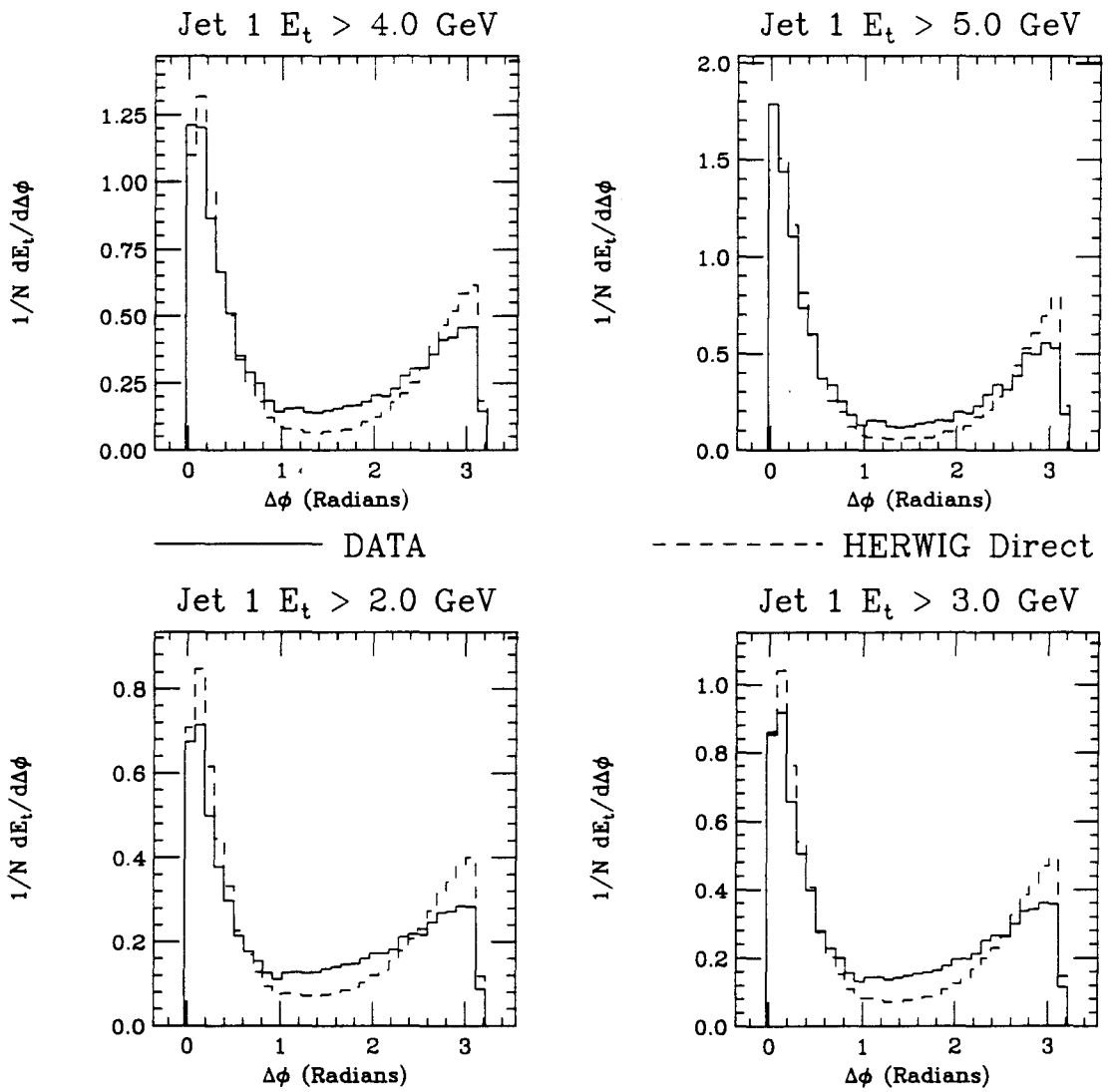

Figure 113: Shown is a comparison between HERWIG direct photons and data of an $E_\perp$ flow plot, for different reconstructed jet thresholds. The thresholds apply to *only to the one required jet* and are listed on the plot, as are the meaning of the lines used.

different, it is possible to take these two distributions as components of the data and fit them to the data. The fitting variables would be the fractions of each beam type seen in the data.

The overwhelming display of plots given in the previous sections shows that such an approach has some hope. Often the data is bracketted by (say) TWISTER extended photons ($k_\perp$ on) and LUCIFER direct photons (especially for the higher $E_\perp$ jet thresholds.) When the data is not bracketted by the Monte Carlo photon types, obviously such an approach is not possible.

Before such a fit can be done, it is necessary to determine the fractional composition of the data set that the Monte Carlo indicates. The way to do this is to ascertain the absolute cross-section of the different photon types. In the absence of trigger effects, the mixture of photon types in our data sample would be reflected in the ratio of the cross sections.

However, the fact that a photon undergoes a hard scatter does not ensure that it will be seen in the final data set. It is possible that a trigger can preferentially select a particular photon type. For this reason, the ratio of triggered events to generated events must be determined. This ratio, taken with the absolute cross sections, yields an 'effective cross section', indicating the mixture of different photon types in our simulated triggered data. The final step of determining the photon mix requires that the jet finding efficiency be folded in by seeing what fraction of the triggered data passes the specified jet finding thresholds. When this efficiency is combined with the 'effective cross section' of triggered data, the final mixture of photon types can be determined. After a few introductory notes, I present below such a calculation for the TWISTER/LUCIFER Monte Carlos.

Since E683 has a range of photon triggered energies ($\approx 200-300$ GeV, see below), it is natural to worry about the energy dependence of the relative proportions of the various photon types. Photon events were generated for direct, QCD (perturbatively extended) and VDM structure types. In all cases the events were generated with a minimum hard scatter $p_\perp$ of 2 GeV. This threshold is low enough that our jet-oriented distributions are insensitive to small variations in this parameter.

Beam Energy (GeV)	Direct	QCD	Ratio (Direct:QCD)
290	1113 nb	996 nb	(1.117:1.000)
250	1045 nb	865 nb	(1.208:1.000)
210	965 nb	692 nb	(1.396:1.000)

Table 3: Integrated cross-sections for various energies and photon types. In all cases, the minimum $\hat{p}_\perp$ generated is 2 GeV.

Table (3) lists the integrated cross sections for the dominant photon types along with their respective ratios for various photon energies. The number of events generated for each bin were distributed with the same proportions measured in the actual photon trigger spectrum, so the statistics on the edges of the energy range are necessarily poor. In the range of high statistics, we can see that the relative cross sections are unchanged at the 10-20% level. This is not surprising as the (maximal) range of $150 < E_\gamma < 350$ GeV corresponds to the rather limited range $17 < E_{\rm CM} < 26$ GeV. Subsequently, the different gamma types were generated and triggered with the ratios appropriate for $E_\gamma = 250$ GeV. This has proved to be an adequate approximation.

At this point, a digression is warranted. The information listed in table[19] (5) is determined using the LUCIFER/TWISTER defaults (modulo the independent fragmentation.) As has been discussed in detail, in the Monte Carlo code one finds that the partons from both the proton and the extended photon have a $k_\perp$ that is an internal degree of freedom of the parent hadron. Figure (114) shows the distribution of extended photon $k_\perp$'s for a 250 GeV photon beam.[20] Clearly a tremendous amount of the event's $E_\perp$ can come from this splitting. Note that the default of the Monte Carlo is to have this $k_\perp$ turned on.

As parton level scatterings are mostly calculated with massless, collinear partons,

[19]Which shows parton level information that is immune to fragmentation function and trigger bias effects, and also lists the triggering efficiencies for independent fragmentation.

[20]Note that $k_\perp$ is distributed according to the functional form $1/k_\perp$ ranging from a lower limit of 0.5 GeV to the kinematically determined upper limit $\sqrt{\hat{s}}/2$.

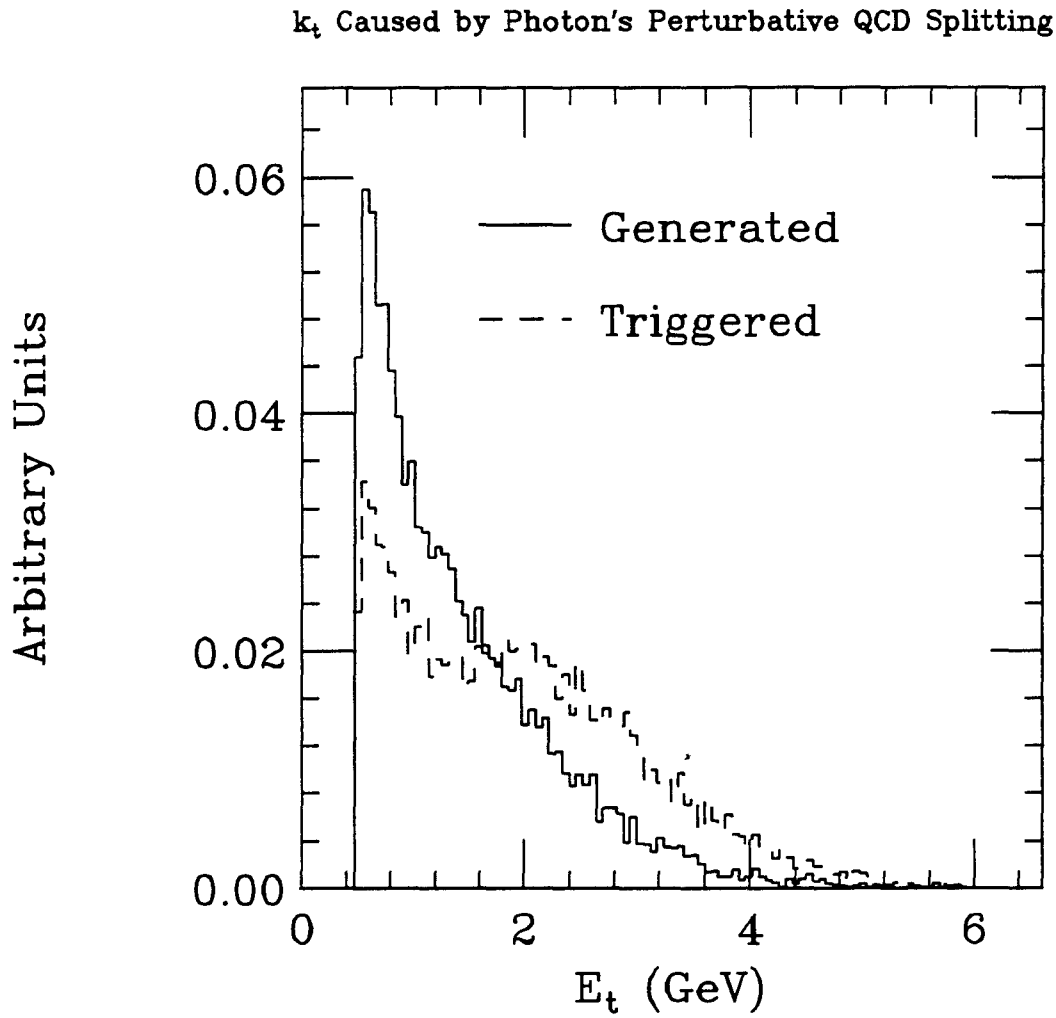

Figure 114: The $k_\perp$ of the partons within the photon generated due to perturbative QCD $q\bar{q}$ splitting according to the TWISTER model. Solid line indicates generated events, dashed line is those events that pass the trigger. The functional form of the generated distribution goes as $1/k_\perp$.

Structure Function	Direct	QCD	VDM
Integrated Cross Section	1042 nb	857 nb	278 nb
Events Needed for 10000 Triggers	94498	111545	149038
Triggering Efficiency (%)	10.6	9.0	6.7
'Effective' Cross Section	110.5 nb	76.8 nb	18.7 nb

Table 4: Triggering efficiency for various QCD photon types, photon $k_\perp$ turned off. In all cases, events were generated according to theoretical predictions, with a minimum $\hat{p}_\perp$ of 2.0 GeV. Because of the steeply falling $p_\perp$ spectrum, most generated events had $\hat{p}_\perp$ very nearly 2.0 GeV.

the effect of the $k_\perp$ does not affect the fundamental cross sections. Since the $k_\perp$ from the QCD splitting is quite large, it has an appreciable effect on the triggering efficiencies. Table (4) shows the number of events needed to generate 10000 triggers with photon $k_\perp$ turned off. Comparing these results with table (5) show that this is a very large effect. The percentage population of triggered events (direct:QCD:VDM) is (52:46:2)% for the default conditions, but changes to (72:25:3)% with the QCD photon's $k_\perp$ turned off.

Table (5) lists the integrated cross section for the different structure functions, the number of events needed to generate 10000 triggers, the triggering efficiency, and then the number of those triggered events in which two jets were found, both with an $E_\perp$ greater than the listed threshold. This is followed by the percentage of events of each photon type in each jet $E_\perp$ bin. Note that QCD implies the QCD Duke and Owens photon structure function, although the results are comparable for all reasonable perturbative structure functions. Broadly speaking, we can say that the Monte Carlo predicts a 50:50 split of extended and pointlike photons for the higher $E_\perp$ thresholds.

Structure Function	Direct	QCD	VDM	Data
Integrated Cross Section	1042 nb	857 nb	278 nb	
Events Needed for 10000 Triggers	94498	60456	149038	
Triggering Efficiency (%)	10.6	16.5	6.7	
'Effective' Cross Section	110.5 nb	160.4 nb	18.7 nb	
Both Jets $E_\perp > 2.0$ GeV	7031	6458	5937	76310
Both Jets $E_\perp > 2.5$ GeV	4460	3833	3166	36147
Both Jets $E_\perp > 3.0$ GeV	2483	1841	1255	14827
Both Jets $E_\perp > 3.5$ GeV	1199	719	379	5257
Both Jets $E_\perp > 4.0$ GeV	522	289	104	1840
Both Jets $E_\perp > 4.5$ GeV	214	99	35	691
Both Jets $E_\perp > 5.0$ GeV	86	46	8	281
Both Jets $E_\perp > 5.5$ GeV	37	19	1	116
Both Jets $E_\perp > 6.0$ GeV	14	9	0	46
Both Jets $E_\perp > 2.0$ GeV	40.4%	53.8%	5.8%	
Both Jets $E_\perp > 2.5$ GeV	42.2%	52.7%	5.1%	
Both Jets $E_\perp > 3.0$ GeV	46.3%	49.8%	4.0%	
Both Jets $E_\perp > 3.5$ GeV	52.0%	45.2%	2.8%	
Both Jets $E_\perp > 4.0$ GeV	54.4%	43.7%	1.8%	
Both Jets $E_\perp > 4.5$ GeV	58.9%	39.5%	1.6%	
Both Jets $E_\perp > 5.0$ GeV	55.8%	43.3%	0.9%	
Both Jets $E_\perp > 5.5$ GeV	57.1%	42.6%	0.3%	
Both Jets $E_\perp > 6.0$ GeV	51.7%	42.6%	0.0%	

Table 5: Summary of the contributions of each structure function to the different jet $p_\perp$ bins for independent fragmentation. The integrated cross-section has a minimum $\hat{p}_\perp$ of 2 GeV. Events are generated according to the $p_\perp$ distributions dictated by the differential cross-sections embedded in TWISTER/LUCIFER. While there must be a $\hat{p}_\perp$ dependence to the triggering efficiency, what is needed here is a $p_\perp$ averaged efficiency. The entries following the 'Both Jets $E_\perp >$ (threshold)' shows how many of 10000 triggers satisfy the listed jet finding condition. The data column shows how many events present in our data sample above the specified thresholds. The last section combines the integrated cross-section, averaged triggering efficiencies and jet finding efficiencies to show the fractional contribution of each structure function that TWISTER/LUCIFER suggests we should have in our data set.

9.7 Measured Ratio of Direct and Extended Photons

One observation that one can make after perusing section (9.4) is that for the highest jet $E_\perp$ cuts, the two trigger types coalesce and that for many distributions, the shape of the data is bracketted by the shapes of the LUND generated extended photons ($k_\perp$ on) and direct photons. Because of this, it is possible to try to fit an appropriate mixture of the two photon types. The result can be compared to the results of section (9.6), which presents the predictions of the LUND Monte Carlo.

The method of fitting is conceptually simple. Each distribution (direct photons, extended photons and data) are normalized to unit area and presented with identical binning. The assumption is made that the data is composed solely of these two possible photon types.[21] If this is the case, there should be a fraction F of LUCIFER events that, when mixed with a fraction $(1-F)$ TWISTER events, should reproduce the data. F is determined by a simple χ^2 fit summed over all of the bins. Conceptually, the procedure can be written:

$$\chi^2 = \sum_{\text{bin}} \frac{[F\cdot(\text{LUCIFER}) + (1-F)\cdot(\text{TWISTER}) - (\text{DATA})]^2}{(\text{ERROR})^2}$$

where the sum is taken over the bins of each histogram. This procedure can be done for any and all distributions, although it will only work for those with the required bracketting of the data by the Monte Carlo.

Such a procedure was attempted for the jet $E_\perp > 4$ GeV data. This particular bin was chosen since it was the lowest $E_\perp$ bin where the trigger types overlapped essentially completely, but still provided with adequate statistics to be somewhat believable. A fit using MINUIT (a CERN minimization package) was performed for all of the distributions shown in section (9.4). A correct mixing was not possible for all of the distributions, due to the fact that the Monte Carlos did not span the data. The results are presented in figure (115). The black bars indicate the minimization procedure failed. It can be seen that for those distributions for which this procedure was possible, the data and Monte Carlo agree reasonably well. This is taken to be suggestive, if not compelling, evidence that the mix of photon types suggested by the

[21] This is justified in part by the high jet $E_\perp$ cuts being used.

Fraction of LUCIFER present in Jet E_t > 4 GeV Data

Prediction	0.544 +/− 0.04	
Ensemble Avg.	0.448 +/− 0.05	
Planarity	0.462 +/− 0.05	
E_t(out)		
$k_{t\ \phi}$		
k_t	0.539 +/− 0.05	
$\Delta\phi$	0.401 +/− 0.05	
<E_t(jet)>	0.464 +/− 0.09	
E_{BCAL}	0.373 +/− 0.06	
E_{MCAL}		
$E_{t\ MCAL}$		
E_{BEAM}	0.504 +/− 0.12	
x_{BEAM}		

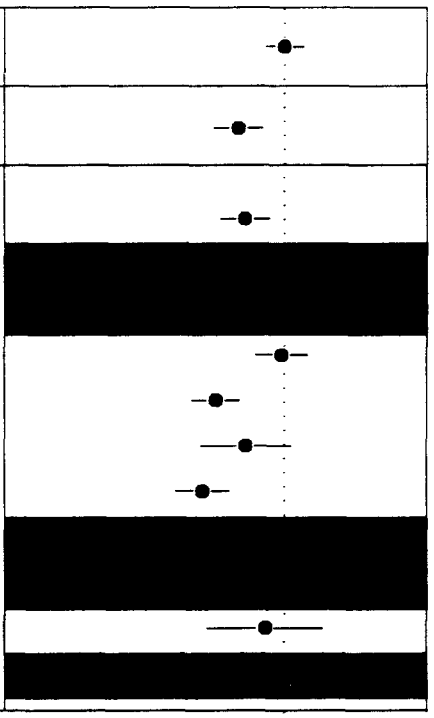

Figure 115: The figure shows the fraction of LUCIFER direct photons seen in E683's data. The remaining fraction is formed by TWISTER ($k_\perp$ on) extended photons. The black bars indicate those distributions which did not converge. The prediction given at the top of the figure is from the previous section. This chart is for events with two reconstructed jets, both with an $E_\perp$ in excess of 4 GeV.

Monte Carlo is correct.

10 Review and Conclusions

The study of the structure of the photon is an interesting endeavor, since no particle is more 'obviously' pointlike and massless. Throughout this dissertation, I have explored the possibility of understanding this structure. The tack I have taken is to first explore direct methods of measuring the photon's x distribution via reconstruction of parton

level kinematics. In section (2) I have outlined the methods that one might use, with some information taken from section (1). The result was that if the parton kinematics could be accurately determined, a direct measurement of the structure of the photon was possible. It was shown that the parton level kinematics were reasonably preserved in the true jets and that the final problem was to find jets accurately.

In section (8) I outline the results of a jetfinding study, initially done with 'flat particles' (i.e. with a uniform x distribution.) The azimuthal angle ϕ of the jet can be determined with a reasonable degree of accuracy. Figure (18) shows that the ability to determine the θ of the hard scatter partons is much worse, with the cause (MCAL acceptance) shown in figure (19 a). It was found that increasing the reconstructed jet $E_\perp$ vastly improved the θ reconstruction, as shown in figure (20.) It has been suggested that this evidence does not entirely support the conclusion that acceptance is the problem and the real problem is that the $E_\perp$ cut off is too low. However, inspection of figure (19 a) shows that the tails come entirely from events when the true jet misses the calorimeter or is near the edges of acceptance, and never when the jet squarely hits the calorimeter. What this means is that when the jet hits the calorimeter it can be found. When it misses the calorimeter, a low $E_\perp$ jet can be manufactured from the underlying event and stray jet related particles. Insisting that the reconstructed jet have a large $E_\perp$ is equivalent to requiring that the true jet hit the calorimeter, since it is very difficult to manufacture a high $E_\perp$ jet from random debris. Increased acceptance would increase the solid angle in which true jets can be captured and would reduce this problem.

Since the photon has many different aspects (direct, perturbatively calculable extended, and VDM), the θ reconstruction ability was checked for each photon type using the fundamentally leading order LUND Monte Carlos and it was discovered that there was a significant problem in reconstructing the θ's of the hard scatter partons for perturbatively calculable extended photons. The culprit was shown to be the $k_\perp$ of the photon, something illustrated in figure (29.) The ability to reconstruct hard scatter kinematics hinges on the amount of $k_\perp$ in the hard scatter process. If $k_\perp$ does not exist, a sufficiently high jet $E_\perp$ cut allows good hard scatter reconstruction.

If $k_\perp$ does exist, then the dramatic asymmetry between the $E_\perp$'s of the two true hard scatter jets makes it impossible to accurately measure the kinematics of the $k_\perp$ retarded jet. The following discussion is coached in terms of leading order language, but this will be followed by a supplementary higher order discussion.

In the event that the $p_\perp$ of one of the hard scatter jets is substantially retarded by the $k_\perp$ of the spectator system, it is likely that the $p_\perp$ of the spectator system $(-\vec{k_\perp})$ is sufficiently high to form a jet that is visible in the detector. We have seen that after high $E_\perp$ cuts on the reconstructed jets are made, we can adequately reproduce the kinematics of the two highest $E_\perp$ partons. However, we see a fundamental ambiguity in interpretation. In the event that both hard scatter jets are visible in the calorimeter, we understand the reconstructed kinematics to reflect the QCD leading order two body process. However, in the event one hard scatter jet is not visible, but the spectator system is of high enough $E_\perp$ to hit the detector, the interpretation is more murky. One of the visible jets is associated with the hard scatter system while the other is associated with an unrelated vertex. Such a behavior reduces the correlation between the two reconstructable jets.

At higher order, the differentiation between the various photon types is no longer applicable. What has been called a perturbatively calculable photon is (in higher order) a direct photon with an additional α_s vertex (see figure (116).) We have seen that the kinematics of the hard scatter (i.e. leading order) system can be adequately reconstructed for direct and VDM photons and that the leading order kinematics of extended photons are not always well reconstructed. However, the kinematics of the two high $E_\perp$ partons in extended photon scattering can be reconstructed. This is tantamount to saying that the higher order interpretation of extended photons suggests that two of the three partons are easily resolvable, but one is not.[22] Coached in this language, we see that the experimental results are (in this model) quite meaningful but that the theoretical calculation necessary to understand them is more complicated than initially hoped.

As the $k_\perp$ associated with the hard scatter process is pivotal in the ability to

[22]With this jet finder.

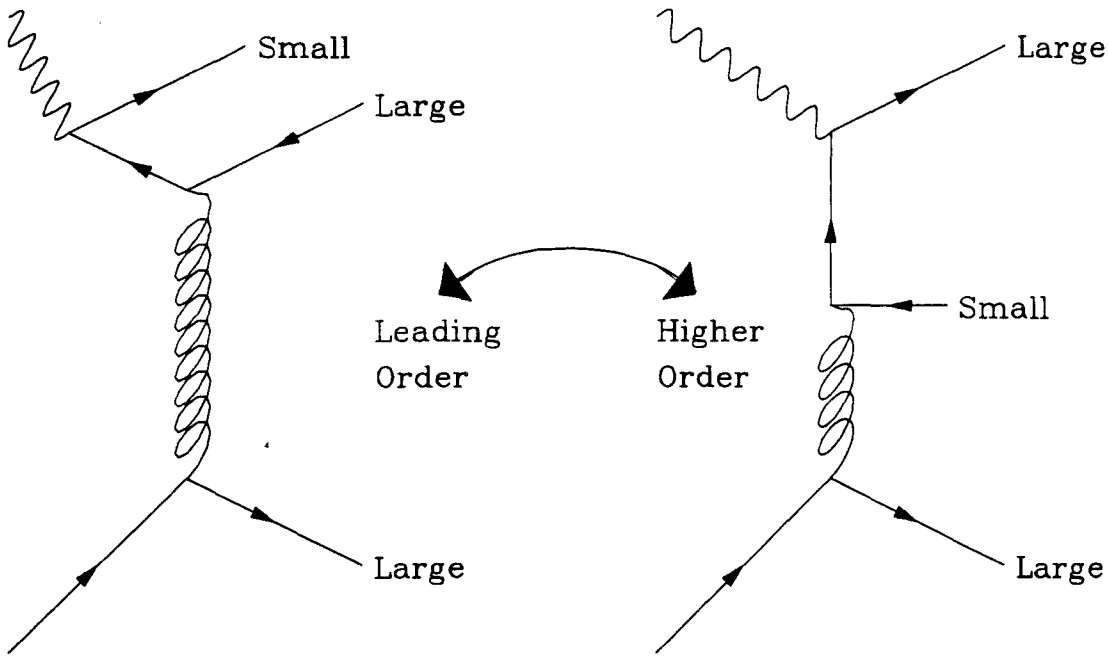

Figure 116: The figure compares two interpretations of a resolved photon type of event. On the left, the photon is interpreted to be a leading order resolved photon. Manifest in this interpretation is the thought that the $E_\perp$ of the recoiling spectator system is small as compared to the leading order hard scatter system. On the right hand side, the possibility that the recoil system can have significant $E_\perp$ (and can exceed the $E_\perp$ of one of the nominally hard scatter system partons) is shown to be a natural consequence of the higher order language. Thus, if the large $k_\perp$ suggested by the TWISTER Monte Carlo is actually present, this figure shows that the leading order ansatz of γp scattering is probably insufficient.

reconstruct hard scatter jet kinematics and to interpret the results of the entire experiment within the framework of the leading order ansatz, I have tried to see if the data sheds light on the amount of $k_\perp$ that is truly present. In order to do this in a convincing way, I decided to do an exhaustive comparison of the data with different Monte Carlo's both with and without $k_\perp$. As a practical matter, a choice needed to be made. Should one try to disentangle the experimental effects from the measurements and compare the result with parton level calculations? Or, should one try to simulate the effects of the experiment, impose these effects on the Monte Carlo, and then compare this result with the uncorrected data? Since it is much easier to demonstrate that the experimental simulation is done correctly than it is to show that the apparatus effects have been removed from the data, I have opted to try the second technique.

Simulation of the experiment requires very close attention to detail. In this case, all of the known experimental effects have been accounted for and include: the photon energy spectrum, multiple bremsstrahlung, acceptance, calorimeter resolutions, detector granularity, variations in response for different particle types, etc. The way in which each of these effects have been modelled has been driven by data, and it is believed that the simulations accurately reflect reality.

With a suitable experimental simulation, it is now possible to compare different Monte Carlo to the uncorrected data distributions. Six different Monte Carlos were tested. These were the LUND models: LUCIFER (direct photons), TWISTER (perturbatively calculable extended photons, both with $k_\perp$ on and off), TWISTER (VDM photons), HERWIG (extended photons, enhanced underlying event off) and HERWIG (direct photons, enhanced underlying event off). For the LUND models, the independent fragmentation model was used.

The first thing that is observed is that none of the Monte Carlos reproduce the triggered data (i.e. the event satisfied the trigger, but no jet finding conditions were imposed.) The data is better represented by the various extended photon models, but the agreement is not very good. As the jet finding requirements are imposed, and the reconstructed jet minimum $E_\perp$ thresholds are increased, the agreement improves.

While a number of the observed distributions have no resolving power (i.e. all Monte Carlos look exactly like the data, c.f. E_{BEAM}), some distributions do exclude certain models.

For the LUND based Monte Carlos, one can see that for the reconstructed jet $E_\perp$ bin $E_\perp > 2$ GeV there are a number of distributions that are visibly different for the different models (c.f. figure (53).) However, as the jet $E_\perp$ distributions are increased, the differences between the distributions narrow considerably. This is taken to be a selection of the event topologies by the cuts. However, since most distributions do not become identical at the high jet $E_\perp$ cuts one can argue that one retains some of the resolving power between different photon types, albeit at a more subtle level.

Another important feature seen in both the Monte Carlo and data distributions is the differences between the trigger types for the low $E_\perp$ bins and the much increased overlap at higher $E_\perp$. These effects are not subtle. At low jet $E_\perp$ (or the triggered level,) the different topologies of the two trigger types shape the data. The Global trigger requires a lot of $E_\perp$ in the MCAL, with no requirement on its disposition. In terms of total MCAL $E_\perp$, the 2HI trigger is a very weak requirement, but mandates that the $E_\perp$ be required to be concentrated in two towers. By definition these triggers select the kind of events that are seen, and the effects are seen in the presented distributions.

As the jet $E_\perp$ is increased, the two trigger types coalesce. As has been mentioned before, the fact that 2HI triggers (two towers, both with an $E_\perp > 0.75$ GeV) identically overlap Global triggers (total MCAL $E_\perp > 8$ GeV) when two jets are required, both exceeding $E_\perp > 4$ GeV, is straightforward. The overlap of Global with 2HI is not as obvious. A typical jet contains 20-40 towers within it. If the four GeV jet $E_\perp$ were uniformly distributed across the jet, each tower would contain between 0.1 and 0.2 GeV of $E_\perp$, depending on the total number of towers. In the lab frame the towers are of different size. If one assumes the $E_\perp$ is uniformly distributed in space, where each tower will integrate a different fraction of the $E_\perp$, one would expect the larger $E_\perp$ fractions to be on the order of 0.2 GeV or so. The fact that there is almost total overlap between Global and 2HI triggers at jet $E_\perp$'s of 4 GeV is suggestive of a jet

signature.

A pivotal question in the ability to reconstruct parton kinematics from jet measurements hinges on the amount of $k_\perp$ in the photon. If one looks at the plots that one might expect to reflect $k_\perp$ (e.g. $k_\perp$, $\Delta\phi$, and $k_{\perp\phi}$ for low jet $E_\perp$ where the extended photon signal is thought to dominate), one is struck by the agreement between TWISTER extended photons ($k_\perp$ on) and the data. If one is to take these plots seriously, TWISTER ($k_\perp$ off) is simply excluded as a possibility. For the nominally $k_\perp$ sensitive plots, TWISTER extended photon ($k_\perp$ off) looks much like LUCIFER direct photon data. This is plausible since both Monte Carlos have little $k_\perp$ as part of their ansatz. TWISTER extended photon ($k_\perp$ on) is favored in these plots and gives a good account of itself in other plots, although the effect is not as marked.

It is expected that at low jet $E_\perp$ the extended photons will dominate, with the direct photon contribution becoming more important at higher jet $E_\perp$'s. This appears to be true, as seen in a number of figures (e.g. figures (51,64,63, 75,87,94,) to mention a few.) However, as the jet $E_\perp$ distributions are raised, the Monte Carlos start to bracket the data, which argues for more equal contributions of the two photon types. Note that this effect appears to be similar for both the LUND and HERWIG Monte Carlos, which argues that the effect is not solely a model dependent result.

Taken as a whole, the HERWIG Monte Carlo does not reproduce our data (especially at low jet $E_\perp$'s) as well as LUND with independent fragmentation. On the whole, the HERWIG Monte Carlo appears to be too jet-like (c.f. figures (86) and (77).) This is somewhat surprising, because HERWIG models our pion data much better than TWISTER. However, the way it does so is by including a phenomenological underlying event. For hadron data, this underlying event has been tuned to account for deficiencies in the HERWIG Monte Carlo. Since we have seen [42] that the standard underlying event is too large for our photon data, this enhancement has been turned off for this dissertation. It would appear that a subdued underlying event is necessary to reproduce our lower $E_\perp$ photon data.

If at higher jet $E_\perp$'s, the data is bracketted by the Monte Carlo, it is reasonable to interpret this as the data containing a mixture of the different types of photons.

In order to explore this idea, I first determined the expected mixture of photons from the LUND Monte Carlos. I then tried to fit a mix of the dominant photon types to the data and came up with a fractional mix that is in good agreement with the Monte Carlo predictions. This is taken to be suggestive evidence that the fractional mix seen in the data is as predicted by the LUND Monte Carlo. The fact that only 55% of the investigated distributions allowed for such a fit highlights the caution one must have while evaluating this result.

The $E_\perp$ flow plots are not conceptually different than the other plots discussed above. However, there is a very important point that can be drawn by using them. When investigating the two jet required plots (for high jet $E_\perp$ cuts) the data and the Monte Carlo agree with each other quite well. The different photon types are not very different, but in order to get agreement with the data, one must mix the direct and extended photons in the ratios predicted by the Monte Carlos. However, when one instead inspects the one-jet-required $E_\perp$ flow plots, the data and Monte Carlo are in varying degrees of disagreement. The peak showing the jet that is required is all but indistinguishable between all Monte Carlos and the data. However, the peak at 180° is always less pronounced in the data. The fact that the required peak in the one-jet-found data looks so much alike and the peak at 180° in the two-jet-found data is so much better than the one-jet-found data suggests that our cuts are quite restrictive. The interpretation of the suppression of $E_\perp$ flow at 180° for the one-jet-found data argues that requiring one jet only is an in-between state between triggered data and normal jet found data. What it says is that the $E_\perp$ flow that hits the MCAL is less balanced on the average than in the Monte Carlos.

Given that a suspicious soul might think that the agreement of the data and the Monte Carlo has been forced by the various triggering and jet finding cuts, I investigated a technique for seeing a jet signal that is as unbiased as possible. If jets are truly present, as the MCAL $E_\perp$ is increased, one would expect that the jets would become more pronounced, dominating the event topology and increasing the overall planarity of the event. When I plotted the $x_\perp$ (MCAL transverse energy, normalized to $\sqrt{s}$) of the event against the average planarity, I found the expected increase at

large $x_\perp$. Individual planarity distributions given for different $x_\perp$'s show a marked change in behavior for $x_\perp \gtrsim 0.55$, and this is taken to be the point at which jet production starts to dominate. The Monte Carlo $x_\perp$ dependence of average event planarity is shown to have the same basic shape as the data, with obvious differences. Within the statistics, the roll over at $x_\perp \sim 0.6$ is present in the data and all the Monte Carlos, with TWISTER extended photon $k_\perp$ on having the best overall agreement.

Taken as a whole, the results of this comparison of the Monte Carlos to the data show reasonable agreement between LUND Monte Carlos (independent fragmentation) and the data. The HERWIG Monte Carlo has poorer agreement for the triggered data and lower $E_\perp$ jet cuts, although this disagreement is less marked for the higher $E_\perp$ jet cuts, where jet data is also more jet-like. The data appears to be a mix of direct and extended photons with fractions essentially as predicted from the LUND Monte Carlo. It appears that there is some experimental evidence for the large $k_\perp$ predicted for perturbatively calculable extended photons.

References

[1] D. Perkins, *Introduction to High Energy Physics*, Addison-Wesley Publishing Company, 3rd Edition, (1987). F.E. Close, *An Introduction to Quarks and Partons*, Academic Press Limited, (1979).

[2] M. Gell-Mann, Phys. Lett., **8**, 214, (1964). G. Zweig, CERN Report 8419/Th 412, (1964).

[3] J.T. Friedman and H.W. Kendall, Ann. Rev. Nucl. Science, **22**, 203, (1972).

[4] R.P. Feynman, Phys. Rev. Lett., **23**, 1415, (1969).

[5] T.F. Walsh, P.M. Zerwas, Phys. Lett., **44B**, 195, (1973).

[6] V.M. Budnev, I.F. Ginzburg, G.V. Meledin, V.G. Serbo, Phys. Rep., **C15**, 4, (1975).

[7] E. Witten, Nucl. Phys. **B20**, 189, (1977).

[8] C.T. Hill, G.G. Ross, Nucl. Phys., **B148**, 373, (1979).

[9] C. Peterson, T. Walsh, P. Zerwas, Nucl. Phys. **B174**, 424, (1980).

[10] C.H. Lewellyn-Smith, Phys. Lett., **79B**, 83, (1978).

[11] W.R. Frazier, J. Gunion, Phys. Rev. **D20**, 147, (1979).

[12] W.A. Bardeen, A.J. Buras, Phys. Rev., **D20**, 166, (1979).

[13] D.W. Duke, J.F. Owens, Phys. Rev., **D22**, 2280, (1980).

[14] I. Antoniadis and G. Grunberg, Nucl. Phys., **B161**, 163, (1985).

[15] W. Wagner, RWTH Aachen preprint PITHA 83/03, (1983).

[16] Ch. Berger and W. Wagner, Phys. Rep., **146**, Nos. 1 & 2, 1, (1987).

[17] C.B. Newman et al., Phys. Rev. Lett., **42**, 951, (1979).

[18] M. Drees and K. Grassie, Z. Phys., **28C**, 451-462, (1985).

[19] H. Abramowicz, K. Charchula, A. Levy, Phys. Lett., **269B**, 458-464, (1991).

[20] JADE Collaboration, W. Bartel, et al., Phys. Lett., **107B**, 163, (1981).

[21] JADE Collaboration, W. Bartel, et al., Phys. Lett., **121B**, 203, (1983).

[22] JADE Collaboration, W. Bartel, et al., Z. Phys., **24C**, 231-245, (1984).

[23] PLUTO Collaboration, Ch. Berger, et al., Phys. Lett., **107B**, 168, (1981).

[24] PLUTO Collaboration, Ch. Berger, et al., Phys. Lett., **142B**, 111, (1984).

[25] PLUTO Collaboration, Ch. Berger, et al., Nucl. Phys., **B281**, 365-380, (1987).

[26] CELLO Collaboration, H.J. Behrend, et al., Phys. Lett., **126B**, 391, (1983).

[27] TASSO Collaboration, M. Althoff, et al., Z. Phys., **31C**, 527-535, (1986).

[28] TPC/Two-Gamma Collaboration, H. Aihara, et al., Phys. Rev. Lett., **58**, 97, (1987).

[29] TPC/Two-Gamma Collaboration, H. Aihara, et al., Z. Phys., **34C**, 1-13, (1987).

[30] AMY Collaboration, T. Sasaki, et al., Phys. Lett., **252B**, 491, (1990).

[31] AMY Collaboration, R. Tanaka, et al., Phys. Lett., **277B**, 215-220, (1992).

[32] G. Flügge, "Jet Fragmentation", from *The Quark Structure of Matter: Proceedings of a topical European meeting in the Rhine Valley*, Ed. M. Jacobs and K. Winter, (1986), Strasbourg-Karlsruhe, 26-Sep - 01-Oct 1985.

[33] F.E. Paige "Simulation of Hadronic Reactions," in the Proceedings of the Oregon Meeting of the Division of Particles and Fields of the APS, Rudolph C. Hwa, Editor, 1985, page 566.

[34] T. Sjöstrand and M. Bengtsson, Computer Physics Commun., **43**, 367, (1987).

[35] G. Marchesini, et al., Cambridge preprint Cavendish-HEP-90/26, (DESY preprint DESY-91-048), also published as Computer Physics Commun., **67**, 465-508, (1992).

[36] G. Alner et al., Nucl. Phys. **B259**, 209, (1991).

[37] G. Altarelli and G. Parisi, Nucl. Phys., **B126**, 298, (1977).

[38] F. Halzen and A. Martin, *Quarks & Leptons: An Introductory Course in Modern Particle Physics*, John Wiley & Sons, (1984).

[39] M. Bengtsson and T. Sjöstrand, Nucl. Phys., **B289**, 810, (1987).

[40] D. Adams, et al., *First Observation of Jet Production with a Real Photon Beam*, to be submitted to Phys. Rev. Lett.

[41] D. Lincoln, *On Determining X_{Bj} from Jet Measurements*, in the Proceedings of the 1992 Meeting of the Division of Particles and Fields of the American Physical Society, Fermilab, November 1992.

[42] D. Naples, *A-Dependence and $K_{t\phi}$ of Photoproduced Jets*, in the Proceedings of the 1992 Meeting of the Division of Particles and Fields of the American Physical Society, Fermilab, November 1992.

[43] J. Bjorken, I. Knowles, J.F. Owens, T. Sjöstrand, personal communication, (1992).

[44] D. Amati and G. Veneziano, Phys. Lett., **83B**, 87, (1979).

[45] P. Kasper et al., *Wide Band to "Double Band" Upgrade*, FNAL Pre-print TM-1552, June 1988.

[46] J. Butler et. al., *Design for a New Wide Band Neutral Beam for the Tevatron*, Fermilab Technical Memo 963.

[47] P.L. Frabetti et al., NIM **A329**, 62-78, (1993).

[48] G. Alimonti, personal communication. G. Alimonti et al., NIM, **A314**, 411, (1992).

[49] G. Morrow, *Calibration of the E683 Main Calorimeter*, Rice University MA Thesis, (1993), Unpublished.

[50] K. Johns, *The Calibration, Response, and Energy Resolution of a Segmented, Sampling Hadron Calorimeter Between 10 and 130 GeV*, Rice University MA Thesis, (1983) Unpublished.

[51] W. Selove, et al., NIM, **161**, 233 (1979).

[52] D. Lincoln and D. Naples, NIM, **A332**, 23, (1993).

[53] D. Lincoln, *Design and Construction of a Beam Calorimeter for E683 at FNAL*, Rice University MA Thesis, (1989) Unpublished.

[54] M. Arenton, et al., IEEE Trans. on Nucl. Sci., **NS30**, 193, (1983).

[55] L. Cormel, et al., IEEE Trans. Nucl. Sci., **NS29**, 307, (1982).

[56] D. Lincoln, *Summary of BCAL Performance Decay*, Unpublished.

[57] D. Lincoln, *E683 BCAL Response Summary Final Report*, Unpublished.

[58] FNAL VAXONLINE manuals, available from the FNAL computing division library. The specific subset used was: EVENT_BUILDER, OUTPUT, BUFFER_MANAGER, RUN_CONTROL, DAQ and the supporting software.

[59] D. Lincoln, *E683 UNPACKER Usage Guide*, Unpublished.

[60] D. Lincoln, *E683 ANALYZER Usage Guide*, Unpublished.

[61] J. Clement, *Topdrawer - Bonner Lab Version - A graphics and data analysis program*, Unpublished. (Note: e-mail inquiries can be sent to INTERNET%"CLEMENT@PHYSICS.RICE.EDU" or DECNET FNBIT::RIPHYS::CLEMENT.)

[62] M. Corcoran, *E683 Analysis Note: Summary of Anti-Muon Cuts*, Unpublished.

[63] B. Flaugher, K. Meier, 'A Compilation of Jet Finding Algorithms', FERMILAB-Conf-90/248-E, also in 1990 Summer Study on High Energy Physics, *Research Directions for the Decade*, Snowmass, Colorado, June 25 - July 13, 1990.

[64] V. Blobel, *Unfolding methods in high-energy physics experiments*, published in the proceedings of the 1984 CERN School of Computing, also CERN 85-09.

[65] G. Ingelman, *LUCIFER - A Monte Carlo for High-$p_\perp$ Photoproduction*, DESY 87-018, also CERN W5047.

[66] G. Ingelman, *TWISTER - A Monte Carlo for QCD High-$p_\perp$ Scattering*, DESY 86-131 plus updates January 1987, also CERN W5048.

[67] T. Sjöstrand, *The Lund Monte Carlo for Jet Fragmentation and e^+e^- Physics - JETSET version 6.2*, LU TP 85-10, also CERN W5035.

[68] D.W. Duke, J.F. Owens, Phys. Rev., **D26**, 1600, (1982).

[69] D. Naples, *A-Dependence of Photoproduced Jets and Comparison with Hadroproduction*, University of Maryland Ph.D. Thesis, Unpublished, (1993).

[70] M. Traynor, Personal communication.

[71] M. Banner, et al., Phys. Lett., **118B**, 203, (1982).

[72] G. Arnison, et al., Phys. Lett., **123B**, 115, (1983).

[73] T. Akesson, et al., Phys. Lett. 123B, 133, (1983); **118B**, 185, (1982); **118B**, 193, (1982); **128B**, 354, (1983).

[74] C. DeMarzo, et al., Phys. Lett., **112B**, 173, (1982); Nucl. Phys., **B211**, 375, (1983); **B234**, 1, (1984).

[75] B. C. Brown, et, al., Phys. Rev. **D29**, 1895, (1984).

[76] K. Johns, *A Study of High Transverse Energy Hadron-Hadron Collisions at 400 GeV/c Using a QCD Monte-Carlo Including Initial and Final State Gluon Bremsstrahlung*, Rice University Ph.D. Thesis, (1985), Unpublished.

A Definitions of x_{Bj}

A.1 Massless Kinematics

Assume that a parton (1) comes from a beam particle (A) and a parton (2) comes from a beam particle (B) (see figure (5).) Partons 1 and 2 undergo some sort of interaction and go to a two parton final state (i.e. pre-fragmentation) with the final state partons denoted 3 and 4. Then the following Lorentz invariant derivation applies. One starts with a *definition* of x.

$$\begin{aligned} p_1^\mu &\equiv x_1 P_A^\mu \\ p_2^\mu &\equiv x_2 P_B^\mu \end{aligned} \tag{12}$$

Writing the simple 4-vector energy conservation:

$$p_1^\mu + p_2^\mu = p_3^\mu + p_4^\mu \tag{13}$$

substituting in equations (12), one gets

$$x_1 P_A^\mu + x_2 P_B^\mu = p_3^\mu + p_4^\mu \tag{14}$$

multiplying equation (14) by $P_{A\mu}$ and $P_{B\mu}$ respectively yields the following:

$$\begin{aligned} x_1 P_A^\mu \cdot P_{A\mu} + x_2 P_B^\mu \cdot P_{A\mu} &= (p_3^\mu + p_4^\mu) \cdot P_{A\mu} \\ x_1 P_A^\mu \cdot P_{B\mu} + x_2 P_B^\mu \cdot P_{B\mu} &= (p_3^\mu + p_4^\mu) \cdot P_{B\mu} \end{aligned}$$

noticing that these two equations are linear equations in x_1 and x_2, one may solve

$$\begin{aligned} x_1 &= \frac{(P_{B\mu} \cdot P_B^\mu)\,[(p_3^\mu + p_4^\mu) \cdot P_{A\mu}] - (P_{B\mu} \cdot P_A^\mu)\,[(p_3^\mu + p_4^\mu) \cdot P_{B\mu}]}{(P_A^\mu \cdot P_{A\mu})(P_B^\mu \cdot P_{B\mu}) - (P_{B\mu} \cdot P_A^\mu)^2} \\ x_2 &= \frac{(P_{A\mu} \cdot P_A^\mu)\,[(p_3^\mu + p_4^\mu) \cdot P_{B\mu}] - (P_{A\mu} \cdot P_B^\mu)\,[(p_3^\mu + p_4^\mu) \cdot P_{A\mu}]}{(P_A^\mu \cdot P_{A\mu})(P_B^\mu \cdot P_{B\mu}) - (P_{B\mu} \cdot P_A^\mu)^2} \end{aligned} \tag{15}$$

Notice that this derivation is completely Lorentz invariant with no assumptions other than conservation of 4-momentum and the definitions of x listed in equations (12). In order to make equations (15) more familiar, some common, but restrictive assumptions are needed.

Recall that $P_A^\mu \cdot P_{A\mu} = M_A^2$ is the mass of hadron (A) squared and similarly for (B) $P_B^\mu \cdot P_{B\mu} = M_B^2$. These masses are often set to zero. Also recall that

$$s = (P_A^\mu + P_B^\mu)^2 = (P_A^\mu \cdot P_{A\mu}) + 2(P_A^\mu \cdot P_{B\mu}) + (P_B^\mu \cdot P_{B\mu})$$

and so $s \approx 2(P_A^\mu \cdot P_{B\mu})$. These approximations reduce the equations for x to the somewhat more friendly:

$$\begin{aligned} x_1 &= \frac{2(p_3^\mu + p_4^\mu) \cdot P_{B\mu}}{s} \\ x_2 &= \frac{2(p_3^\mu + p_4^\mu) \cdot P_{A\mu}}{s} \end{aligned} \tag{16}$$

Equation (9) shows equation (16) written in the CM frame of the beam-target system.

A.2 Generalized Kinematics

In the event that it is appropriate to include the virtual masses of both the incoming and outgoing partons and intrinsic (primordial) $p_\perp$, a more generalized approach is needed. The following derivation is done in the beam-target CM system. Using the light-cone momentum fraction as the proper definition of x:

$$x = \frac{e + p_z}{E + P_z}$$

where lower case letters denote parton quantities and upper case denotes hadronic quantities. Note that P_z is always taken to be positive. This is from the definition, where each hadron defines its own frame and its direction of travel is always in the locally $+\hat{z}$ direction. One must be careful of the implications of such a definition and the consequences are pointed out below.

Given such a definition, it is possible to calculate a kinematic relationship between initial state x and (mostly) final state quantities. We start with the simple definitions of x_1 and x_2.

$$\begin{aligned} x_1 &= \frac{e_1 + p_{z1}}{E_A + P_{zA}} \\ x_2 &= \frac{e_2 + p_{z2}}{E_B + P_{zB}} \end{aligned}$$

which can be trivially manipulated into the more useful:

$$\begin{aligned} e_1 + p_{z1} &= x_1(E_A + P_{zA}) \\ e_2 + p_{z2} &= x_2(E_B + P_{zB}) \end{aligned} \tag{17}$$

Now, using the relationship $e^2 - \vec{p} \cdot \vec{p} = m^2$,

$$\begin{aligned} (e_1 - p_{z1})(e_1 + p_{z1}) &= m_1^2 + p_{\perp 1}^2 \\ (e_2 - p_{z2})(e_2 + p_{z2}) &= m_2^2 + p_{\perp 2}^2 \end{aligned}$$

which may be rearranged and combined with equations (17):

$$\begin{aligned} (e_1 - p_{z1}) &= \frac{m_1^2 + p_{\perp 1}^2}{x_1(E_A + P_{zA})} \\ (e_2 - p_{z2}) &= \frac{m_2^2 + p_{\perp 2}^2}{x_2(E_B + P_{zB})} \end{aligned} \tag{18}$$

Now write the energy and momentum conservation equations. (Note that the second equation has an asymmetry in it between partons 1 and 2 due to the definition of p_z (or $\hat{z}$) in the light-cone momentum fraction x.)

$$\begin{aligned} e_1 + e_2 &= e_3 + e_4 \\ p_{z1} - p_{z2} &= p_{z3} + p_{z4} \end{aligned}$$

Adding and subtracting these two equations yields

$$\begin{aligned} e_1 + p_{z1} + e_2 - p_{z2} &= e_3 + p_{z3} + e_4 + p_{z4} \\ e_1 - p_{z1} + e_2 + p_{z2} &= e_3 - p_{z3} + e_4 - p_{z4} \end{aligned} \tag{19}$$

substituting in equations (17) and (18), one gets

$$\begin{aligned} x_1(E_A + P_{zA}) + \frac{m_2^2 + p_{\perp 2}^2}{x_2(E_B + P_{zB})} &= e_3 + p_{z3} + e_4 + p_{z4} \\ \frac{m_1^2 + p_{\perp 1}^2}{x_1(E_A + P_{zA})} + x_2(E_B + P_{zB}) &= e_3 - p_{z3} + e_4 - p_{z4} \end{aligned} \tag{20}$$

This must be solved for x_1 and x_2. Since this equation is somewhat messy, the following definitions are made:

$$\begin{array}{llll} X_1 = x_1(E_A + P_{zA}) & & X_2 = x_2(E_B + P_{zB}) & \\ M_1 = m_1^2 + p_{\perp 1}^2 & & M_2 = m_2^2 + p_{\perp 2}^2 & \\ A_+ = e_3 + p_{z3} + e_4 + p_{z4} & & A_- = e_3 - p_{z3} + e_4 - p_{z4} & \end{array}$$

so equations (20) can be written architecturally as:

$$X_1 + \frac{M_2}{X_2} = A_+$$
$$\frac{M_1}{X_1} + X_2 = A_-$$

which may be solved to give the following result

$$\begin{aligned} X_2 &= \frac{A_+A_- + M_2 - M_1 + \sqrt{(M_1 - M_2 - A_+A_-)^2 - 4M_2A_+A_-}}{2A_+} \\ X_1 &= A_+ - \frac{M_2}{X_2} \end{aligned} \tag{21}$$

Notice that m_1 and m_2 can be (*and usually are*) imaginary numbers. This is due to the virtuality of the incoming parton states and implies that M_1 and/or M_2 can be negative.

This leads us to another problem. While equations (21) primarily contain final state information, they also contain information from both the incident parton virtuality scale and the primordial transverse momentum, both intrinsically unmeasurable quantities. (These dependencies are contained entirely in the M_1 and M_2 terms.) So in the case where these quantities are significant, it is impossible to determine the x variables from final state measurements.

In the event that the mass and primordial k_t are not relevant, it is not possible to simply set M_1 and M_2 to zero in equations (21,) due to divisions by zero in the derivation. In this case, it is necessary to apply these conditions much earlier (say in equation (18).) In this limit, the equivalent to equations (21) is:

$$x_{1,2} = \frac{E_3 \pm p_{z3} + E_4 \pm p_{z4}}{\sqrt{s}} \tag{22}$$

B Jet Finding Algorithm

The jet finding algorithm used in this dissertation was the following:

1. Find those particles/towers with an $E_\perp > 0.5$ GeV. Order them in $E_\perp$.

2. Boost each particle/tower from the lab to the CM of the γp system. Assume each particle/tower is massless in the boost.

3. Use the towers described in (1.) as jet seeds.

   a. Start with the hottest remaining seed. Call it a jet candidate.

   b. Calculate the $(\eta/y, \phi)$ centroid of those particles/towers within a radius R of the jet candidate. Notice that conventional wisdom mandates that you use a simple (η, ϕ) jet cone, but this requires that the particles and jets be sufficiently massless that the assignment $y = \eta$ is valid. For the case of E683, the jet mass is not small as compared to the jet energy. Therefore, we realize that the technically correct type of centroid to find is (y, ϕ). For the particles and towers, $y = \eta$ is a good approximation, but not for the jet ensemble. Because of this, a hybrid jet finder is used. The improvement in jet finding is small and is visible only for very low jet $E_\perp$'s. Recall the definitions of y, η, and R (with θ and ϕ being the polar and azimuthal angle respectively.)

$$\begin{aligned} y &= \frac{1}{2}\ln[\frac{E+p_z}{E-p_z}] \\ \eta &= -\ln(\tan(\frac{\theta}{2})) \\ R &= \sqrt{(\eta_{\text{particle}} - y_{\text{jet}})^2 + (\phi_{\text{particle}} - \phi_{\text{jet}})^2} \end{aligned}$$

   c. The centroids mentioned in the (3.b) are calculated by finding the jet's $(E, \vec{p})$ which are defined as the vector sum of the momenta and the scaler sum of the energies of the particles/towers that make up the jet and then deducing the jet's ϕ, θ and y.

$$E = \sum_i E_i$$

$$p_{x,y,z} = \sum_i p_{(x,y,z)i}$$

d. The $E_\perp$ contained within the jet cone (i.e. those particles/towers within a radius R) is calculated by finding the energy contained and multiplying it by the $\sin\theta$ of the jet direction.

e. This $E_\perp$ is compared with the $E_\perp$ of the jet candidate. If the change in $E_\perp$ is less than a maximum $E_\perp$ shift, the jet is declared to have settled down. If the change in $E_\perp$ is greater than this maximum, the newly determined jet axis is declared to be a jet candidate and the program returns to step (3.b). There is a maximum of 5 iterations allowed. If the found jet $E_\perp$ has not settled down, the program gives up and returns to (3.a), with the next hottest remaining seed as the jet candidate.

f. If the $E_\perp$ shift is less than the maximum, then the jet is declared to have settled down. The $E_\perp$ of this jet is compared to a minimum jet $E_\perp$ cut off. If the jet candidate has less $E_\perp$ than the cut off, the candidate is declared to not be a jet and the program gives up and returns to (3.a), with the next hottest remaining seed as the jet candidate.

g. If the jet candidate $E_\perp$ exceeds the cut off, it is declared to be a jet and the jet's various kinematic variables are returned to the user. Those particles/towers used in the jet are declared 'off limits' and can not be used for subsequent jet finding attempts. This includes those towers declared to be seeds in (1.)

h. This loop is repeated until all seeds have been tried as jet candidates or included in a found jet.

4. As a 'last gasp' effort, of those particles/towers that had not been associated with a jet, the three highest in $E_\perp$ are ordered and defined to be a new series of seeds. The initial seeds are excluded, since they have either been used or tried and failed. Step (3.) is repeated for these new seeds and any additional found jets are noted.

5. At this point the jet finder reports the number of jets found, their kinematic measurements and then quits.

6. The tunable jet finding parameters used were:

Tunable Parameter	**Default Value**
R	1.0
Minimum jet finding seed ($E_\perp$)	0.5 GeV
Maximum $E_\perp$ shift between iterations	0.1 GeV
Minimum jet $E_\perp$	2.0 GeV

C Justification of Some Aspects of Cone Based Jet Finding Algorithms

In the jet finding algorithm used in this thesis (see Appendix (B)) a cone radius R has bee defined $R = \sqrt{\Delta\phi^2 + \Delta\eta^2}$. η is a non-linear function of θ, the polar angle, and it is therefore not obvious that η and ϕ should both contribute to R with equal weight. At the very least, one would expect a relationship $R = \sqrt{\Delta\phi^2 + (a\Delta\eta)^2}$ where a is a constant, and more likely, one would expect a definition for R of $R = f(\Delta\phi, \Delta\eta)$ where f is a not yet determined function. Why should $\Delta\phi$ and $\Delta\eta$ both contribute to R so symmetrically?

Another question one must ask is concerned with the relationship between the Lorentz invariant mass algorithms [63] and the (η, ϕ) cone based algorithms. The answer to both questions are related and are surprisingly easy to answer.

A rather simple, but surprisingly clarifying picture of what constitutes a jet is the following: if two particles come from a single point (e.g. the interaction point) at wildly different angles, they probably are not in the same jet. Further, if two particles move with a non-zero angle between them, the two body system must have an invariant mass.

So consider two massless particles (1) and (2) travelling with four-momentum vectors given in terms of $(\phi, \eta, E_\perp)$ which is equivalent to $(\phi, \theta, E_\perp)$ and, along with the massless condition, fully describes the four-vector kinematics of each particle. Further define the angle $\Delta\psi$ to be the three dimensional angle between the two particles (determined by the three-vector dot product.) Then the invariant mass squared of the (1,2) system can be written:

$$\begin{aligned} (p_1^\mu + p_2^\mu)^2 &\overset{m_1=m_2=0}{=} 2p_1^\mu \cdot p_{2\mu} \\ &= 2E_1E_2(1 - \cos\Delta\psi) \end{aligned} \tag{23}$$

which for $\Delta\psi$'s that aren't too large can be approximated by the usual Taylor series

$\cos\Delta\psi = 1 - \Delta\psi^2/2! + \cdots$ and therefore

$$(p_1^\mu + p_2^\mu)^2 \simeq E_1 E_2 \Delta\psi^2 \tag{24}$$

Also recall that $p^\mu = (E, p_x, p_y, p_z) = E_\perp(\cosh\eta, \cos\phi, \sin\phi, \sinh\eta)$ (this is easy to verify for massless kinematics), we see

$$\begin{aligned} 2p_1^\mu \cdot p_{2\mu} &= 2E_{\perp 1}E_{\perp 2}(\cosh\eta_1\cosh\eta_2 - \cos\phi_1\cos\phi_2 - \sin\phi_1\sin\phi_2 - \sinh\eta_1\sinh\eta_2) \\ &= 2E_{\perp 1}E_{\perp 2}(\cosh\Delta\eta - \cos\Delta\phi) \end{aligned} \tag{25}$$

where $\Delta\eta = \eta_1 - \eta_2$ and $\Delta\phi = \phi_1 - \phi_2$. If the particles are near each other (i.e. likely to be part of the same jet,) then $\cosh\Delta\eta$ and $\cos\Delta\phi$ can be expanded and one gets

$$\begin{aligned} 2p_1^\mu \cdot p_{2\mu} &= 2E_{\perp 1}E_{\perp 2}(1 + \frac{\Delta\eta^2}{2} + \cdots - 1 + \frac{\Delta\phi^2}{2} + \cdots) \\ &\simeq E_{\perp 1}E_{\perp 2}(\Delta\eta^2 + \Delta\phi^2) \end{aligned} \tag{26}$$

Combining equations (23), (24) and (26) one finds

$$E_1 E_2 \Delta\psi^2 = E_{\perp 1}E_{\perp 2}(\Delta\eta^2 + \Delta\phi^2) \tag{27}$$

While the structure of the LHS is unclear, the RHS is constituted of only Lorentz invariant quantities which implies the LHS must be Lorentz invariant as well and so finally,

$$\Delta\eta^2 + \Delta\phi^2 = \frac{E_1 E_2 \Delta\psi^2}{E_{\perp 1}E_{\perp 2}} \equiv R^2 \tag{28}$$

which is again a Lorentz invariant equation. Thus the isomorphic nature of the (η, ϕ) metric is shown, as is the linkage between invariant mass and cone based algorithms.

A final note must be made. Equation (28) shows the physical meaning of R when $\theta_1 \simeq \theta_1 \simeq 90°$. Then $E \simeq E_\perp$ and $R \simeq \Delta\psi$. As the particles deviate from 90°, the interpretation of R becomes less clear. However, if both particles are at $\theta \simeq 45°$, then the assignment $R^2 = \Delta\psi^2$ is still valid at the factor of two level.